Molecular sensors for evaluating substandard Anti-retroviral medication using Surface-enhanced Raman spectroscopy.

Setumo Lebogang Thobakgale

A thesis submitted in fulfilment of the requirement for the

degree of

Doctor of Philosophy in Physics

School of Chemistry and Physics

27 March 2023

Molecular sensors for evaluating substandard Anti-retroviral medication using Surface-enhanced Raman spectroscopy.

Setumo Lebogang Thobakgale

Supervisor: Dr. Patience Mthunzi-Kufa

Co-supervisor: Dr. Yaseera Ismail

Co-supervisor: Dr. Saturnin Ombinda Lemboumba

A thesis submitted in fulfilment of the requirement for the

degree of

Doctor of Philosophy in Physics

School of Chemistry and Physics

EXAMINER'S COPY

27 March 2023

As the candidate's supervisor, I have approved this thesis for submission.

Signed.....[redacted]..... Date.....28 March 2023.....

Declaration – Plagiarism

I, Setumo Lebogang Thobakgale, declare that;

1. The research reported in this thesis, except where otherwise indicated, is my original research.

2. This thesis has not been submitted for any degree or examination at any other university.

3. This thesis does not contain other persons' data, pictures, graphs or other information, unless specifically acknowledged as being sourced from other persons.

4. This thesis does not contain other persons' writing, unless specifically acknowledged as being sourced from other researchers. Where other written sources have been quoted, then:

(a) Their words have been re-written, but the general information attributed to them has been referenced,

(b) Where their exact words have been used, then their writing has been placed in italics and inside quotation marks and referenced.

5. This thesis does not contain text, graphics or tables copied and pasted from the Internet, unless specifically acknowledged, and the source being detailed in the thesis and in the references sections.

Signed: 

Date: 27/03/2023

Declaration – Publications

1. Thobakgale SL, Ombinda-Lemboumba S, Mthunzi-Kufa P. A Molecular Study of Aspirin and Tenofovir Using Gold/Dextran Nanocomposites and Surface-Enhanced Raman Spectroscopy. Molecules. 2022;27(8).

2. Thobakgale SL, Ombinda-Lemboumba S, Mthunzi-Kufa P. Chemical Sensor Nanotechnology in Pharmaceutical Drug Research. Nanomaterials. 2022;12(15).

3. Ombinda Lemboumba, Saturnin & Manoto, Sello & Maphanga, Charles & Malabi, Rudzani & Thobakgale, Lebogang & Lugongolo, Masixole & Mthunzi-Kufa, Patience. Raman spectroscopy and gold thin film for biosensing and detection. (2020). 92. 10.1117/12.2546617.

4. Manoto, Sello & Elhussein, Ahmed & Malabi, Rudzani & Thobakgale, Lebogang & Ombinda Lemboumba, Saturnin & Attia, Yasser & Kasem, Mohamed & Mthunzi-Kufa, Patience. Exploring optical spectroscopic techniques and nanomaterials for virus detection. Saudi Journal of Biological Sciences. (2021). 28. 78-89. 10.1016/j.sjbs.2020.08.034.

5. Lebogang Thobakgale, Sello Manoto, Saturnin Ombinda Lemboumba, Patience Mthunzi-Kufa, "Surface-enhanced Raman spectroscopy on polymer-graphene oxide scaffolds for drug screening applications," Proc. SPIE 11246, Single Molecule Spectroscopy and Superresolution Imaging XIII, 112460X (13 February 2020); https://doi.org/10.1117/12.2546455

6. Lebogang Thobakgale, Saturnin Ombinda Lemboumba, and Patience Mthunzi-Kufa "Investigation and calibration of non-essential amino acids using a custom built Raman spectroscopy system", Proc. SPIE 10885, Optical Diagnostics and Sensing XIX: Toward Point-of-Care Diagnostics, 108850N (20 February 2019); https://doi.org/10.1117/12.2509839

7. Thobakgale, SL., Manoto, S., Lemboumba, S. O., & Mthunzi-Kufa, P. (2020, March). Gelatine-based biosensor for molecular screening of aspirin and paracetamol via surface-enhanced Raman spectroscopy. In Synthesis and Photonics of Nanoscale Materials XVII (Vol. 11269, pp. 14-22). SPIE.

Declaration- Achievements

1. Best Master's award, CSIR Excellence awards.2018

2. Presented at BRICS Young Scientist Competittion.2018

3. Best oral presenter at International Conference on Laser Applications, Cairo, Egypt. 2019

4. Best poster presenter at Photonics West conference, SPIE, San Francisco,USA.2020

5. Patent award: A method and system for analyzing a biological sample of label-free cells for presence of an infective agent. ZL 201880020729.1

6. Best Emerging Researcher, CSIR Manufacturing awards. 2022

Dedication

This work is dedicated to my Father, Rev. Moroko Eliphas Thobakgale, your abundant wisdom, guidance and strength has helped me see this project through. Thobakgale sa molokwana, re leboga Modimo, Ditlou, Bashabi le Bakgalaka.

Acknowledgements

The author would like to acknowledge contributions of the following people towards the success of this PhD thesis: Mr Selomo (late), Mr Nirosh Monhallal, Dr Lunga Bam, Dr Sello Manoto, Dr Yaseera, Dr Saturnin Ombinda-Lemboumba for the inspiration, mentorship, technical advice, and thesis compilation.

Special thanks to Dr Patience Mthunzi-Kufa for her supervision, guidance and creating opportunities towards the success of the project.

Finally, thank you to the CSIR, NRF and DSI for providing the facilities and funding in support of the project.

Abstract

Africa has the highest number of people living with HIV and AIDS, with South Africa housing the largest Anti-retroviral treatment (ART) program in the world. In addition, the continent is troubled by the continuing growth of substandard ART medication which is imported from external continents. The World Health Organization also states that due to the limited information on this issue, adequate remedial measures cannot be put into place. As such, this study proposed the application of surface-enhanced Raman spectroscopy (SERS) as a drug screening method for ART. Sensing platforms were synthesized using a combination of metals, crosslinker organic molecules, deposition, and self-assembly methods. The platforms were used for tailored adsorption of three ART medications in their active pharmaceutical ingredient (API) form: Tenofovir (TDF), Lamivudine (LAM) and Dolutegravir (DLG) prior to evaluation with Raman spectroscopy. Molecular interactions, signal enhancement and statistical methods such as linear regression were carried out on the analytes and data from the SERS analysis showed significant differences in the sensing capabilities of the platforms based on the calibration sensitivity, analytical sensitivity, and limit of detection. The molecular composition and chemical functionality of the sensors allowed specific adsorption and preference to the complementary functional groups of the API samples which led to enhanced Raman signals on each platform. From the results obtained, it was concluded that the synthesis of tailored platforms for molecular sensing of ART medication was successful, providing potential application of these sensors in the quality control of anti-retroviral medication. Future work will entail routine molecular screening of ARVs to monitor changes in ART quality with respect to geographical location, shelf life and formulation methods.

Table of Contents

List of Figures

List of Tables

List of Acronyms

PVD- Physical Vapor Deposition

MNP- Metallic nanoparticle

Au- Gold

Ag- Silver

Cit- Citrate

Cys- Cysteamine

API-Active pharmaceutical ingredient

MNP- Metallic nanoparticles

TEM- Transmission Electron Microscopy

RS- Raman spectroscopy

SERS- Surface-enhanced Raman spectroscopy

TDF- Tenofovir Disoproxil Fumarate

LAM- Lamivudine

DLG- Dolutegravir

LOD- Limit of detection

EDS- Energy-dispersive X-ray spectroscopy

FDA- Federal Drug Administration

Preface

The research discussed in this dissertation is carried out in the College of Agriculture, Engineering and Science of the University of Kwa-Zulu Natal, Durban, from January 2019 until December 2022 by Setumo Lebogang Thobakgale under the supervision of Dr Patience-Mthunzi-Kufa and co-supervised by Dr Yaseera Ismail. As the candidate's supervisor, I, Dr Patience Mthunzi-Kufa, agree to the submission of this dissertation.

Signed:..... Date:28 March 2023

As the candidate's co-supervisor, I, Dr Yaseera Ismail, agree to the submission of this dissertation.

Signed:..... Date:28 March 2023

As the candidate's co-supervisor, I, Dr Saturnin Ombinda-Lemboumba, agree to the submission of this dissertation.

Signed:..... Date:28 March 2023

I, Setumo Lebogang Thobakgale, hereby declare that all the material incorporated in this dissertation are my own original work, except where acknowledgement is made by name or in the form of a reference.

The work contained in herein has not been submitted in any form for any degree or diploma to any other institution.

Signed: ..... Date: 27/03/2023

University of KwaZulu-Natal, 27 March 2023

Introduction

Africa has been plagued with the issue of HIV/AIDS related deaths since the 1980s when the virus and syndrome became rampant. Furthermore, the number of people living with the illness keeps increasing year after year across the continent according to the World Health Organization (WHO). This reality implies a continued growth in demand for HIV/AIDS treatment mostly in the form of pharmaceutical drugs. WHO also states that South Africa has the largest budget for antiretroviral treatment (ART) in the world, which makes the country a top consumer of the medication. Unfortunately, the facts outlined above do fall prey to the problem of substandard medication that is being manufactured and sent to the continent for financial gain, which automatically has a negative impact on the quality of health in the various countries of Africa. As such, there is a need for investigation into novel quality control methods that can give insight into the standard of medication and differentiate between the authentic and untrusted products. Since pharmaceutical agents are molecular in nature, an approach from a chemistry standpoint would be a promising starting point to investigate the medication.

Research on nanomaterials and photonics for sensor applications has opened a new window of opportunities in small molecule detection applications. The synthesis of chemical sensor platforms for the purpose of characterizing biological, chemical and environmental related molecules has become a fast-growing area of research. Nanomaterials of gold, silver and other transition metals have been thoroughly investigated and functionalized with various types of molecular connectors or crosslinkers which, together with the metal, form the sensing constituents. Detection of small molecules can occur via different methods; such include the electrical approach in the form of field effect transistors and electrochemical detection cells. Another popular group of methods uses optical detection, such as surface plasmon resonance spectroscopy, UV-Vis spectroscopy and Raman spectroscopy. Other techniques include immunoassays where fluorescence is the main signal detected. In this study, chemical sensors of gold and silver, stabilized with crosslinkers citrate and cysteamine, were synthesized using bench top techniques namely chemical reduction and self-assembly methods. Raman spectroscopy was chosen as the detection method to focus on the molecular vibrations that make up both the chemical sensors and the analytes. A major challenge with the technique is the low signal output and the interference from the glass substrate where the coating is layered. To eliminate the issue, physical vapor deposition of gold and silver thin layers was performed prior to functionalizing with the above-mentioned nanoparticles. The components of the chemical sensors were characterized using UV-Vis spectroscopy and Transmission Electron Microscopy for adsorption, morphology and size distribution. Raman microscopy was used to assess the surface of the chemical sensors prior to application on the analytes. ARV medication Tenofovir (TDF), Lamivudine (LAM) and Dolutegravir (DLG) in active pharmaceutical ingredient form (API) were dropped on the sensors and analyzed for molecular characterization and signal response.

Samples of the APIs were prepared in serial dilutions and used to construct the linear regression performance of selected API Raman peaks. This was done to determine the quality of the

response of the technique by R^2 values. Furthermore, the slopes of the graphs produced gave calibration sensitivity values for the linear assessment which, together with the standard error, were used to determine the analytical sensitivity of the technique. And lastly, another important parameter explored in this study was the limit of detection for the gold and silver chemical sensors, which was essential in elucidating the lowest amount of analyte the sensor can detect.

The findings from the above-mentioned objectives are discussed in terms of molecular interactions, chemical sensor performance and statistical differences. Such a focus on the synthesis of chemical sensors for ARV medication detection using SERS is not well documented in the literature. As such, the study offers a novel approach for manufacturing chemical sensing methods specifically for HIV medication, with the potential of providing a quality control platform, that monitors changes in the supply of the pharmaceutical products provided to government hospitals. The first chapter is a literature view of chemical sensor research focusing on synthesis and applications.

1. Literature Review

The increase in demand for pharmaceutical treatments due to pandemic related illnesses has created a need for increased quality control in drug manufacturing. Understanding the physical, biological, and chemical properties of APIs is an important area of health-related research. As such, research into enhanced chemical sensing and analysis of pharmaceutical ingredients (APIs) for drug development, delivery and monitoring has become immensely popular in the nanotechnology space. Nanomaterial based chemical sensors have been used to detect and analyze APIs related to the treatment of various illnesses pre and post administration. Furthermore, electrical, and optical techniques are often coupled with nano-chemical sensors to produce data for various applications which relates to the efficiencies of the APIs. In this review, we focus on the latest nanotechnology applied to probing the chemical and biochemical properties of pharmaceutical drugs, placing specific interest in the several types of nanomaterial based chemical sensors, their characteristics, detection methods and applications. This study offers insight into the progress in drug development and monitoring research for designing improved quality control methods for pharmaceutical and health related research. Lastly, the work in this chapter has been published in the journal Nanomaterial titled ”Chemical Sensor Nanotechnology in Pharmaceutical Drug Research” https://doi.org/10.3390/nano12152688.

1.1 Introduction

With the surge of pandemic symptoms on the rise, the need for more therapeutic medication is also increasing. Secondly, it is worth noting that with the upcoming variants of the COVID virus, we should expect the demand for medication to increase further. As such, pharmaceutical companies at both the research and industrial phases will experience pressure to produce more drugs in mass without compromising quality control. In the former case, research into drug design is paramount to produce new medication with better properties, fewer side effects and better efficiencies. Once successful, industrial production of new and existing medication will require extensive and thorough quality screening performed in a timely and cost-effective manner. These concerns have inspired the compilation of this review article to assess the current detection, monitoring and analysis methods used in the pharmaceutical industry. Nanomaterials, which are compounds with size dimensions between 1-100 nanometers (nm) play a key role in drug research as adsorption platforms [1-3]. These materials carry special properties such as electrical conductivity, optical transmittance, easy surface modification, thermal conductivity and large surface areas which are all essential requirements of a good chemical and biochemical sensor [4-5]. Furthermore, the chemical modification of nanoparticles allows the design of tailored scaffolds for the recognition and adsorption of analytes. Chemical interactions such as hydrogen bonding, electrostatics, intermolecular forces, pi-pi stacking and ligand binding allow the sensors to collect the analyte for high sensitivity and selectivity applications [6-10].

Another important aspect of chemical sensors is the detection method used to produce the signal. An efficient detector must be able to recognize changes in the sensing platform upon

interaction with the analyte. Therefore, careful consideration needs to be applied when choosing a sensor and detector combination [11-12]. Most research in nanomaterial based pharmaceutical investigations employ electrical and optical detection methods for signal collection [13-14]. In the former case, electrical apparatus such as surface modified electrodes, conductors and electrolytes are combined to form a circuit that can produces electrical signals like impedance, voltage, and currency as a means of analyte detection [15-17]. Examples of electrical methods discussed in this review are field effect transistors (FET) and electrochemical devices [18-20]. Optical detection is also a key feature of this publication where photonics-based methods are explored in relation to pharmaceutical research. Organic molecules like therapeutic drugs interact with light sources to produce signals that are used in detection [21]. Nanomaterials, especially gold and silver offer surface plasmons that produce signal enhancing resonance effects necessary for amplification. Localized Surface Plasmon Resonance (LSPR) is an example of a detection method where surface plasmons are used for the detection of analytes, mostly with the aid of metallic nanoparticles (MNPs) [22-25]. Another consequence of light-matter interaction is the production of inelastic scattered radiation which corresponds to the molecular bond of the analyte. Raman spectroscopy is a method that uses this scattered radiation to characterize a variety of compounds [26-28]. When combined with nanomaterials, signal enhancement effects occur, which provide a detection method of high sensitivity and selectivity [29-30].

In this review, properties of polymeric, metallic, and graphene-based nanomaterials are explored as adsorption platforms for a variety of pharmaceutical drugs for a wide range of diseases. Secondly, a discussion on electrical and optical detection methods based on parameters such as limit of detection, linear range and sensitivity is given. Lastly, we end with future prospects and shortcomings of nanomaterial based pharmaceutical research in relation to drug monitoring and quality control.

1.2 Nanomaterial scaffolds and therapeutic drug applications

Sensor platforms play a pivotal role in chemical sensing because they interact with the target analyte to produce a detectable change in their physical and chemical properties. Such interactions occur via chemical bonding or intermolecular forces which cause attachment of the analyte to the nanomaterial-based sensor [31-32]. This property of a chemical sensor is crucial to the signal output quality and reliability of the detection methods and as such, in this section we explore the different nanomaterials used to produce sensing platforms for detection of therapeutic drugs. Figure 1 below shows several types of polymeric nanomaterials used in drug delivery applications.

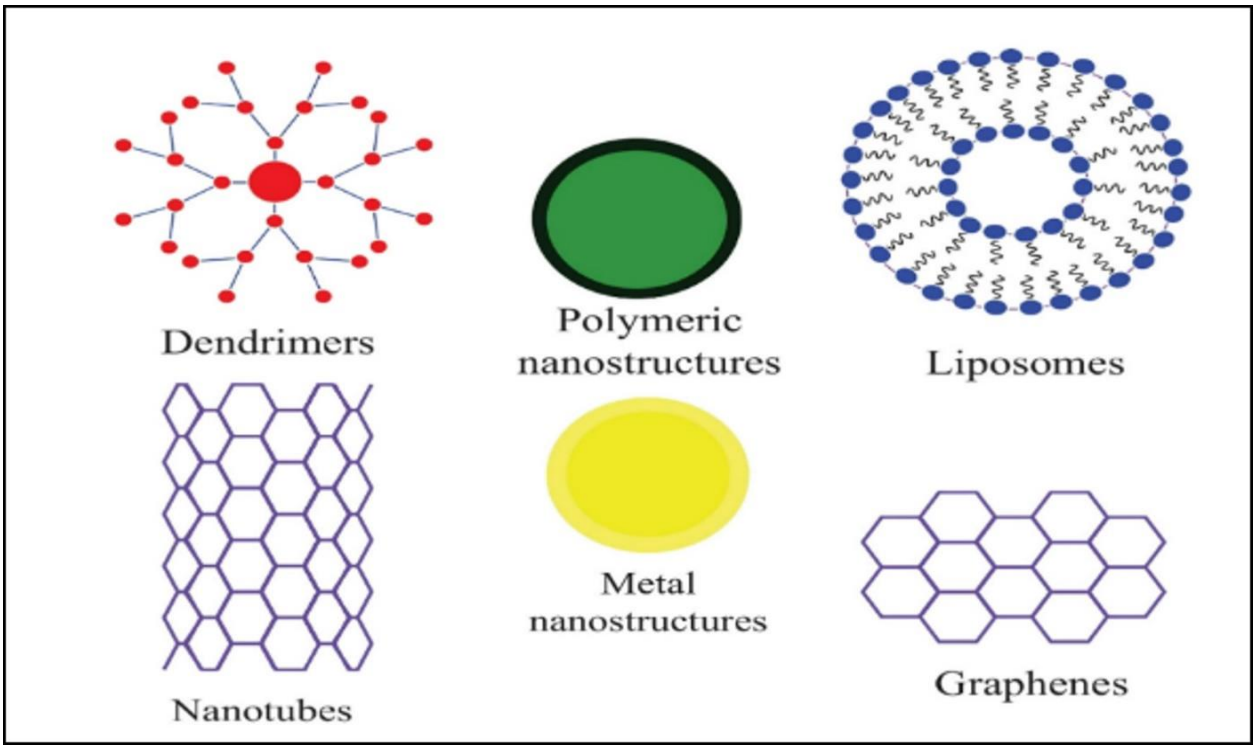

Figure 1.1:Classifications of nanoparticles and nanomaterials. [33]

The nanoparticles in the image above have been used in various applications regarding therapeutic drugs and drug delivery [33-35]. In the following sections, we focus on the polymer and inorganic nanoparticles as well as graphene-based sensors to cover a broader scope of an already expanding field of nanoparticles.

1.2.1 Polymeric nanomaterials and their applications

The key factors challenging the efficiency of therapeutic medicines arise from the biological barriers present in the human tissues which affect drug delivery and intracellular transport [36-37]. As a potential solution, nano-based polymers of various chemical functionalities are explored as controlled drug delivery agents for a variety of drug treatments. The interest comes from their flexibility in surface modification, biocompatibility and loading capacity for both hydrophobic and hydrophilic drugs [38-42]. The current advanced methods for producing polymeric nanoparticles include sonication, emulsification, self-assembly, electro-dropping, nanoprecipitation, microfluidic and ionic gelation. The general design of polymeric nanoparticles for drug delivery applications are nano capsules (polymeric membranes with an empty core) and nanospheres (matrix systems in solid form) [43]. Examples of nano capsules include polymersomes, which are artificial vesicles that consist of a double membrane made from amphiphilic block copolymers. Polymersomes are known for their good stability and efficiency in drug retention during transit to the cytosol. Dendrimers are a popular example of nanocomposites which comprise of hyperbranched polymers that form a three-dimensional matrix for crosslinking purposes. They have well defined intramolecular spaces where drug encapsulation can take place [44]. The

maximum amount of cargo that can be carried relies on the shape and size of the drug molecules and the number of cavities in a dendrimer. In application, the functionality or surface chemistry, as well as the size and shape can be tailored for specific therapeutic drugs and biomolecules [45]. There are many ways that nano polymers carry pharmaceutical drugs to the target sites. Depending on the polymer design, a drug can be encapsulated in the core of the polymer, adsorbed in the polymer matrix, or conjugated to the surface of the nanoparticle. Figure 2 below shows the synthesis and application of polymeric nanoparticles in drug delivery

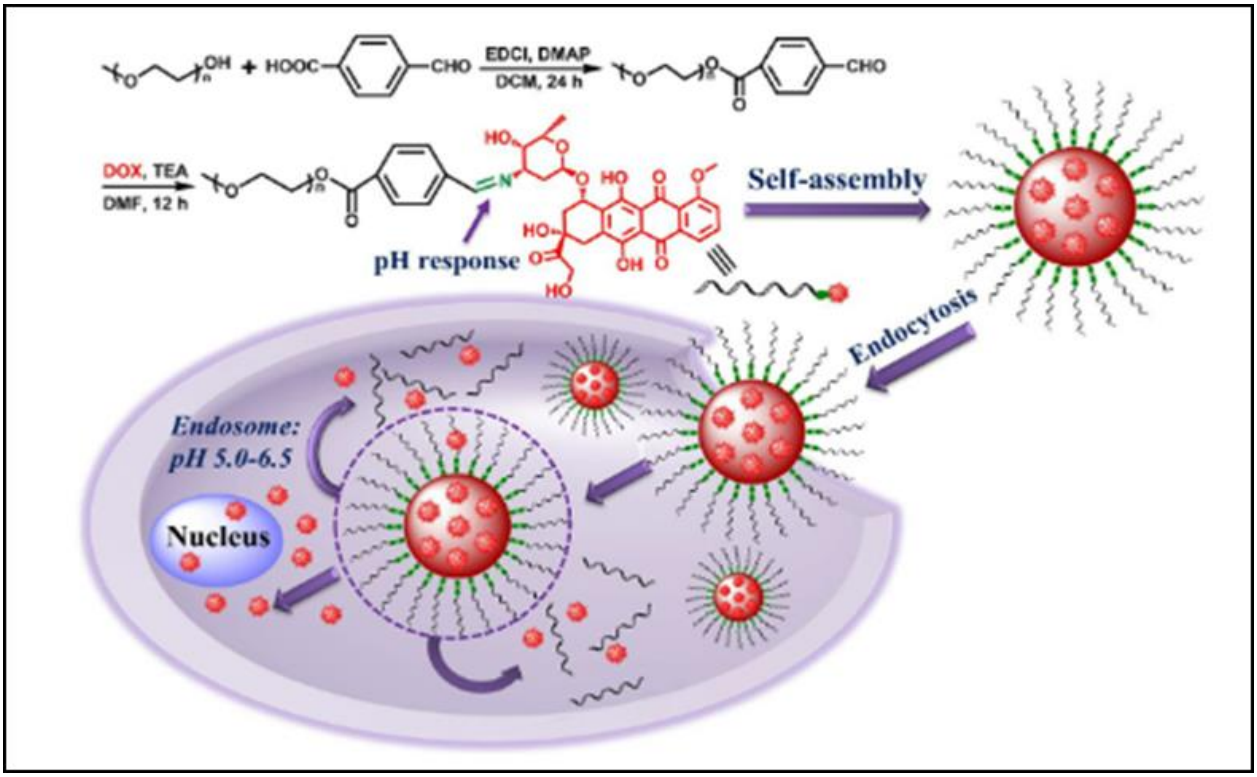

Figure 1.2:Illustration of self-assembled polymer PEG-Schiff nanoparticles and DOX drug delivery using pH sensitive conjugate PEG-Schiff-DOX. [46]

In figure 1.2 shown above describes the chemical process of synthesizing PEG-Schiff-DOX conjugates for drug delivery. Anticancer drug DOX was encapsulated in a PEG-Schiff nanosphere which transports the drug into the target cell via endocytosis [46]. Using these mechanisms, a combination of modified polymers is often applied as drug carriers. For example, a pH/redox responsive stimuli sensor made from copolymers poly-ethylene-glycol (PEG) and poly-L-Lysine (PLL) functionalized with platinum nanoparticles, was used to transport Gemcitabine, a small molecule for the treatment of lung cancer [47]. Poly (propylene imine) (PPI) dendrimers were chemically modified with folate for targeting the anticancer drug Docetaxel [48]. HIV medication Efavirenz and Lamivudine were also targeted using PPI dendrimers which resulted in improved drug uptake and efficacy respectively [49-50]. In another study, an anticancer drug Oxaliplatin (IV), was cross-linked with polyethylenimine (PEI) for the delivery of reactive oxygen species during chemotherapy [51]. Co-drug delivery studies have also been explored where two drugs

are delivered simultaneously using polymer nanoparticles. For example, PLGA nanoparticles coated with poly vinyl alcohol (PVA) were used to transport the antitumor medication Paclitaxel/methotrexate complex [52]. Polymersomes of polylactic-co-glycolic acid (PLGA, inner shell) and PEG (outer shell) were loaded with anticancer therapeutics as a promising cancer drug delivery platform [53]. The survey done on polymeric nanoparticles shows that these nano sensors have been invaluable in pharmacology and oncology research. However, literature has also cited a few disadvantages of polymeric nanoparticles such as toxicity and particle aggregation which weakens drug loading. As of late, only a few nano polymer-based medicines have been FDA-approved, thus this field of research is relatively new and more experimental work and clinical trials are still required [54].

1.2.2 Metallic nanomaterials and their applications

In the past decades, noble metals and some transition metals have gained interest in a variety of nano-based applications, including pharmaceutical research. The main attraction for metallic nanoparticles (MNPs) is the resonant plasmon feature that arises from the electron oscillations at the surface of metallic atoms [55]. Because of this, MNPs have played a key role in many optical detection methods as a signal enhancement platform [56]. Furthermore, the high electrical conductivity of MNPs makes them efficient electrochemical sensors in many biomedical applications. MNPs can also be tailored into various shapes and sizes as well as chemically modified with polymers and other recognition elements to suit the intended applications [57]. Nanoparticle synthesis is usually described in terms of two major groups: Top-down and Bottom Up. In the former method, the bulk material is broken down into smaller fragments with sizes less than 100 nm using diverse sources of energy. Most techniques under this group are used in the fabrication of thin film sensors usually from silicon or quartz substrates [58-59]. Examples of top-down techniques include Physical Vapor deposition (PVD), Chemical vapor deposition (CVD), and optical and electrical lithography [60-61]. For the latter case, bottom-up techniques assemble precursor reagents into nanostructures using chemical and physical methods. Examples of popular synthesis routes include self-assembly and chemical reduction [62]. Stabilizers like sodium citrate, cellulose, thioester, dextran, gelatin etc. are often used to prepare the MNPs and provide the starting chemical functionality for further modification [63-64]. Figure 1.3 below shows the basic process for the preparation of Gold NP using chemical reduction by Turkevich and Burst methods [65-66].

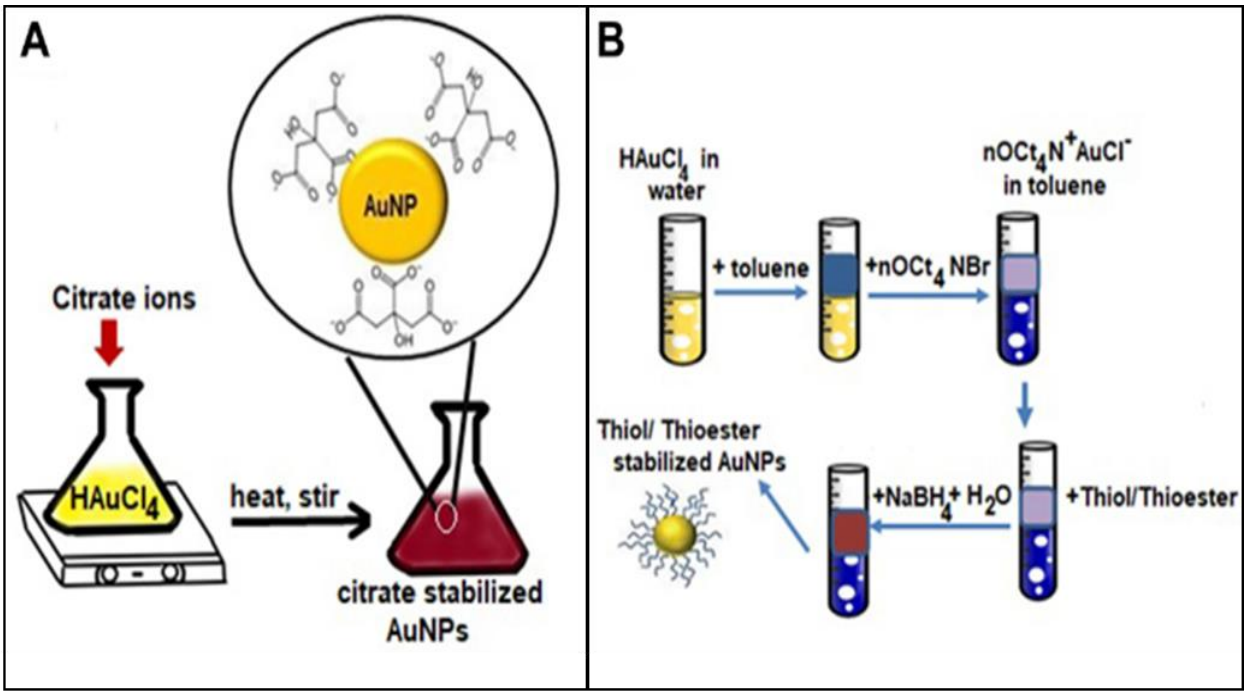

Figure 1.3:Synthesis of functionalized gold nanoparticles. A) Turkevich method, citrate stabilized. B) Burst method, thioester stabilized. [65-66]

The above A and B are two examples of how gold nanoparticles of various functionality are prepared using bottom-up methods. Popular shapes of MNPs produced using these methods include nanospheres, nanorods, nano-urchins, nano cubes, nano stars and nanocages [67-68]. Imaging techniques such as Atomic Force Microscopy (AFM), Transmission Electron Microscopy (TEM) and Scanning Electron Microscopy (SEM) have become the standard for characterizing MNPs for most synthesis methods [69-70]. Figure 4 below shows images of MNP acquired using different microscopy techniques.

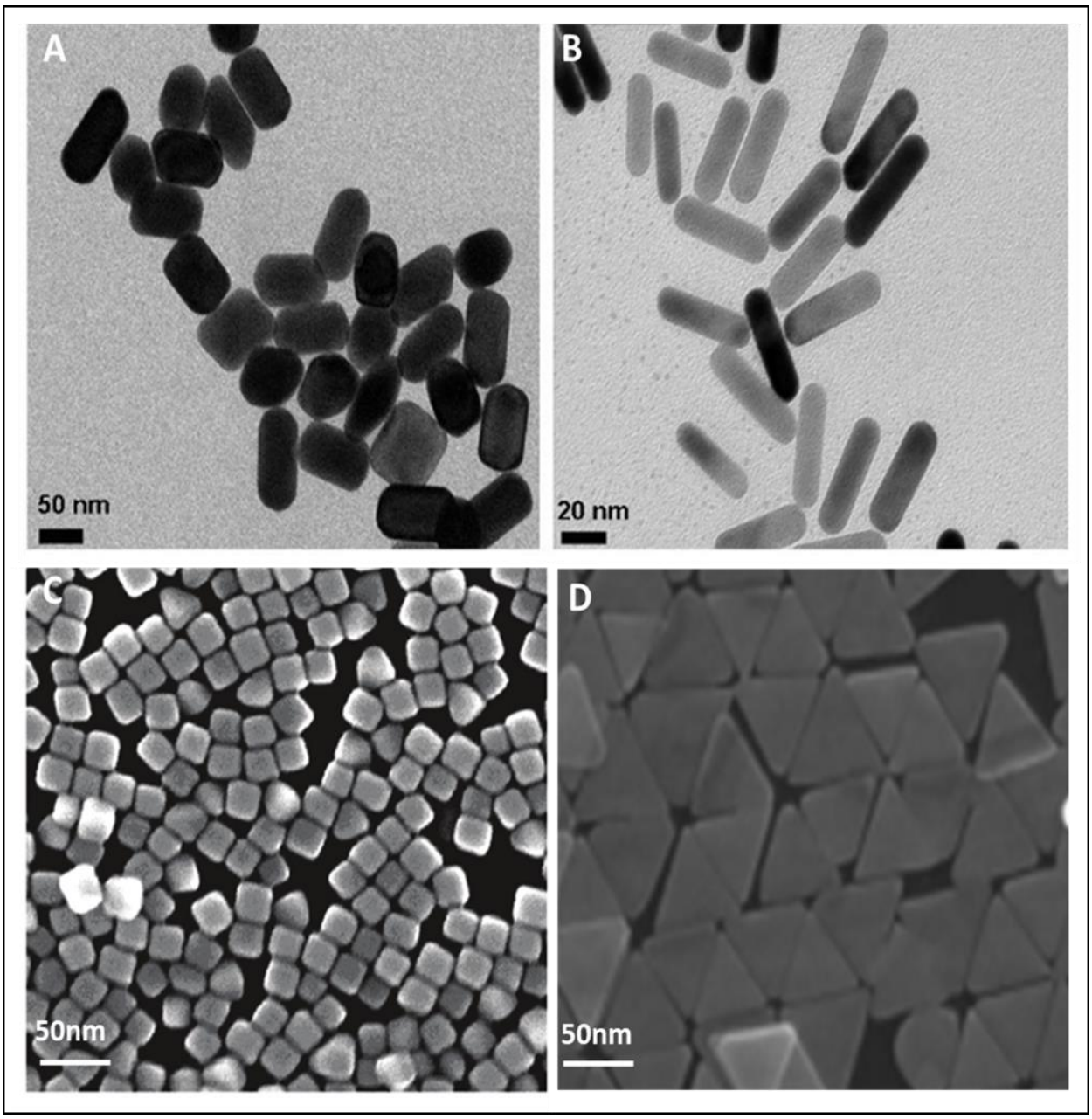

Figure 1.4: Images of different shapes of nanoparticles used in drug detection. A-B) TEM images of gold nanorods. C) SEM image of silver nanocubes. D) SEM image of triangular nanoplates. [71-72]

Metals such as gold (Au), silver (Ag), Titanium (Ti), Platinum (Pt) and Copper (Cu) have been extensively explored as sensors for a wide range of therapeutic and biomedical experiments [71-72]. Amongst them, gold has received the most attention owing to its inertness, easy functionalization, and biocompatibility. For example, gold nanoparticles were modified with PEG to form PEGAuNP composite for targeted drug delivery of pancreatic cancer medication Doxorubicin and Varlitinib [73]. AuNPs have also been explored as novel diagnostic tools for the management of melanoma cancer [74]. In other works, gold was shown to reduce toxicity, and

improve immunogenetic activity and stability when used as a vaccine carrier in nanomedicine [75]. Glucose detection was demonstrated using AuNP in serum, showing detection limits in the nanomole region [76]. Metals like silver have also played a role in therapeutic drug research space as in the case where gallic acid-coated silver nanoparticles were used as drug carriers for doxorubicin [77]. Silver NPS are also capable of detecting uric acid, lidocaine hydrochloride, Thiamine, Lomefloxacin and Propafenone in urine samples with detection limits in the micromolar per litre range [78-82]. MNPs are showing increased value in pharmaceutical research and will grow our understanding of therapeutic agents as future work is published.

1.2.3 Graphene based nano-sensors and applications

In the past decade, the fabrication of sensors and biosensors has improved with the incorporation of graphene as a scaffolding material. The chemical and physical properties of graphene such as high surface-to-volume ratio, electrical conductivity, optical transmittance, thermal conductivity, and high mechanical strength give the nanomaterial a considerable edge over most materials in sensing applications [83]. Furthermore, due to the sp2 hybridization of carbon bonds, graphene is easily modified with various chemical and biochemical agents making it a material with versatile applicability. Graphene is usually used in its oxygenated form, known as graphene oxide (GO) as well as reduced graphene oxide (rGO) for research work that investigates hydrophilic molecules [84]. The figure below shows the molecular shapes of Graphene, GO and rGO.

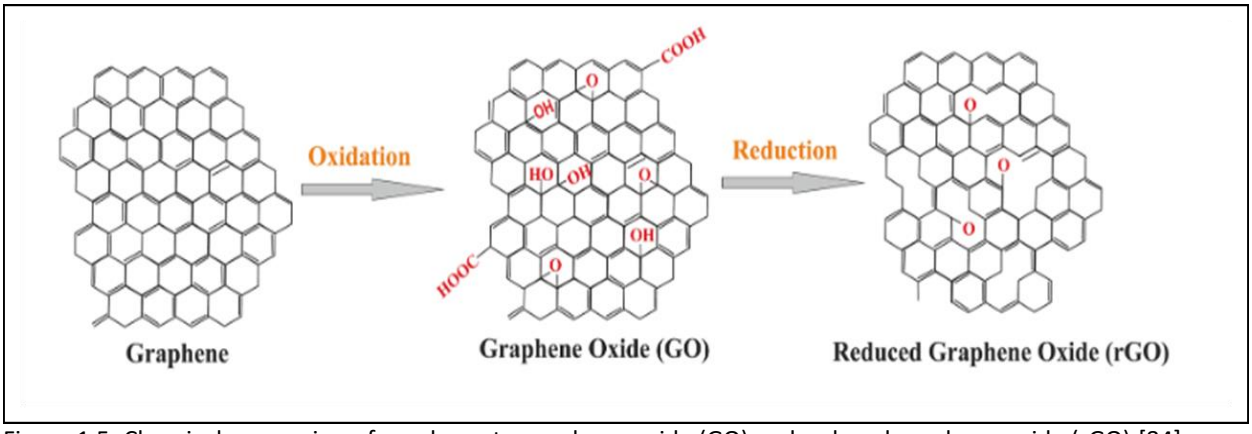

Figure 1.5: Chemical conversion of graphene-to-graphene oxide (GO) and reduced graphene oxide (rGO).[84]

Graphene is synthesized using various methods such as the Hummers method, exfoliation or mechanical cleavage of graphite and chemical vapor deposition [84]. To obtain GO, strong oxidizing agents such as sodium permanganate and sulphuric acid are reacted with graphite or graphene to produce hydroxyl (OH) and carboxylic acid (COOH) functional groups on the surface of the substrate. The oxygen content on GO is reduced using photochemical, microwave and bacterial methods to produce reduced graphene oxide. GO and rGO offer extra properties suitable for chemical and biochemical sensor applications. [84] Adsorption of drug molecules,

anticancer medication, polymers, proteins, genes, and other biomolecules is possible using GO and rGO because the OH and COOH groups allow easy conjugation bonding. Electrostatic interactions using the oxygen lone pair of electrons, pi-pi stacking via the aromatic rings, hydrogen bonding and van der Waals forces are the various mechanisms by which GO and rGO absorb materials onto their surfaces [85]. Figure 1.6 below shows the adsorption of the protein BSA on rGO nanosheets.

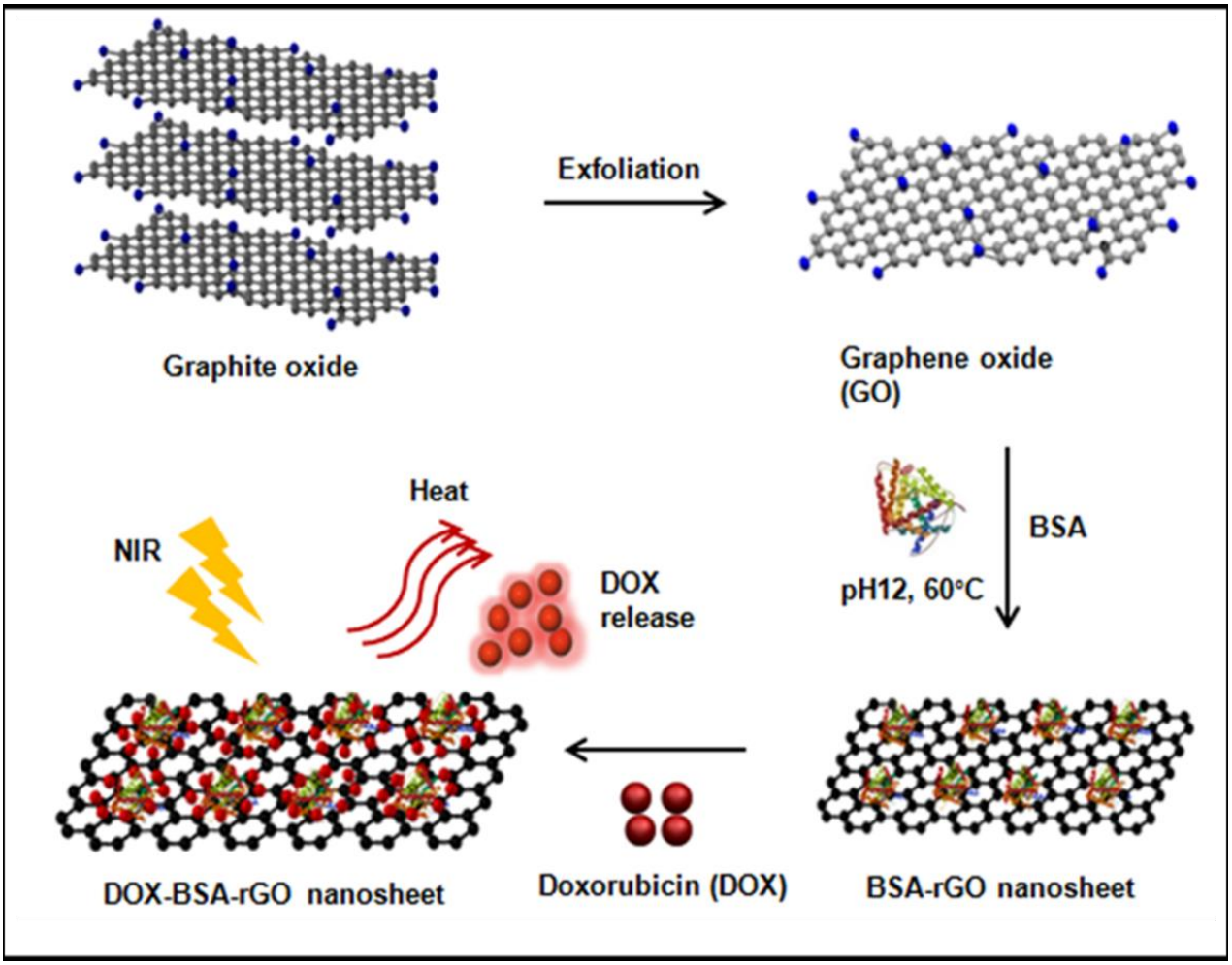

Figure 1.6:Synthesis and application of rGO as a DOX drug carrier. [86]

The image above shows the synthesis of rGO from graphite oxide for the intention of delivering anti-cancer medication DOX supported by the protein BSA. The scaffolding material is then investigated using optical methods to release the DOX from the adsorption site [86]. Similar work is available in different research applications where a combination of graphene members, crosslinkers and analyte recognition elements are combined for targeted drug delivery. For example, amino acid functionalized iron oxide nanoparticles adsorbed on graphene sheets, were used as a sensor for dopamine and ascorbic acid detection [87]. Secondly, GO functionalized with platinum nanoparticles was explored as a chemical sensor for glucose at concentrations in the

millimolar range [88]. Chitosan functionalized GO used in the controlled release of the anti-inflammatory drug Ibuprofen [89]. In the next section more examples of graphene sensor are discussed, taking into consideration the detection methods and parameters used to classify the efficiency of a chemical sensor.

1.3 Detection methods and sensing techniques

Adsorption of the analyte to the sensing material is a crucial element of a sensor, as explained in section 2, the chemical properties of the sensor and the analyte need to be compatible for the adsorption to occur. A second and equally important characteristic of a sensor is the detection method employed to produce a reliable and reproducible signal. There are currently various methods used for the chemical sensing of pharmaceuticals, each of which has its own advantages and disadvantages. In this section, we explore electrical and optical detection methods, comparing their sensor performance using parameters such as limit of detection, linear range, and other additional information.

1.3.1 Electrical detection methods

The electrical potential of a chemical agent has been investigated as a means of quantifying changes in concentration or molecular bonding because of interaction with an analyte. Electrical signals such as resistance, capacitance, conductance, and impedance are the ones used to study the thermodynamic and kinetic properties of the analyte [90]. Furthermore, electron exchange between oppositely charged species in redox reactions produces a signal that can be used as a sensing mechanism. Many nanoparticle scaffolds, conjugates and analyte recognition elements have been coupled with electrochemical detection using surface functionalized electrodes [91].

1.3.1.1 Field Effect Transistor (FET) based detection method

Field Effect Transistors are devices that use an electric field to control the flow of current in a semiconductor. In a typical FET system, source (S) and draining (D) electrodes are connected to a semiconductor path that is functionalized with sensing elements for high specificity and binding affinity. When target analytes are detected, a change in channel conductance is recorded and processed to acquire an electrical signal. There are two kinds of FETs based on the PN junction theory: n-type where electrons are the main charge carriers and p-type with holes as the primary charge carriers. In an n-type FET system, positively charged molecules are detected and charge carriers (electrons) accumulate on the sensing channels and increase the signal. However, when negatively charged targets are detected, the conductivity decreases caused by depletion of the electrons. The second type is a p-type FET system, which binds to positive charges causing a decline in conductivity decline due to a reduction of the charge carriers (holes). The inverse occurs when capturing negative charges raises because conductivity of holes increases.

Application of this principle allows improved detection by coating nanomaterials like carbon nanotubes, graphene, MNPS on the electrodes and the sensing platforms [92]. In this way, biosensors can be designed for various pharmaceutical and therapeutic drug related work. Figure 1.7 below shows a FET sensor used in the detection of glucose oxidase using a graphene biosensor.

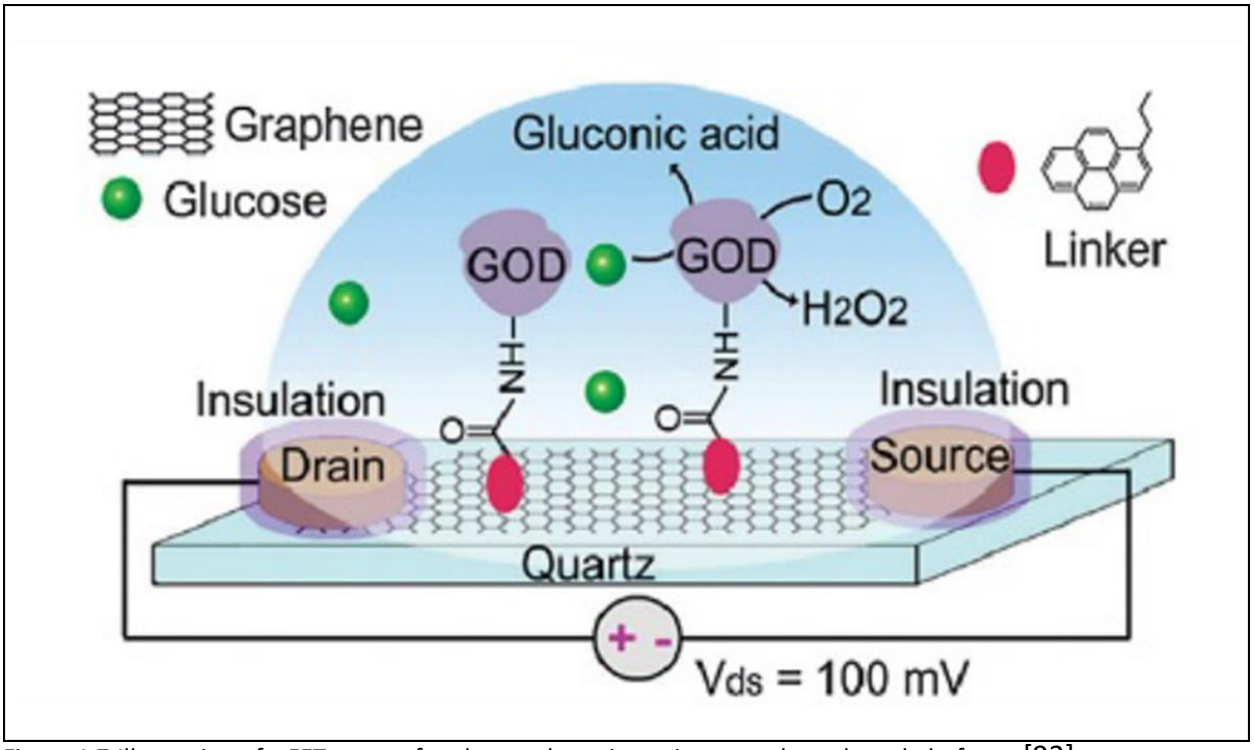

Figure 1.7:Illustration of a FET system for glucose detection using a graphene-based platform. [93]

In figure 1.7, graphene is used as a high electrical conducting platform which changes the current on both the source and the drain electrodes when a substance absorbs on its surface. In this case, glucose oxidase enzyme (GOD), is used together with a crosslinker molecule to detect changes in conductance when glucose binds to the enzyme [93]. Other applications of FET sensors for various pharmaceutical agents have been published. Zinc oxide nanoribbons were used as transducer materials for the detection of glucose in phosphate buffer solution (PBS) and a LOD of 70 µM and linear range of 0- 80 mM was reported [94]. In another study, Insulin was analyzed in PBS on graphene transducers with detection limits at 35pM [95]. Although FET devices offer high sensitivity, selectivity, miniaturization and low power use as advantages, dielectric membranes are sensitive to motion, which affects the accuracy of detection. Lastly, because FET uses biomarkers, it is not regarded as a label free method, which affects the applicability of this technique due to cost implications [96].

1.3.1.2 Electrochemical detection methods

Electrochemical detection involves the use of functionalized electrodes for the detection of target analytes and signal transduction. Like FET devices, electrochemical methods translate binding affinities into readable electrical signals. The difference between the two methods is that electrochemical techniques require the use of an electrolyte solution as a conducting medium instead of solid-state transducers found on FET devices [97]. Figure 1 below shows a general schematic of an electrochemical system.

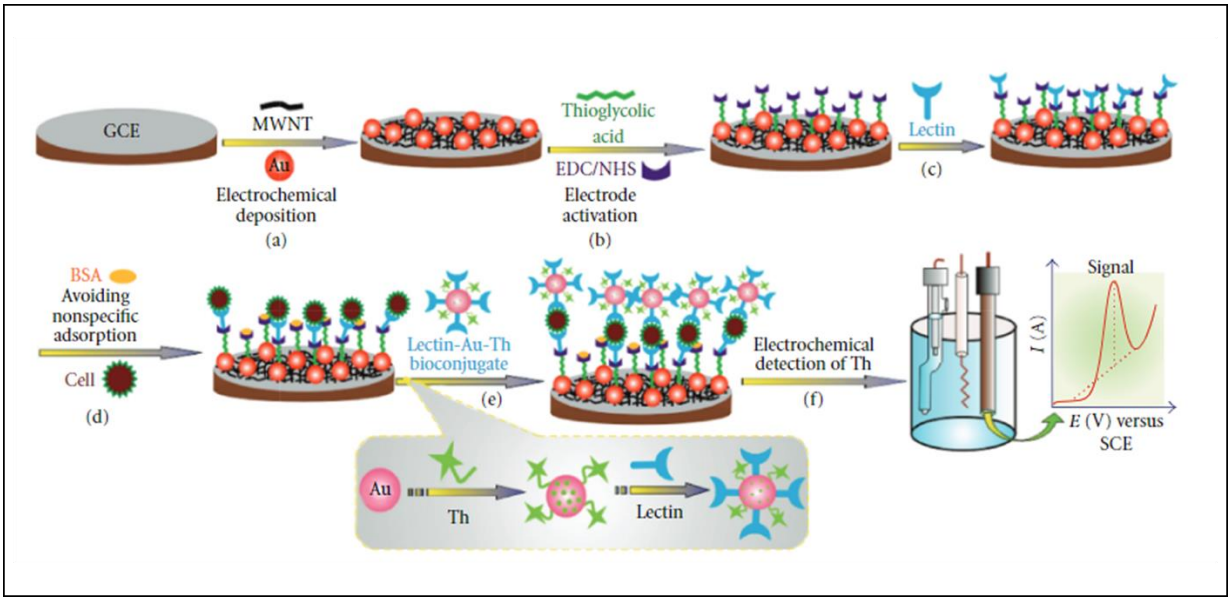

Figure 1.8:Schematic of synthesis and application of a glycan electrochemical sensor. [97]

Figure 1.8 above shows how an electrochemical sensor is prepared and used in detection experiments. From position a) A glass-based carbon (GCE) electrode was functionalized with gold nanoparticles followed by thioglycolic acid and lectins (b-c), while simultaneously blocking nonspecific adsorption to the electrode using BSA (d). Lectin-Au-thionine bioconjugates were adsorbed on the electrode as recognition elements(e). Finally, the electrochemical apparatus is assembled and utilized to produce a signal of intensity (amperes) versus electric volts(f) [98]. Systems like these have been designed for a wide range of applications of pharmaceutical and therapeutic targets. For example, studies have shown the detection of dopamine using graphene functionalized with PVP as the sensing platform on the GCE. The study reported a LOD of 0.2 nM and a linear range up to 10^{-10} with a r^2 of 0.99 [99]. Research on cholesterol was also undertaken using chitosan, graphene hybrid nanocomposites, reaching an LOD of 0.75 µM and a linear range of 2.2-520 µM [100]. Furthermore, extensive research into antineoplastic drugs using electrochemical sensing has been explored. Flutamide detection by silver coated GCE produced LOD (mol L^{-1}) in the 10^{-6} and a linear range of 1-100x 10^{-5}(mol L^{-1}) [101]. In a similar study, Gemcitabine was detected and analyzed using amino thiophenol functionalized gold nanoparticles where LOD was in the 10^{-15} and a linear range of 10^{-8} to 10^{-15} (mol L^{-1}) [102]. The

use of electrochemical sensing is clearly a prominent field of study, and its success can only bring more advantages for chemical sensing related to a variety of pharmaceutical drugs. Although the LOD and linear range of this method are extremely sensitive, the short lifespan is still a limitation and as such [103], other techniques have been approached to solve this issue.

1.3.2 Optical detection methods

A key future of molecules is the ability to investigate them by focusing on a response after interaction with light photons. As such, a lot of research has been channeled towards using optical methods for detecting and collecting information on analytes adsorbed on nanomaterial scaffoldings or sensors. Nanomaterials carry the property of surface plasmons which aid in the detection method of the techniques [104]. Thus, in this section, we discuss popular plasmon-related methods used in pharmaceutical drug applications.

1.3.2.1 Surface Plasmon Resonance spectroscopy

Surface plasmons found on the surface of a nanomaterial can be used for trace detection and monitoring of small molecules using changes in refractive index as a signal in real-time. In principle, when light photons approach a nanomaterial like gold NPs at an angle, a refractive index can be obtained from the plasmon wave and set as a calibration point. When the MNP is functionalized with polymers, recognition elements and analyte, changes in the refractive index are then recorded again and compared. Since the refractive index is related to the surface of the substrate, changes in the refractive index can also be correlated to binding affinities and used in medical diagnostics, drug detection and virus monitoring, amongst other applications [105]. Figure one below shows the principle of SPR and how it is used in biomedical applications.

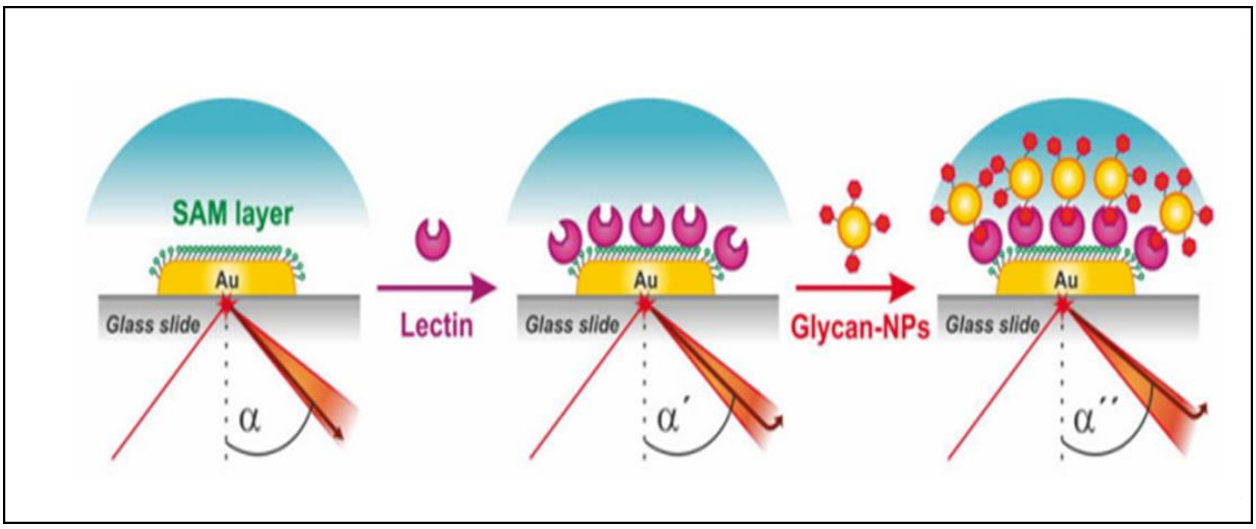

Figure 1.9:Schematic of SPR configuration used in the detection of glycan. [106]

Figure 9 above shows the principle of SPR used in protein detection applications. From left to right, a glass slide is seen coated with layers of gold (Au) and Alkanethiol (green) using the self - assembly method. In the second step, lectins are used as biorecognition elements for the detection of glycans. The third step follows with glycan functionalized nanoparticles adsorbed to the surface through binding with the lectins on the SPR scaffold. At each step, laser light is directed to the biosensors and changes in the refractive index in relation to the binding of molecules [106]. Examples of SPR applications can be seen in a wide range of biomedical and pharmaceutical experiments. Studies have shown the diagnosis of malignant and infectious diseases using the biomarker Rhodamine 6G and SPR detection [107]. In industrial applications, Aflatoxin, a small toxic molecule found in dairy products was detected at LOD values of seventy-six pM using a silicon photonic biosensor [108]. Smartphone platforms are also being incorporated into SPR detection where 50nm gold nanofilms are used for sensing immunoglobin G (IgG), producing LOD values between 15-47 nM [109]. Silver nanospheres and nano rods on titanium oxide substrates were used for the detection of Streptavidin, obtaining a LOD value of 0.3 µg/ml using halogen lamp technology [110]. Bromocriptine, a pharmaceutical drug used to treat menstrual problems, was investigated using laccase immobilized on a carboxymethyl dextran functionalized SPR sensor, where a detection limit of 10^{-2} ng/ml to 10^{3} ng/ml was reported [111]. The values reported above show that the common feature of the SPR technique is high sensitivity and rapid analysis. However, SPR has limitations such as long lag times, sensitivity to temperature and motion as well as continuous optical alignment and maintenance [112].

1.3.2.2 Surface-enhanced Raman spectroscopy (SERS)

Amongst non-destructive methods of detection, Raman spectroscopy has become a favorite method for qualitative experiments because it allows molecular fingerprinting of organic and organometallic substances. Light-matter interaction produces scattered radiation which is collected at right angles to the surface. The scattered radiation produces different frequencies from the laser wavelength due to inelastic scattering caused by photon-molecule interactions. Raman shifts expressed in wavenumbers can be correlated to bond fragments of analytes as a means of detection. A major limitation of this method is low signal output which is normally 0,01% of the radiation. To solve this issue, nanomaterials were incorporated into the technique by employing surface plasmonic resonance for signal enhancement purposes. Such as, surface-enhanced Raman spectroscopy (SERS) has brought renewed interest and trust in SERS as a pharmaceutical drug detection method [113]. The figure below illustrates the both the fabrication of SERS scaffolds and their application in qualitative analysis.

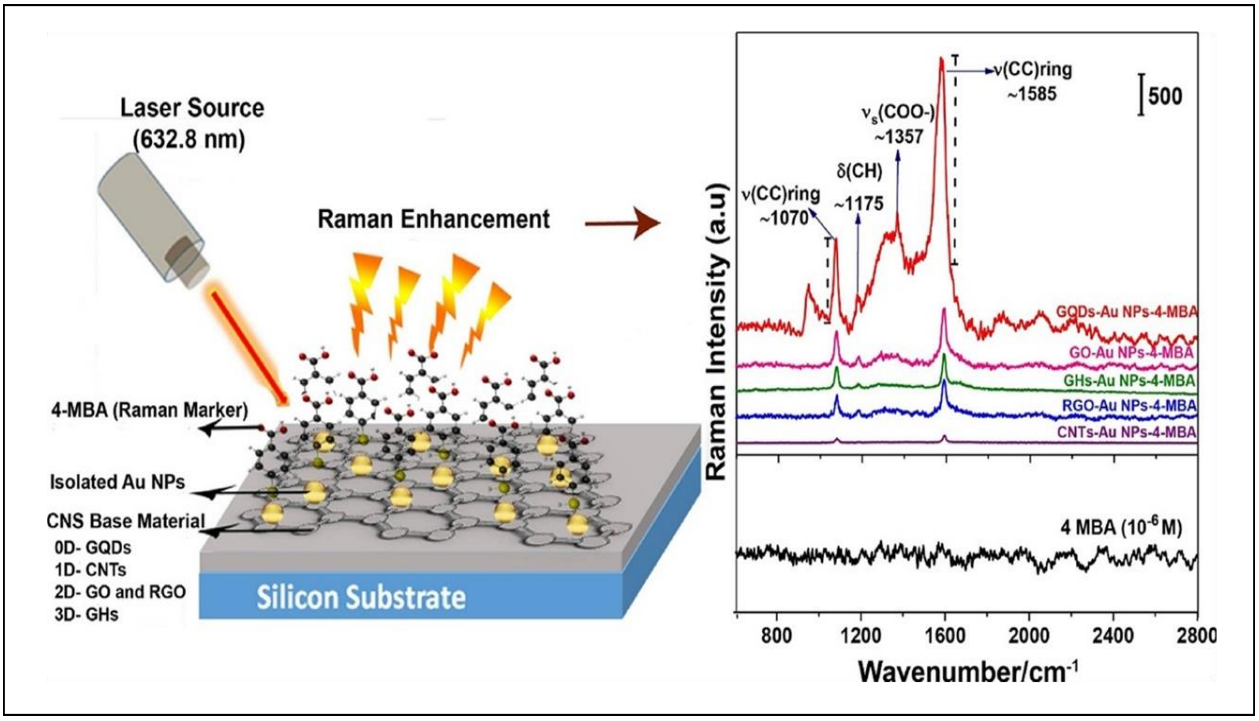

Figure 1.10: Schematic of a carbon-based SERS substrate of various functional groups. (left). SERS spectra of the analyte 4-Mercaptobenzoic acid (MBA) adsorbed on the scaffolds (right). [114]

In the above image, a 632.8 nm laser source is exciting a set of carbon-based scaffolds of various dimensions and functionality. Gold quantum dots (GQDs, 0D), Carbon nanotubes (CNTs,1D), Graphene oxide (GO,2D) and reduced graphene oxide (rGO, 2D) and Gold nanohybrids (GHs, 3D) were further functionalized with 4-mercaptobenzoic acid (4-MBA, 10^{-6}M) as the analyte. From observation of the Raman spectra, it is seen that vibrational modes are associated with 4-MBA. The spectra also show increased signal intensity amongst the scaffolds, with GQDs providing the highest intensity. Specifically, the study reports surface enhancement factors of 10^7 from GQDs followed by 10^6 from GO-Au NPs, which is a significant improvement on the Raman signals obtained, making SERS a reliable technique for small molecule detection [114]. More examples like the one above has been reported in the literature. Levofloxacin (antibiotic) was detected from artificial urine using hydroxylamine silver nanoparticle microfluidic devices and SERS where the quantitative analysis yielded an LOD of 0.07 mM [115]. A similar pharmaceutical study quantified Promethazine using the same microfluidic device and detected concentrations as lows 10^{-7}M [116]. Medication for the treatment of hypertension known as Captopril was obtained from human blood and analyzed using SERS and citrate functionalized silver nanoparticles. It was reported that an LOD of 0,4 µM was achieved from the quantitative calculations [117]. And lastly, the common over-the-counter medication Aspirin, was analyzed on silver nanoparticles supported by filter paper, the linear range reported in this study spanned from 0.1 to 1mM [118]. The examples shown indicate that SERS is a highly versatile, sensitive, and non-destructive detection method, however; issues such as fluorescence noise, long acquisition time, and

unstable lasers still hamper the full potential of this method [119]. With further research and optimization, SERS systems will surely improve knowledge of pharmaceutical drug design and quality control, which is essential for healthcare reasons.

1.4. Prospects and Shortcomings

The pharmaceutical industry is one of the pillars of our health systems around the world. Research and knowledge dissemination in this field is important for our global health status. This review provided a brief overview of technologies used in the detection and analysis of therapeutic drugs that are used to treat serious diseases like cancer, hypertension, viruses, and tumors. Nanotechnology has made great strides in providing sensor applications for pharmaceutical drug design and monitoring. Properties of polymeric, metallic, and carbon-based substrates can be fabricated into sensor platforms that allow the adsorption of analytes for analysis purposes. Furthermore, electrical and optical detection methods coupled to nanomaterials have enhanced sensor application research which is a positive for the pharmaceutical industry. Parameters such as limit of detection, linear range and sensitivity show improved response towards analytes being investigated. With future research and design, challenges related to toxicity, shelf life and API quality can be overcome by improved drug design, monitoring, and targeted sensing. The major limitations observed from this study, start with the challenges in reproducing sensing platforms consistently using less expensive methods. Secondly, electrical-based detection methods are sensitive to motion, and they struggle to detect multiply layered sensors, which makes calibration and label free applications a tedious process. Thirdly, optical methods suffer from long acquisition times, laser instability, continuous alignment maintenance and fluorescence noise, which requires optimization steps prior to acquisition. Technical challenges aside, nanomaterial-based research into pharmaceutical drugs is a very important field of science and its understanding can only be improved by more research, innovation, and application.

References

1. Jeevanandam J, Barhoum A, Chan YS, Dufresne A, Danquah MK. Review on nanoparticles and nanostructured materials: history, sources, toxicity and regulations. Beilstein J Nanotechnol. 2018; 9:1050–74.
2. Bai Y, Wu F, White JC, Xing B. 00 Nanometers: A Potentially Inappropriate Threshold for Environmental and Ecological Effects of Nanoparticles. Environ Sci Technol [Internet]. 2014;48. Available from: https://pubs.acs.org/sharingguidelines
3. Murthy SK. Nanoparticles in modern medicine: State of the art and future challenges. Vol. 2, International Journal of Nanomedicine. 2007.
4. Shen H, Zhang L, Liu M, Zhang Z. Biomedical applications of graphene. Theranostics. 2012;2(3):283–94.
5. Xu C, Shi X, Ji A, Shi L, Zhou C, Cui Y. Fabrication and characteristics of reduced graphene oxide produced with different green reductants. PLoS One. 2015;10(12).
6. Yadav S, Sharma AK, Kumar P. Nanoscale Self-Assembly for Therapeutic Delivery. Nanoscale Self-Assembly Ther Deliv Front Bioeng Biotechnol [Internet]. 2020;8:127. Available from: www.frontiersin.org
7. Bissantz C, Kuhn B, Stahl M. A Medicinal Chemist's Guide to Molecular Interactions. J Med Chem [Internet]. 2010;53:5061. Available from: https://pubs.acs.org/sharingguidelines
8. Shovsky A, Varga I, Makuška R, Claesson PM. Formation and stability of water-soluble, molecular polyelectrolyte complexes: Effects of charge density, mixing ratio, and polyelectrolyte concentration. Langmuir. 2009;25(11):6113–21.
9. Lombardo D, Kiselev MA, Magazù S, Calandra P. Amphiphiles self-assembly: Basic concepts and future perspectives of supramolecular approaches. Adv Condens Matter Phys. 2015;2015.
10. Huang R, Carney RP, Stellacci F, Lau BLT Protein-nanoparticle interactions: the effects of surface compositional and structural heterogeneity are scale dependent. Nanoscale. (2013) 5:6928–6935
11. Naresh V., Lee N. A Review on Biosensors and Recent Development of Nanostructured Materials-Enabled Biosensors. A Rev Biosens Recent Dev Nanostructured Mater Biosensors Sensors. 2021;21:1109.
12. Saha K, Agasti SS, Kim C, Li X, Rotello VM. Gold nanoparticles in chemical and biological sensing. Chem Rev. 2012 May 9;112(5):2739–79.
13. Amina SJ, Guo B. A review on the synthesis and functionalization of gold nanoparticles as a drug delivery vehicle. Int J Nanomedicine. 2020;15:9823–57.
14. Bhalla, N.; Jolly, P.; Formisano, N.; Estrela, P. Introduction to biosensors. Essays Biochem. 2016, 60, 1–8
15. Radhakrishnan R, Suni II, Bever CS, Hammock BD. Impedance Biosensors: Applications to Sustainability and Remaining Technical Challenges. 2014; Available from: https://pubs.acs.org/sharingguidelines.

16. Bharti K, Sadhu KK. Syntheses of metal oxide-gold nanocomposites for biological applications. Results Chem. 2022 Jan 1;4:100288.
17. Mohammad-Rezaei R, Golmohammadpour M. Controlled Electrodeposition of Au-Copper Oxide Nanocomposite on a Renewable Carbon Ceramic Electrode for Sensitive Determination of NADH in Serum Samples. Electroanalysis. 2020;32(3):606–12.
18. Gooding, J.J.; Chou, A.; Liu, J.; Losic, D.; Shapter, J.G.; Hibbert, D.B. The Effects of the Lengths and Orientations of Single-Walled Carbon Nanotubes on the Electrochemistry of Nanotube-Modified Electrodes. Electrochem. Commun. 2007, 9, 1677–1683.
19. Heller, I.; Kong, J.; Heering, H.A.; Williams, K.A.; Lemay, S.G.; Dekker, C. Individual Single-Walled Carbon Nanotubes as Nanoelectrodes for Electrochemistry. Nano Lett. 2005, 5, 137–142
20. Gao, X.P.A.; Zheng, G.; Lieber, C.M. Subthreshold Regime Has the Optimal Sensitivity for Nanowire FET Biosensors. Nano Lett. 2010, 10, 547–552.
21. Tu Q, Chang C. Diagnostic applications of Raman spectroscopy. Nanomedicine Nanotechnology, Biol Med [Internet]. 2012;8(5):545–58. Available from: http://dx.doi.org/10.1016/j.nano.2011.09.013
22. Kazuma E, Tatsuma T. Localized surface plasmon resonance sensors based on wavelength-tunable spectral dips †. 2014; Available from: www.rsc.org/nanoscale
23. Ràfols, C.P.; Serrano, N.; Díaz-Cruz, J.M.; Ariño, C.; Esteban, M. A Chemically-Bound Glutathione Sensor Bioinspired by the Defense of Organisms against Heavy Metal Contamination: Optimization of the Immobilization Conditions. Chemosensors 2017, 5, 12. [CrossRef]
24. M. Li, S.K. Cushing, N.Q. Wu, Plasmon-enhanced optical sensors: a review, Analyst 140 (2015) 386–406.
25. J.R. Lakowicz, K. Ray, M. Chowdhury, H. Szmacinski, Y. Fu, J. Zhang, et al., Plasmon-controlled fluorescence: a new paradigm in fluorescence spectroscopy, Analyst 133 (2008) 1308–1346.
26. Meyer SA, Le Ru EC, Etchegoin PG. Quantifying resonant Raman cross sections with SERS. AIP Conf Proc. 2010;1267:204–5.
27. Cao YC, Jin R, Nam JM, Thaxton CS, Mirkin CA. Raman Dye-Labeled Nanoparticle Probes for Proteins. J Am Chem Soc. 2003;125(48):14676–7.
28. Bertoldo Menezes D, Reyer A, Marietta A, Musso M. Glass transition of polystyrene (PS) studied by Raman spectroscopic investigation of its phenyl functional groups. Mater Res Express. 2017;4(1).
29. Littleford RE, Cunningham D, Matousek P, Towrie M, Parker AW, Khan I, et al. Surface-enhanced resonance Raman scattering using pulsed and continuous-wave laser excitation. J Raman Spectrosc. 2005;36(6–7):600–5.
30. Bumbrah GS, Sharma RM. Raman spectroscopy – Basic principle, instrumentation and selected applications for the characterization of drugs of abuse. Egypt J Forensic Sci [Internet]. 2016;6(3):209–15. Available from: http://dx.doi.org/10.1016/j.ejfs.2015.06.001

31. Liu J, Cui L, Losic D. Graphene and graphene oxide as new nanocarriers for drug delivery applications. Acta Biomater [Internet]. 2013;9(12):9243–57. Available from: http://dx.doi.org/10.1016/j.actbio.2013.08.016
32. Liu Z, Robinson JT, Sun XM, Dai HJ. PEGylated nanographene oxide for delivery of water-insoluble cancer drugs. J Am Chem Soc 2008;130:10876–7.
33. Truong, N. P., Whittaker, M. R., Mak, C. W., and Davis, T. P. The importance of nanoparticle shape in cancer drug delivery. Expet Opin. Drug Deliv. (2015).12,129–142. doi:10.1517/17425247.2014.950564
34. Car A, Baumann P, Duskey JT, Chami M, Bruns N, Meier W. PH-responsive PDMS-b-PDMAEMA micelles for intracellular anticancer drug delivery. Biomacromolecules. 2014;15(9):3235–45.
35. Song J, Xu B, Yao H, Lu X, Tan Y, Wang B, et al. Schiff-Linked PEGylated Doxorubicin Prodrug Forming pH-Responsive Nanoparticles With High Drug Loading and Effective Anticancer Therapy. Available from: www.frontiersin.org
36. Mitchell MJ, Billingsley MM, Haley RM, Wechsler ME, Peppas NA, Langer R. Engineering precision nanoparticles for drug delivery. Nat Rev Drug Discov [Internet]. Available from: https://doi.org/10.1038/
37. Taylor J, Huefner A, Li L, Wingfield J, Mahajan S. Nanoparticles and intracellular applications of surface-enhanced Raman spectroscopy. Analyst [Internet]. 2016;141(17):5037–55. Available from: http://xlink.rsc.org/?DOI=C6AN01003B
38. Zhang L, Beatty A, Lu L, Abdalrahman A, Makris TM, Wang G, et al. Microfluidic-assisted polymer-protein assembly to fabricate homogeneous functionalnanoparticles. Mater Sci Eng C [Internet]. 2020;111(September 2019):110768. Available from: https://doi.org/10.1016/j.msec.2020.110768
39. R.N. Alyaudtin, A. Reichel, R. Löbenberg, P. Ramge, J. Kreuter, D.J. Begley, Interaction ofpoly(butylcyanoacrylate) nanoparticles with the blood-brain barrier in vivo and in vitro,J. Drug Target. 9 (2001) 209–221.
40. Yavuz B, Bozdag Pehlivan S, Sumer Bolu B, Nomak Sanyal R, Vural I, Unlu N.Dexamethasone - PAMAM dendri- mer conjugates for retinal delivery: preparation, characterization and in vivo evaluation. J Pharm Pharmacol.2016. 68(8):1010– 1020
41. Lima, T., Bernfur, K., Vilanova, M., and Cedervall, T. Understanding the lipid and protein corona formation on different sized polymeric nanoparticles. Sci. Rep. (2020).10, 1129. doi:10.1038/s41598-020-57943-6
42. Osorno LL, Brandley AN, Maldonado DE, Yiantsos A, Mosley RJ, Byrne ME, et al. Review of Contemporary Self-Assembled Systems for the Controlled Delivery of Therapeutics in Medicine. 2021; Available from: https://doi.org/10.3390/nano11020278
43. Scarpa E, Bailey JL, Janeczek AA, Stumpf PS, Johnston AH, Oreffo ROC, et al. Quantification of intracellular payload release from polymersome nanoparticles. Nat Publ Gr [Internet]. 2016; Available from: www.nature.com/scientificreports

44. Canal F, Sanchis J, Vicent MJ. Polymer--drug conjugates as nano-sized medicines. Curr Opin Biotechnol. 2011 Dec;22(6):894-900. doi: 10.1016/j.copbio.2011.06.003. Epub 2011 Jul 1. PMID: 21724381.
45. A. C. Braun, M. Gutmann, T. D. Mueller, T. Lu¨hmann and L. Meinel, J. Controlled Release, 2018, 279, 17–28
46. Song J, Xu B, Yao H, Lu X, Tan Y, Wang B, et al. Schiff-Linked PEGylated Doxorubicin Prodrug Forming pH-Responsive Nanoparticles With High Drug Loading and Effective Anticancer Therapy. Available from: www.frontiersin.org
47. Shi H, Xu M, Zhu J, Li Y, He Z, Zhang Y, Xu Q, Niu Y, Liu Y. Programmed co-delivery of platinum nanodrugs and gemcitabine by a clustered nanocarrier for precision chemotherapy for NSCLC tumors. J Mater Chem B. 2020 Jan 14;8(2):332-342. doi: 10.1039/c9tb02055a. Epub 2019 Dec 11. PMID: 31825452.
48. Thakur S, Tekade RK, Kesharwani P, Jain NK.The effect of polyethylene glycol spacer chain length on the tumor- targeting potential of folate-modified PPI dendrimers. J Nanopart Res. (2013) 15(5):1625
49. Dutta T, Agashe HB, Garg M, Balakrishnan P, Kabra M, Jain NK Poly (propyleneimine) dendrimer based nanocontainers for targeting of efavirenz to human monocytes/macrophages in vitro. J Drug Target. (2007) 15(1):89–98
50. Dutta T, Jain NK Targeting potential and anti-HIV activity of lamivudine loaded mannosylated poly (propyleneimine) dendrimer. Biochim Biophys Acta. (2007) 1770(4):681–686
51. 1. Lim WQ, Zeng S, Phua F, Zhao Y. Redox-Responsive Polymeric Nanocomplex for Delivery of Cytotoxic Protein and Chemotherapeutics. 2019; Available from: www.acsami.org
52. Lee, K.S.; Chung, H.C.; Im, S.A.; Park, Y.H.; Kim, C.S.; Kim, S.-B.; Rha, S.Y.; Lee, M.Y.; Ro, J. Multicenter phase II trial of Genexol-PM, a Cremophor-free, polymeric micelle formulation of paclitaxel, in patients with metastatic breast cancer. Breast Cancer Res. Treat. 2008, 108, 241–250.
53. Noori Koopaei, M.; Khoshayand, M.R.; Mostafavi, S.H.; Amini, M.; Khorramizadeh, M.R.; Jeddi Tehrani, M.; Atyabi, F.; Dinarvand, R. Docetaxel Loaded PEG-PLGA Nanoparticles: Optimized Drug Loading, In-vitro Cytotoxicity and In-vivo Antitumor Effect. Iran. J. Pharm. Res. 2014, 13, 819–833. [PubMed]
54. Taghipour-Sabzevar, V., Sharifi, T., and Moghaddam, M. M. Polymeric nanoparticles as carrier for targeted and controlled delivery of anticancer agents. Ther. Deliv. (2019). 10, 527–550. doi:10.4155/tde-2019-0044
55. Kahraman M, Mullen ER, Korkmaz A, Wachsmann-Hogiu S. Fundamentals and applications of SERS-based bioanalytical sensing. Nanophotonics. 2017 Aug 28;6(5):831–52.
56. Lee C, Robertson CS, Nguyen AH, Kahraman M, Wachsmann- Hogiu S. Thickness of a metallic film, in addition to its roughness, plays a significant role in SERS activity. Scientific Reports 2015;5:11644, 1–10.

57. C.I.L. Justino, A.C. Freitas, R. Pereira, A.C. Duarte, T.A.P. Rocha-Santos, Recent developments in recognition elements for chemical sensors and biosensors, Trends Anal. Chem. 68 (2015) 217.
58. Ahmed SR, Kim J, Tran VT, Suzuki T, Neethirajan S, Lee J, et al. In situ self-assembly of gold nanoparticles on hydrophilic and hydrophobic substrates for influenza virus-sensing platform. Sci Rep [Internet]. 2017;7(February):1–11. Available from: http://dx.doi.org/10.1038/srep44495
59. 1. Bao LL, Mahurin SM, Liang C Du, Dai S. Study of silver films over silica beads as a surface-enhanced Raman scattering (SERS) substrate for detection of benzoic acid. J Raman Spectrosc. 2003;34(5):394–8.
60. Baptista A, Silva F, Porteiro J, Míguez J, Pinto G. coatings Sputtering Physical Vapour Deposition (PVD) Coatings: A Critical Review on Process Improvement and Market Trend Demands. Available from: www.mdpi.com/journal/coatings
61. Mattevi, C.; Kim, H.; Chhowalla, M. AReviewof Chemical Vapour Deposition of Graphene on Copper. J. Mater. Chem. 2011, 21, 3324–3334.
62. Keeney M, Jiang XY, Yamane M, Lee M, Goodman S, Yang F. Nanocoating for biomolecule delivery using layer-by-layer self-assembly. J Mater Chem B. 2015;3(45):8757–70.
63. Mengwei Gao, Yuanbo Song, Yidan Liu, Wentao Jiang, Jianchao Peng, Liyi Shi, Rongrong Jia, Yaseen Muhammad, Lei Huang, Controlled fabrication of Au@MnO2 core/shell assembled nanosheets by localized surface plasmon resonance,Applied Surface Science,Volume 537,2021,147912,ISSN 0169-4332,https://doi.org/10.1016/j.apsusc.2020.147912.
64. Park S, Han U, Choi D, Hong J. Layer-by-layer assembled polymeric thin films as prospective drug delivery carriers: design and applications. Biomater Res. 2018;22(1):1–13.
65. Mocan, T.; Matea, C.; Tabaran, F.; Iancu, C.; Orasan, R.; Mocan, L. In Vitro Administration of Gold Nanoparticles Functionalized with MUC-1 Protein Fragment Generates Anticancer Vaccine Response via Macrophage Activation and Polarization Mechanism. J. Cancer 2015, 6, 583–592. [CrossRef]
66. Brust M, Walker M, Bethell D, Schiffrin DJ, Whyman R. Synthesis of thiol-derivatised gold nanoparticles in a two-phase liquid-liquid system. J Chem Soc Chem Commun. 1994;7:5–7.
67. Prajapati S, Padhan B, Amulyasai B, Sarkar A. Nanotechnology-based sensors. Biopolym Formul Biomed Food Appl. 2020 Jan 23;237–62.
68. Khuong Vo Q, Thu Nguyen A, Tien Ho H, Thanh Nguyen Huynh L, Phuong Phong Nguyen T, Hong-Tham Nguyen T. Environmentally Friendly Controlled Synthesis of Gold Nanostars with Collagen by One-Step Reduction Method. 2022; Available from: https://doi.org/10.1155/2022/4046389
69. Soroory H, Mashak A, Rahimi A. Application of PDMS-based coating in drug delivery systems using PVP as channeling agent. Iran Polym J (English Ed. 2013;22(11):791–7.
70. Lee B, Yoon S, Lee JW, Kim Y, Chang J, Yun J, et al. Statistical Characterization of the Morphologies of Nanoparticles through Machine Learning Based Electron Microscopy Image Analysis. ACS Nano [Internet]. 2020;14:17125–33. Available from: https://dx.doi.org/10.1021/acsnano.0c06809

71. Ting Xiao, Jianshe Huang, Dewen Wang, Tian Meng, Xiurong Yang,Au and Au-Based nanomaterials: Synthesis and recent progress in electrochemical sensor applications,Talanta,Volume 206,2020,120210,ISSN 0039-9140,https://doi.org/10.1016/j.talanta.2019.120210
72. Huynh KH, Pham XH, Kim J, Lee SH, Chang H, Rho WY, et al. Synthesis, properties, and biological applications of metallic alloy nanoparticles. Int J Mol Sci. 2020;21(14):1–29.
73. Castro Coelho S, Reis DP, Pereira MC, Coelho MAN. pharmaceutics Doxorubicin and Varlitinib Delivery by Functionalized Gold Nanoparticles Against Human Pancreatic Adenocarcinoma. Available from: www.mdpi.com/journal/pharmaceutics
74. Bagheri S, Yasemi M, Safaie-Qamsari E, Rashidiani J, Abkar M, Hassani M, Mirhosseini SA, Kooshki H. Using gold nanoparticles in diagnosis and treatment of melanoma cancer. Artif Cells Nanomed Biotechnol. 2018;46(sup1):462-471. doi: 10.1080/21691401.2018.1430585. Epub 2018 Jan 26. PMID: 29373944.
75. Dykman LA. Gold nanoparticles for preparation of antibodies and vaccines against infectious diseases. Expert Rev Vaccines. 2020 May;19(5):465-477. doi: 10.1080/14760584.2020.1758070. Epub 2020 Apr 28. PMID: 32306785; PMCID: PMC7196924.
76. Sehit E, Drzazgowska J, Buchenau D, Yesildag C, Lensen M, Altintas Z. Ultrasensitive nonenzymatic electrochemical glucose sensor based on gold nanoparticles and molecularly imprinted polymers. Biosens Bioelectron. 2020 Oct 1;165:112432. doi: 10.1016/j.bios.2020.112432. Epub 2020 Jul 12. PMID: 32729546.
77. Nemčeková K, Svitková V, Sochr J, Gemeiner P, Labuda J. Gallic acid-coated silver nanoparticles as perspective drug nanocarriers: bioanalytical study. Available from: https://doi.org/10.1007/s00216-022-03955-2
78. Amjadi, M., Rahimpour, E. Silver nanoparticles plasmon resonance-based method for the determination of uric acid in human plasma and urine samples. Microchim Acta 178, 373–379 (2012). https://doi.org/10.1007/s00604-012-0849-7
79. Yao Dou, Xiaoming Yang, Zhongde Liu, Shanshan Zhu,Homocysteine-functionalized silver nanoparticles for selective sensing of Cu2+ ions and Lidocaine hydrochloride,Colloids and Surfaces A: Physicochemical and Engineering Aspects,Volume 423,2013,Pages 20-26,ISSN 0927-7757, https://doi.org/10.1016/j.colsurfa.2013.01.027.
80. Ramar Rajamanikandan, Malaichamy Ilanchelian,Simple and visual approach for highly selective biosensing of vitamin B1 based on glutathione coated silver nanoparticles as a colorimetric probe,Sensors and Actuators B: Chemical, Volume 244,2017,Pages 380-386,ISSN 0925-4005,https://doi.org/10.1016/j.snb.2016.12.129.
81. Mengmeng Gao, Lili Li, Suxiang Lu, Qiang Liu, Hua He.Silver nanoparticles for the visual detection of lomefloxacin in the presence of cystine,Spectrochimica Acta Part A: Molecular and Biomolecular Spectroscopy,Volume205,2018,Pages72-78,ISSN1386-1425, https://doi.org/10.1016/j.saa.2018.05.072.
82. Ji-chun Qu, Yan-ping Chang, Yan-hua Ma, Jin-min Zheng, Hong-hong Li, Qian-qian Ou, Cuiling Ren, Xing-guo Chen,A simple and sensitive colorimetric method for the determination of

propafenone by silver nanoprobe,Sensors and Actuators B: Chemical,Volume 174,2012,Pages 133-139,ISSN 0925-4005,https://doi.org/10.1016/j.snb.2012.08.045.
83. Priyadarsini S, Mohanty S, Mukherjee · Sumit, Basu S, Mishra M. Graphene and graphene oxide as nanomaterials for medicine and biology application. J Nanostructure Chem [Internet]. 2018;8:123–37. Available from: https://doi.org/10.1007/s40097-018-0265-6
84. Loh, K.P., Bao, Q., Eda, G., Chhowalla, M.: Graphene oxide as a chemically tunable platform for optical applications. Nat. Chem. (2010) 2(12), 1015
85. Genix, A.-C., and Oberdisse, J. Nanoparticle self-assembly: from interactions in suspension to polymer nanocomposites. Soft Matter (2018). 14, 5161– 5179. doi: 10.1039/c8sm00430g
86. Cheon YA, Bae JH, Chung BG. Reduced Graphene Oxide Nanosheet for Chemo-photothermal Therapy. Langmuir. 2016 Mar 22;32(11):2731-6. doi: 10.1021/acs.langmuir.6b00315. Epub 2016 Mar 10. PMID: 26930106
87. Peik-See T, Pandikumar A, Nay-Ming H, Lim H-N, Sulaiman Y. Simultaneous Electrochemical Detection of Dopamine and Ascorbic Acid Using an Iron Oxide/Reduced Graphene Oxide Modified Glassy Carbon Electrode. Sensors [Internet]. 2014;14:15227–43. Available from: www.mdpi.com/journal/sensorsArticle
88. Hoa LT, Sun KG, Hur SH. Highly sensitive non-enzymatic glucose sensor based on Pt nanoparticle decorated graphene oxide hydrogel. Sensors Actuators B Chem. 2015 Apr 1;210:618–23.
89. Li, N., Zhang, Q., Gao, S., Song, Q., Huang, R., Wang, L., Liu, L., Dai, J., Tang, M., Cheng, G.: Three-dimensional graphene foam as a biocompatible and conductive scaffold for neural stem cells. Sci. Rep. (2013) 3, 1604.
90. Naresh, V.; Lee, N. A Review on Biosensors and Recent Development of Nanostructured Materials-Enabled Biosensors. *Sensors* **2021**, *21*, 1109. https://doi.org/10.3390/s21041109
91. Grieshaber, D.; MacKenzie, R.; Vörös, J.; Reimhult, E. Electrochemical Biosensors - Sensor Principles and Architectures. Sensors 2008, 8, 1400-1458. https://doi.org/10.3390/s80314000
92. Vu C-A, Chen W-Y. Field-Effect Transistor Biosensors for Biomedical Applications: Recent Advances and Future Prospects. Available from: www.mdpi.com/journal/sensors
93. Pandit, Subhendu.. Graphene and Graphene Oxide Based Biosensors. (2015) 10.13140/RG.2.1.1372.8088.
94. Bhat, K.S.; Ahmad, R.; Yoo, J.-Y.; Hahn, Y.-B. Nozzle-Jet Printed Flexible Field-Effect Transistor Biosensor for High Performance Glucose Detection. J. Colloid Interface Sci. 2017, 506, 188–196.
95. Hao, Z.; Zhu, Y.; Wang, X.; Rotti, P.G.; DiMarco, C.; Tyler, S.R.; Zhao, X.; Engelhardt, J.F.; Hone, J.; Lin, Q. Real-Time Monitoring of Insulin Using a Graphene Field-Effect Transistor Aptameric Nanosensor. ACS Appl. Mater. Interfaces 2017, 9, 27504–27511
96. Martinkova, P.; Kostelnik, A.; Valek, T.; Pohanka, M. Main streams in the construction of biosensors and their applications. Int. J. Electrochem. Sci. 2017, 12, 7386–7403.

97. Alhadrami, H. A. Biosensors: Classifications, medical applications, and future prospective. Biotechnology and Applied Biochemistry, (2018). 65(3), 497?508. Available from: https://doi.org/10.1002/bab.1621
98. Germarie Sánchez-Pomales, Rebecca A. Zangmeister, "Recent Advances in Electrochemical Glycobiosensing", International Journal of Electrochemistry, vol. 2011, Article ID 825790, 11 pages, 2011. https://doi.org/10.4061/2011/825790
99. Qin Liu, Xu Zhu, Zhaohui Huo, Xulun He, Yong Liang, Maotian Xu.Electrochemical detection of dopamine in the presence of ascorbic acid using PVP/graphene modified electrodes,Talanta, Volume 97,2012,Pages 557-562,ISSN 0039-9140,https://doi.org/10.1016/j.talanta.2012.05.013.
100. Chigo, E & Soto, A. & Cocoletzi, Gregorio. (2013). Studies of graphene–chitosan interactions and analysis of the bioadsorption of glucose and cholesterol. Applied Nanoscience. 4. 911-918. 10.1007/s13204-013-0283-0.
101. Farzaneh Ahmadi, Jahan Bakhsh Raoof, Reza Ojani, Mehdi Baghayeri, Moslem Mansour Lakouraj, Hamed Tashakkorian,Synthesis of Ag nanoparticles for the electrochemical detection of anticancer drug flutamide,Chinese Journal of Catalysis,Volume 36, Issue 3,2015,Pages 439-445,ISSN 1872-2067,https://doi.org/10.1016/S1872-2067(14)60209-6.
102. Radhapyari, Keisham & Khan, Raju. Biosensor For Detection Of Selective Anticancer Drug Gemcitabine Based On Polyaniline-Gold Nanocomposite. Advanced Materials Letters. 6. (2015). 13-18. 10.5185/amlett.2015.5607.
103. Monzó J, Insua I, Fernandez-Trillo F, Rodriguez P. Fundamentals, achievements and challenges in the electrochemical sensing of pathogens. Analyst. 2015 Nov 7;140(21):7116-28. doi: 10.1039/c5an01330e. PMID: 26339688.
104. Miyazaki CM, Shimizu FM, Ferreira M. Surface Plasmon Resonance (SPR) for Sensors and Biosensors. Nanocharacterization Tech. 2017 Jan 1;183–200.
105. Canovi M, Lucchetti J, Stravalaci M, et al. Applications of surface plasmon resonance (SPR) for the characterization of nanoparticles developed for biomedical purposes. Sensors (Basel). 2012;12(12):16420-16432. Published 2012 Nov 27. doi:10.3390/s121216420
106. Tkac J, Bertok T, Nahalka J, Gemeiner P. Chapter 37 Perspectives in Glycomics and Lectin Engineering. 2014;(January).
107. Perdomo SA, Marmolejo-Tejada JM, Jaramillo-Botero A. Laser Physics Letters Development of surface plasmon resonance (SPR) biosensors for use in the diagnostics of malignant and infectious diseases You may also like Review-Bio-Nanosensors: Fundamentals and Recent Applications. 2018; Available from: https://doi.org/10.1088/1612-202X/aab43f
108. Chalyan T, Potrich C, Schreuder E, et al. AFM1 Detection in Milk by Fab' Functionalized Si3N4 Asymmetric Mach-Zehnder Interferometric Biosensors. Toxins (Basel). 2019;11(7):409. Published 2019 Jul 14. doi:10.3390/toxins11070409
109. Liu Y, Liu Q, Chen S, Cheng F, Wang H, Peng W. Surface Plasmon Resonance Biosensor Based on Smart Phone Platforms. Sci Rep. 2015;5:12864. Published 2015 Aug 10. doi:10.1038/srep12864

110. Blasi, Davide & Sarcina, Lucia & Tricase, Angelo & Stefanachi, Angela & Leonetti, Francesco & Alberga, Domenico & Mangiatordi, Giuseppe & Manoli, Kyriaki & Scamarcio, Gaetano & Picca, Rosaria & Torsi, Luisa. Enhancing the Sensitivity of Biotinylated Surfaces by Tailoring the Design of the Mixed Self-Assembled Monolayer Synthesis. ACS Omega. (2020). XXXX. 10.1021/acsomega.0c01717.
111. Jabbari S, Dabirmanesh B, Arab SS, Amanlou M, Daneshjou S, Gholami S, et al. A novel enzyme based SPR-biosensor to detect bromocriptine as an ergoline derivative drug. Sensors Actuators B Chem. 2017 Mar 1;240:519–27.
112. Villena Gonzales W, Mobashsher AT, Abbosh A. The Progress of Glucose Monitoring-A Review of Invasive to Minimally and Non-Invasive Techniques, Devices and Sensors. Sensors (Basel). 2019 Feb 15;19(4):800. doi: 10.3390/s19040800. PMID: 30781431; PMCID: PMC6412701.
113. Izo J, Jesus S De, Löbenberg R, Bou-chacra NA. Raman Spectroscopy for Quantitative Analysis in the Pharmaceutical Industry. 2020;24–46.
114. Shiju A, Matthias K, Sunil K. Srivastava, Vinod K, Bernd W, Anchal Srivastava, Carbon nanostructure (0-3 dimensional) supported isolated gold nanoparticles as an effective SERS substrate,Sensors and Actuators B: Chemical,Volume 273,2018,Pages 455-465,ISSN 0925-4005,https://doi.org/10.1016/j.snb.2018.06.066.
115. Hidi, Izabella & Jahn, Martin & Pletz, Mathias & Weber, Karina & Cialla-May, Dana & Popp, Juergen. (2016). Towards Levofloxacin Monitoring in Human Urine Samples by Employing the LoC-SERS Technique. The Journal of Physical Chemistry C. 120. 10.1021/acs.jpcc.6b01005.
116. Garrido E, Pla L, Lozano-Torres B, El Sayed S, artínez-MµÇez R, Sancenón Fø. Chromogenic and Fluorogenic Probes for the Detection of Illicit Drugs. ChemistryOpen [Internet]. 2018;7:401–28. Available from: https://doi.org/10.1002/open.201800034.
117. Long S, Chen Z, Chen Y, Yu R. Quantitative detection of captopril in tablet and blood plasma samples by the combination of surface-enhanced Raman spectroscopy with multiplicative effects model. 2015;(April):605–9.
118. Sallum LF, Soares FL, Ardila JA, Carneiro RL. Determination of acetylsalicylic acid in commercial tablets by SERS using silver nanoparticle-coated filter paper. Spectrochim Acta A Mol Biomol Spectrosc. 2014 Dec 10;133:107-11. doi: 10.1016/j.saa.2014.04.198. Epub 2014 May 27. PMID: 24929322.
119. Ouyang, Lei, Ren, Wen, Zhu, L and Irudayaraj, J. "Prosperity to challenges: recent approaches in SERS substrate fabrication" Reviews in Analytical Chemistry, vol. 36, no. 1, 2017, pp. 20160027. https://doi.org/10.1515/revac-2016-0027
120. Cai X, Wang CL, Chen HH, Chien CC, Lai SF, Chen YY, et al. Tailored Au nanorods: Optimizing functionality, controlling the aspect ratio and increasing biocompatibility. Nanotechnology. 2010 Aug 20;21(33).

2. Methodology

In this chapter, the methods that were followed during the study are explained from optimized experimental procedures that were used to synthesize and apply the chemical sensors. The succeeding sections begin with physical vapor deposition (PVD) which was used for coating glass substrates with thin metallic layers. Secondly, the chemical functionalization of the coated substrates using organic crosslinkers is explained followed by the synthesis of metallic nanoparticles for enhanced applications. Thirdly, characterization techniques such as UV-Vis spectroscopy, transmission electron microscopy and Raman spectroscopy are reported based on their applicability to the study. Lastly, statistical methods that generate information on the analytical quality of the study are outlined with emphasis on the mathematical equations relating to the calibration and analytical sensitivity and limit of detection of the chemical sensors.

2.1 Thin layer coating using Physical Vapor Deposition (PVD)

Physical vapor deposition (PVD) technique is a deposition method that coats thin layer films on substrates one atom at a time to produce pristine, smooth platforms [1-2]. The general process entails vaporization and atomization of target sources under vacuum, plasma, electrolytic and gaseous conditions. The film thickness produced from the process ranges between atomic layers to microns [3]. The main benefits of PVD are the structural control of the substrate and strong adhesion to the surface upon material deposition. In this manner, substrate properties can be altered both physical and chemically to design layers for sensing applications [4]. As a result of its continued growth in research and application, PVD contains a variety of sub-techniques that are categorized into two main groups: Evaporation and Sputtering [5-6]. In this study, magnetron sputtering, and electron beam (E-Beam) evaporation methods were used concurrently to create the first few layers of the chemical sensors. These methods were chosen based on the type of metal targets that were available for the coating processes. Figure 2.1 below shows illustrates the design of both PVD methods.

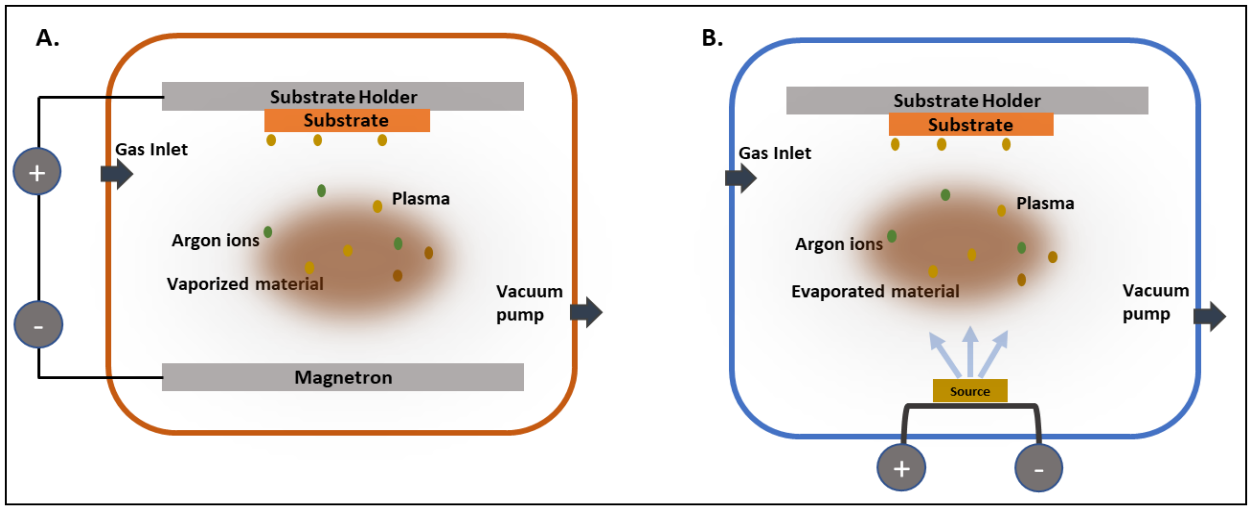

Figure 2.1:Schematic of Physical Vapor Deposition methods: A) Magnetron Sputtering, B). E-Beam evaporation.[7]

For this study, A Korvex ™ PVD system was used in the coating experiments which were controlled using the manufacturer's software. Using figure 1A as a reference for the sputtering method, an argon gas plasma of positively charged ions was created in a vacuum chamber maintained at a pressure of 5.00 10^{-5} bar. A voltage was then applied to a titanium magnetron which directed the ions to the surface, causing a high-impact collision resulting in the release of metallic atoms towards the substrate [7-8]. The metallic atoms arranged themselves on the substrate while being rotated at a constant speed of 30 cycles per minute using the substrate holder. Furthermore, a quartz crystal microbalance (QCM) inside the PVD instrument was used to control the film thickness with the aid of a profilometer which calibrates the measured thickness using tooling factor calculations [9]. For the deposition of gold and silver metals, the e-beam method in figure 1B was used. In this technique, a target metal is subjected to a voltage by a filament, which causes an increase in temperature that evaporates the metallic atoms towards the substate [10]. The QCM was used to control the layer thickness similar to the sputtering method while a tooling factor set by the software, is used to correct minor errors in coating thickness that may arise from the technical process. Table 1 below is a summary of the deposition experiments taken for metal deposition.

Table 2.1: Settings for PVD coating of gold and silver.

Method	Metal	Tooling factor	Film thickness (nm)
Sputtering			
	Titanium	250	10
E Beam			
	Gold (Au)	150	25,50,100
	Silver (Ag)	150	25,50,100

In the table above, four metals were chosen for producing the first layers of the chemical sensors. A Titanium layer (Ti, 10nm) was coated with gold (Au) and silver (Ag) separately, each layer consisting of 25-100nm of the metal. The Ti/Au and Ti/Ag combination was done to enforce adherence of the precious metals to the surface prior to functionalization with organic crosslinkers.

2.2 Metallic nanoparticles for surface enhancement.

Surface modification using nanomaterials was used in this study to support the adsorption of the analytes to the chemical sensor and to provide chemical signal enhancement [11]. Furthermore, such an approach allows the designing of substrates capable of adsorption towards the analytes via intermolecular forces. As such, two benchtop techniques; chemical reduction, and the self-assembly method (SAM), were selected to fabricate metallic nanoparticles and use them to chemically functionalize the coated samples from section 2.1. The chemical reduction method used to synthesize the metallic nanoparticles (MNPs) follows three key steps: reduction of metal salts using a reducing agent, stabilizing the ionic mixtures and lastly control of the size distribution using a capping agent [12-15]. The newly formed MNPs are then used to coat the thin metallic films using the self-assembly method. In SAM, molecules from the surrounding media that is the

MNPs are chemisorbed or physiosorbed onto the surface embedded in the solution [16]. In this manner, the nanomaterials arrange themselves on the surface via chemical interactions that foster the stereochemistry of the adsorption process, forming well-ordered structures of various shapes and sizes on the platform. Figure 2.2 below is a schematic of the chemical reduction and self-assembly methods used in this study.

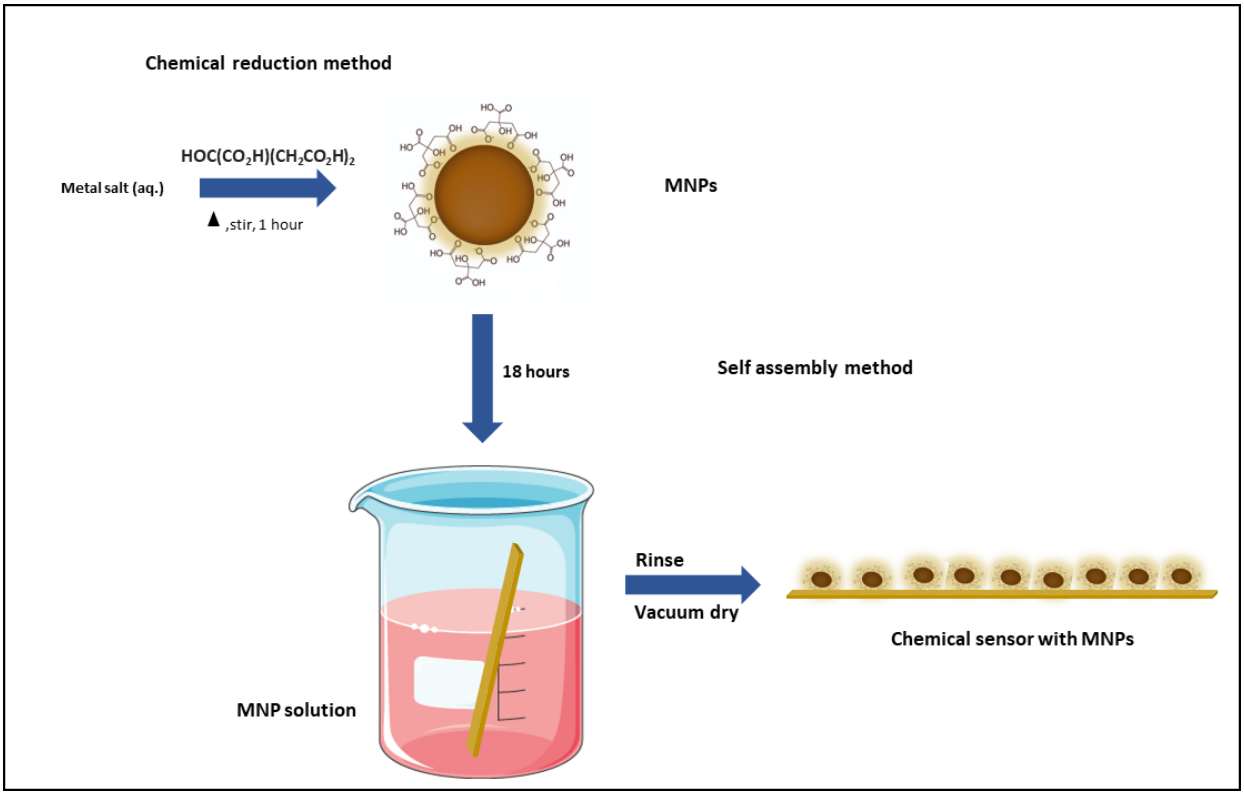

Figure 2.2:Schematic of the functionalization process using chemical reduction and the self-assembly method

Two crosslinkers were investigated for this study based on the presence of their functional groups which serve as active sites for chemical adsorption. Sodium citrate tribasic and cysteamine were selected because the former contains hydroxyl (-OH) and carboxylate groups ($-COO^-$) while the latter possesses amine ($-NH_2$) and possibly thiol groups (-SH) depending on preferred orientation. The sections that follow explain the processes undertaken to synthesize MNPs of gold (Au) and silver (Ag) using the above crosslinkers as well as the coating steps followed during self-assembly on the gold slides. Calculations of the theoretical concentrations are given in the supplementary section C1.

2.2.1 Citrate (Cit) crosslinking metallic nanoparticles of gold and silver on coated slides.

Citrate stabilized MNPs were prepared using an adjusted version of the Turkevich method [17] as follows. For gold/citrate nanoparticles (Au@Citrate), 60 mg of sodium tetrachloroaurate (III) dihydrate ($NaAuCl_4$, Sigma: 298174) was dissolved in 125 mL deionized water and brought to a boil. Meantime, a 1 % solution sodium citrate tribasic dihydrate (Sigma, 71409) was prepared in

deionized water and 12.5 mL of the solution was pipetted into the $AuCl_4$ solution. The reaction mixture was stirred vigorously on a heated magnetic stove for 1 hour. The solution turned wine red which indicates the formation of gold nanoparticles [18-19]. The chemical reaction for the Au@Cit synthesis is explained by the balanced equation below.

$$3C_6H_5O_7^{-3} + 6OH^- + 2Au^{+3} = 2Au^0 + 3O_{2\uparrow} + 3H_2O$$

Silver citrate nanoparticles were synthesized using a revised version of the Lee and Meisel method [20]. Briefly, 22.5 mg of silver nitrate ($AgNO_3$, Sigma: 101510) was dissolved in 125 mL deionized water and brought to a boil. 12.5 mL of 1 % citrate solution was pipetted into the boiling solution and stirred for 1 hour. The solution turned yellow-green which indicated the presence of silver nanoparticles. The chemical reaction of this process can be explained by the equation.

$$4Ag^+ + C_6H_5O_7Na_3 + 2H_2O = 4Ag^0 + C_6H_5O_7H_3 + 3Na^+ + H^+ + O_{2\uparrow}$$

The Au@Citrate and Ag@Citrate solutions were subsequently analyzed using UV-Vis spectroscopy. After spectroscopic confirmation of MNPs, 60 mL of each solution was diluted 1:1 with water and filtered using a 0.45 µm filter and a 10 mL syringe. 20 mL of the filtered solutions were pipetted on petri dishes containing metal-coated slides: Au@Citrate on Au slide and Ag@Citrate on Ag. The MNPs were allowed to self-assemble on the substrates overnight and then subsequently rinsed with water to remove unbound MNPs. The slides were dried under vacuum for 3 hours prior to analysis with Raman microscopy.

2.2.2 Cysteamine (Cys) crosslinking metallic nanoparticles of gold and silver on coated slides.

For Au@cysteamine MNPs, 400 µL of 0.213 M cysteamine hydrochloride and 40 mL of 1.40 mM HAuCl4 were mixed in a 100 mL glass bottle. The mixture was stirred for 20 min at room temperature in the dark. 10 mL of freshly prepared NaBH4 solution (10 mM) was then quickly added into the above aqueous solution under vigorous stirring, and the mixture was further stirred for 30 min at room temperature in the dark. The resulting wine-red solution was filtered by 0.45 µm Millipore membrane filter and stored in the refrigerator (4 °C) before use [21]. The reaction equation for this synthesis is as follows:

$$HAuCl_4 + 3HS(CH_2)_2NH_2 = Au(S(CH_2)_2NH_2)_3 + 4HCl$$

In the case of Ag@cysteamine MNPs, a 30 mL portion of 0.2 mM sodium borohydride (NaBH4) was taken in an Erlenmeyer flask fitted with a magnetic stir bar and placed in an ice bath with constant stirring for 20 min. In another flask, 20 mL of 0.1 mM $AgNO_3$ solution was placed in an ice bath and 3 mL of 0.3% of cysteamine hydrochloride was mixed with it. Then cold $NaBH_4$ solution was added to it dropwise at a very slow rate until the solution became vivid yellow. The flask containing yellow Ag-Nps was removed from the ice bath and was allowed to come at room temperature with constant stirring. The solution was centrifuged and washed several times with dionized water [22]. The reaction for the above process is described by the following equation:

$$AgNO_3 + HS(CH_2)_2NH_2 = Ag(CH_2)_2NH_2 + HNO_3$$

2.3 UV-Vis spectroscopy of metallic nanoparticles.

A Thermofischer Nanodrop 2000 instrument was used to analyze the metallic nanoparticles (MNPs) from section 2.2. The instrument sample holders were cleaned with 70% ethanol prior to calibration by blanking with water. Each metal (MNP) was treated separately as a group to compare the two crosslinkers used: citrate (1) and cysteamine (2). The MNP solutions were all diluted 1 in 100 prior to analysis. 10 µL of the analytes was pipetted on the sample holders as follows: blank solution (water), reference solutions (crosslinker 1&2), MNP 1, MNP 2. The instrument was set on UV-Vis mode and the measurements were acquired in triplicates. The data obtained was exported and plotted on Microsoft excel for analysis [23]

2.4 Characterization of functionalized MNPs using Transmission Electron Microscopy.

A JEOL JEM 2100 High-Resolution Transmission Electron Microscope was used to analyze the synthesized nanomaterials from section 2.2 as follows. A drop of the nanoparticle sample was placed into a Cu grid and allowed to adsorb it for +- 3 minutes. They were then allowed to dry for a few minutes and placed in the sample holder. Analysis was conducted using a focal length of 2.7 mm, 1500x magnification and a resolution of 0.5 nm. The images were processed using ImageJ software where 100 particle sizes were recorded and used to plot frequency distribution graphs to determine the particle size distribution [24].

2.5 SERS analysis of ARVs on functionalized chemical sensors.

As mentioned in chapter 1, Raman spectroscopy provides and inherently weak signal which is overpowered by the laser source. Many efforts have been explored to overcome this limitation and to produce higher Raman signals, one such approach being surface-enhanced Raman spectroscopy (SERS) [25]. This method incorporates nanomaterials as support structures that amplify the Raman signal [26–30] to achieve improved sensitivity, detection limit and enhancement [31]. Figure 3 below is a schematic representation of the surface enhancement sensor platform with the major components labelled in the image.

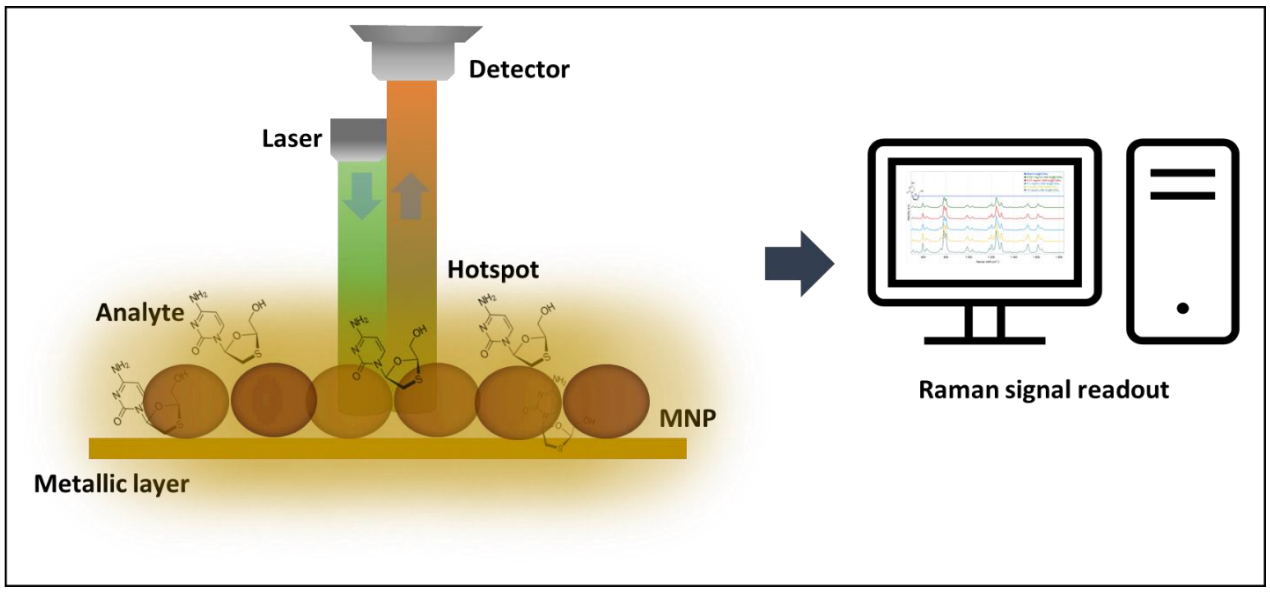

Figure 2.3:Schematic of surface enhancement platform for Raman spectroscopy.

Although the exact mechanism of SERS is still under discussion, it is widely accepted that the surface enhancement effect arises from two processes: electromagnetic and chemical enhancement [32-33]. In the case of electromagnetic enhancement (EM), the SERS effect occurs from the interaction between the incident laser photons and the surface plasmons, which are the collective oscillating frequencies of the conducting electrons found on the surface of the metallic nanostructure [34-35]. As seen in figure 2.3, the efficiency of this method relies on the distance between the analyte and the metal nanoparticle (MNP) where, a "hotspot" is created by the nanoparticle and the laser beam which together, amplify the analyte signal in the vicinity [36-37]. The chemical enhancement model (CM) employs molecular interactions such as covalent bonding, charge-selective mechanism, hydrophobic interactions and -stacking between the analyte and the NP to increase the Raman cross-scattering area, thereby improving the Raman signal intensity. In this study, ARV medication Tenofovir (TDF), Lamivudine (LAM) and Dolutegravir (DLG) were kindly supplied by Aurogen ™ pharmaceuticals. Each sample was dissolved in 20 ml deionized water and subsequently diluted 0; 0.001; 0.01; 0.1; 1; 10 mg/ml. Water and crosslinker stabilized MNPs on metal-coated glass were used as the blank and reference for the glass and the sensor respectively. 20 µL of each sample was placed on the sensing platform to cover an area of and allowed to dry under vacuum prior to signal acquisition. Thereafter, a Raman map was obtained from one hundred points acquired using 12 mW power, 10x magnification, 200 µm slid width, 10 seconds per scan, and averaged at 3 scans per point. The data was saved for further processing using statistical methods.

2.6 Statistical evaluation of ARVs using SERS.

Raman bands arising from the anti-HIV medication were selected and evaluated using statistical methods with the aim of comparing, calibration and analytical sensitivities and limit of detection for selected functional groups present. Each of the above parameters was evaluated using their corresponding mathematical equations that are well-published in literature.

The calibration sensitivity was calculated from plotting the peak area against the sample concentration. A linear equation was derived from the plot along with a R^2 values which were used to determine the quality of the fit. The resulting equation was

$$S = mc + S_{bl} \quad (1)$$

where S is the signal (peak area), m is the slope or calibration sensitivity and S_{bl} is the signal from the blank sample. The calculations began with recording the standard error of the mean s_m for each selected peak provided by the instrumental software and using that value to calculate the standard deviation s using the following equation where N is the number of replications for each sample group

$$s = \frac{s_m}{\sqrt{N}}$$

The calibration sensitivity and the standard deviation values were used to calculate the analytical sensitivity as follows

$$\gamma = m/s_s$$

where m is the slope from equation 1 and s_s is the standard deviation of the measurements. The limit of detection was determined by using the average values of the blank signal $\overline{S_{bl}}$ and the corresponding standard deviation s_{bl} with a standard multiple *k* (valued at 3*)* using the equation.

$$S_m = \overline{S_{bl}} + \mathrm{k}s_{bl}$$

The slope from equation 1 is then used to determine c_m, the lowest detectable concentration or limit of detection from the equation.

$$C_m = \frac{S_m - S_{bl}}{m}$$

From these equations, comparisons between the API and API were made possible to determine the efficiency of the sensors across the analytes [38] .

References

1. Hacking SA, Zuraw M, Harvey EJ, Tanzer M, Krygier JJ, Bobyn JD. A physical vapor deposition method for controlled evaluation of biological response to biomaterial chemistry and topography. J Biomed Mater Res A. 2007 Jul;82(1):179-87. doi: 10.1002/jbm.a.31131. PMID: 17269149

2. Baptista A, Silva F, Porteiro J, Míguez J, Pinto G. coatings Sputtering Physical Vapour Deposition (PVD) Coatings: A Critical Review on Process Improvement and Market Trend Demands. Available from: www.mdpi.com/journal/coatings

3. Kravanja KA, Finšgar M. A review of techniques for the application of bioactive coatings on metal-based implants to achieve controlled release of active ingredients. Mater Des. 2022 May 1;217:110653.

4. Oviroh PO, Akbarzadeh R, Pan D, Coetzee RAM, Jen TC. New development of atomic layer deposition: processes, methods and applications. Sci Technol Adv Mater [Internet]. 2019;20(1):465–96. Available from: https://doi.org/10.1080/14686996.2019.1599694

5. E. Reinhold, J. Faber,Large area electron beam physical vapor deposition (EB-PVD) and plasma activated electron beam (EB) evaporation — Status and prospects, Surface and Coatings Technology,Volume 206, Issue 7,2011,Pages 1653-1659, ISSN 0257-8972.

6. Naseri, N.; Sangpour, P.; Mousavi, S.H. Applying alloyed metal nanoparticles to enhance solar assisted water splitting. RSC Adv. 2014, 4, 46697–46703.

7. Sangpour, P.; Akhavan, O.; Moshfegh, A. The effect of Au/Ag ratios on surface composition and optical properties of co-sputtered alloy nanoparticles in Au–Ag:SiO2 thin films. J. Alloy. Compd. 2009, 486, 22–28

8. Juhasz, J.A.; Best, S.M. Surface Modification of Biomaterials. In 6-Surface Modification of Biomaterials by Calcium Phosphate Deposition; Williams, R., Ed.; Woodhead Publishing: Cambridge, UK, 2011; pp. 143–169.

9. Matusiak A, Żak AM. Affordable Open-Source Quartz Microbalance Platform for Measuring the Layer Thickness. Sensors. 2022;22(17).

10. Abrar S, Hanif MB, Alghamdi AS, et al. Synthesis and Characterization of Nanostructured Multi-Layer Cr/SnO2/NiO/Cr Coatings Prepared via E-Beam Evaporation Technique for Metal-Insulator-Insulator-Metal Diodes. Materials (Basel). 2022;15(11):3906

11. Tang L, Liu Y, Liu G, Chen Q, Li Y, Shi L, et al. A Novel SERS Substrate Platform: Spatially Stacking Plasmonic Hotspots Films. Available from: https://doi.org/10.1186/s11671-019-2928-8.

12. Pengo P, Şologan M, Pasquato L, Guida F, Pacor S, Tossi A, et al. Gold nanoparticles with patterned surface monolayers for nanomedicine: current perspectives. Eur Biophys J. 2017;46(8):749–71.

13. Zongtao Zhang, Bin Zhao, Liming Hu,PVP Protective Mechanism of Ultrafine Silver Powder Synthesized by Chemical Reduction Processes,Journal of Solid State Chemistry,Volume 121, Issue 1,1996,Pages 105-110,ISSN 0022-4596,https://doi.org/10.1006/jssc.1996.0015.

14. Desai R, Mankad V, Gupta SK, Jha PK. Size distribution of silver nanoparticles: UV-visible spectroscopic assessment. Nanosci Nanotechnol Lett. 2012;4(1):30–4.

15. Cai X, Wang CL, Chen HH, Chien CC, Lai SF, Chen YY, et al. Tailored Au nanorods: Optimizing functionality, controlling the aspect ratio and increasing biocompatibility. Nanotechnology. 2010 Aug 20;21(33).

16. Sheila Hernandez, Juan V. Perales-Rondon, Aranzazu Heras, Alvaro Colina, Enhancement factors in electrochemical surface oxidation enhanced Raman scattering, Electrochimica Acta,Volume 380,2021,138223,ISSN 0013-4686,https://doi.org/10.1016/j.electacta.2021.138223.

17. Dong J, Carpinone PL, Pyrgiotakis G, Demokritou P, Moudgil BM. Synthesis of Precision Gold Nanoparticles Using Turkevich Method. *Kona*. 2020;37:224-232. doi:10.14356/kona.202001

18. P. Gaviña, M. Parra, S. Gil, and A. M. Costero, "Red or Blue? Gold Nanoparticles in Colorimetric Sensing", in Gold Nanoparticles - Reaching New Heights. London, United Kingdom: IntechOpen, 2018 [Online]. Available: https://www.intechopen.com/chapters/63055 doi: 10.5772/intechopen.80052

19. Teixeira A, Paris JL, Roumani F, Diéguez L, Prado M, Espiña B, et al. Multifuntional gold nanoparticles for the SERS detection of pathogens combined with a LAMP-in-microdroplets approach. Materials (Basel). 2020;13(8).

20. Zhang Y, Wang F, Yin H, Hong M. Nonuniform Distribution of Capping Ligands Promoting Aggregation of Silver Nanoparticles for Use as a Substrate for SERS. Adv Nanoparticles. 2013;02(02):104–11.

21. Wai JL, New SY. Cysteamine-coated gold nanoparticles for bimodal colorimetric detection with inverse sensitivity: A proof-of-concept with lysozyme. RSC Adv. 2019;10(2):1088–94.

22. Siewdorlang Diamai, Devendra P.S. Negi,Cysteine-stabilized silver nanoparticles as a colorimetric probe for the selective detection of cysteamine,Spectrochimica Acta Part A: Molecular and Biomolecular Spectroscopy,Volume 215, 2019, Pages 203-208,ISSN 1386-1425,https://doi.org/10.1016

23. Mäntele W, Deniz E. UV-VIS absorption spectroscopy: Lambert-Beer reloaded. Spectrochim Acta A Mol Biomol Spectrosc. 2017;173:965-968. doi:10.1016/j.saa.2016.09.03

24. Bian K, Schunk H, Ye D, Hwang A, Luk TS, Li R, et al. Formation of self-assembled gold nanoparticle supercrystals with facet-dependent surface plasmonic coupling. Nat Commun [Internet]. 2018;9(1):1–7. Available from: http://dx.doi.org/10.1038/s41467-018-04801-9

25. Kant, K.; Abalde-Cela, S. Surface-Enhanced Raman Scattering Spectroscopy and Microfluidics: Towards Ultrasensitive Label-Free Sensing. Biosensors 2018, 8, 62. https://doi.org/10.3390/bios8030062

26. Cialla, D., März, A., Böhme, R., Theil, F., Weber, K., Schmitt, M., & Popp, J. (2012). Surface-enhanced Raman spectroscopy (SERS): progress and trends. Analytical and bioanalytical chemistry, 403(1), 27–54. https://doi.org/10.1007/s00216-011-5631-x

27. Yuen C, Zheng W, Huang Z. Surface-enhanced raman scattering: Principles, nanostructures, fabrications, and biomedical applications. J Innov Opt Health Sci. 2008;1(2):267–84.

28. Banchelli M, Tiribilli B, Pini R, Matteini P, Caminati G, Fiorentino S. Graphene oxide / silver nanocube composites for SERS detection of biomolecules. 2015;1–3.

29. Wong CL, Dinish US, Buddharaju KD, Schmidt MS, Olivo M. Surface-enhanced Raman scattering (SERS)-based volatile organic compounds (VOCs) detection using plasmonic bimetallic nanogap substrate. Appl Phys A Mater Sci Process. 2014;117(2):687–92.

30. Junbin Fang, Junjia Zhu, Meng Fu, Yu Gu, Guanghuan Li, Honghao Hou, Zihua Lin, Xingyuan Chen, Xiangming Li,A SERS substrate with remarkable reproducibility: Adsorbing and detecting both hydrophobic and hydrophilic molecules using rGO/PEI/PAA/CD-AgNP nanocomposites,Applied Surface Science,Volume 542,2021,148708, ISSN 0169-4332,https://doi.org/10.1016/j.apsusc.2020.148708.

31. Grys D-B, De Nijs B, Salmon AR, Huang J, Wang W, Chen W-H, et al. Citrate Coordination and Bridging of Gold Nanoparticles: The Role of Gold Adatoms in AuNP Aging. ACS Nano [Internet]. 2020;14:8689–96. Available from: https://dx.doi.org/10.1021/acsnano.0c03050

32. Yamamoto YS, Ozaki Y, Itoh T. Recent progress and frontiers in the electromagnetic mechanism of surface-enhanced Raman scattering. J Photochem Photobiol C Photochem Rev. 2014 Dec 1;21:81–104.

33. Kim J, Jang Y, Kim NJ, Kim H, Yi GC, Shin Y, et al. Study of Chemical Enhancement Mechanism in Non-plasmonic Surface-enhanced Raman spectroscopy (SERS). Front Chem. 2019;7:1–7.

34. Baba A, Imazu K, Yoshida A, Tanaka D, Tamada K. Surface plasmon resonance properties of silver nanoparticle 2D sheets on metal gratings. Springerplus. 2014;3(1):1–10.

35. Patching SG. Surface plasmon resonance spectroscopy for characterisation of membrane protein-ligand interactions and its potential for drug discovery. Biochim Biophys Acta - Biomembr [Internet]. 2014;1838(1 PARTA):43–55. Available from: http://dx.doi.org/10.1016/j.bbamem.2013.04.028

36. Tahghighi M, Janner D, Ignés-Mullol J. Optimizing gold nanoparticle size and shape for the fabrication of sers substrates by means of the langmuir–blodgett technique. Nanomaterials. 2020 Nov 1;10(11):1–11.

37. Amane Shiohara, Yusong Wang, Luis M. Liz-Marzán, Recent approaches toward creation of hot spots for SERS detection,Journal of Photochemistry and Photobiology C: Photochemistry Reviews,Volume 21,2014,Pages 2-25,ISSN 1389-5567,https://doi.org/10.1016/j.jphotochemrev.2014.09.001.

38. Skoog, A.; Holler, J.; Crouch, S. Principles of Instrumental Analysis; ISE: Balmont, CA, USA, 2007.

3. Results

In this chapter of the study, the outcomes of the experiments using the methods described are reported. Firstly, the chemical sensors fabricated by physical vapor deposition, chemical reduction and self-assembly are characterized using spectroscopy and microscopy techniques where the morphology and molecular properties of the sensors are explained based on the Raman spectroscopic data. Secondly, HIV medication Tenofovir (TDF), Lamivudine (LAM) and Dolutegravir (DLG) in API form are tested using Surface-enhanced Raman spectroscopy (SERS) supported by the fabricated chemical sensors of gold and silver motif. Lastly, statistical analysis of the data is explained with a specific focus on calibration and analytical sensitivity and limit of detection. All data presented were subjected to background subtraction.

3.1 Characterization of chemical sensors using UV-Vis spectroscopy and Transmission Electron Microscopy.

3.1.1 UV-Vis spectroscopy of gold and silver nanoparticles

Samples synthesized in section 2.2 were tested using UV-Vis spectroscopy to characterize their adsorption bands to confirm the presence of nanoparticles in the crosslinker solutions. Figure 3. 1 shows the UV-Vis spectra of gold and silver nanoparticles after chemical reduction.

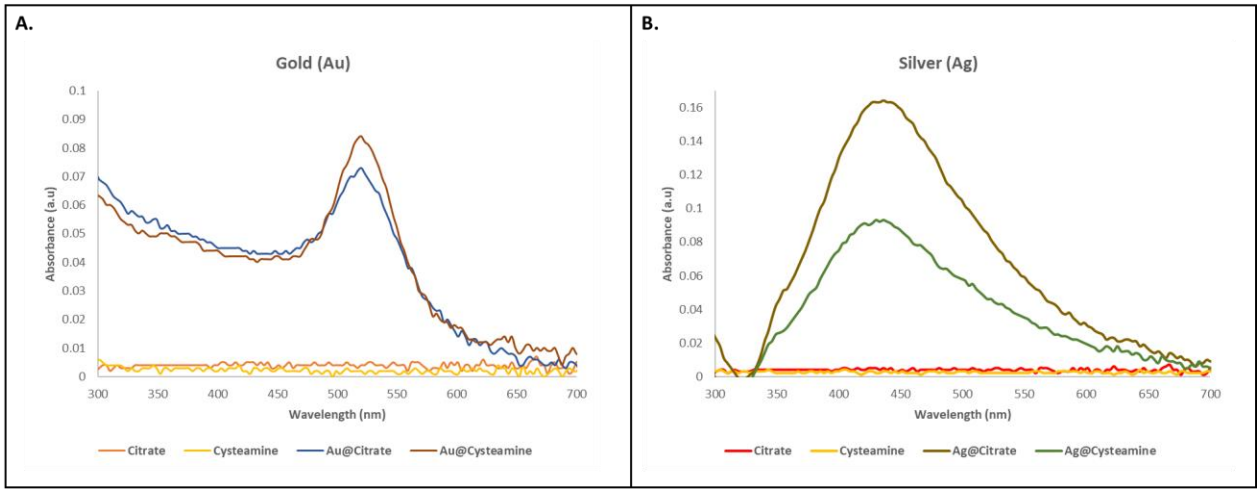

Figure 3.1:UV-Vis spectra of gold (A) and silver (B).

The UV-Vis spectra in figure 3.1 show gold nanoparticles (A) stabilized by crosslinkers citrate (red) and cysteamine (yellow). The blue line is citrate crosslinked nanoparticles of gold (Au@Cit) while the maroon line is the cysteamine counterpart (Au@Cys). These bands are characteristic of gold at a wavelength of 520 nm [1-2]. In figure 1B, two large bands of silver nanoparticles are observed with the green line representing cysteamine stabilized Ag@Cys samples and the bronze band assigned to the silver citrate Ag@Cit. A large absorbance at 440 nm is seen for Ag@Cit which is characteristic of silver nanoparticles, as further confirmed by the Ag@Cys below that is in the same absorbance range but lower in absorbance [3-4]. Detection of the gold and silver bands was a confirmation of functionalized nanoparticles in the crosslinker/stabilizer solution. Peak shifting

because of changes in chemical functionality was not clear in this data however, experiments with Raman spectroscopy will provide a detailed report on the molecular properties of the nanoparticles [5]. In the next section, samples were tested using TEM for further characterization prior to Raman microscopy.

3.1.2 Transmission Electron Microscopy of gold and silver nanoparticles.

The nanoparticles produced by chemical reduction methods were evaluated using TEM to observe the morphology and particle size distribution. These properties play a key role in the signal enhancement process of the chemical sensor because they affect the behavior of the surface plasmons which transfer energy to the adsorbed analyte [6-8]. Figure 3.2 below is a group of images that display nanoparticles of citrate with gold and silver.

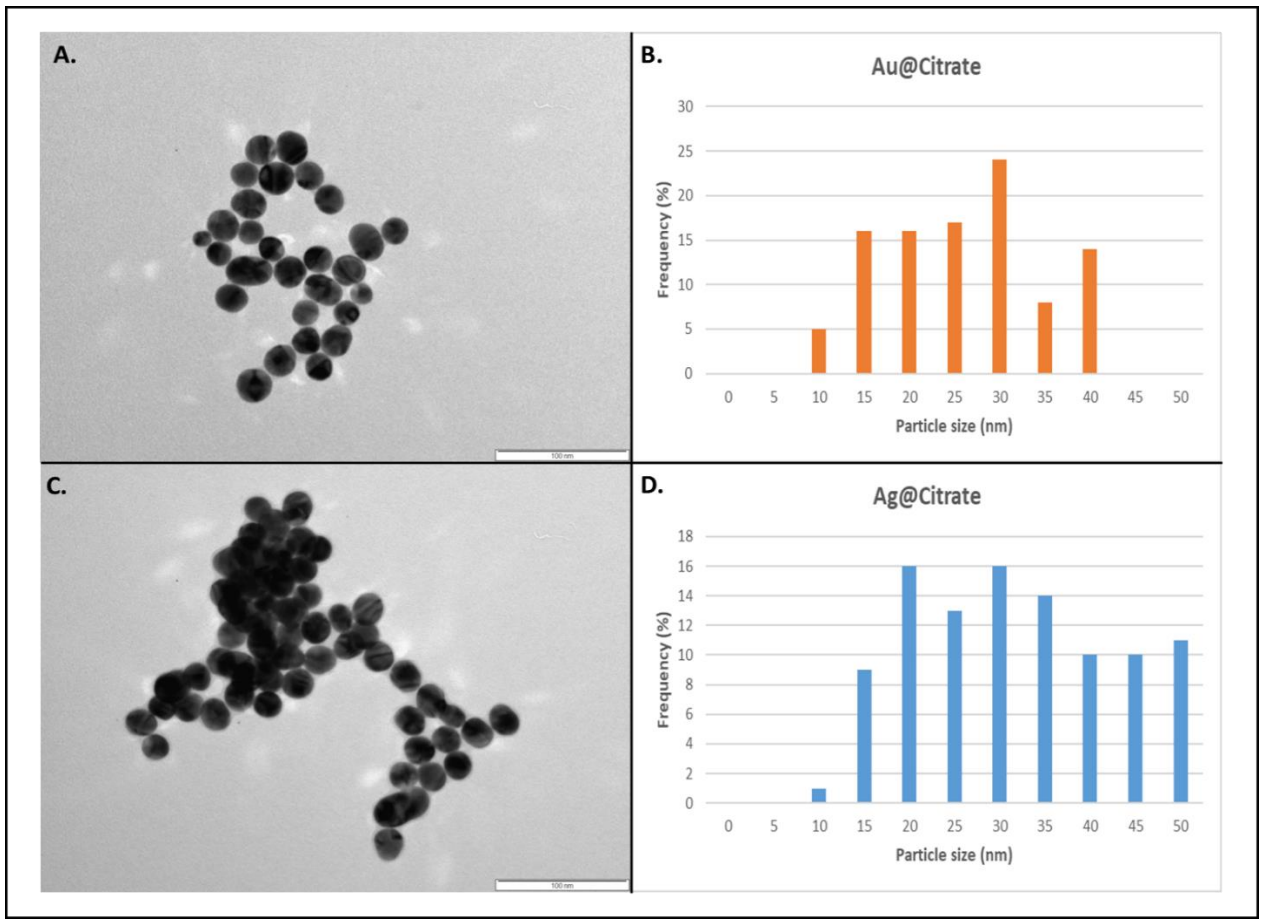

Figure 3.2:TEM images and size distribution of nanoparticles: Au@Cit (A-B), Ag@Cit(B-D)

Figure 3.2 above shows the morphology and particle size distribution of gold and silver nanoparticles stabilized by citrate. In 2A, the Au@Cit shows spherical and oval morphology ranging from 10-40 nm with predominately 30 nm sizes at 25 % frequency. The Ag@Cit data shows a mixture of spherical and oval shapes within a 10-50 nm range, where 20-30 nm sizes contribute the most at 16% frequency. These results also show that the Au@Cit is mostly smaller

in size distribution than Ag@Cit with its largest size at 40 nm with less than 15 % frequency while the latter contained particles of 45-50 nm in size with over 10 % frequency. This was important to note because signal enhancement is also size-dependent [9-11]. Figure 3 below shows the results from experiments conducted on gold and silver nanoparticles stabilized with cysteamine.

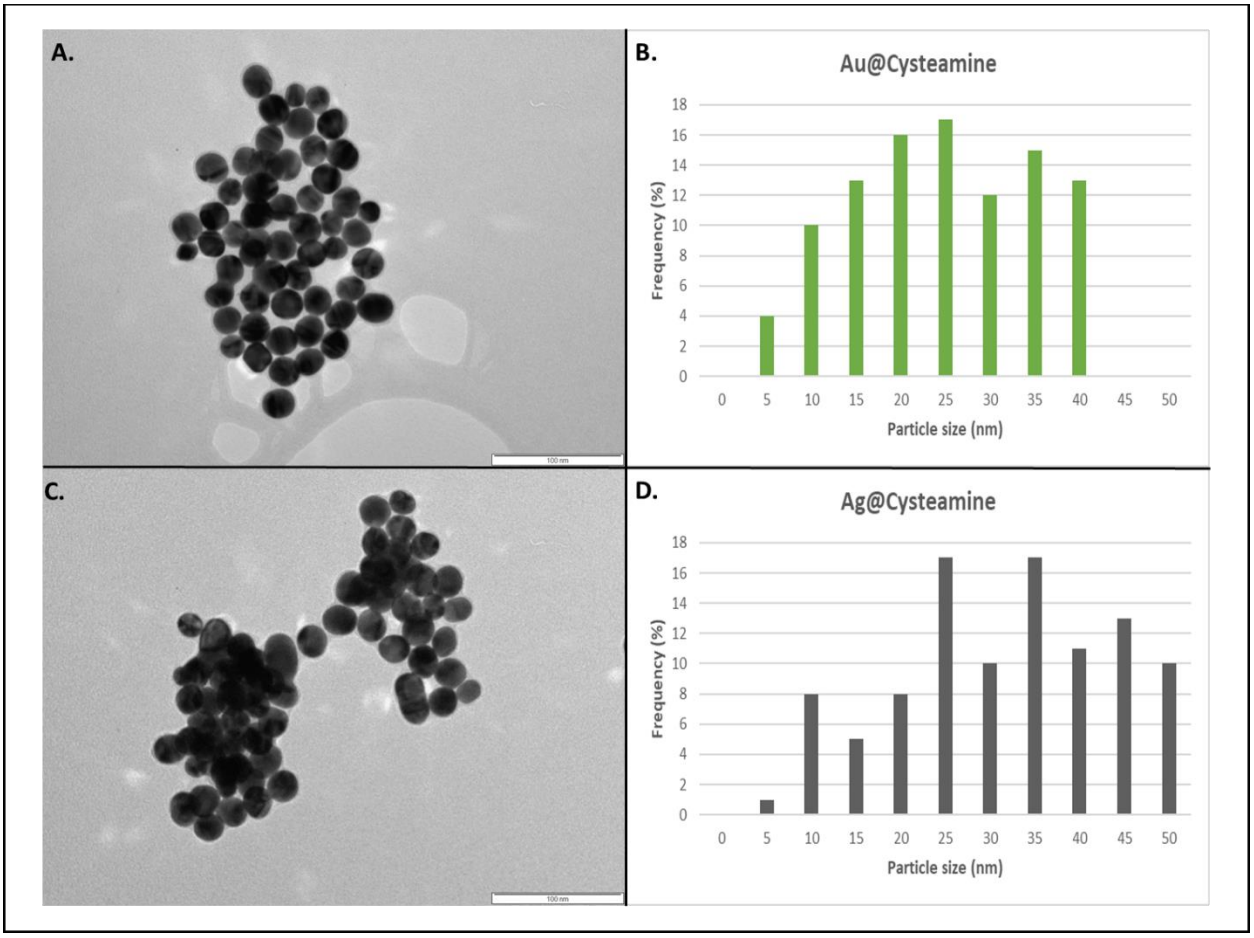

Figure 3.3:TEM images and size distribution of nanoparticles: Au@Cys (A-B), Ag@Cys(B-D).

In figure 3.3 above, nanoparticles of gold and silver are depicted with their size distribution seen as histograms on the right. For Au@Cys, the nanoparticles show a spherical to the oval shape of and a size distribution of 5 to 40 nm dominated by particles of 25 nm at a frequency of 17%. On average, the Au@Cys distribution is smaller than the citrate counterpart with its largest frequency contribution of less than 18 % compared to the 22% of citrate. For the Ag@Cys sample group, the size distribution spans from 5 to 50 nm with the most input seen in the 25-35 nm range at 16%. Again, with silver nanoparticles, the largest size reached was 50 nm with 45 nm providing over 12 % of the frequency. In addition, the gold-based nanoparticles seem to have no contribution from particle sizes of over 40 nm using both crosslinkers, this observation aligns with larger UV-Vis absorption bands found on silver samples compared to gold. The explanation for these results can result from a higher yield of nanoparticles from silver, supported by the broad UV band of the metal, which according to Beer Lambarts law, is dependent on concentration.[12-14]. Due to the disparity in particle size, a consistent evaluation of the nanoparticles in the laser

focal could not be determined at this point. In the next section, Raman microscopy of these nanoparticles post self -assembly is reported.

3.2 Raman microscopy of fabricated chemical sensors

3.2.1 Citrate/Gold and Citrate/Silver.

The gold and silver coated slides from section 2.2 were functionalized with Au@Cit solution to functionalize the surface with hydroxyl (-OH) and carboxylate functional groups ($-COO^-$). This step was necessary to create conditions for intermolecular forces between them and the ARV analytes The results below show the differences between the citrate tribasic nanoparticles on gold, and silver layers. Figure 3.4 below is a microscopic analysis of the gold coated surfaces before and after coating with nanoparticle coating.

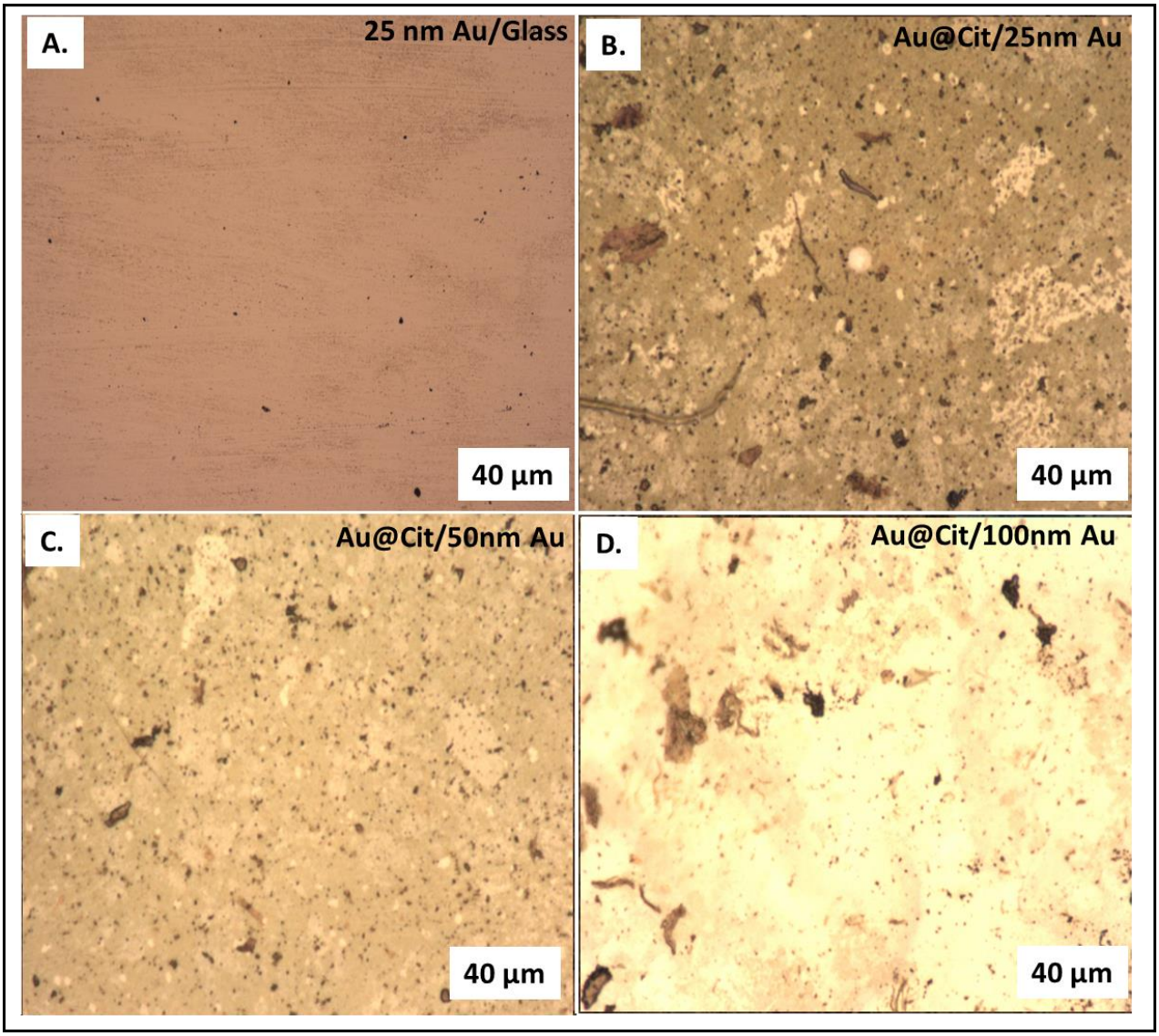

Figure 3.4:10X Microscopic images of gold coated glass (25-100nm) before and after chemical modification with Au@Cit . A) 25 nm (plain), B) 25 nm, C) 50 nm, D) 100 nm.

Figure 3.4 shows the morphology of MNPs on gold coated surfaces of different layers. Figure 3.4A is a 25 nm gold coated before the nanoparticles were coated by the self-assembly method for comparison. When the metal surfaces are coated with Au@Cit solution, a new layer of coating is observed with the presence of debris visible at varying degrees. Furthermore, the reflection from the metal surface increases intensity as the layer thickens from 25 to 100 nm (B-D) using the same microscope settings. These differences from the control were sufficient to conclude that the physical adsorption of the MNPs was successful. Inspection of the molecular properties of the samples was performed using Raman spectroscopy to confirm the presence of MNPs on the surface using the vibration bands of citrate. Figure 5 below is a Raman overlay of spectra that compares the different layers of gold coated with Au@Citrate solution. For each sample, a map of 100 spots was acquired using a 6-mW laser power, 532 nm wavelength, magnified using a 10X objective, with a scanning time of 3 accumulations at 1 second per scan. The image of the sampling map which applies to all Raman experiments as well as the Raman spectrum of citrate powder is provided in the supplementary section as figure S3 and S4 respectively.

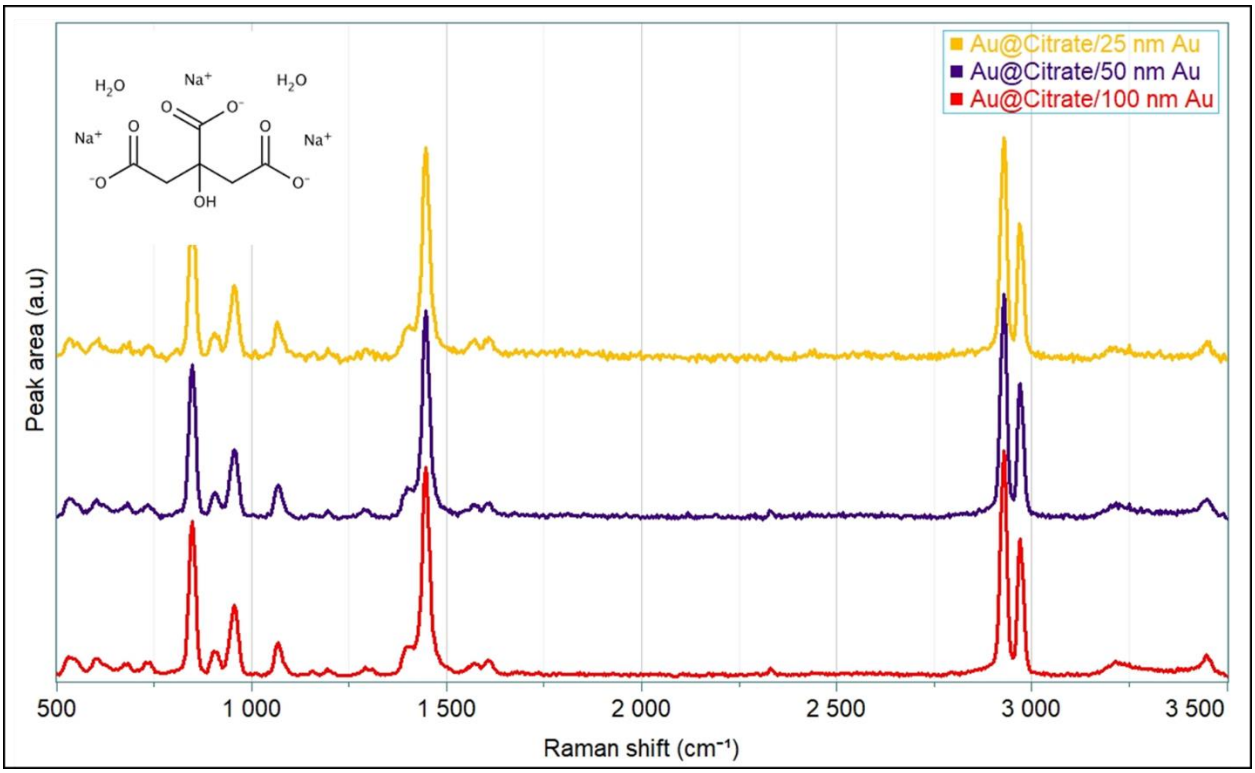

Figure 3.5:Raman spectra of gold thin films coated with Au@Cit. Top-bottom: 25 nm (yellow) 50 nm (purple) and 100 nm (red).

The Raman spectra in figure 3.5 above show the Raman bands obtained from citrate on the gold coated surfaces. From left to right, an in-plane vibration is observed in the region 525-530 cm^{-1} for all three samples. A strong peak arising from the stretching mode of the alpha carbon bonded to the carboxylate ($CCOO^-$) appears at 846 cm^{-1}, which is a blue shift from the reference value of 842 cm^{-1} which indicates molecular interactions between the functional group and the metal

surface. A similar vibration for the $CCOO^-$ bonds are seen between the 900 and 1070 cm^{-1} region. A red shift in this region is present, and it implies there has been an interaction between the metal and the negative carboxylate ion, which decreased the frequency of the mode. Further down the spectra, a sharp peak assigned to the carboxylate ion is observed at 1444 cm^{-1} supported by the presence of carbon hydrogen bonds in the same region [15-17]. A weak peak around the 1600 cm^{-1} region was detected and suspected to arise from a carboxylate ion forming a carbon double bond while in a state of resonance. At the far end of the spectra, alkyl bonds between carbons and hydrogens appear as sharp double peaks in the 2900 cm^{-1} region while a hydroxyl functional group appears as a weak peak at 3200 cm^{-1}. The red shift seen on the hydroxyl peak implies hydrogen bonding with the metal surface via the oxygens of the citrate and the hydrogens of the analyte. The largest shift in this regard was found at50 nm, which implies the most interaction and bond strain [18-19]. Overall, the samples displayed a blue shift character when compared to the powder and table 1 below summarizes the peak signals obtained from comparing the three gold layers [20].

Table 3.1:Raman bands of Au@Cit on gold nanothin layers.

Citrate (Powder)	25 nm Au	50 nm Au	100 nm Au	Reference	Reference	Assignment
531	531	531	531	560	568	ν in-plane (COO)
842	846	846	846	832		ν(C-COO)
899	900	900	900	832		ν(C-COO)
955	956	956	957	944		ν(C-O)
1063	1063	1067	1067	1077		ν(CH)
1429	1444	1444	1444	1388	1420	ν_s (COO)
1580	1606	1610	1606		1640	δ(OH)
2923	2926	2926	2926		2929	ν_s (CH)
3270	3250	3214	3214		3508	ν (OH)
3449	3455	3449	3449		3508	ν(OH)

ν= stretching, ν_s= symmetric stretching, δ=deformation, ν_{as}= asymmetric stretching. [20],[21]

For silver coated samples, microscopic images were acquired and analysis in terms of morphology. Raman data were also collected using the same parameters optimized for the gold samples. Figure 5 below shows the 10X magnification images of the silver samples with citrate compared with the plain silver slide.

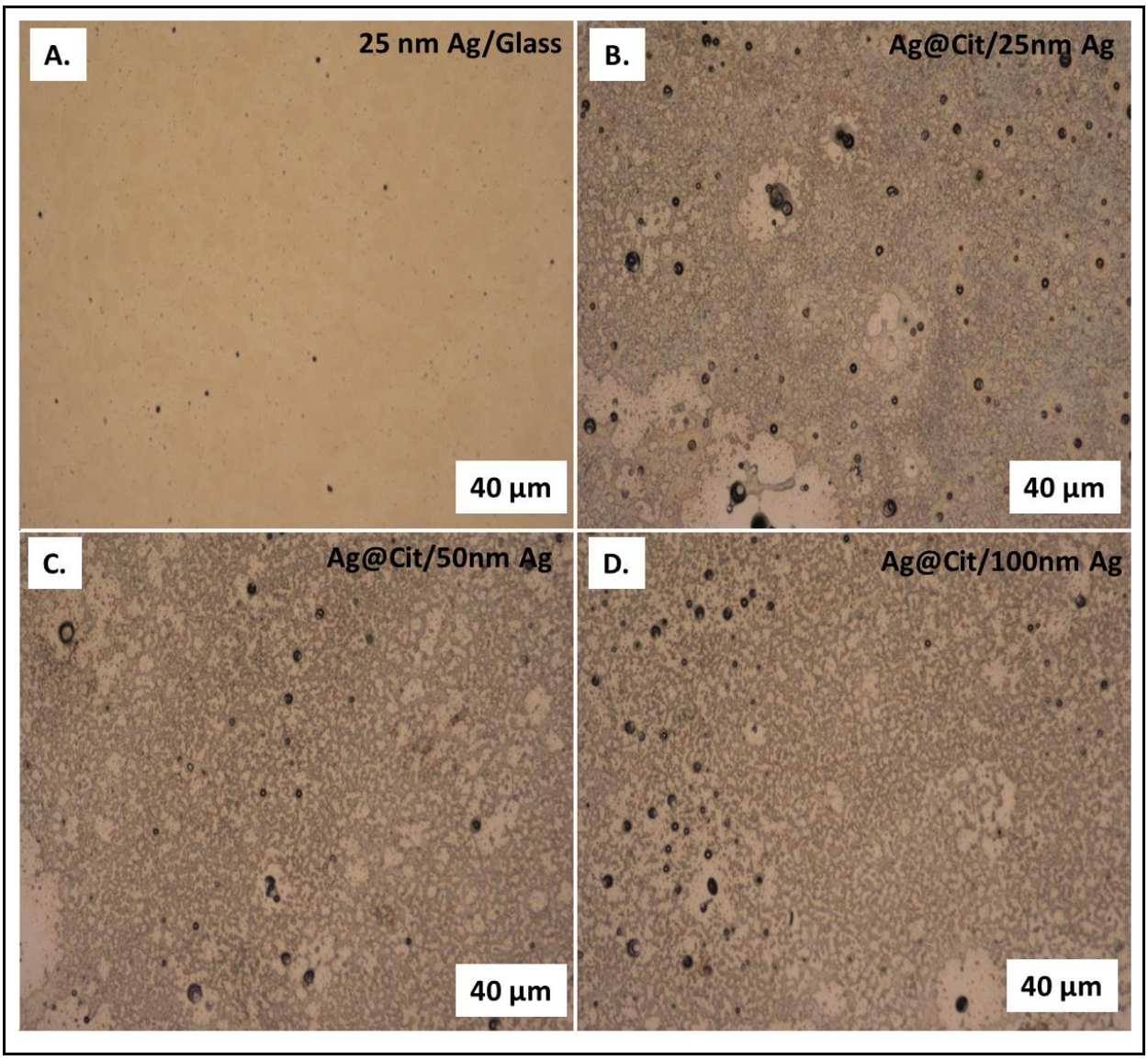

Figure 3.6:Microscopic images of silver coated glass (25-100nm) before and after chemical modification with Ag@Cit. A) 25 nm (plain), B) 25 nm, C) 50 nm, D) 100 nm.

In figure 3.6, the Ag@Citrate coating was compared with the silver coated slide shown in figure 6A. The morphology changes when Ag@Cit is added to the 25,50 and 100 nm silver samples which are labelled as figure 6B-6D respectively. The silver samples showed a similar morphology across the different layers where dark spots are visible on the coated substrates surrounded by rod-like structures with the metal layer seen in the empty spaces. The debri-like imagery on the gold substrates was not observed on the silver probably due to the oxygenation character of silver when exposed to the atmosphere. Raman data was acquired from the silver samples to analyze the surface morphology from a molecular aspect. Figure 7 is a Raman comparison of the citrate on the 25, 50 and 100 nm layers of silver.

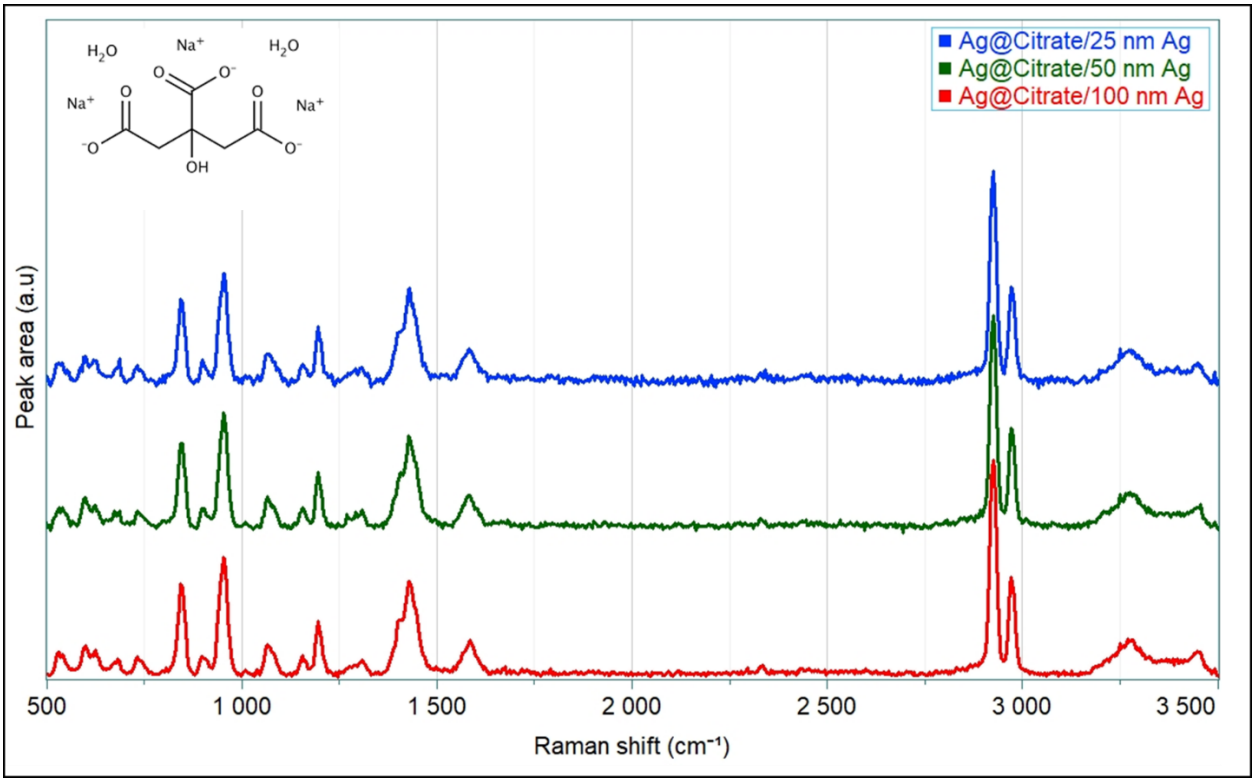

Figure 3.7:Raman spectra of silver thin films coated with Ag@Cit. Top-bottom:25 nm (blue), 50 nm (green) and 100 nm (red).

The spectral overlay above shows the Raman bands of Ag@Citrate obtained from silver nanothin films. The in-plane vibration of the carboxylate was observed at 598 cm^{-1} for all the layers, which is a sign of blue shift or bond shortening because of interaction with the metal. A red shift was noted at the carbonyl bond of the carboxylate at 951 cm^{-1} for the 50 and 100 nm layers while the 25 nm sample was 955 cm^{-1} [21]. This redshift is a consequence of the layer increase, which allows more interaction between the crosslinker and the metal [22]. A similar red shift observation was made at 1400 cm^{-1} region where the strong stretching of the carboxylate exists. The hydroxyl groups in the citrate molecule showed a mixture of red and blue shifts when compared to the powder reference. Firstly, the 1580 cm^{-1} band caused by the deformation of the functional group blue-shifted on the 100 nm layer, implying bond shortening because of the intermolecular interaction with the metal [23]. Similarly, the stretch mode of the hydroxyl remained blue-shifted on the 50 nm in the 3200 cm^{-1} regions while the 20 and 100 nm cm^{-1} layers redshifted; the mixed response is unclear in terms of molecular interactions. Table 3.2 below summarizes the peak profiles obtained for Ag@Cit on silver monolayers.

Table 3.2:Raman bands of Ag@Cit on gold nanothin layers.

Citrate (Powder)	25 nm Ag	50 nm Ag	100 nm Ag	Reference	Reference	Assignment
531	598	598	598	560	568	ν in-plane (COO)
842	840	840	840	832		ν(C-COO)
955	951	951	951	944		ν(C-O)
1063	1063	1063	1063	1077		ν(CH)
1429	1425	1425	1425	1388	1420	ν_s (COO)
1580	1580	1580	1584		1640	δ(OH)
2974	2923	2923	2923		2982	ν_s (CH)
3270	3250	3264	3268		3508	ν (OH)
3449	3449	3455	3446		3508	ν(OH)

ν= stretching, ν_s= symmetric stretching, δ=deformation, ν_{as}= asymmetric stretching, [20],[21]

In order to determine the optimum layer thickness to be used for future experiments, selected Raman band regions 800-900 cm^{-1} and 1400-1450 cm^{-1} and their peak areas were compared against layer type and thickness. Figure 8 is a histogram of the three groups expressed as peak areas.

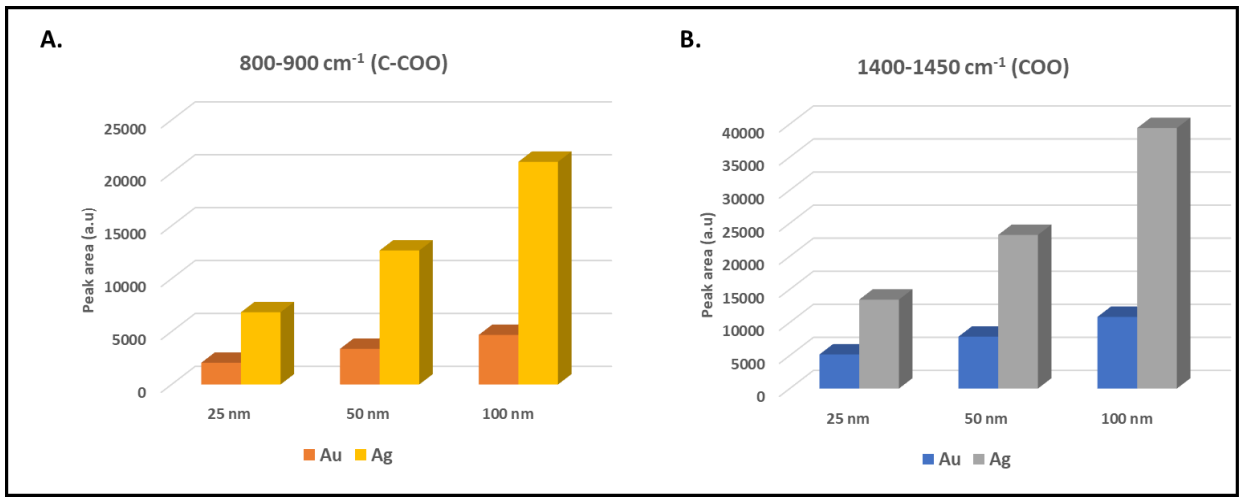

Figure 3.8:Histogram of Raman peak areas for citrate on gold and silver. A) C-COO (800-900 cm-1) B) COO (1400-1450 cm-1).

The histograms in figure 3.8 above depict the signal response from citrate functional groups from self-assembled nanoparticles on the coated substrates. In figure 3.8A, the alpha carbon bond found at 800-900 cm^{-1} is analyzed where the Ag@Cit was seen to dominate the peak area response across layer thickness 25-100 nm compared against gold. As a group, the peak area also increases with layer thickness, which implies some contribution from the metallic layers coated on the glass using PVD to improve the signal. The same trend was observed on the COO bond of the carboxylate found in the 1400 cm^{-1}- 1450 cm^{-1} region where the silver values far exceed the gold, which can be further be explained by the nanoparticle distribution and the metal yield, where signal enhancement is more probable on the larger nanoparticles by comparison. Furthermore, the narrow bands and blue shifting seen on gold compared to the broad band, and red shift character seen on silver, indicates some influence by the metal substrates on the crosslinker. From a molecular aspect, the carboxylate ion is one of the ways the citrate crosslinker

can stabilize the nanoparticles by engaging in chemical bonding with the metal, where signal improvement arises where there is the greatest number of nanoparticles. Because of these reasons, silver peak areas are more pronounced than gold on citrate. The 50 nm layer thickness was chosen as the optimum MNP/crosslinker combination because with both functional groups, it showed an intense signal compared to the 25 nm, layers while a layer thickness of less than 100 nm is desired if a good signal is still achieved. In the next section, a comparison of gold and silver with cysteamine is conducted using Raman microscopy.

3.2.2 Cysteamine/Gold and Cysteamine/Silver.

The gold and silver coated slides from section 2.2 were functionalized with Au@Cys to observe the interaction of the amine and thiol functional groups with the gold metal. Microscopic images were taken at 10x magnification for comparison before and after functionalizing with cysteamine crosslinked nanoparticles. Figure 3.9 below shows images from gold coated substrates.

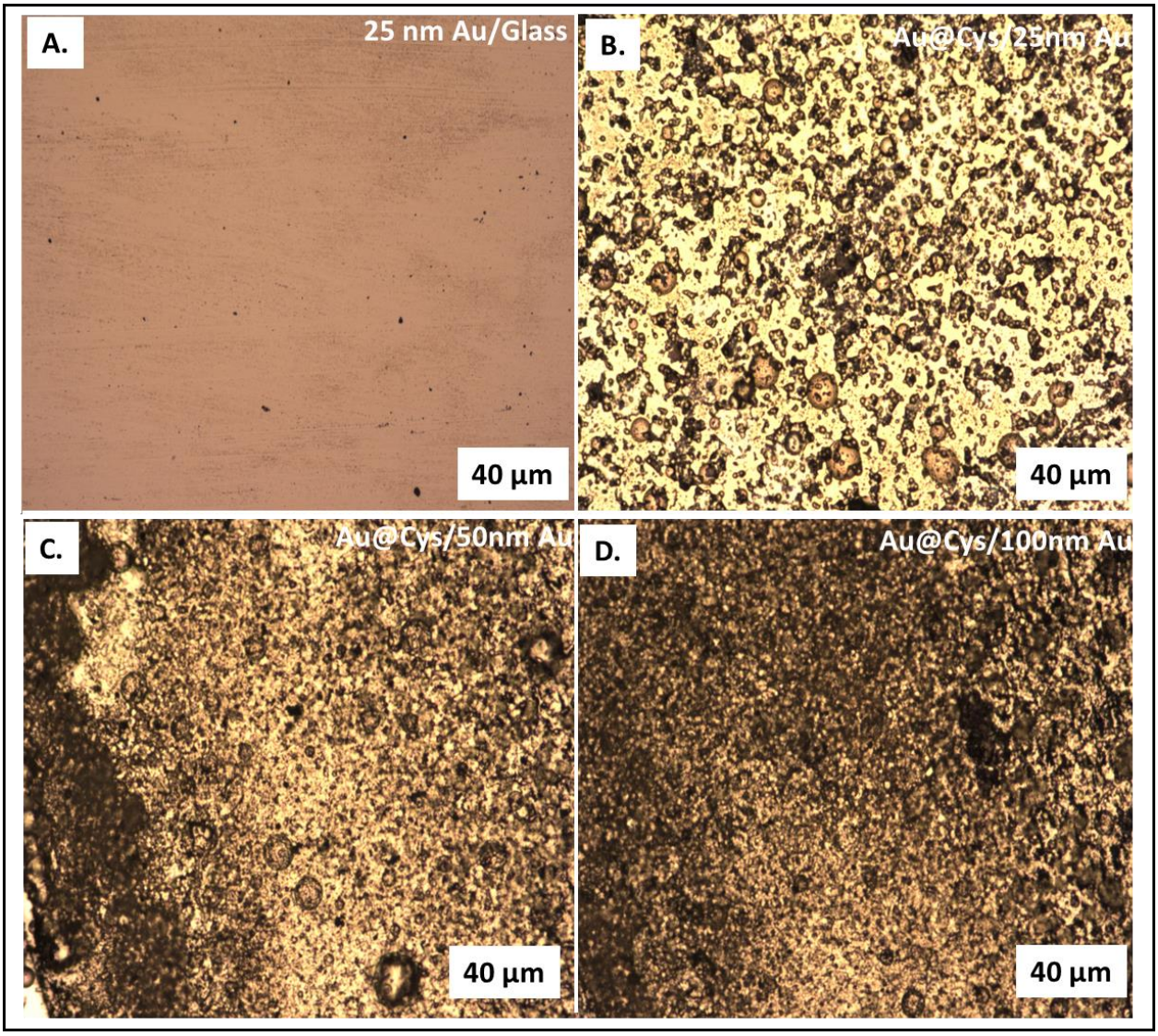

Figure 3.9:Microscopic images of gold coated glass (25-100 nm) before and after chemical modification with Au@Cys. A) 25 nm (plain), B) 25 nm, C) 50 nm, D) 100 nm.

Figure 9A is a 25nm gold slide which serves as a reference of the morphology before functionalization. Figure 9B depicts a 25 nm gold surface coated with cysteamine and imaged at 10x. Similarly, figures 9C and 9D show 50 nm and 100 nm gold layers after modification with cysteamine. The images of the 25 nm sample show a layer of coating with spherical components and debris reflected by the gold surface. The spherical particles are reduced substantially at 50 and 100 nm with the thicker layers displaying a darker appearance compared to the 25 nm. A Raman map of each ROI was taken with the parameters outlined for the citrate experiment (section 3.3.1). The averaged spectra of the three samples were evaluated in terms of spectral content and molecular bond shifts. Figure 3.10 below is a Raman overlay of the three gold layers depicted above, post functionalization with Au@Cys.

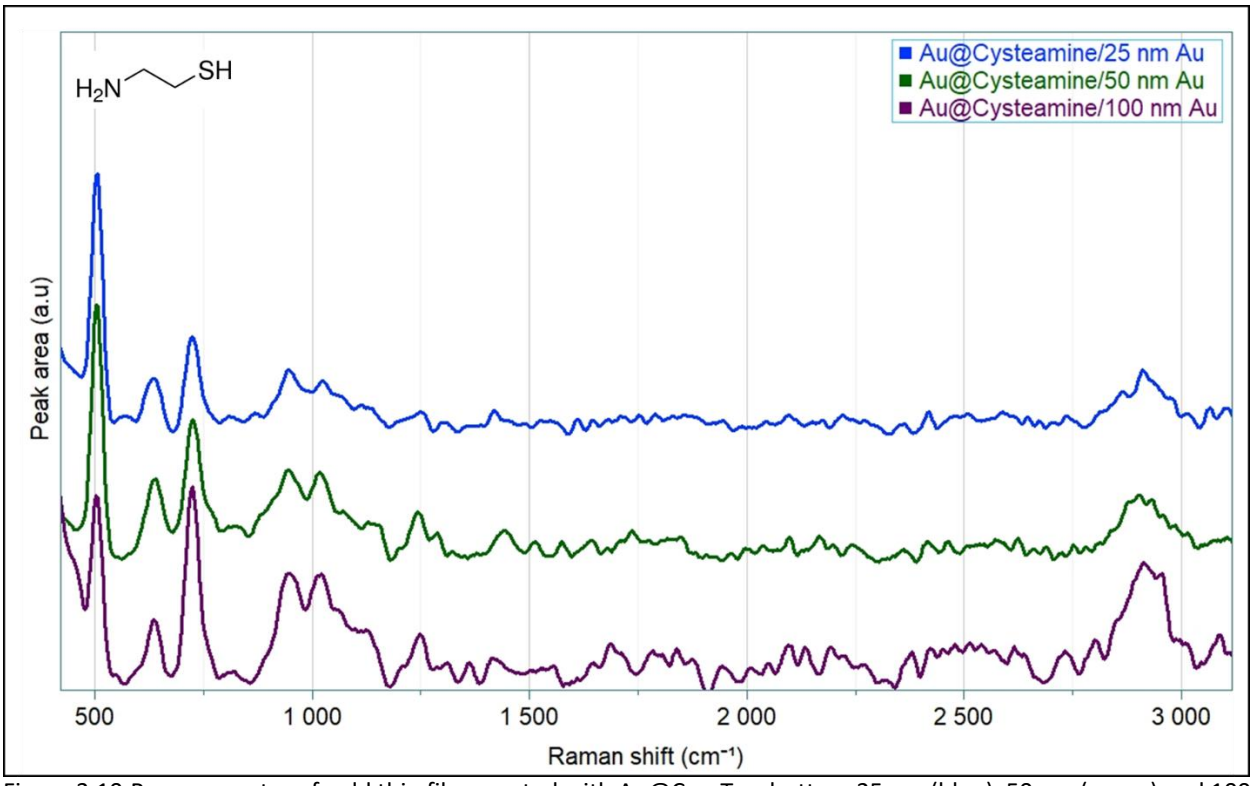

Figure 3.10:Raman spectra of gold thin films coated with Au@Cys. Top-bottom 25 nm (blue), 50 nm (green) and 100 nm (purple). Molecular structure of Cysteamine (insert).

The figure above shows the band profile for cysteamine stabilized gold nanoparticles absorbed on gold coated slides of 25, 50 and 100 nm thickness. A spectrum of cyteamine powder which was used to compare the peaks is provided in the supplementary section (S5). From this data, a strong peak of the disulphide bond in stretching mode was observed at 501 cm^{-1} on 25 nm and 50 nm like the powder while the 100 nm showed a blue shift at 504 cm^{-1}. A carbon-sulphur bond was detected twice in stretching mode vibrations in the 600 cm^{-1} to 760 cm^{-1} regions with a 3 cm^{-1} red shift seen for 100 nm. Amine bands contributed in the middle of the spectra region between

900 and 1000 cm^{-1} where the 25 nm layer produced a blue shift while the thicker layers moved in the red direction of the spectrum. Carbon bonds of the aliphatic chain were detected in stretching mode vibration at 1200 cm^{-1} followed by a thiol bond stretching mode red shifting with an increase in layer thickness. At the end of the spectra, the aliphatic and amine bonds are observed in the 3000 cm^{-1} regions [24]. Table 3 below is a summary of the peaks observed from the Au@Cysteamine study.

Table 3.3:Raman bands of Au@Cys on gold nanothin layers.

Cysteamine (Powder)	25 nm Au	50 nm Au	100 nm Au	Reference	Assignment
501	501	501	504	510	v(S-S)
635	632	632	632	666	v(C-S)
722	720	720	720	753	v(C-S)
943	940	938	938	936	v(C-N)
1019	-	1017	1011	1012	v(C-C(-N)
1248	1244	1250	1250	1252	v(C-C)
2584	-	-	-	2577	v(S-H)
3017	-	3079	3092	2931	v(CH)
3319	-	3337	3340	3350	v(NH)

v= stretching, vs= symmetric stretching, δ=deformation, vas= asymmetric stretching. [24]

The procedure used to obtain the data from gold was used to evaluate silver coated samples functionalized with the Ag@Cys. In figure 10 below, a microscope analysis of plain silver thin films before and after chemical functionalization is provided.

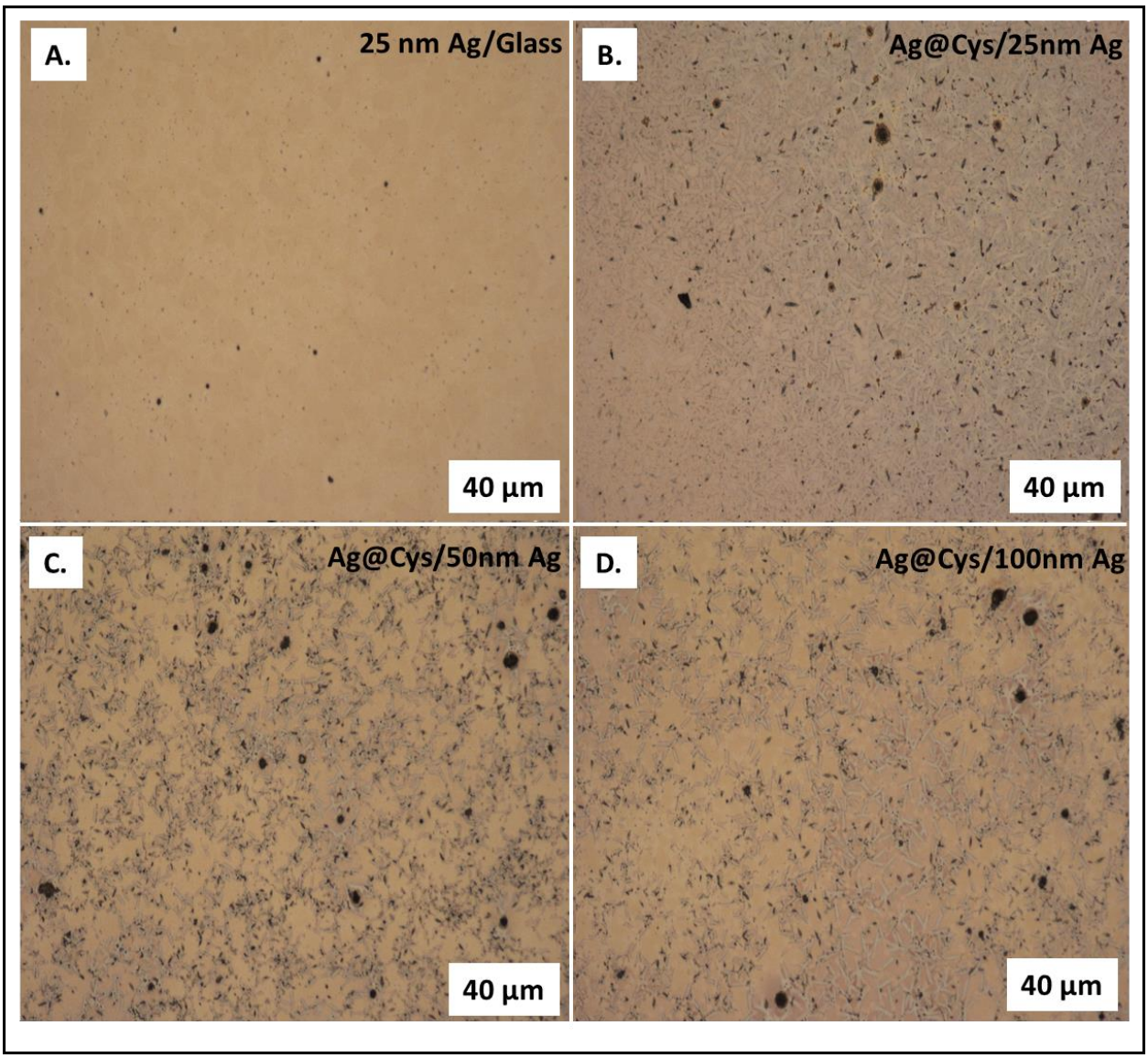

Figure 3.11:Microscopic images of silver coated glass (25-100nm) before and after chemical modification with Ag@Cys. A) 25 nm (plain), B) 25 nm, C) 50 nm, D) 100 nm.

Figure 3.11A is a 25nm silver slide which serves as a reference of the morphology before functionalization. 3.11B is the 25 nm silver layer coated with Ag@Cysteamine, while 3.11C and 3.11D show the MNPs adsorbed to 50 and 100 nm silver coatings. The images show a rodlike crystal structure with dark spots appearing at random locations. Unlike the gold experiment, rai the coatings appear greyish in color with large spacings between crystals and debris. A Raman analysis was performed on the samples to determine the molecular characteristics of their surfaces. Figure 3.12 below is a Raman overlay of the Ag@Cysteamine on silver thin layers.

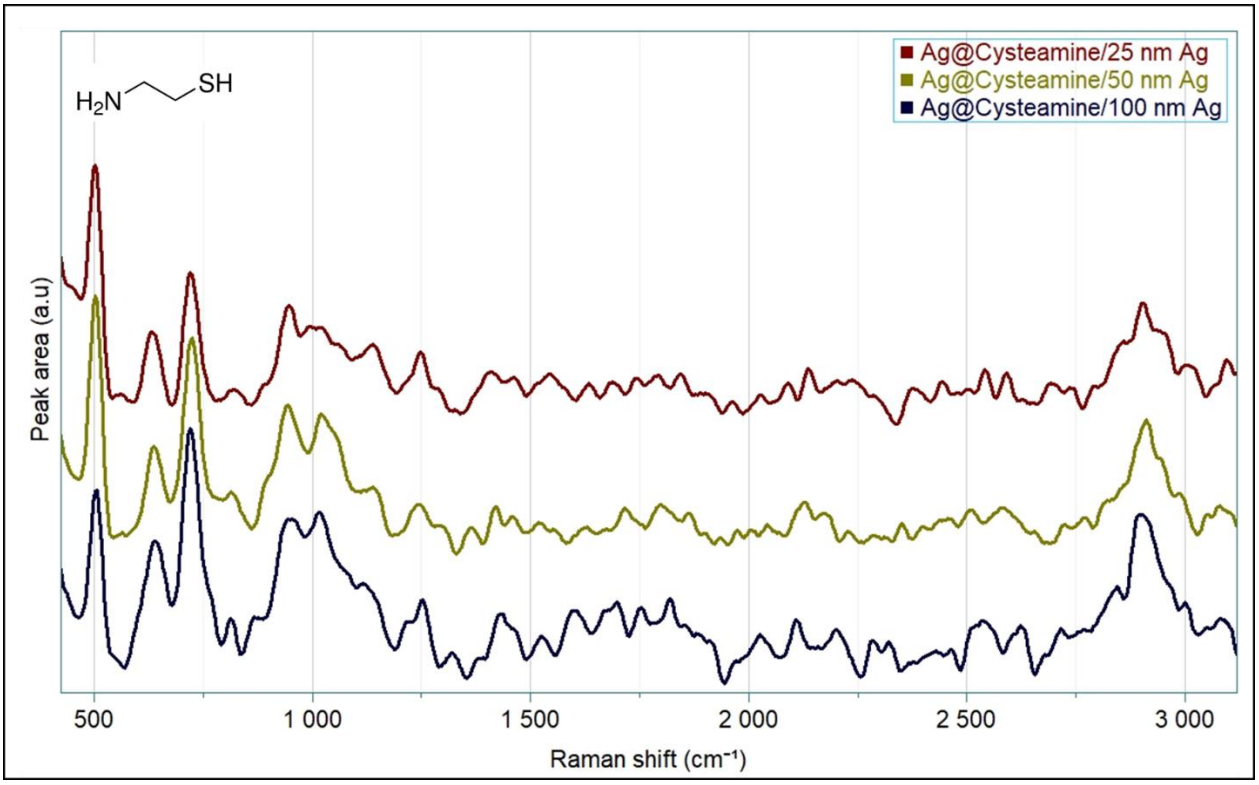

Figure 3.12:Raman spectra of gold thin films coated with Ag@Cys. Top-bottom: 25 nm (red), 50 nm (yellow) and 100 nm (blue). Molecular structure of Cysteamine (insert).

The results from figure 3.12 above show a similar Raman fingerprint for cysteamine across the three layers, however, differences in spectral quality and peak shifts were observed. For the 25 nm sample, the disulphide bond arises in the same value as the powder sample at 504 cm^{-1} while the 50 and 100 nm layers gave values of 504 and 506 cm^{-1} all red-shifted from the powder sample. The carbon-sulphur bonds reappeared in stretching mode at 635 cm^{-1} except for the 50 nm sample appearing blue-shifted at 639 cm^{-1} while its second vibration indication a red shift of 2 cm^{-1} on the 25 nm layer only. The primary amine bonds were detected in the 943 cm^{-1} for the powder and the 25 nm sample while a blue shift resulted for the 50 and 100 nm in stretching mode. Towards the end of the spectra, aliphatic bonds in stretching mode in a mixture of Raman peak shifts while the thiol appeared red-shifted for the 50 and 100 nm in the 2500 cm^{-1}. A decrease in wavenumber was also detected from 100 nm to 50 nm for the amine group in the 3000 cm^{-1} regions [24].

Table 3.4: Raman bands of Ag@Cys on silver nanothin layers.

Cysteamine (Powder)	25 nm Ag	50 nm Ag	100 nm Ag	Reference	Assignment
501	504	504	506	510	v(S-S)
635	630	630	630	666	v(C-S)
722	718	718	718	753	v(C-S)
943	932	933	933	936	v(C-N)
1019	1019	1015	1019	1012	v(C-C(-N)
1248	1244	1240	1240	1252	v(C-C)
2584	-	-	-	2577	v(S-H)
3017	2901	2901	3088	2931	v(CH)
3319	-	3331	3295	3350	v(NH)

v= stretching, vs= symmetric stretching, δ=deformation, v_{as}= asymmetric stretching. [24].

In order to determine the optimum layer thickness to be used for future experiments, selected Raman bands of interesting bond shift and chemical functionality were chosen, and their peak areas were compared against layer type and thickness. A histogram analysis was conducted to compare the peak areas of the C-S and C-N peaks to elucidate the most prominent molecular arrangement of the cysteamine to the metal surfaces and select the most optimized metal/crosslinker combination for the adsorption of analytes. The image below shows the peak areas with respect to metal type and layer thickness.

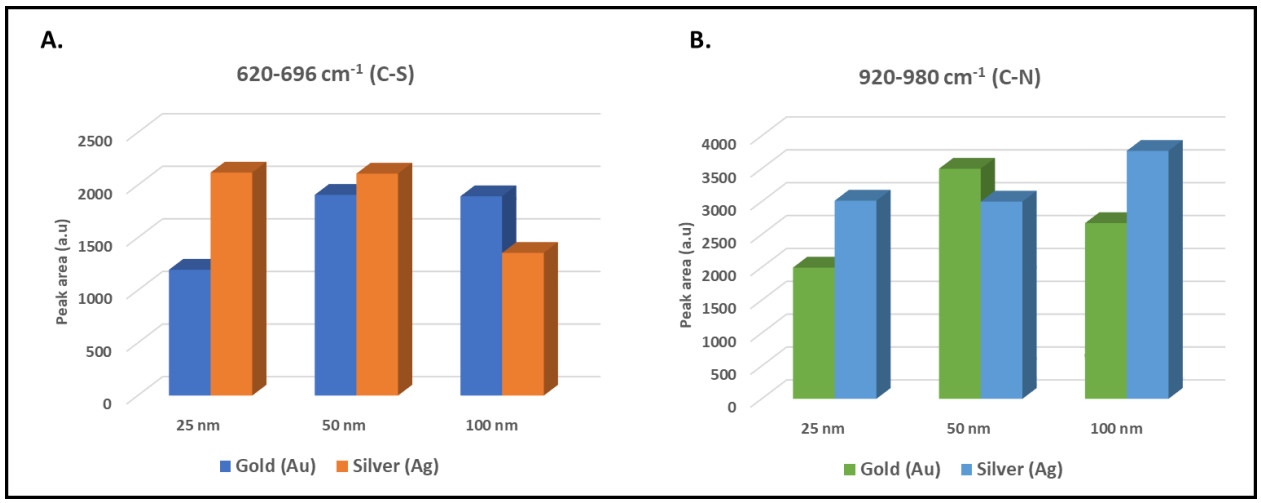

Figure 3.13:Histogram of Raman peak areas for cysteamine. A) C-S (620-696 cm-1) B) C-N (920-980 cm-1).

From figure 3.13 above, the C-S bond in 13A shows the peak area increases with thickness for gold, with a major change seen between 25 and 50 nm while the latter is in the range of 100 nm. Conversely, the silver layers show an increase in peak area for the thinner layers with the 100 nm resulting in the lowest value. The reason could be a combination of the layer thickness and the

particle sizes whereas seen in section 3.1.2, silver contains larger nanoparticles sizes which could affect the stereochemistry of the cysteamine molecule. The 50 nm layers for both metals are comparable in value while the 25 and 100 nm layers varied substantially. In the case of XB, the C-N bond peak areas for gold show a varied response with an increase in layer thickness, with the 50nm layer producing the largest peak area value. For silver, the randomness is less pronounced because 25 and 50 nm layers have the same peak area value range, with 100 nm giving the highest value. Between the metals, the 50 nm again shows a comparable range while the other layers have a pronounced difference. When comparing both figures, the trend seems to be reversed because, in figure 13A, the sensor shows more response from silver at 50 nm, which implies a preference for the functional group more on silver than gold at that layer. For figure 13B, the opposite occurs at 50 nm where the C-N bond is more intense on the gold platform compared to silver. In addition, at 100 nm the C-S bond is dominant on gold and substantially lower for silver whereas with the C-N bond, the silver is much higher. This difference shows a preference for amine bonds at this layer thickness. From the correlations made above, the 50 nm layer shows the most consistency in peak area between the two metals while showing unique molecular responses towards the selected functional groups. For these reasons, the 50 nm layer was chosen for future experiments involving ARV analytes. In the next section, SERS experiments are conducted on ARV medication in API form using chemical sensors.

3.3 SERS analysis of APIs on citrate-based chemical sensors

Samples of active pharmaceutical ingredients (API) of ARVs prepared in section 2.5 were tested using MNP based chemical sensors; gold citrate (Au@Cit/Au) and silver citrate (Ag@Cit/Ag). The APIs used in this study consist of Tenofovir (TDF), Lamivudine (LAM) and Dolutegravir (DLG). The aim was to determine changes in molecular behavior in the form of peak shifting because of chemical interactions with the sensor. The spectra were compared against values obtained from powder samples which were used to prepare the solutions, the spectrum for which is supplied in the supplementary section. The data from the spectra were further processed to determine the calibration sensitivity, analytical sensitivity, and limit of detection of Au@Citrate and Ag@Citrate chemical sensors.

3.3.1 Tenofovir on citrate based chemical sensors.

TDF experiments were carried out on the glass and the two citrate sensors to compare changes in peak characteristics. Raman spectra of five concentrations of TDF ranging from 0.001- 10 mg/ml were dried on glass, Au@Cit/Au and Ag@Cit/Ag. Figure 14 below is a spectral overlay of TDF on the glass substrate. The spectrum for TDF powder is given in the supplementary section as figure S6.

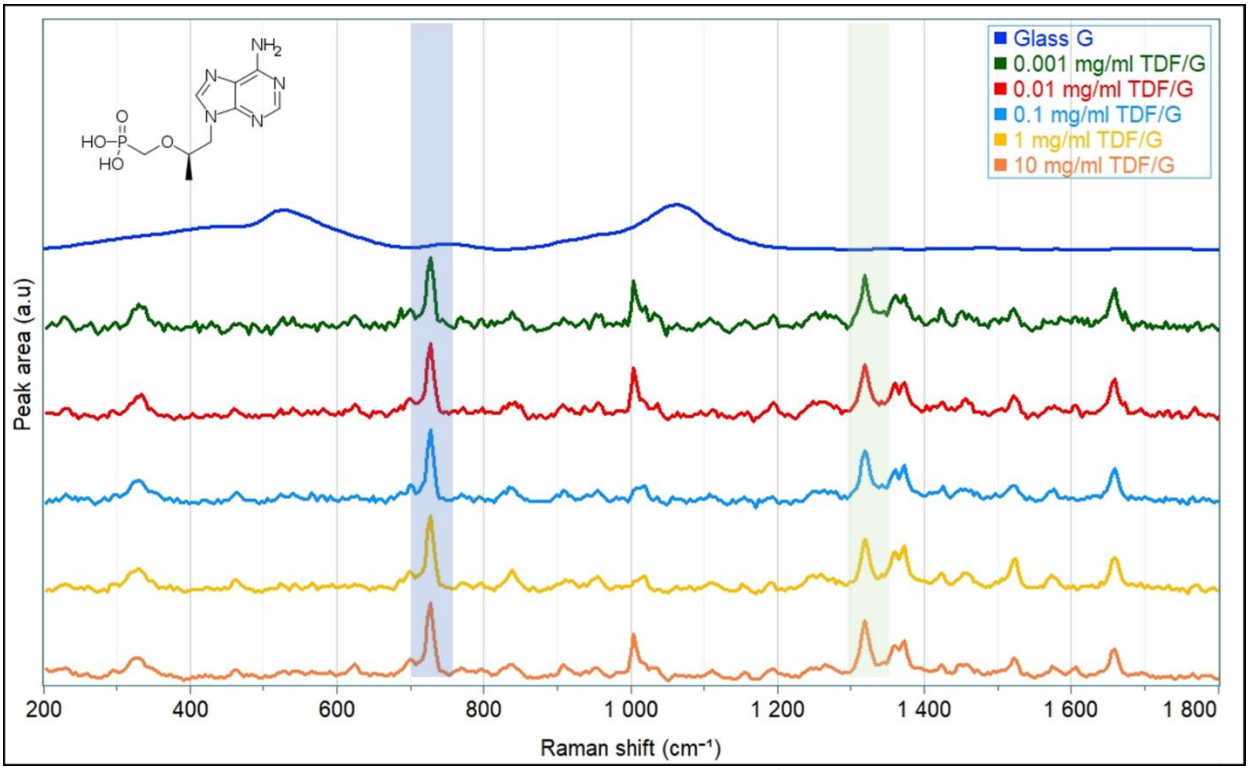

Figure 3.14:Raman spectral overlay of Tenofovir on glass, 0.001-10 mg/ml. Acquired from 200-1800 cm-1. 532 nm, 12 mW laser power, 100 scans, 10 seconds per scan. Insert: TDF molecular structure.

Figure 3.14 above shows the characteristic vibrations of plain glass and TDF samples, where the former shows broad peaks of silicon oxide between 500 cm^{-1} and 1200 cm^{-1}. Background subtraction was performed on the TDF samples to remove the effects of the glass peaks, which led to a large decrease in signal strength. Beginning with the in-phase ring breathing of the adenine functional group at 727 cm^{-1}, followed by the phosphate band at 1004 cm^{-1}. Individual stretching vibration modes of the ring are also seen at 1318 cm^{-1} with the deformation mode of alkyl groups seen at 1372 cm^{-1}. An imidazole ring in deformation mode was detected at 1520 cm^{-1} alongside the stretching mode of the aromatic group at 1658 cm^{-1} [25-26]. When considering peak shifting, the 727 cm^{-1} adenine breathing mode showed a 4 cm^{-1} blue shift from the powder sample; this indicates a decrease in bond length during ring expansion through the π electrons. This feature was also observed for the individual bonds of the ring, C=N, C-N and CH_2 seen at 1311 cm^{-1} region, where a 15 cm^{-1} blue shift from the powder. These changes were noted as significant, and thus peaks 727 cm^{-1} and 1318 cm^{-1} were chosen for statistical analysis.

Figure 3.15 below is a spectral overlay of TDF on the gold-based sensor platform Au@Cit/Au. The same samples used on the glass were analyzed on the sensor to observe changes that arise due to molecular interactions.

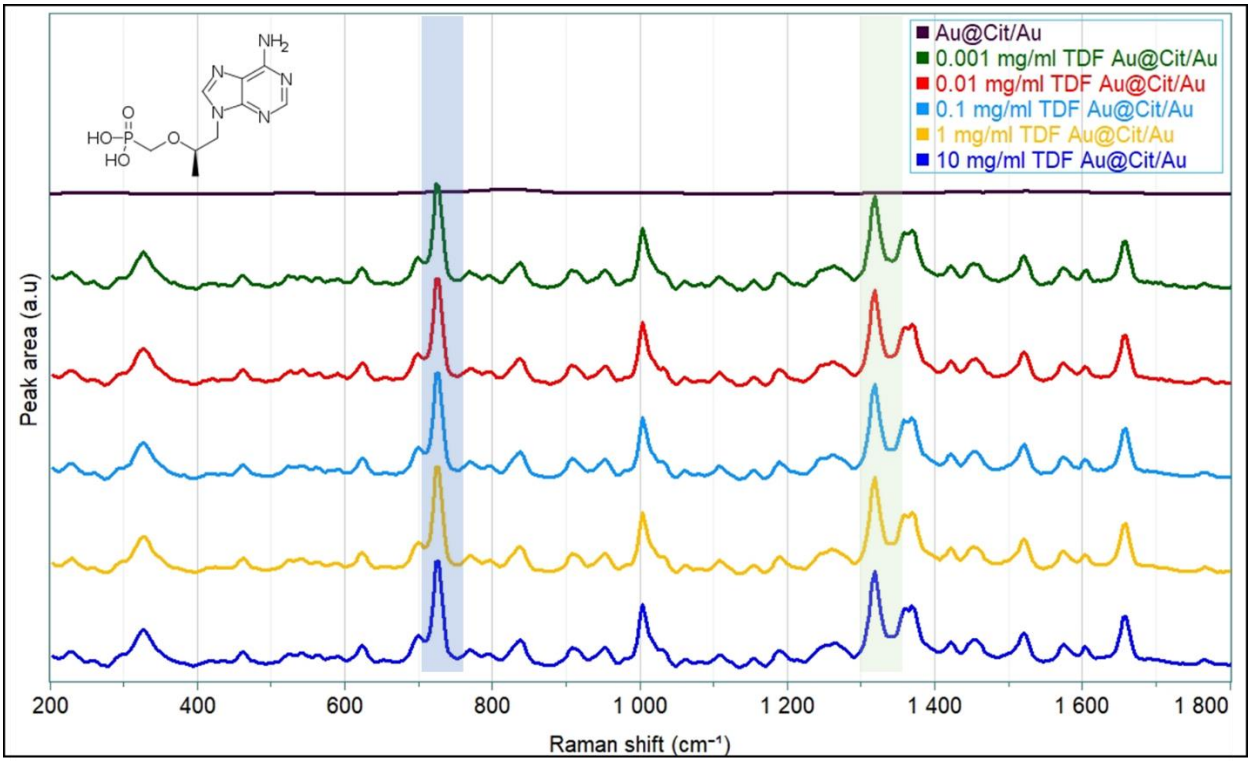

Figure 3.15:Raman spectral overlay of Tenofovir on Au@Cit/Au, 0.001-10 mg/ml. Acquired from 200-1800 cm-1. 532 nm, 12 mW laser power, 100 scans, 10 seconds per scan. Insert: TDF molecular structure.

The Raman overlay shows the spectrum of the chemical sensor Au@Cit/Au after background subtraction using the data from section 3.2.1, which resulted in a flat line that implies no interference from the crosslinker molecules. As a result, Raman peaks of TDF were clearly visible with higher spectral quality than the glass platform. From left to right, the vibration band of alkyl groups are detected in 300 cm^{-1} regions, followed by bending modes from the skeletal structure of TDF at 614 cm^{-1}. The adenine ring breathing mode reappeared in 727 cm^{-1} like the glass samples and a skeletal breathing mode was detected at 838 cm^{-1}, which is an 8 cm^{-1} blue shift from the powder value. Stretching modes of the phosphate group appeared more sharply on the gold sensor compared to the glass at 1004 cm^{-1} succeeded by the stretching bands of the molecular bonds of the adenine group at 1264 cm^{-1}. These functional groups also appeared at 1318 cm^{-1}, which is a red shift of 8 cm^{-1} from the powder sample. Other red shifts were detected at 1368 cm^{-1},1452 cm^{-1} and 1573 cm^{-1} for the alkyl groups and the amine group respectively [25-26]. The peaks of interest selected during the experiments on glass substrates were also chosen for the gold sensor group for comparison purposes.

In the next figure, an overlay of Raman data obtained from silver-based sensor Ag@Cit/Ag is depicted. A comparison with the spectrum of the powder sample was made to observe changes in vibrational modes.

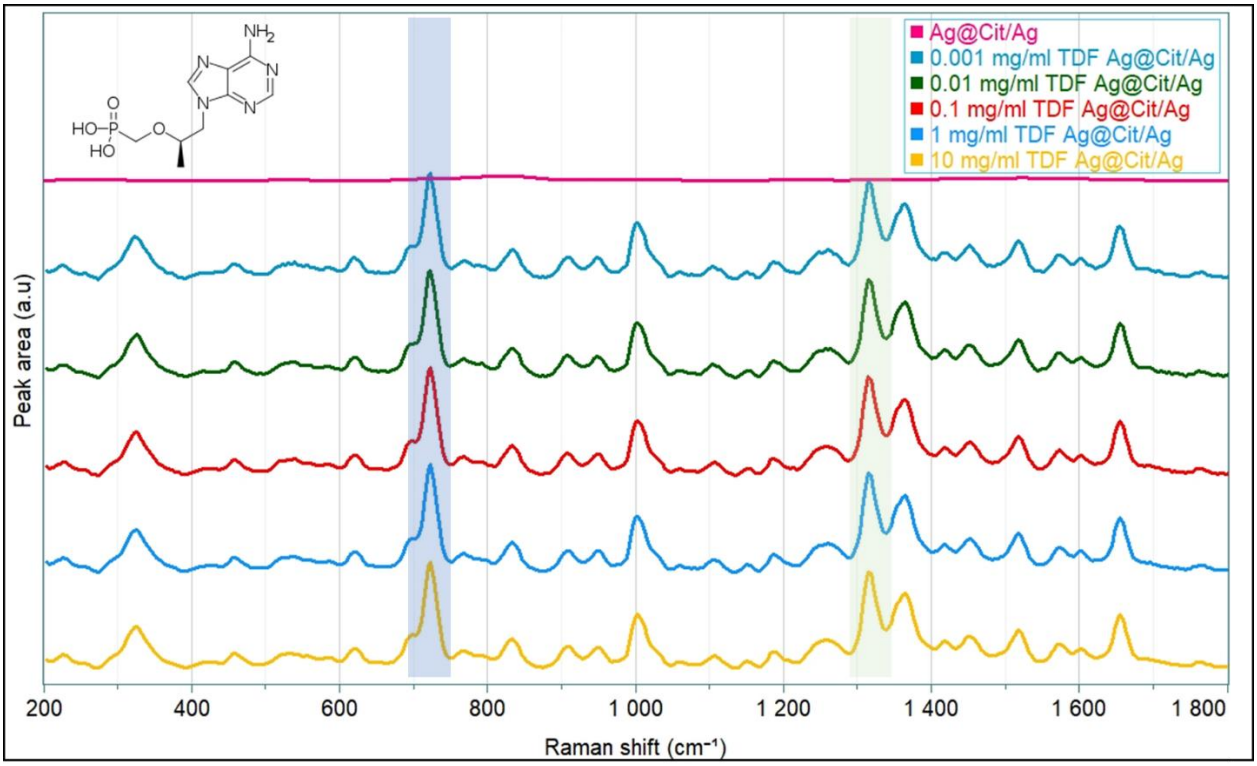

Figure 3.16:Raman spectral overlay of Tenofovir on Ag@Cit/Ag, 0.001-10 mg/ml. Acquired from 200-1800 cm-1. 532 nm, 12 mW laser power, 100 scans, 10 seconds per scan. Insert: TDF molecular structure

Raman data from the silver chemical sensor shows a similar spectral profile to the powder as well as the glass and gold samples. The adenine ring breathing that appears at 723 cm^{-1} on the powder, was detected at 726 cm^{-1} for the silver sensor, like the skeletal bending mode at 834 cm^{-1}, which is a 4 cm^{-1} blue shift from the powder sample. Further down the spectral range, carbon and nitrogen double bonds of the adenine ring appear at 1314 cm^{-1} which is a 12 cm^{-1} red shift from the powder band. A similar behavior was detected at 1452 cm^{-1} and 1573 cm^{-1} for the methyl and amine groups, each showing a red shift of 45 cm^{-1} and 3 cm^{-1} respectively. The changes in molecular bond response seen on 727 cm^{-1} and 1314 cm^{-1} were chosen for statistical evaluation of the sensing platform. Table 3.5 below is a summary of the Raman peaks observed with the vibrational bands of interest highlighted.

Table 3.5:Raman bands of Tenofovir on glass, gold and silver sensors.

Glass	Au@Cit/Au	Ag@Cit/Ag	Reference	Assignment
727	725	724	722	Adenine ring
830	838	834	830	Skeletal breathing
1004	1007	1007	1027	Phosphate
1260	1264	1262	1249	ν(C=N), ν(C-NH_2), ν(C-N)
1318	1316	1314	1321	ν(C=N), ν(C-N)
1372	1368	1367	1379	$\delta(CH_2)$
1462	1452	1452	1497	$\delta(CH_3)$
1520	1520	1518	1517	δ(CNH)
	1573	1573	1576	$\alpha(NH_2)$
1658	1657	1657	1658	C=O(aromatic)

ν=stretching, δ=rocking, ρ=bending (in plane), ω= bending (out of plane), τ= twisting, α= wagging, [26]

In the next section, a statistical evaluation of the peaks highlighted in the table was conducted. Peak area and standard error values were used to determine numerical data for parameters that are used to evaluate chemical sensors as explained in section 2.6.

3.3.2 Statistical analysis of Tenofovir on glass, gold, and silver chemical sensors.

Raman spectroscopy experiments conducted in section 2.5 were used to determine statistical differences between the three scaffolds in response to TDF. The calculations begin with enhancement efficiency (EF) linear regression, where the R^2 and slope or calibration sensitivity were determined.

Figure 17 below shows three plots of peak area versus sample concentration of the 723 cm^{-1} Adenine ring of the TDF analyte.

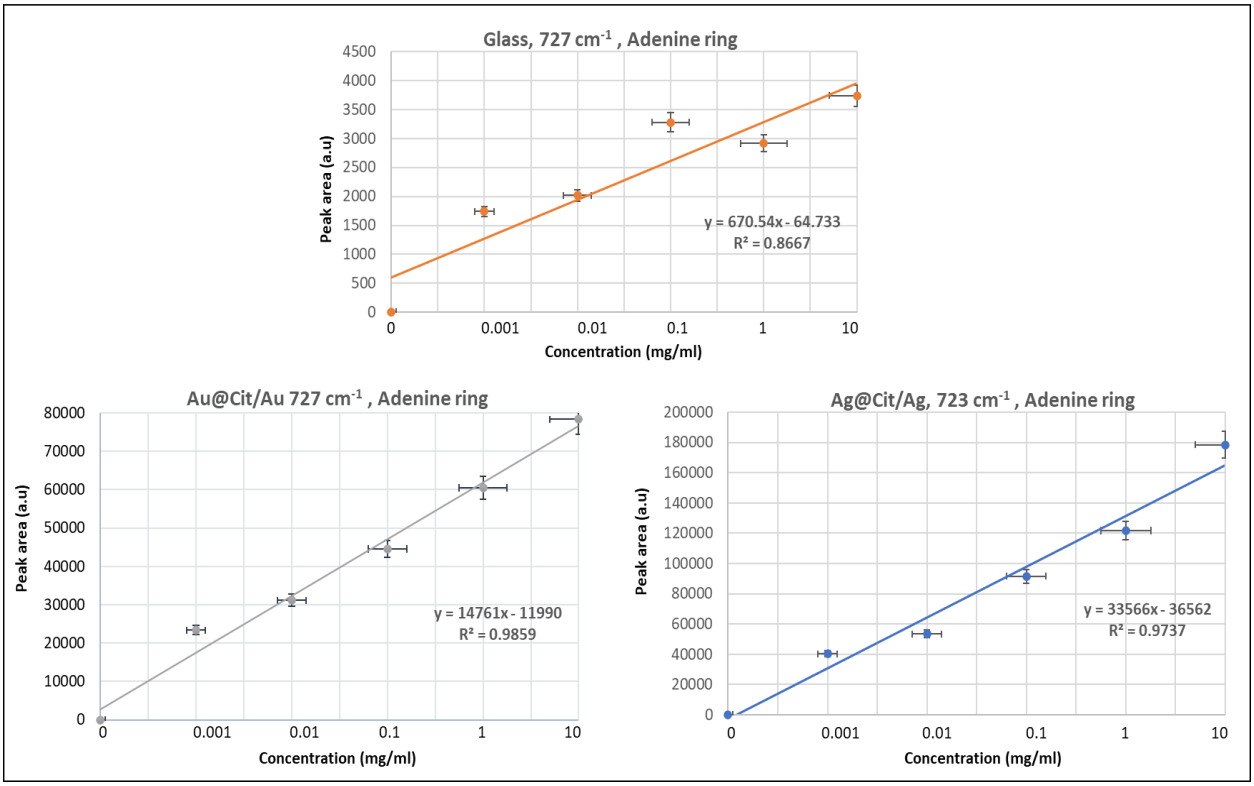

Figure 3.17:Linear regression analysis of Tenofovir using the adenine ring functionality (723 cm-1). Peak area vs concentration on Glass (Top), Au@Cit/Au (left) and Ag@Cit/Ag (right).

The graphs shown in figure 3.17 depict the differences in the peak area of the adenine functional group in response to the different scaffolds. The glass sample shows a low R^2 value of 0.86 ($p< 0.10$) and calibration sensitivity of 670. This result can be attributed to the interference from the glass signal during Raman acquisition whereby, the background subtraction also attenuated the analyte signal. In the case of the gold sensor, a significant improvement in R^2 of 0.98 ($p <0.01$) and calibration sensitivity of 14761 was the outcome due to the signal enhancement of the sensor as well as the lack of interference from the plain glass scaffold. The silver sensor also showed a better R^2 value of 0.97 ($p<0.01$) with a calibration sensitivity of 33566. The increase in the latter value shows a better molecular interaction between the sensor and the analyte functional group, which resulted in signal enhancement that supersedes that of the gold platform. This observation is further supported by the larger peak shift on the silver sensor, which is caused a by tensile strain that occurs when the adenine ring is in a closely confined space like a SERS hotspot [27-28]. A similar calculation was performed using peak area data from the 1326 cm^{-1} vibrational mode to compare the two groups for consistency. Figure 3.18 below is a collection of linear graphs obtained from the data plotted against TDF concentration.

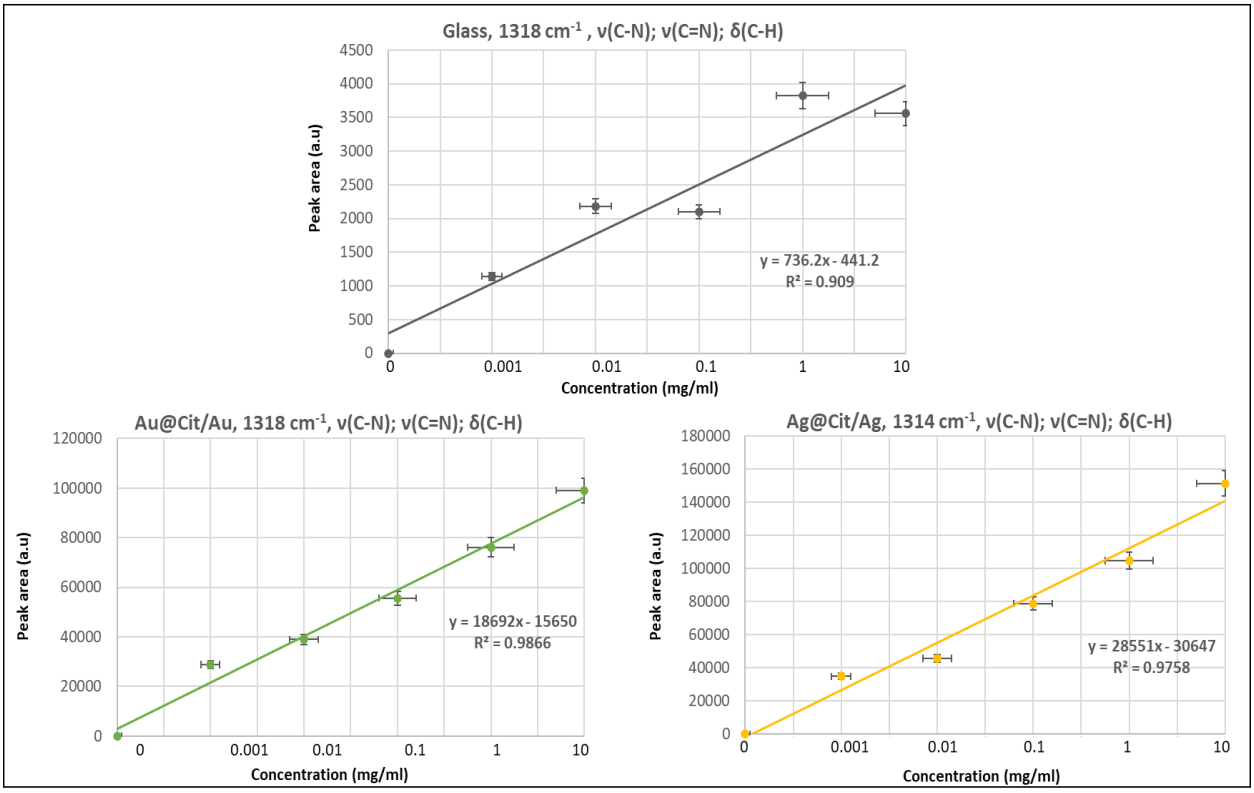

Figure 3.18: Linear regression analysis of Tenofovir using the C=N, C-N, C-H functionality (1326 cm-1). Peak area vs concentration on Glass (Top), Au@Cit/Au (left) and Ag@Cit/Ag (right).

The top graph is of the glass substrate where the R^2 value improved to 0.90 ($p<0.05$) from the adenine analysis, likewise the calibration sensitivity also increased to 736. These changes are attributed to the stereochemistry of the functional groups because when evaluating two atom bonds within a ring, the atoms themselves have direct access to intermolecular forces with the surface as they adsorb, especially through hydrogen bonding between the carboxylate groups and the hydrogens of the C-H bond[29]. Alternatively, the nitrogen lone pairs can also contribute to the interaction towards the alpha and carbonyl carbons of the carboxylates. These two factors can improve the signal quality and sensitivity compared to the whole adenine group which is likely to be sterically hindered and thus less responsive [30]. For the gold sensor platform, the R^2 value was again 0.98 ($p<0.01$) and the calibration sensitivity improved to 18692. The differences from the adenine ring evaluation in figure 3.17 are attributed to the stereochemistry of the molecule, with the two atom bonds being closer or within the SERS hotspot and thus able to experience the enhancement effect from the sensing platform. For the silver sensor platform, the R^2 value remained at 0.97 ($p<0.01$) while calibration sensitivity decreased to 28551 compared to the ring data, again possibly due to steric effects as seen by the larger peak shift from the powder value. Overall, the gold scaffold seems to outperform silver in terms of consistency with linear fitting however, the latter has higher values in terms of calibration sensitivity. The data were further processed to determine analytical sensitivity, and the limit of detection (LOD) for

the two sensing platforms compared to plain glass. The calculations for LOD for TDF are given in the supplementary section as C2. Table 6 below is a summary of the values obtained during the experiments and subsequent statistical analysis.

Table 3.6:Statistical values of TDF on glass, Au@Cit/Au and Ag@Cit/Ag.

Parameter	Glass	Au@Cit/Au	Ag@Cit/Ag
727 cm^{-1} Adenine ring			
R^2	0.86	0.98	0.97
Calibration sensitivity (m)	670	14761	33566
Analytical sensitivity (Y)	39.26	57.48	63.09
L.O.D (mg/ml)	0.05	0.01	0.005
RSD (%)	0.74	0.64	0.65
1310 cm^{-1} ν(C-N); ν(C=N); δ(C-H)			
R^2	0.90	0.98	0.97
Calibration sensitivity (m)	736	18692	28551
Analytical sensitivity (Y)	43.13	72.79	53.98
L.O.D (mg/ml)	0.04	0.009	0.006
RSD (%)	0.79	0.51	0.76

The numerical data in table 6 shows significant differences in the analytical sensitivity of the sensors towards different parts of the TDF molecule. For the adenine ring, analytical sensitivity increases from glass to gold and then silver, which agrees with the LOD values, where silver has the lowest detection value of 0.005 mg/ml compared to glass and gold at 0.05 and 0.01 respectively. For the 1310 cm^{-1} band, the gold substrate shows a better analytical sensitivity compared to glass and silver with a value of 72.79; however, the silver sensor platform showed a lower LOD at 0.006 mg/ml compared to the 0.009 mg/ml value found for gold. Overall, both metal platforms show improved results in the molecular and statistical evaluation of TDF using citrate as a crosslinker as seen from the data and the RSD values. In the next section, an analysis of Lamivudine using the citrate-based sensor is performed to evaluate significant molecular changes because of the sensing platforms.

3.3.3 Lamivudine on citrate based chemical sensors.

LAM experiments were conducted on glass and the two citrate metallic sensor platforms to compare changes in peak characteristics between the three groups. Raman spectra of five concentrations of TDF ranging from 0.001- 10 mg/ml were dried on glass, Au@Cit/Au and Ag@Cit/Ag. Figure 19 below is a spectral overlay of LAM on the glass substrate. The spectrum for LAM powder is given in the supplementary section as figure S7.

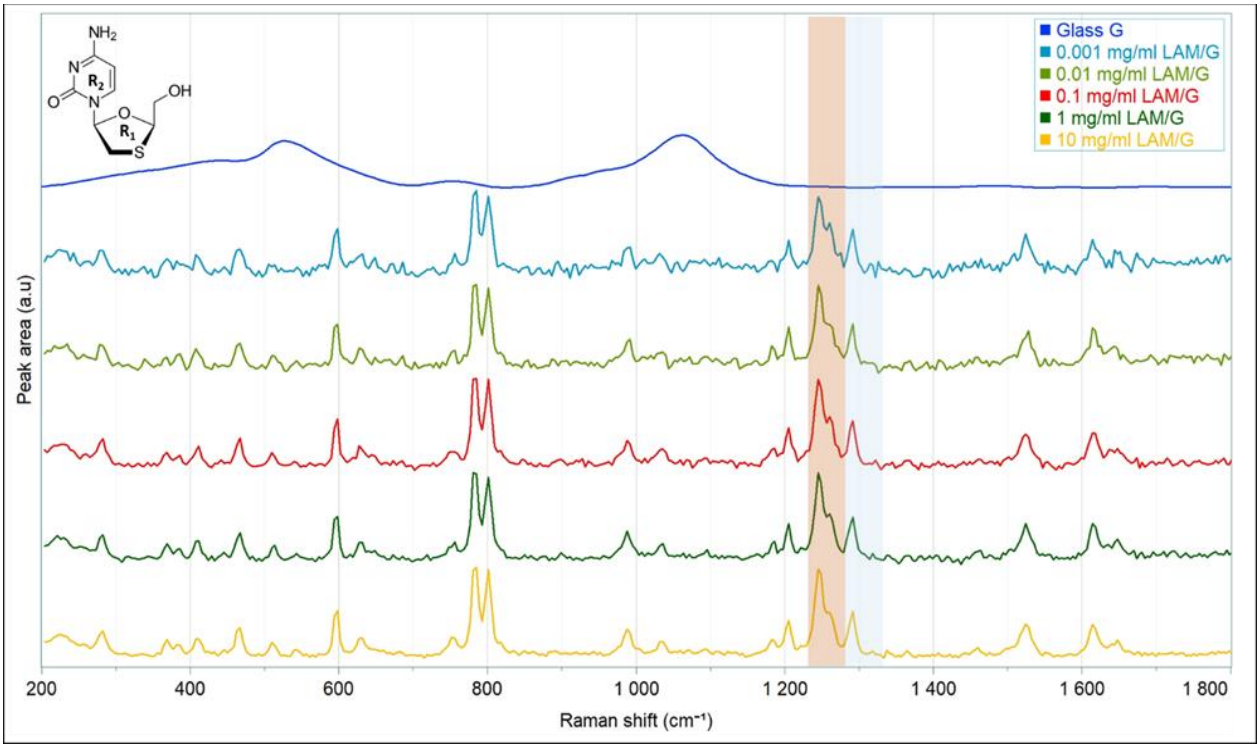

Figure 3.19:Raman spectral overlay of Lamivudine on glass, 0.001-10 mg/ml. Acquired from 200-1800 cm-1. 532 nm, 12 mW laser power, 100 scans, 10 seconds per scan. Insert: LAM molecular structure.

The spectral overlay shown in figure 3.19 compares the blank sample of glass (red) and a series Lamivudine samples (LAM) on glass substrates. Spectral data was acquired in the region 200-1800 cm^{-1} where the amine ($-NH_2$) bending mode was detected at 284 cm^{-1} followed by the twisting mode of C-S at 466 cm^{-1} alongside the bending mode of hydroxyl group (-OH). Both peaks display a blue shift from the powder, which indicates bond shortening. A skeletal twisting vibration of the lamivudine molecule was observed in the 600 cm^{-1} regions next to the ring deformation vibration modes of the two rings R_1 and R_2. Carbon-oxygen bonds of ring 1 are seen in the middle of the spectral range 1034 cm^{-1}, succeeded by the stretching mode carbon-nitrogen bonds of ring 2 at 1245 cm^{-1}[31]. The above-mentioned peaks show blue shifting because of bond shortening on the glass substrate. At the end of the spectrum, more peaks arising from ring 2, specifically the deformation of amine bonds (1615 cm^{-1}) and the stretching mode of the carbonyl bond (1645 cm^{-1}), were detected, which is the smallest blue shift in the series of samples. Although vibrational modes were obtained across the sample group, their signals were heavily attenuated by the broad band signals from the glass post background subtraction. Figure 19 below shows Raman spectral data of the same samples analyzed on the fabricated chemical sensor Au@Cit/Au.

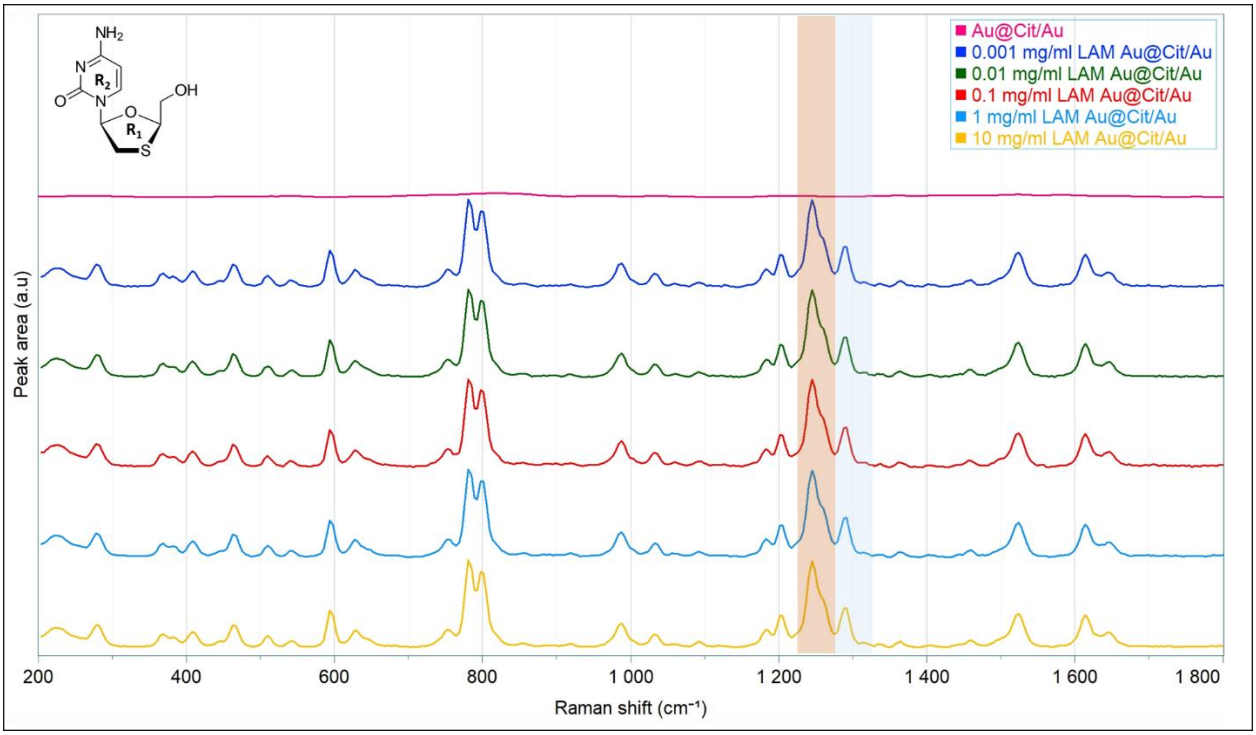

Figure 3.20:Raman spectral overlay of Lamivudine on Au@Cit/Au, 0.001-10 mg/ml. Acquired from 200-1800 cm-1. 532 nm, 12 mW laser power, 100 scans, 10 seconds per scan. Insert: LAM molecular structure

The spectral data in figure 20 shows a similar peak profile as seen in the glass sample group. However, key differences in peak values were observed. Firstly, a red shift was observed for the amine (277 cm^{-1}) and O-H (462 cm^{-1}) groups of ring 2 and ring 1 respectively which indicates hydrogen bonding between the analyte and the carboxylate and hydroxyl groups of the crosslinker. This is further supported by the red shift of ring 2, observed as 751 cm^{-1} ring deformation, possibly due to the amine interaction with the sensor. Further down the spectra (1245-1645 cm^{-1}), ring 2 shows dominance in vibration modes over ring 1, which is also seen by the weak peaks of the C-O (1031 cm^{-1}), which belongs to the latter, this implies that the amine group intermolecular interactions with the crosslinker is more favorable than the alternative. In addition, the aromatic character of ring 2 found on the double bonds between carbon and nitrogen, can lead to increased signal and red shifting because of the polarizability of these functional groups when the amine undergoes hydrogen bonding with the sensor. The lack of strong C-O contribution implies that the carboxylate and hydroxyl groups of the crosslinker repel the hydroxyl group of ring 1 and prefers the amine group of ring 2 for intermolecular interaction. Figure 21 below is a SERS overlay of LAM on silver sensing platform. The same parameters were followed as above.

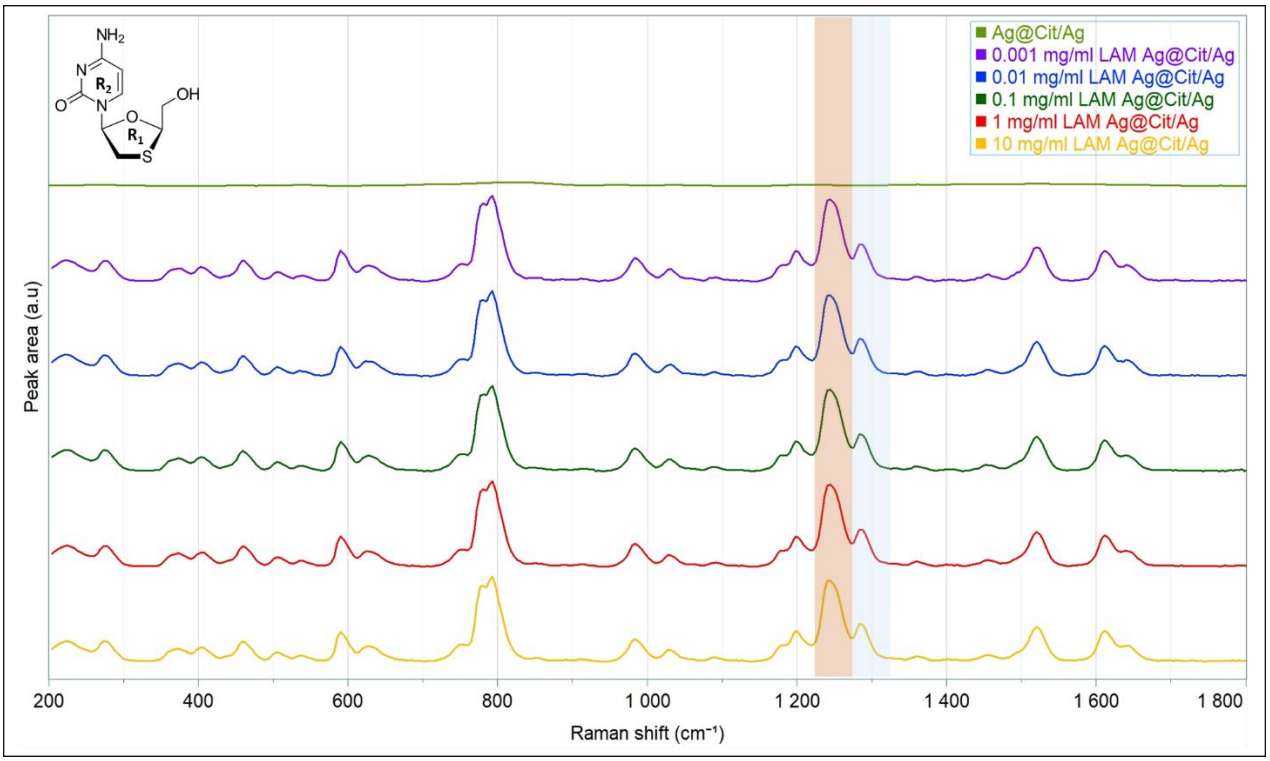

Figure 3.21:Raman spectral overlay of Lamivudine on Ag@Cit/Ag, 0.001-10 mg/ml. Acquired from 200-1800 cm-1. 532 nm, 12 mW laser power, 100 scans, 10 seconds per scan. Insert: LAM molecular structure.

In the above figure, a spectral overlay of LAM on Ag@Cit/Ag shows significant differences between glass and gold. Firstly, a red shift from the bending vibration of the amine group is seen at 225 $cm^{-1,}$ which is the only red shift of this functional group at that spectral range. Secondly, peaks 458 cm^{-1} and 590 cm^{-1} of ring 2 (R2) and the skeleton respectively, both show a red shift from the powder value of 462 cm^{-1} and 593 cm^{-1}. A similar red shift profile is also seen for ring 1 (R1) and R2 between the 1200 cm^{-1} region. At the far end of the spectra, the amine and carbonyl bonds appear red-shifted by 3 and 1 cm^{-1} at 1610 cm^{-1} and 1644 cm^{-1} respectively [32]. From the data, R1 and R2 were chosen as functional groups of interest because of the close connection to the amine and hydroxyl groups respectively for all three scaffolds. Table 7 below is a summary of the vibrational bands obtained during experiments on the silver scaffolds.

Table 3.7: Raman bands of Lamivudine on glass, gold, and silver sensors.

Glass	Au@Cit/Au	Ag@Cit/Ag	Reference (cm^{-1})	Assignment
284	277	225	227	ω(H-N-H)
466	462	458	462	τ(C_2-S), ρ (O-H)
599	593	590	593	τ skel
629	631	627	627	τ skel
753	751	752	780	δ Ring 2
799	780	793	796	δ (Ring 1),δ(Ring 2)
1034	1031	1028	1031	ν(C_2-O), ω(C_6-H),
1245	1244	1241	1244	ν(C_2-N), ρ (-NH_2),
1290	1291	1292	1287	ω(C_5-H_2), ρ(C_2-H)
1525	1523	1520	1523	δ(-NH_2),ν (C=N)
1615	1613	1610	1613	δ(-NH_2),ν (C=C)
1645	1644	1644	1643	ν (C=O)

ν=stretching, δ=rocking, ρ=bending (in plane),ω= bending (out of plane), τ= twisting , [33]

In the next section, a statistical evaluation of the peaks highlighted in the table was conducted using equations from section 2 .6. Peak area and standard error values were used to determine differences for parameters associated with a chemical sensor.

3.3.4 Statistical analysis of Lamivudine on glass, gold, and silver chemical sensors.

Peak area values of the functional groups of interest 1245 cm^{-1} and 1920 cm^{-1} were used together with their corresponding concentrations to plot linear graphs and determine R^2 and calibration sensitivity values. Figure 22 below shows three graphs that belong to the glass, gold, and silver scaffolds for the 1244 cm^{-1} of R2.

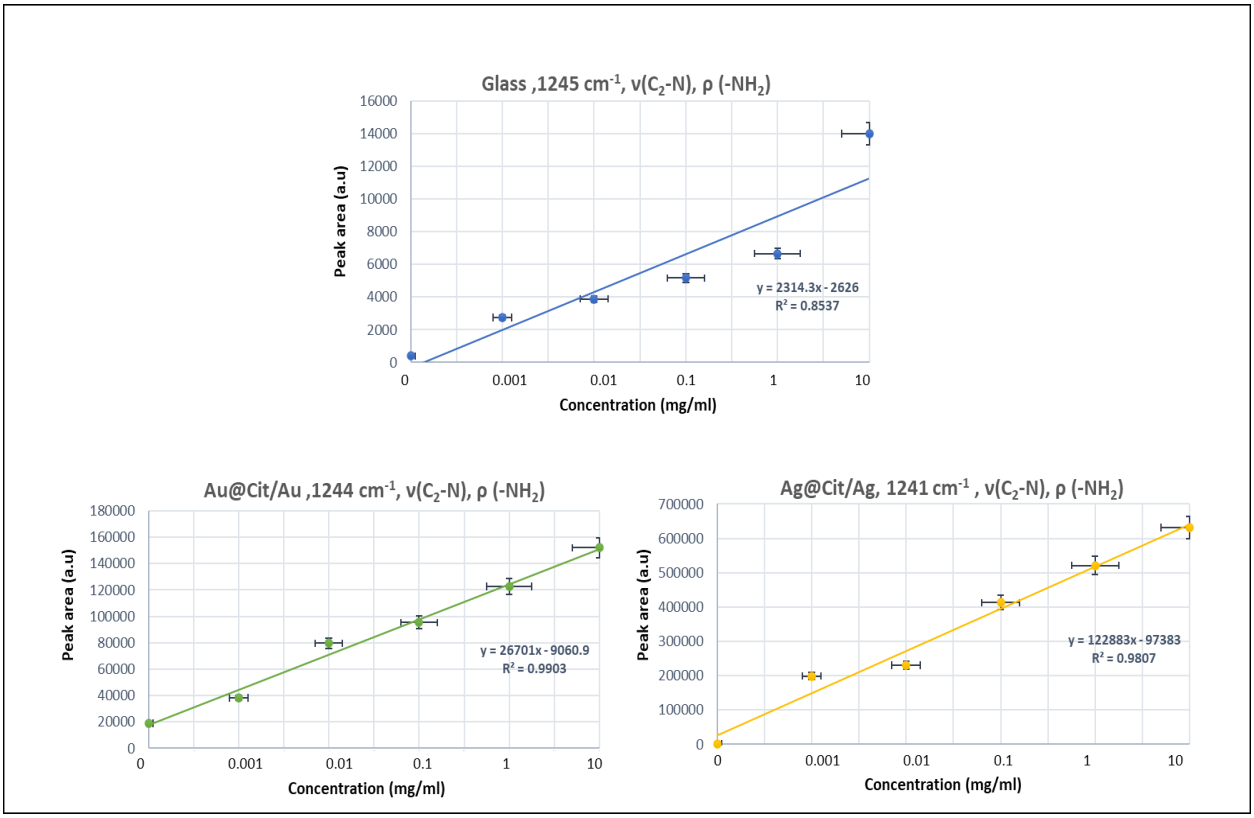

Figure 3.22:Linear regression analysis of Lamivudine using the ring 2 (R2) functionality (1244 cm-1). Peak area vs concentration on Glass (Top), Au@Cit/Au (left) and Ag@Cit/Ag (right).

The results from the graphs in figure 3.22 show a linear relationship between the LAM concentration and the peak area values. The top graph which shows results from glass, gave an R^2 value of 0.85 ($p < 0.10$) with a calibration sensitivity of 2314. The plot from the gold experiments showed a satisfactory R^2 value of 0.99 ($p < 0.01$) and calibration sensitivity of 26701 from the signal enhancement. Lastly, calculations from the silver sensor group resulted in an R^2 value of 0.98 and a calibration sensitivity of 122883 towards the LAM samples. The metallic sensors outperform the glass scaffold in both linear quality and sensitivity, this is a result of forces like hydrogen bonding between the analyte hydrogens and the oxygen atoms of the crosslinker on the nanomaterials which result in a better signal output [33]. Also, from the spectral overlay of figures X and X, the most sterically unhindered species such as the amine, gave the most intense signals and such as, and they provided signal enhancement R2. Figure 23 below is a similar analysis of LAM where the R2 was evaluated using peak 1244 cm^{-1} of the R1.

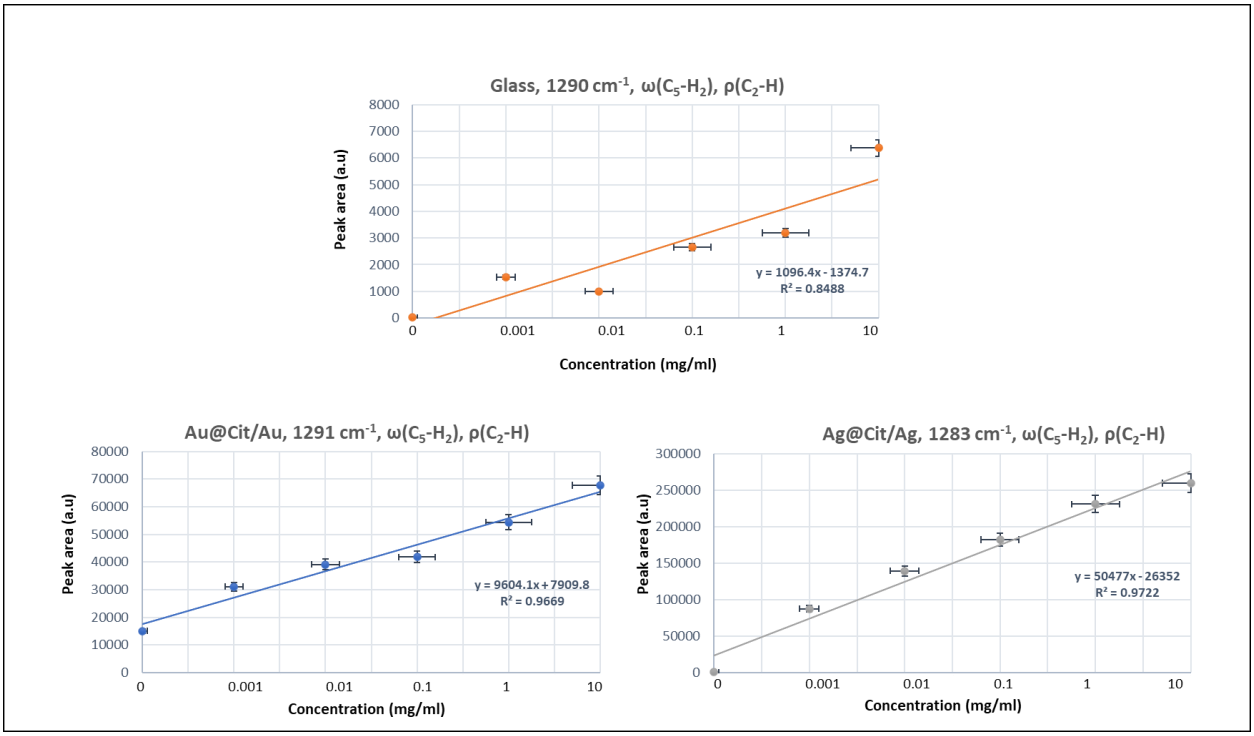

Figure 3.23:Linear regression analysis of Lamivudine using the ring 2 (R2) functionality (1287 cm-1). Peak area vs concentration on Glass (Top), Au@Cit/Au (left) and Ag@Cit/Ag (right).

Figure 3.23 is a collection of linear graphs for the glass, gold and silver sample groups. The linear relationship observed in figure 3.22 is also seen above where the glass group resulted in a R^2 value of 0.84 ($p<0.10$) and a calibration sensitivity value of 1096. The results from the gold experiments showed an R^2 value of 0.96 and a calibration sensitivity of 9604. The improvement is a result of the intermolecular forces between the amine group via hydrogen bonding which supplied the signal improvement. For silver experiments, the R^2 value obtained was 0.97 ($p< 0.01$) with a calibration sensitivity of 50477. The large increase in calibration sensitivity arises from the signal enhancement provided by the silver sensor through molecular interaction like R1. This observation is supported by the change in red shifting for the silver group, which indicates tensile strain caused by the sensor interaction with the analyte. The table that follows gives a summary of the analytical sensitivity and limit of detection of the three scaffolds towards the API Lamivudine. The calculations used to determine these values were conducted in the same fashion as explained in SA.

Table 3.8:Statistical values of LAM on glass, Au@Cit/Au and Ag@Cit/Ag.

Parameter	Glass	Au@Cit/Au	Ag@Cit/Ag
1245 cm^{-1}, $\nu(C_2\text{-}N)$, ρ ($\text{-}NH_2$)			
R^2	0.85	0.99	0.98
Calibration sensitivity (m)	2134	26701	122883
Analytical sensitivity (Y)	15.81	54.54	53.51
L.O.D (mg/ml)	0.79	0.0067	0.0014
RSD (%)	2.67	0.58	0.69
1290 cm^{-1}, $\omega(C_5\text{-}H_2)$, $\rho(C_2\text{-}H)$			
R^2	0.84	0.96	0.97
Calibration sensitivity (m)	1096	9604	50477
Analytical sensitivity (Y)	7.49	19.60	11.62
L.O.D (mg/ml)	1.67	0.018	0.0067
RSD (%)	5.94	1.17	1.52

The data from table 3.8 shows the values for LAM on the three scaffolds calculated using the example shown in SA. For the 1245 cm^{-1} data, the analytical sensitivity was lowest on glass with a value 15.81, followed by silver at 53.51 and gold at 54.54. This sequence arises from the calibration sensitivities for each group. However, the standard deviations contributed to the values obtained, with gold showing an improved linear fit and hence a better analytical sensitivity value. The limits of detection for all three groups decreased from 0.79 mg/ml on the glass followed by 0.0067 mg/ml of gold and 0.0014 mg/ml for silver, which shows a pronounced improvement for the metal scaffolds. In the case of the 1290 cm^{-1}, gold gave the largest analytical sensitivity of 19.60, followed by silver and glass at 11.62, 7.49, respectively. This sample group shows an improved response from gold towards the R1, possibly due to the high affinity for the hydroxyl group via intermolecular forces [34-36]. However, the limit of detection values gave the highest result on silver platform due to the better linear fit and calibration sensitivity. Overall, the silver outperformed the gold scaffolds in terms of limit of detection while the gold showed a better sensitivity profile towards the analyte.

3.3.5 Dolutegravir on citrate based chemical sensors.

Dolutegravir (DLG) samples prepared with the procedures in section 2.6 were analyzed using Raman spectroscopy and their bands were compared across the glass, gold, and silver scaffolds. Because DLG dissolves poorly in water, the samples were allowed to settle in the solution overnight to allow as much dissolution as possible. The exact concentrations of the samples may not be accurate as prepared. Nonetheless, Raman spectra were obtained and figure 3.24 below is the spectral overlay of DLG on glass. The samples were background corrected against the large peaks found on the scaffold.

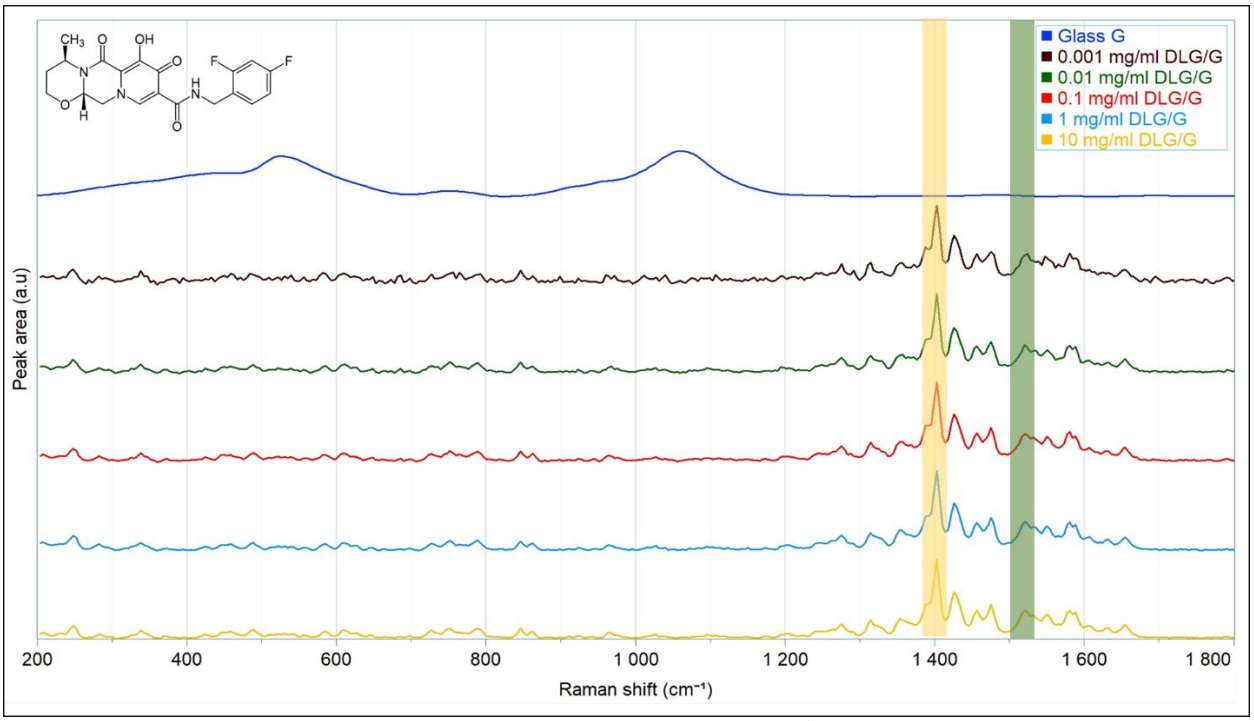

Figure 3.24: Raman spectral overlay of Dolutegravir on glass, 0.001-10 mg/ml. Acquired from 200-1800 cm-1. 532 nm, 12 mW laser power, 100 scans, 10 seconds per scan. Insert: DLG molecular structure.

The Raman spectra seen above show the vibrational bands from DLG on plain glass. The peaks from the plain glass appeared strongly just as on the previous APIs, thus the data was background subtracted to remove them. When comparing the samples above with the DLG powder spectrum (see S6), the peaks from the former show the amine bending mode at 247cm^{-1} followed by a stretching mode of carbon nitrogen bonds at 1276 cm^{-1}. The latter also reappears red-shifted by 8 cm^{-1} at 1314 cm^{-1} followed by alkyl groups also red-shifted at 1353 cm^{-1} and 1403 cm^{-1} which appeared strongly from the methyl group. A weak bending mode appeared from amines in the 1500 cm^{-1} region followed by imines and aromatic carbon double bonds around 1600 cm^{-1} [37-38]. The difference in peak number speaks to the changes in bond length mediated by intermolecular forces between the oxygens on the glass and the hydrogens of the analyte [39-41]. As a result, peaks 1403 cm^{-1} and 1520 cm^{-1} of the methyl and primary amine respectively, were chosen for statistical evaluation because of their hydrogens that engage in hydrogen bonding with the surface as seen by the peak shifts. The following spectral data is from DLG on the gold sensor.

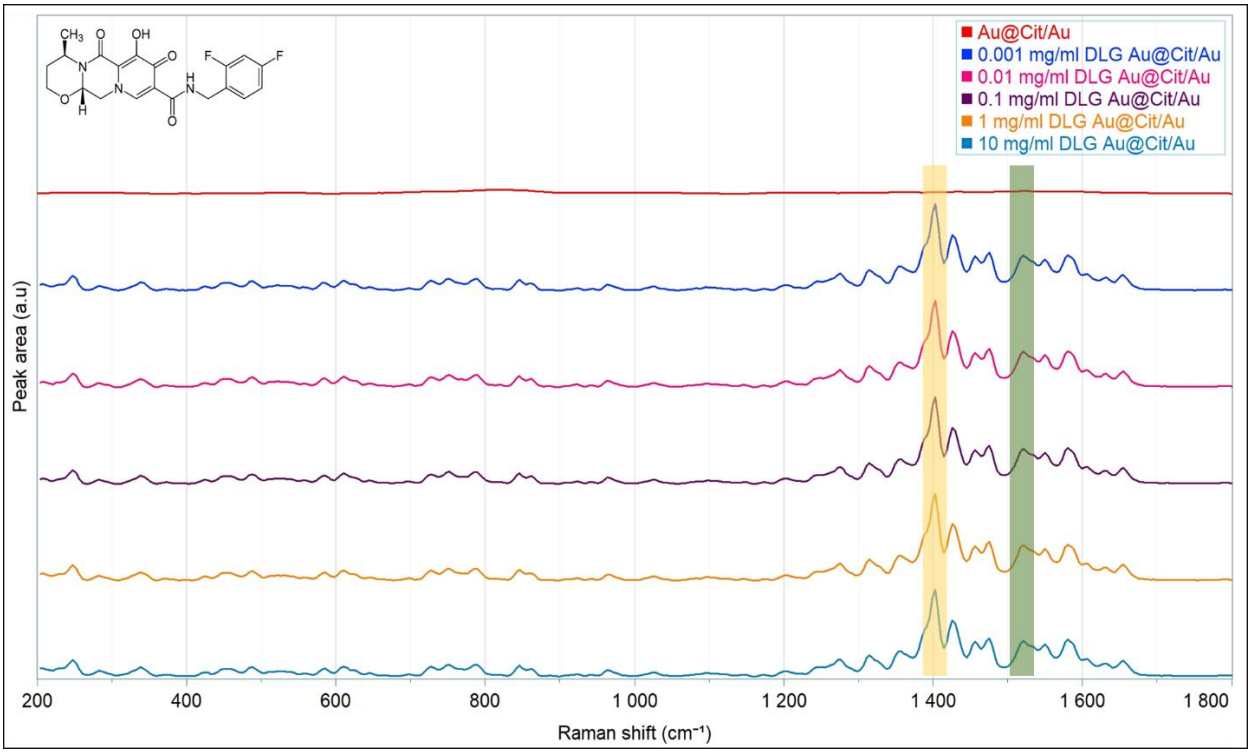

Figure 3.25:Raman spectral overlay of Dolutegravir on gold, 0.001-10 mg/ml. Acquired from 200-1800 cm-1. 532 nm, 12 mW laser power, 100 scans, 10 seconds per scan. Insert: DLG molecular structure.

The gold chemical sensor Au@Cit/Au was used to adsorb DLG samples which were subsequently analyzed using SERS. From figure 3.25 above, a peak profile like DLG powder was obtained were the peaks appeared more enhanced than the signals from the glass sample group. Starting from left to right, a weak peak of the amine group is seen at 247 cm^{-1} which is a value like glass, the next peak was detected from imine bonds appearing in stretching mode at 1276 cm^{-1}. A red shift is also seen from the same functional group at 1314 cm^{-1}, followed by the methyl group at 1400 cm^{-1} [42]. Contributions from the deformation of imines and bending modes of methyl groups occur in a peak overlap at 1425 cm^{-1} , followed by a large red shift at 1456 cm^{-1} from amines also in bond deformation. Primary amines reappeared in the deformation mode at 1514 cm^{-1}, which is a 6 cm^{-1} red shift from the powder, while at the far end of the spectrum, amines and imines were detected at 1580 cm^{-1} and 1629 cm^{-1} respectively. Lastly, the deformation mode and stretching mode of amines and aromatic carbon double bonds were seen as peak 1645 cm^{-1}[43-45]. Although the spectra from the gold samples provided peaks at higher intensities, the choice to adhere to the methyl and primary amine at 1400 and 1514 cm^{-1} arises from keeping consistency with the glass group. Furthermore, the bulky molecule DLG creates a limitation in terms of which functional groups can have reliable access to the hotspot based on stereochemical conditions, the chosen functional groups hold the most probability because of their positions on the molecule. The next figure is an overlay of DLG on silver sensors, which were analyzed in a similar process as above.

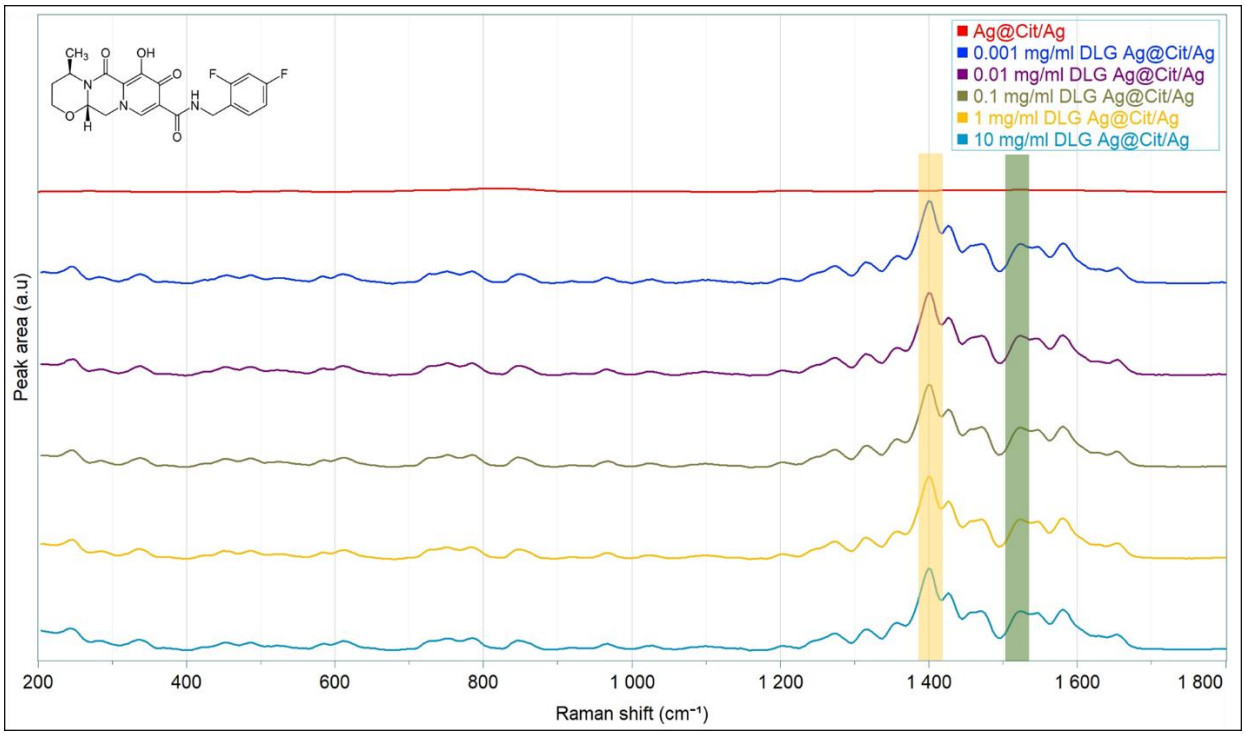

Figure 3.26:Raman spectral overlay of Dolutegravir on silver, 0.001-10 mg/ml. Acquired from 200-1800 cm-1. 532 nm, 12 mW laser power, 100 scans, 10 seconds per scan. Insert: DLG molecular structure.

The figure above shows the response of DLG on the silver sensor after Raman spectroscopy experiments. The spectra have an improved quality compared to the glass like the gold, which implies the sensing platforms of both metals greatly assist in improving the signal by blocking out the interference from the glass. Assessment of the peaks shows the presence of the amine group at 204 cm^{-1}, making it the largest red shift of this vibration [46]. The imine stretching modes were detected at 1272 cm^{-1} and 1314 cm^{-1}, red-shifted by 3 and 8 cm^{-1} respectively. Further down the spectra, the methyl band of interest appeared at 1399 cm^{-1} compared to 1408 cm^{-1} of the powder, succeeded by the primary imine and methyl combination at a red-shifted peak 1422 cm^{-1} [47]. The deformation band of primary amine was also detected at 1513 $cm^{-1,}$ making it the largest shift within the scaffolding groups while carbon and nitrogen double bonds appeared as stretching modes at 1629 cm^{-1}. Lastly, double bonds of the aromatic benzene ring were detected at 1645 cm^{-1} like the values obtained in the other platforms. Overall, the Raman peaks on the silver sample seem to be more intensified compared to the other groups, with red shift values showing the largest difference in the functional groups selected for statistical analysis. Table 9 below summarizes the peaks obtained in this section of Raman experiments where the values are compared against the powder sample acquired using the same parameters.

Table 3.9:Raman bands of Dolutegravir on glass, gold and silver sensors.

Glass	Au@Cit/Au	Ag@Cit/Ag	Reference (cm^{-1})	Assignment
247	247	204	247	ω(H-N-H)
1276	1276	1272	1275	ν (C=N), ν(C-N)
1314	1314	1314	1322	ν (C=N), ν(C-N)
1353	1357	1357	1370	δ(C-H)
1403	1400	1399	1408	$\delta(CH_3)$
1425	1425	1422	1425	$\delta(N=CH), \omega(CH_3)$
1456	1456	1434	1471	$\delta(-NH_2)$
1516	1514	1513	1520	δ(C-N-H)
1580	1580	1580	1581	$\delta(-NH_2)$
1655	1629	1629	1631	ν(C=N)
1647	1645	1645	1655	$\delta(-NH_2)$,ν (C=C)

ν=stretching, δ=rocking, ρ=bending (in plane), ω= bending (out of plane), τ= twisting. [33]

In the next section, a statistical analysis of the peaks highlighted in table 9 was conducted. Peak area values were explored using known equations from chapter 2, to calculate parameters such as sensitivity and LOD.

3.3.6 Statistical analysis of Dolutegravir on glass, gold, and silver chemical sensors.

Peak area values of the functional groups of interest 1408 cm^{-1} and 1520 cm^{-1} were used together with their corresponding concentrations to plot linear graphs and determine calibration sensitivity values. Figure 27 below shows three graphs that belong to the glass, gold, and silver, for peak 1408 cm^{-1} of the methyl group.

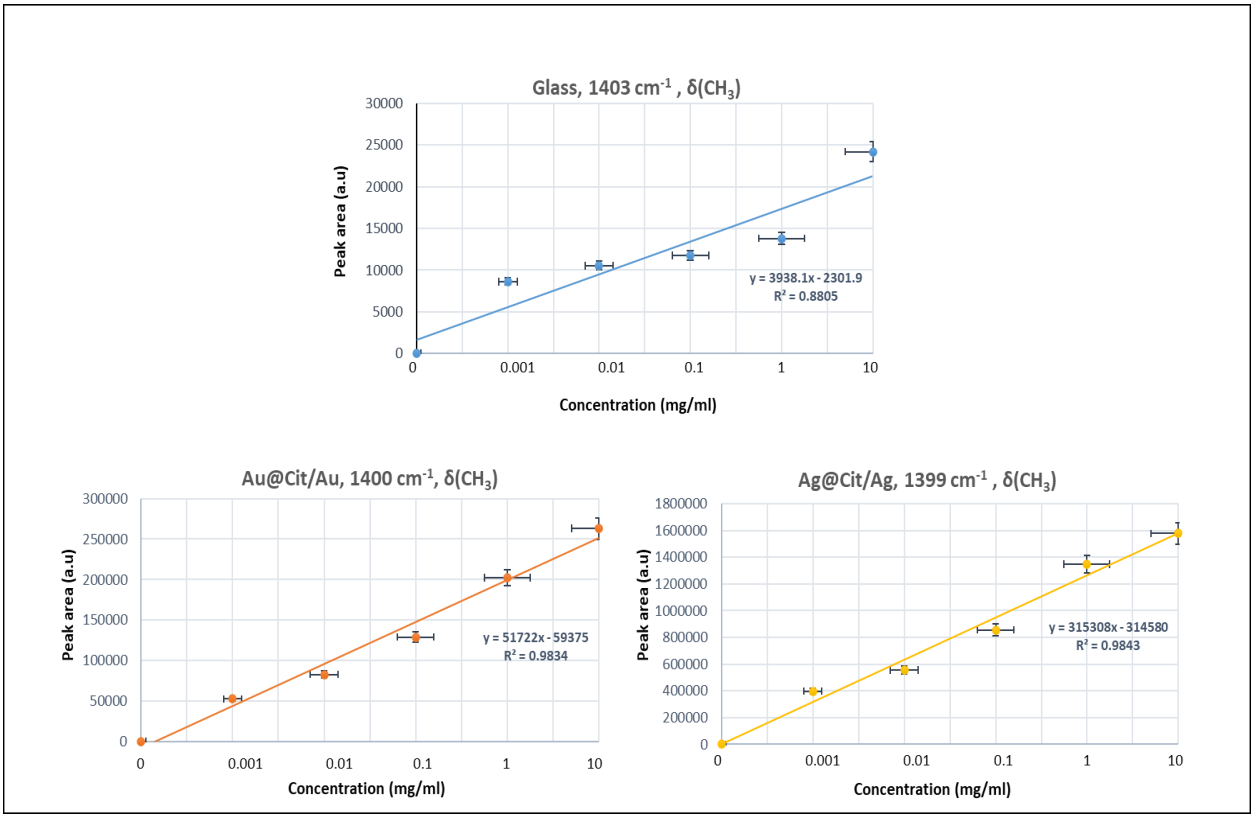

Figure 3.27:Linear regression analysis of Dolutegravir using the methyl group functionality (1408 cm-1). Peak area vs concentration on Glass (Top), Au@Cit/Au (left) and Ag@Cit/Ag (right).

The linear graph plots in figure 3.27 were compared in terms of R^2 and calibration sensitivity using the peak area from the methyl group vibration at 1408 cm^{-1}. The glass curve is seen at the top with a R^2 value of 0.88 ($p<0.10$) and a slope value of 3938.1. In the bottom left, the gold sensor plot produced a R^2 value of 0.98 ($p< 0.01$) and a calibration sensitivity of 51722. Lastly, the silver data resulted in a plot with a fitting R^2 value of 0.98 ($p<0.01$) and a calibration sensitivity of 315308. From the above data, the glass performed the least satisfactory amongst the group due to the interference effects from the glass as well as the solubility of DLG in water, which added a level of randomness to the concentrations prepared. The R^2 value improved on the gold samples because the glass signal was suppressed and the chemical interaction between gold and the analyte promoted the chemisorption process and thus enhanced the calibration sensitivity [48-50]. Thus far, the silver group shows large intensity values probably due to the larger particle sizes of the silver group, which adds to the signal enhancement process. In the next figure, linear plots of peak area vs concentration were constructed using the primary amine vibration.

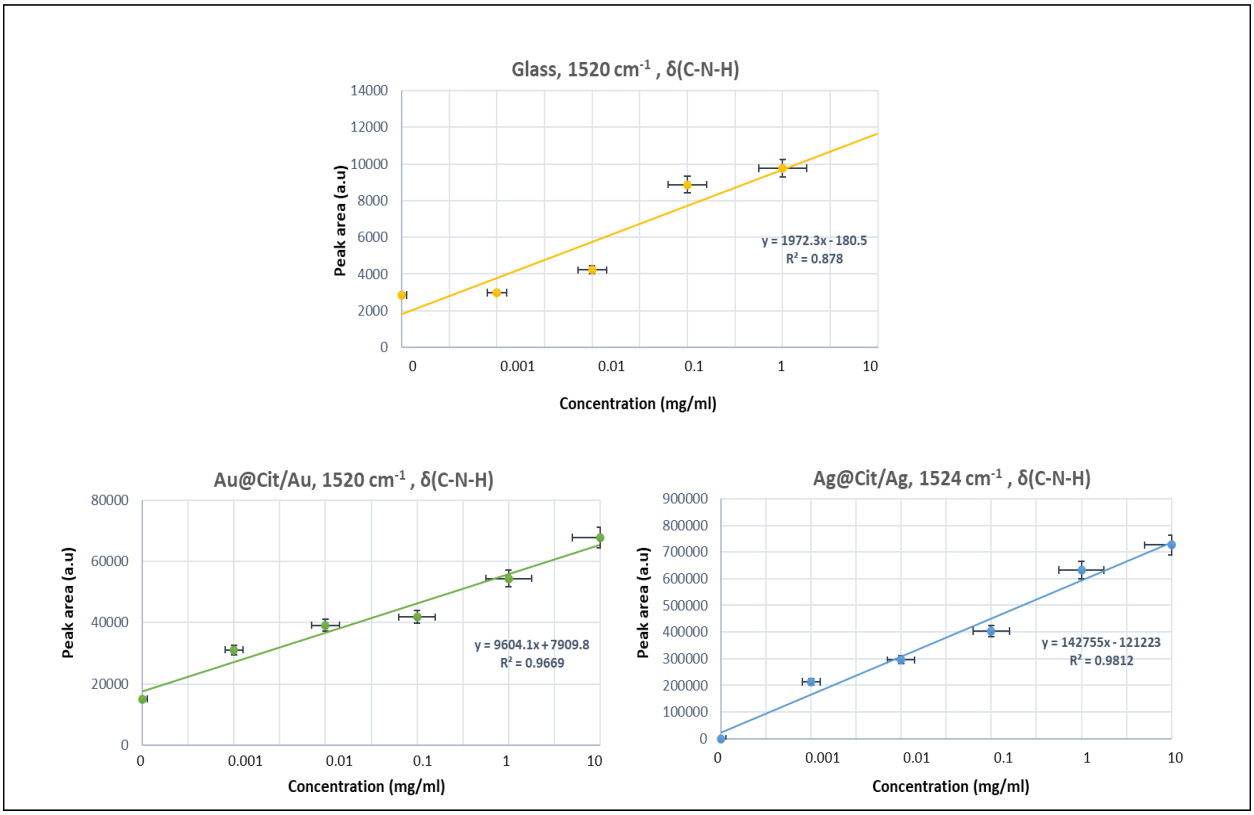

Figure 3.28:Linear regression analysis of Dolutegravir using the primary amine functionality (1520 cm-1). Peak area vs concentration on Glass (Top), Au@Cit/Au (left) and Ag@Cit/Ag (right).

The linear regression analysis shown above is of the primary amine using peak 1520 cm^{-1}. The R^2 value for the glass plot (top) was 0.87 ($p< 0.10$) and the calibration sensitivity 1972. The low values are consistent with effects from the glass interference as seen in the methyl group study. For the gold experiments, higher values were determined with a R^2 value of 0.98 ($p<0.01$) and a calibration sensitivity of 39700. This change occurred due to the enhanced signal response from the gold hotspots and chemical interaction with the analyte. Data from silver was plotted and produced a R^2 value of 0.98 ($p<0.01$) and a calibration sensitivity of 142775. From the results above, it appears the sensors improve the signal response from the analyte via chemisorption mediated improvement. This is expected considering the probability of hydrogen bonding between the hydrogen of the primary amine and the oxygen of the crosslinker that coating the nanoparticles. Furthermore, the pronounced red shifting supports this notion because the bond distortion that arises from confinement in the hotspot can only exist from the forces between the above-mentioned atoms. The table below summarizes the values for the calculated parameters, analytical sensitivity, and limit of detection to compare the efficiency of the sensor with respect to DLG. The calculation steps followed are the same as the example given for TDF in the supplementary section.

Table 3.10: Statistical values of DLG on glass, Au@Cit/Au and Ag@Cit/Ag.

Parameter	Glass	Au@Cit/Au	Ag@Cit/Ag
1408 cm^{-1} , $\delta(CH_3)$			
R^2	0.88	0.98	0.98
Calibration sensitivity (m)	3938	51772	315308
Analytical sensitivity (Y)	44.8	48.33	50.15
L.O.D (mg/ml)	0.01	0.003	0.0006
RSD (%)	0.67	0.87	0.79
1520 cm^{-1} , δ(C-N-H)			
R^2	0.87	0.98	0.98
Calibration sensitivity (m)	1972	39700	142775
Analytical sensitivity (Y)	29.56	194.81	133
L.O.D (mg/ml)	0.01	0.0041	0.001
RSD (%)	1.39	1.03	0.28

The data in table 10 above shows the calculated values for the parameters used to test the three scaffolds for chemical sensing. Starting with the methyl group results, the analytical sensitivity was fairly comparable across the different scaffolds, with glass producing the lowest value at 44.8 while gold and silver were 48.33 and 50.15, respectively. The limit of detection was also highest on glass at 0.01 mg/ml while gold reached 0.003 mg/ml and silver went as low as 0.0006 mg/ml. This series of data is consistent with the prediction that hydrogen bonding plays a key role in the enhancement of the methyl group signal using the oxygens of citrate. For the primary amine, analytical sensitivity increased from glass at 26.56 to silver at 133 and gold with the highest value of 194.81. The L.O.D was again highest on glass at 0.01 mg/ml and gold at 0.004 mg/ml, silver produced the lowest value of 0.001 mg/ml. From this data, consistency in the trend is seen for the calibration sensitivity and LOD however, gold produced a higher analytical sensitivity than silver. The reason for the change in value arises from the lower standard deviation from the gold data because both metals produced the same R^2 value. The LOD was better on silver in both functional groups which implies that the plasmonic nature of silver towards photons of 532 nm wavelength greatly enhances the signal intensity through electromagnetic effects. The relative standard deviation values show the statistical variation in the set of data used in the calculations.

In the next section, SERS experiments using cysteamine as the crosslinker were conducted across the three API analytes to assess the performance of the chemical sensors.

3.4 SERS analysis of APIs on cysteamine-based chemical sensors.

Experiments on active pharmaceutical ingredients (API) of ARVs prepared in section 2.5 were undertaken using MNP based chemical sensors; gold cysteamine (Au@Cys/Au) and silver cysteamine (Ag@Cys/Ag). The APIs used in this study consist of Tenofovir (TDF), Lamivudine (LAM) and Dolutegravir (DLG). The aim was to determine changes in molecular characteristics from peak shifting because of chemical interactions with the sensor. The spectra were compared against values obtained from powder samples which were used to prepare the solutions. The differences observed were used to determine peak area values and other numerical data for statistical calculations. All data relating to glass has already been discussed in section 3.4

3.4.1 Tenofovir on cysteamine-based sensors.

TDF experiments were conducted on cysteamine sensors to compare changes in peak characteristics as the analyte absorbed on the surface. Raman spectra of five concentrations of TDF ranging from 0.001- 10 mg/ml were dried on Au@Cys/Au and Ag@Cys/Ag. Figure 29 below is a spectral overlay of TDF on the glass substrate. The spectrum for TDF powder is given in the supplementary section as figure S4.

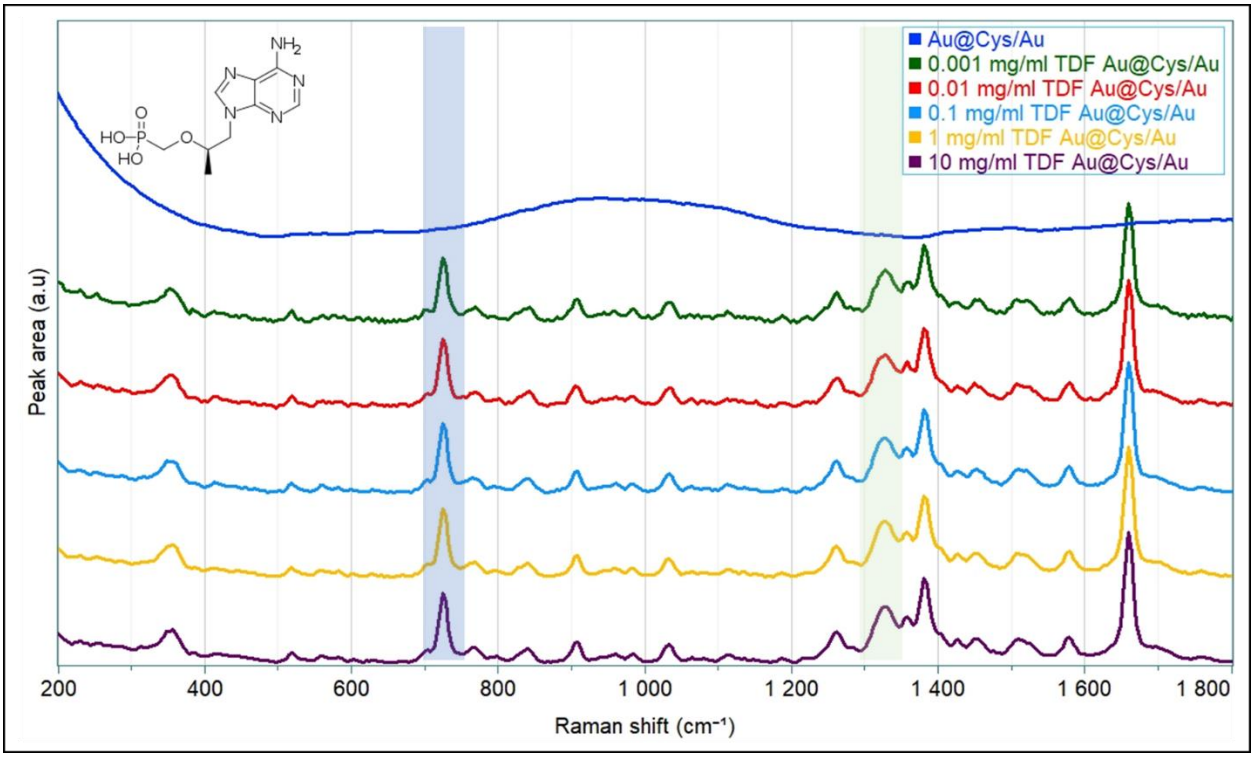

Figure 3.29:Raman spectral overlay of Tenofovir on Au@Cys/Au, 0.001-10 mg/ml. Acquired from 200-1800 cm^{-1}. 532 nm, 12 mW laser power, 100 scans, 10 seconds per scan. Insert: TDF molecular structure.

Figure 29 above shows a combination of Raman spectra for TDF across a series of concentrations. The spectrum of Au@Cys/Au seen as a blue line, was removed by background subtracted which resulted in the TDF spectra seen underneath. In all the samples, peaks associated with TDF were

detected, starting with the 724 cm^{-1} and 839 cm^{-1} vibrations from the adenine ring and the molecular skeleton respectively. Both bands appear blue-shifted from the powder value of 830 cm^{-1} like the adjacent phosphate group at 1032 cm^{-1} for the samples and 1027 cm^{-1} for the reference. Imine bonds and primary amines were detected in the middle of the spectra at 1261 cm^{-1} and 1330 cm^{-1}, both blue-shifted by 1 cm^{-1} and 4 cm^{-1} respectively. A deformed vibration from the methyl group was observed alongside other alkyl bonds in the 1400 cm^{-1} region while amine bands in bending vibration were detected at the far end of the spectrum between 1500 cm^{-1} and 1660 cm^{-1}. The blue-shifted bands obtained in this experiment can be explained by considering the interaction between nitrogen lone pairs from the cysteamine crosslinker, where a possible hydrogen bonding can occur with the hydrogens of the analyte [51-52]. The following figure is a spectral overlay of TDF on the silver sensor crosslinked with cysteamine.

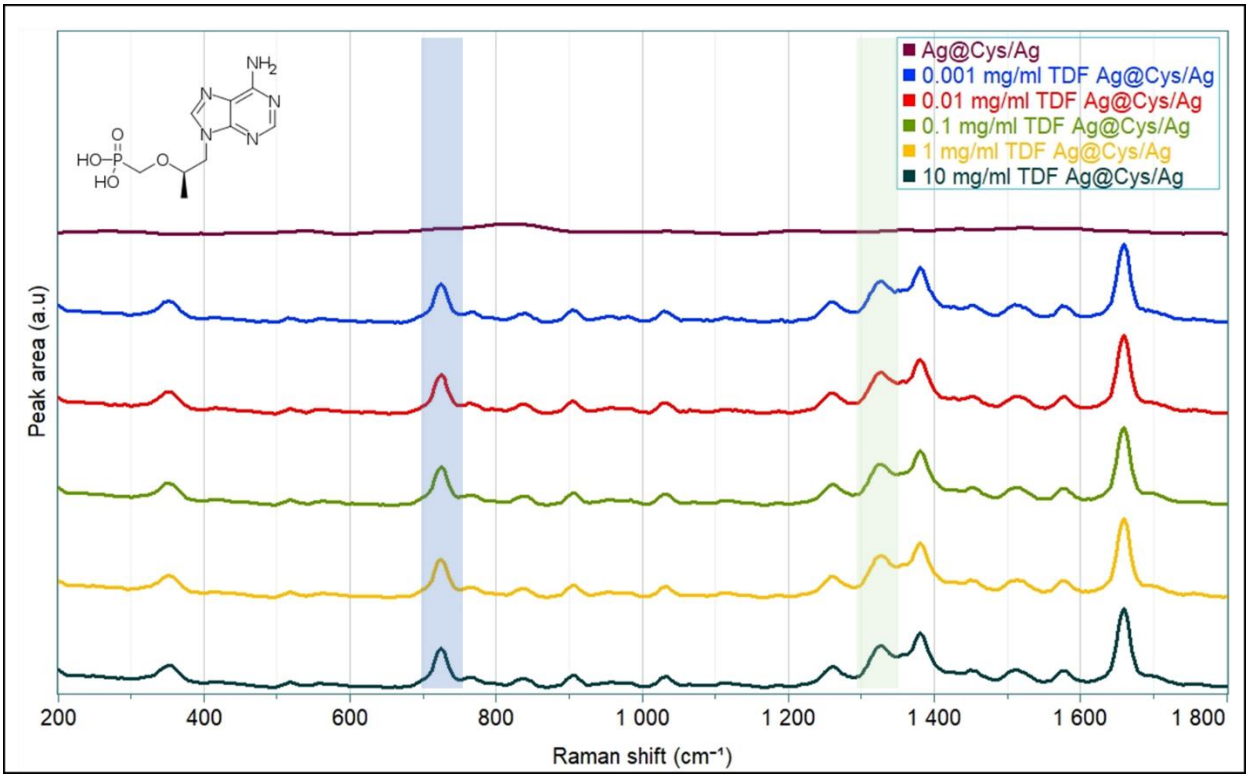

Figure 3.30:Raman spectral overlay of Tenofovir on Ag@Cys/Ag, 0.001-10 mg/ml. Acquired from 200-1800 cm-1. 532 nm, 12 mW laser power, 100 scans, 10 seconds per scan. Insert: TDF molecular structure.

In figure 30 above, the adenine ring breathing was detected at 724 cm^{-1} adjacent to the 835 cm^{-1} of the skeletal breathing band and the phosphate group at 1032 cm^{-1}. The three bands display blueshift which are like the gold samples which indicates a bond shortening when analytes are placed on the sensors with the oxygen-rich phosphate group and the skeletal group showing the highest peak shifts of 5 cm^{-1}. Imine bonds of the adenine ring reappeared at 1261 cm^{-1} and 1330 cm^{-1} respectively, which are also blue-shifted values. Alkyl groups in deformation mode were observed blue-shifted by 10 cm^{-1} for CH_2 at 1380 cm^{-1} and red shift of the CH_3 by 48 cm^{-1} at 1449 cm^{-1}. The large shift seen on the methyl group can arise from the strain arising from

intermolecular forces between its hydrogens and the lone pairs of the nitrogen group. The primary amine of TDF was detected at 1510 cm^{-1} followed by the amine group and the imine at 1577 cm^{-1} and 1659 cm^{-1} respectively. Table 3.11 below gives a summary of the vibrational bands obtained for TDF under the three scaffolds.

Table 3.11:Raman bands of Tenofovir on glass, gold, and silver sensors.

Glass	Au@Cys/Au	Ag@Cys/Ag	Reference	Assignment
727	724	724	722	Adenine ring
830	839	835	830	Skeletal breathing
1004	1032	1032	1027	Phosphate
1260	1261	1261	1249	v(C=N), v(C-NH_2), v(C-N)
1318	1330	1327	1321	v(C=N), v(C-N)
1372	1380	1380	1379	δ(CH_2)
1462	1449	1449	1497	δ(CH_3)
1520	1510	1510	1517	δ(CNH)
-	1577	1577	1576	α(NH_2)
1658	1655	1656	1658	C=O(aromatic)

v=stretching, δ=rocking, ρ=bending (in plane), ω= bending (out of plane), τ= twisting, α= wagging, [26]

The peaks that were studied in the citrate based experiments in section 3.4, 727 cm^{-1} and 1310 cm^{-1} were investigated statistically in the section that follows. The data obtained from the TDF glass experiments were incorporated into this data set for comparison purposes.

3.4.2 Statistical evaluation of Tenofovir on glass and cysteamine-based chemical sensors.

Linear curves of TDF on glass, Au@Cys and Ag@Cys substrates were constructed and compared using peak area versus concentration. The graphs were used to determine the R^2 values and the calibration sensitivity as the slope of the line. Figure 31 below is three graphs of the 727 cm^{-1} adenine ring breathing mode.

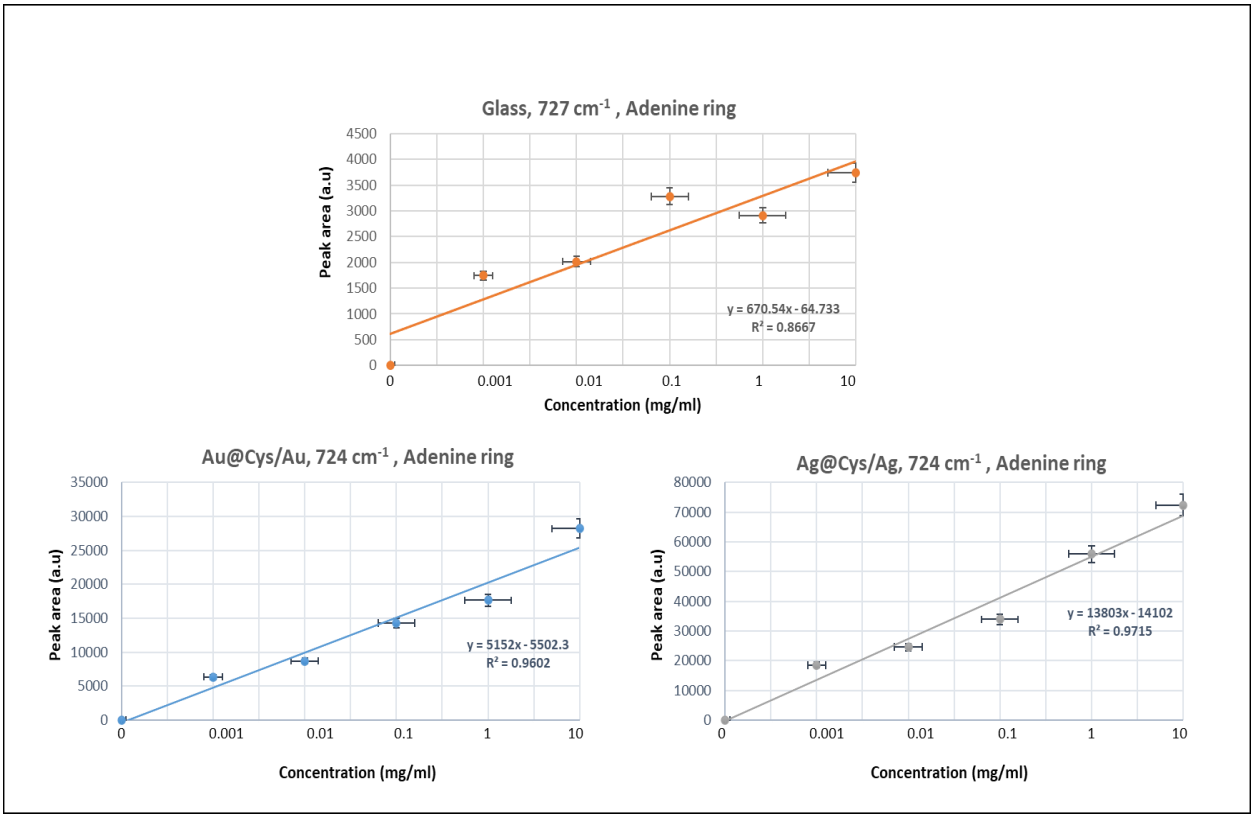

Figure 3.31:Linear regression analysis of Tenofovir using the adenine ring functionality (723 cm-1). Peak area vs concentration on Glass (Top), Au@Cys/Au (left) and Ag@Cys/Ag (right).

Figure 3.31 above gives the statistical outlook of TDF Raman response on the different platforms, using the adenine peak area as a signal. The glass produced a R^2 value of 0.86 ($p<0.10$) compared to the 0.96 ($p<0.01$) and 0.97 ($p<0.01$) values of the gold and silver samples respectively. In addition, the silver sensor showed the highest calibration sensitivity value of 13803, followed by the gold sensor at 5152 and the plain glass gave the lowest value of 670. The explanation for the observed statistical data can be addressed from the Raman shifts which show the most blue shift on the glass as the ring is more compressed, while the metal nanomaterial sensors show ring strain caused by molecular interactions that led to a relative red shift. This progression in values also shows that the metals played role in improving the linearity of the TDF signals by increasing the signal-to-noise response where the glass interference is reduced gradually as the thickness increases [53-54]. Furthermore, the improved calibration sensitivity speaks to the ability of the metals to improve the signal when the molecules are in the hotspot, indicated by Raman shifts mediated by intermolecular forces. The R^2 and calibration values obtained in these experiments were used to calculate the other parameters to assess the efficiency of the sensors. Figure 32 below is an evaluation of the 1310 cm^{-1} peak area which is attributed to the combined contribution of the imine and the primary amine stretching modes.

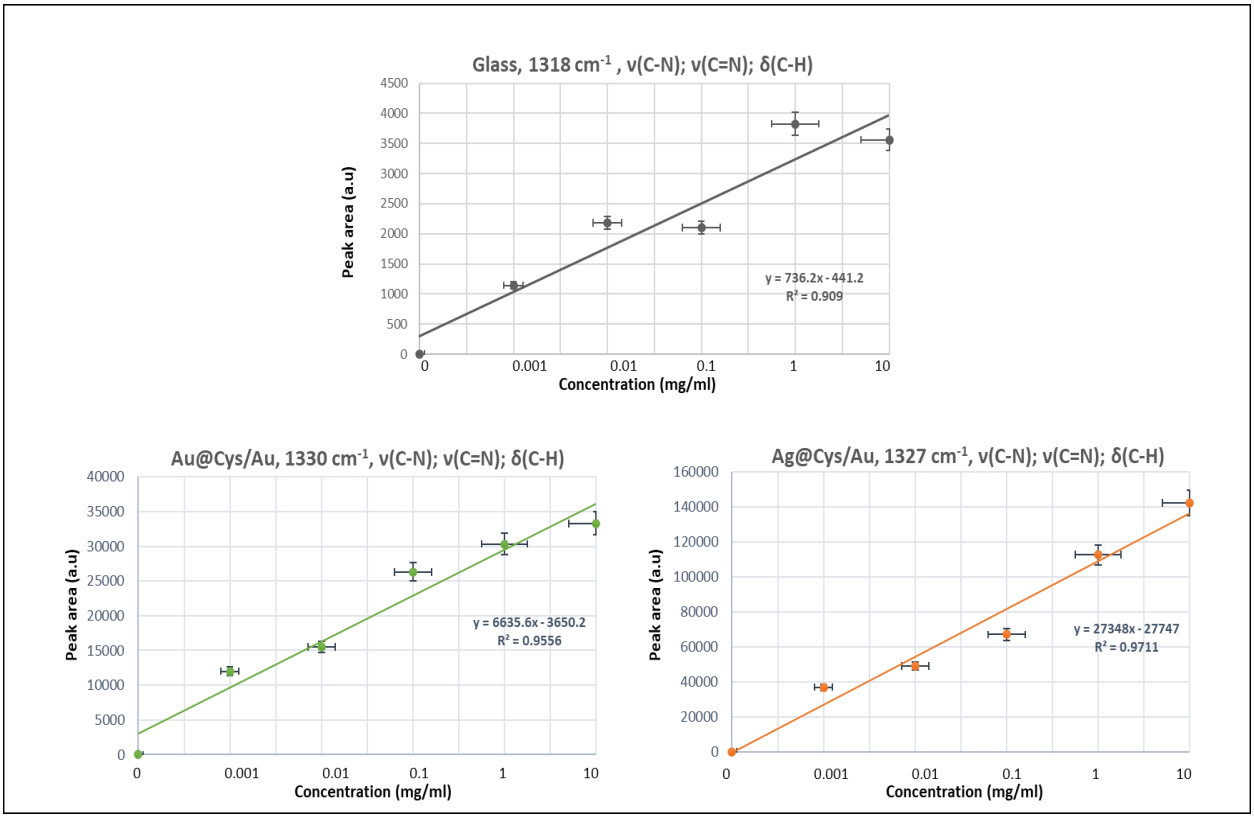

Figure 3.32:Linear regression analysis of Tenofovir using the adenine ring functionality C=N, C-N, C-H functionality (1326 cm-1). Peak area vs concentration on Glass (Top), Au@Cys/Au (left) and Ag@Cys/Ag (right).

The data in the figure above shows the statistical response from the 1330 cm^{-1} vibrational band of the primary amide of TDF. The R^2 of the glass, gave the lowest value of 0.90 ($p< 0.05$) while the gold value was 0.95 ($p< 0.05$) and the highest value was from the silver substrate at 0.97 ($p<0.01$). The calibration sensitivity from this set of experiments resulted in the glass substrate producing the lowest output of 736.2 followed by the gold sensor at 6635 and silver again with the highest value of 27348. The trend in this experimental group correlates with the peak shifting observed where the red-shifted glass value implies that the TDF ring functional groups are not compressed individually compared to the ring itself, which is blue shifting due to bond length shortening [55-57]. In addition, the metallic sensors showed consistency in blue shift because the functional group is compressed in stretching mode possibly by intermolecular forces. The results obtained from this statistical analysis were used to determine values for additional parameters that characterize the performance of chemical sensors. Table 12 below is a summary of statistical values obtained for TDF on the three substrates.

Table 3.12:Statistical values of TDF on glass, Au@Cys/Au and Ag@Cys/Ag.

Parameter	Glass	Au@Cys/Au	Ag@Cys/Ag
727 cm^{-1} Adenine ring			
R^2	0.86	0.95	0.97
Calibration sensitivity (m)	670	5152	13803
Analytical sensitivity (Y)	39.26	16	26.36
L.O.D (mg/ml)	0.05	0.01	0.003
RSD (%)	0.74	2.56	1.53
1310 cm^{-1} ν(C-N); ν(C=N); δ(C-H)			
R^2	0.90	0.95	0.97
Calibration sensitivity (m)	736	6635	227348
Analytical sensitivity (Y)	43.13	20.6	52.24
L.O.D (mg/ml)	0.04	0.01	0.001
RSD (%)	0.79	0.51	0.77

According to the table above, the chemical sensors showed a trend in analytical sensitivity towards the adenine ring as follows: the glass gave the highest value of 39.26 followed by silver with 26.36 and lastly gold produced a low value of 16. This trend can arise by considering the standard deviation of the data from glass decreased relative to the slope or calibration sensitivity whose linearity is confirmed by the R^2 value. Since the latter was low in magnitude, implying a poor linear fitting, the analytical sensitivity value received is not considered reliable. When comparing the nanomaterial sensors, silver surpassed the gold value due to the high calibration sensitivity and lower standard deviation. The limit of detection from glass was found to be 0.05 mg/ml, while lower values were obtained from gold at 0.01 mg/ml and silver and 0.003 mg/ml respectively. In the case of the amine bonds of the ring at 1310 cm^{-1}, the analytical sensitivity of glass was higher than gold at 43.13 and 20.6 respectively, while the silver sensor held the highest value at 52.24. For this functional group, the R^2 value on glass improved from the adenine ring. However, it remained lower than the chemical sensors with an additional lower significance value and thus it was regarded unreliable. The limit of detection significantly dropped on the chemical sensors compared to the glass substrate, with silver producing the lowest value of 0.001 mg/ml and gold at 0.01 mg/ml. The overall observation from the table above is that silver produced the most optimum combination of parameter values against gold and glass. In the next section, experiments with Lamivudine were conducted to compare the performance of the chemical sensors against the glass.

3.4.3 Lamivudine on cysteamine-based sensors.

After the production of cysteamine stabilized chemical sensors, Lamivudine was experimented on and compared to the glass data. The figures that follow are Raman spectral overlays only on

gold and silver chemical sensors because the glass samples were already explored and discussed in the citrate-based section of 3.4

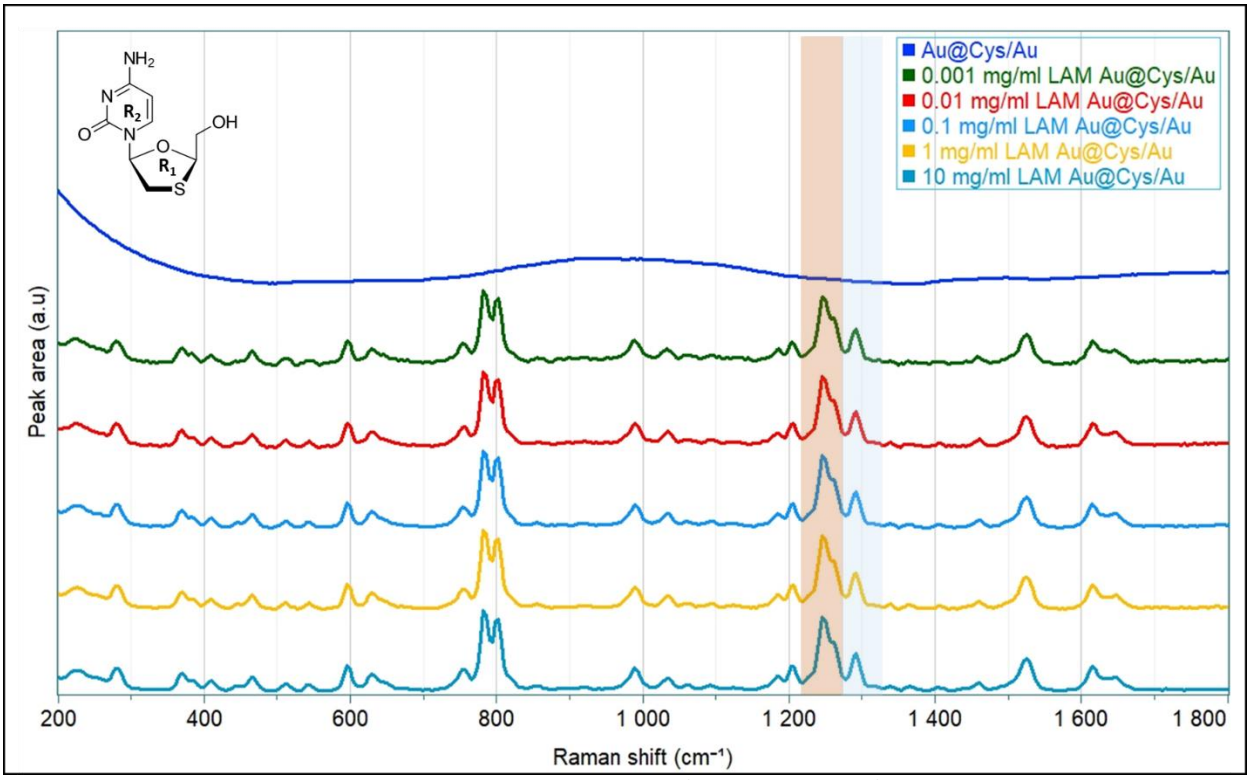

Figure 3.33: Raman spectral overlay of Lamivudine on Au@Cys/Au, 0.001-10 mg/ml. Acquired from 200-1800 cm-1. 532 nm, 12 mW laser power, 100 scans, 10 seconds per scan. Insert: LAM molecular structure.

Samples of Lamivudine were run on the Raman microscope system to analyze the molecular properties of the Au@Cys/Au chemical sensor. The blue line in the spectral overlay shows the Au@/Cys/Au contribution from section 3.2 which was background subtracted. The succeeding spectral lines are from the LAM samples. The bands observed from the samples showed the amine bending mode red-shifted by 5 cm^{-1} at 222 cm^{-1} followed by the combination of the twisting mode of carbon sulphur bonds of ring 1 and the bending mode of the hydroxyl group (R1) at 463 cm^{-1} . The molecular skeleton is seen twisting in two bands 595 cm^{-1} and 628 cm^{-1} which are slight blue shifts of less than 4 cm^{-1}. In the 800 cm^{-1} regions a doublet peak was detected and assigned to deformation modes of R1 and R2 both red-shifted, implying the rings were expanding under tensile strength. Carbon oxygen bonds from R1 were detected at 1032 cm^{-1}. The rest of the spectral range was dominated by R2, with the amine bonds in bending mode and carbon nitrogen bonds seen wagging and stretching at 1246 cm^{-1}, 1292 cm^{-1} and 1525 cm^{-1} respectively. At the end of the spectral range, amine bands and aromatic carbon bonds are detected in combined stretching and deformation modes in the 1600 cm^{-1} region, with the carbonyl carbon bond in stretching mode at 1643 cm^{-1}. Thus, as seen in the citrate study, the R1 seems to dominate the signal response via the aromatic character and the amine groups again in this sample group and as such, the same bands of interest selected in 3.4.3 were chosen for

comparison and statistical analysis with cysteamine. The next figure is a spectral overlay of LAM on Ag@Cys/Ag sensor.

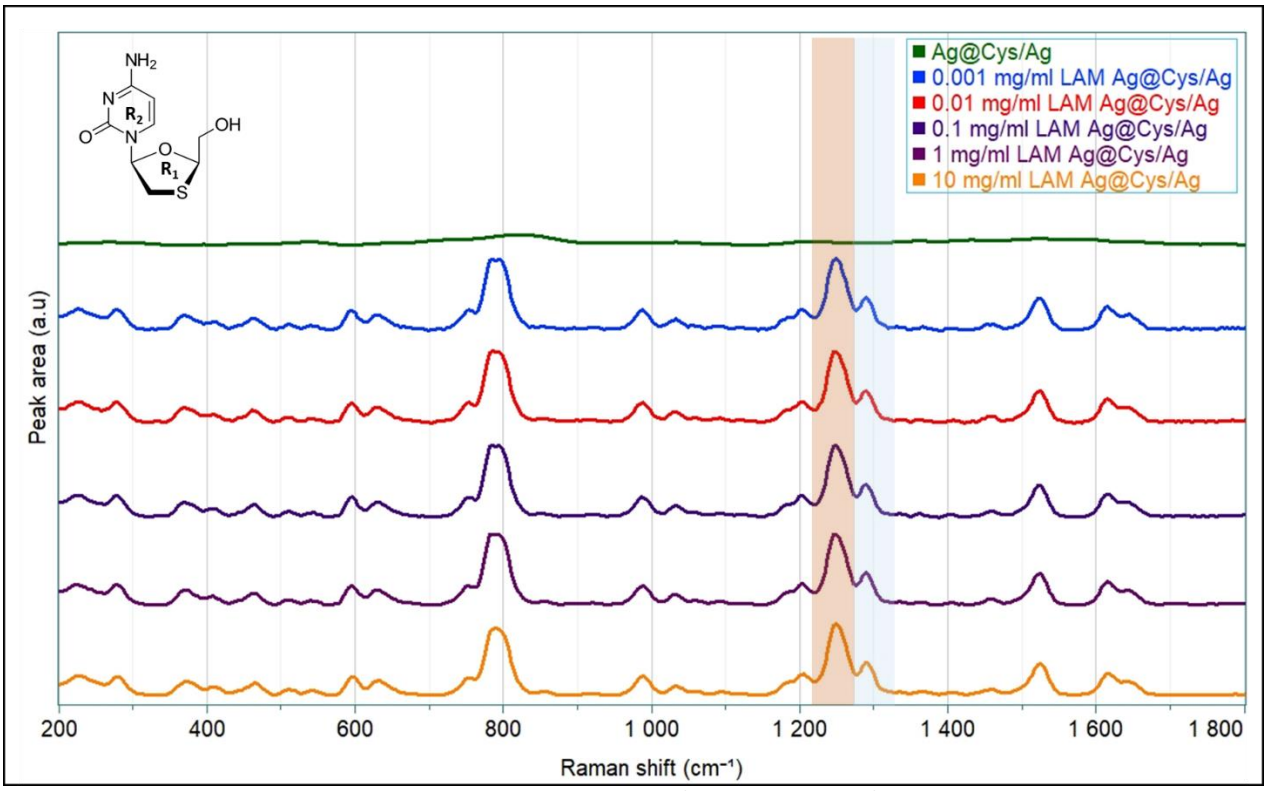

Figure 3.34:Raman spectral overlay of Lamivudine on Ag@Cys/Ag, 0.001-10 mg/ml. Acquired from 200-1800 cm-1. 532 nm, 12 mW laser power, 100 scans, 10 seconds per scan. Insert: LAM molecular structure.

The Raman spectral overlay in figure 3.34 above shows the response of LAM on Ag@Cys/Ag sensor. The amine bending mode was again detected in bending mode at 226 cm^{-1} which is closer to the powder value compared to gold. R1 thiol and hydroxyl groups were seen at 463 cm^{-1} twisting modes alongside the skeletal bands in 600 cm^{-1} also in twisting mode [58-59]. The doublet seen in figure 33 was absent in this sample group, instead a broad peak in the 800 cm^{-1} region was detected arising from the vibrational bands of the two rings in deformation mode. The C-O bond of R2 was again detected at 1032 cm^{-1}. A blueshift character is seen on the rest of the spectrum with R2 bands, C-N and the amine group appearing in bending mode in the 1200-1300 cm^{-1} region followed by the deformation of the amine group coupled with the imine stretching vibration at 1525 cm^{-1}. In addition, the amine group deformation reappeared again coupled with the carbon double bonds of the R1. This implies most of the vibration bands in this region were in a compressed state which indicates bond shortening of the molecule in response to the chemical sensor and laser photons [60]. Lastly, the stretching vibration of the carbonyl group was seen at 1640 cm^{-1} at the end of the spectral range.

Table 3.13:Raman bands of Lamivudine on glass, gold and silver sensors.

Glass	Au@Cys/Au	Ag@Cys/Ag	Reference (cm^{-1})	Assignment
284	222	226	227	ω(H-N-H)
466	463	463	462	τ(C_2-S), ρ (O-H)
599	595	595	593	τ skel
629	628	632	627	τ skel
753	781	790	780	δ Ring 2
799	855	855	796	δ (Ring 1),δ(Ring 2)
1034	1032	1032	1031	ν(C_2-O), ω(C_6-H),
1245	1246	1249	1244	ν(C_2-N), ρ (-NH_2),
1290	1292	1292	1287	ω(C_5-H_2), ρ(C_2-H)
1525	1525	1525	1523	δ(-NH_2),ν (C=N)
1615	1614	1615	1613	δ(-NH_2),ν (C=C)
1645	1641	1640	1643	ν (C=O)

ν=stretching, δ=rocking, ρ=bending (in plane),ω= bending (out of plane), τ= twisting, [33].

The peak areas of 1249 cm-1 and 1292 cm-1 for both gold and silver were used in the next section to perform statistical analysis on the bands in response to the samples in the spectral shown in this section.

3.4.4 Statistical evaluation of Lamivudine on glass and cysteamine-based chemical sensors.

In this section, linear regression on the data obtained from LAM on glass and cysteamine based chemical sensors was conducted similarly to the previous approach used on citrate sensors. The objective was to determine the R^2 and calibration sensitivity (slope) values of LAM across the various concentrations. Peaks 1244 cm^{-1} and 1287 cm^{-1} of R2 stretching and bending vibrations were used as the signals of interest.

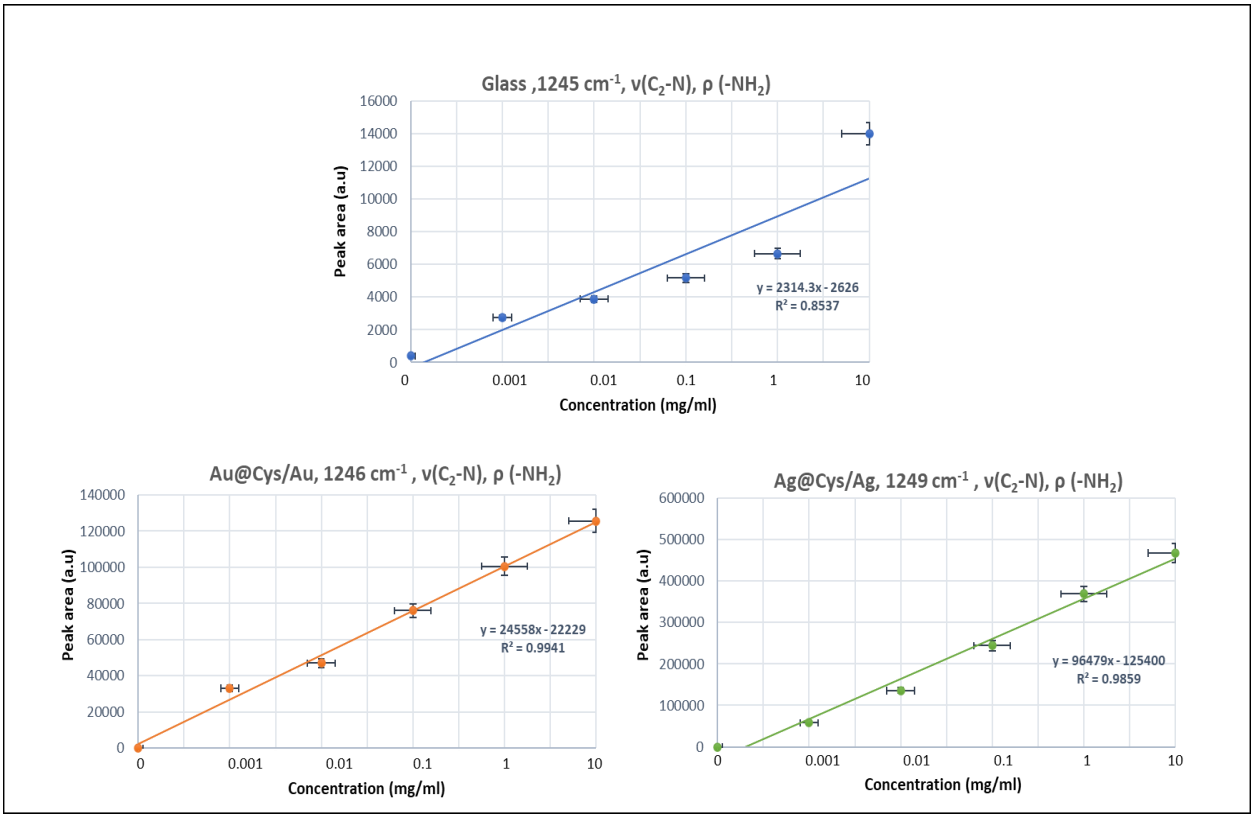

Figure 3.35:Linear regression analysis of Lamivudine using the ring 2 (R2) functionality (1244 cm-1). Peak area vs concentration on Glass (Top), Au@Cys/Au (left) and Ag@Cys/Ag (right).

Figure 3.35 above is a group of linear curves for LAM on glass, gold, and silver substrates. The data shows the glass graph seen at the top produced an R^2 value of 0.85 ($p<0.05$) and a slope of 2314. On the bottom left are the statistical values of the gold linear fit with an improved R^2 value of 0.99 ($p<0.01$) and a calibration sensitivity (slope) of 24558. These values can be attributed to the high solubility of LAM in water, which allowed controlled sample preparation that yielded highly satisfactory results. As seen in the previous experiment, the silver experiments yielded the highest sensitivity value of 96479 but could not match the gold R^2 and rather produced a value of 0.98. Also of interest, the peak shifts for this series of experiments show a blue shift from the powder value progressing as 1245 cm^{-1}, 1246 cm^{-1} and 1249 cm^{-1} for glass, gold, and silver respectively. It appears the sensitivity trend increases with the peak shift; this was also observed in the previous statistical work. Bond compression appearing as blue shifting could arise from the energy transfer to an analyte molecule in the hot spot of the SERS platform [60-61]. This signifies molecular interactions between the analyte and sensing platform, which is considered favorable. In this next section, a similar regression analysis was performed for the bending modes of R1 found in the 1300 cm^{-1}.

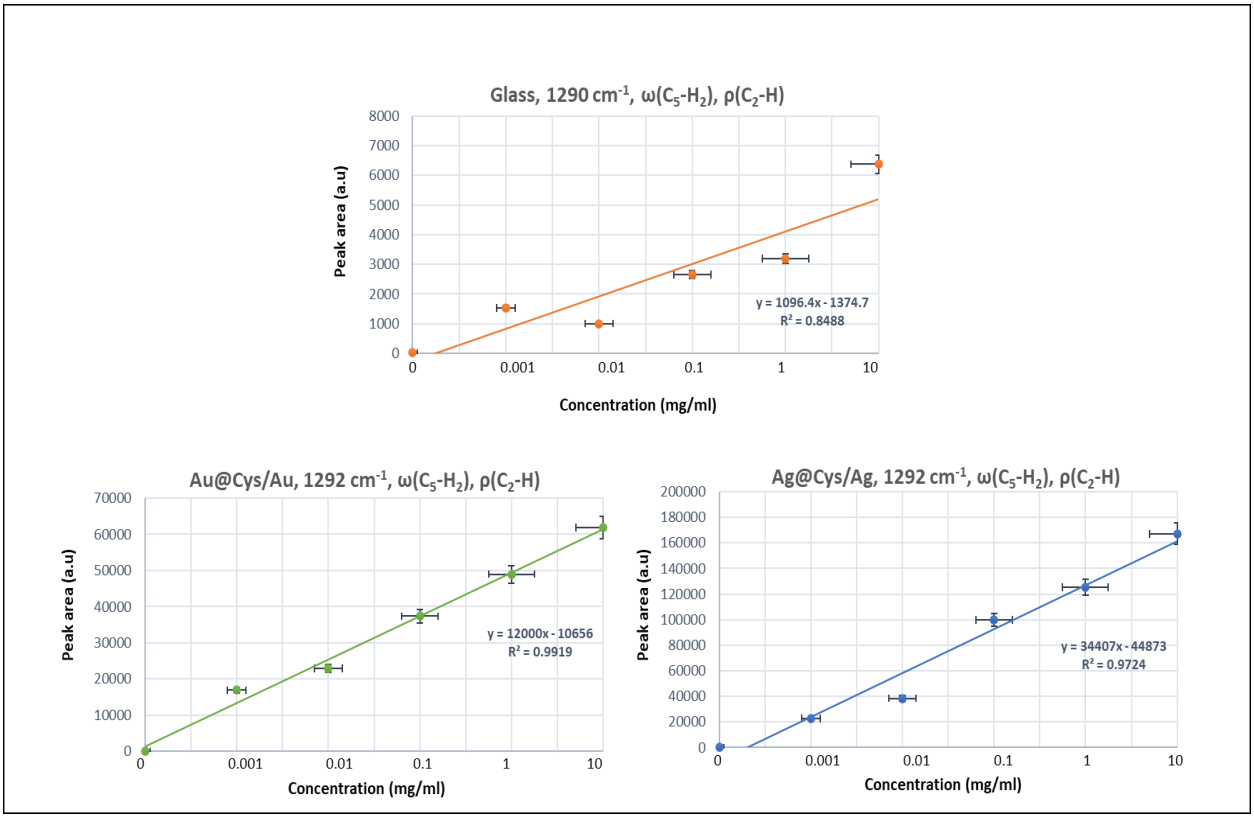

Figure 3.36:Linear regression analysis of Lamivudine using the ring 2 (R2) functionality (1287 cm-1). Peak area vs concentration on Glass (Top), Au@Cys/Au (left) and Ag@Cys/Ag (right).

The in-plane and out-of-plane bending of the R2 bonds was investigated on glass, gold, and silver substrates. Figure 36 above shows the linear regression of the LAM samples which were serially diluted. Beginning with the glass samples, the R^2 was a value of 0.84 ($p<0.05$) and a calibration sensitivity of 1096, which is the lowest in the series. Gold samples again produced an R^2 of 0.99 ($p<0.01$) with a corresponding calibration sensitivity of 12000. The silver counterpart resulted in an R^2 value of 0.97 ($p< 0.01$), while a much higher calibration sensitivity value of 34470 was realized. The peak shifting in this followed the same pattern as the 1244 cm^{-1} data however, the metal sensor had the same blue shift value. The results obtained from the two sets of experiments were used to calculate the analytical sensitivity and limit of detection for the chemical sensor and compared against thr glass. Table 14 below summarizes the values obtained from LAM study on cysteamine stabilized chemical sensors.

Table 3.14:Statistical values of LAM on glass, Au@Cys/Au and Ag@Cys/Ag.

Parameter	Glass	Au@Cys/Au	Ag@Cys/Ag
1245 cm^{-1}, $\nu(C_2\text{-}N)$, ρ ($\text{-}NH_2$)			
R^2	0.85	0.99	0.98
Calibration sensitivity (m)	2134	24558	96479
Analytical sensitivity (Y)	15.81	26.74	91.24
L.O.D (mg/ml)	0.79	0.0026	0.0004
RSD (%)	2.67	1.44	1.65
1290 cm^{-1}, $\omega(C_5\text{-}H_2)$, $\rho(C_2\text{-}H)$			
R^2	0.84	0.99	0.97
Calibration sensitivity (m)	1096	12000	34407
Analytical sensitivity (Y)	7.49	13.1	32.53
L.O.D (mg/ml)	1.67	0.005	0.0012
RSD (%)	5.94	2.92	1.39

Table 14 shows the parameters explored to assess the capabilities of the chemical sensor to enhance the signals of the ARV medication. Using equations from chapter 2, the slopes of the linear regressions were further investigated to determine the analytical sensitivity where the 1244 cm^{-1} sample group showed an increase in this parameter from glass to gold and silver with values 15.81, 26.74 and 91.24 respectively. The reason can be placed on the high calibration sensitivity and the relatively low standard deviation of the silver substrate compared to gold and glass. In the latter case, the background noise from the glass signal increased the standard deviation of the sample group which lowered the analytical sensitivity. The gold managed to produce a high calibration sensitivity and standard deviation. However, the silver sensor calibration sensitivity was still significantly higher and thus produced a higher analytical sensitivity. In terms of the limit of detection, the glass produced the highest value of 0.79 mg/ml followed by a 3-fold lower value of 0.0026 mg/ml and an even lower value for silver at 0.0004 mg/ml. These values are again attributed to the calibration sensitivity which has an inverse relationship with the limit of detection. For 1290 cm^{-1} data set, analytical sensitivities were lower than in the previous case with glass producing 7.49, gold 13.1 and silver at 32.53. This large change can be assigned to the lower calibration values for this vibrational mode, which is likely a result of the intermolecular force interactions with the chemical sensors. Nonetheless, the trend was determined to be consistent in both groups. The limit of detection also remains consistent with 1.67, 0.005 and 0.0012 mg/ml, respectively. This confirms that the high calibration sensitivities of the metallic sensors and the lower standard deviation values, which are affected by molecular interactions, greatly improve the detection efficiency of the chemical sensors compared to glass. The next section shows the SERS analysis of Dolutegravir on the three scaffolds for sensing applications.

3.4.5 Dolutegravir on cysteamine based chemical sensors.

Dolutegravir (DLG) samples as outlined in section 2.6 were analyzed using Raman spectroscopy and the vibration bands were compared across the glass, gold, and silver scaffolds. Because of the DLG dissolution challenge expressed in the citrate study, the samples were allowed to settle in the solution overnight to allow as much dissolution which may have affected the exact concentrations of the samples. However, Raman spectra were overlayed in figure 37 below and the samples were background corrected against the peaks found on the scaffold.

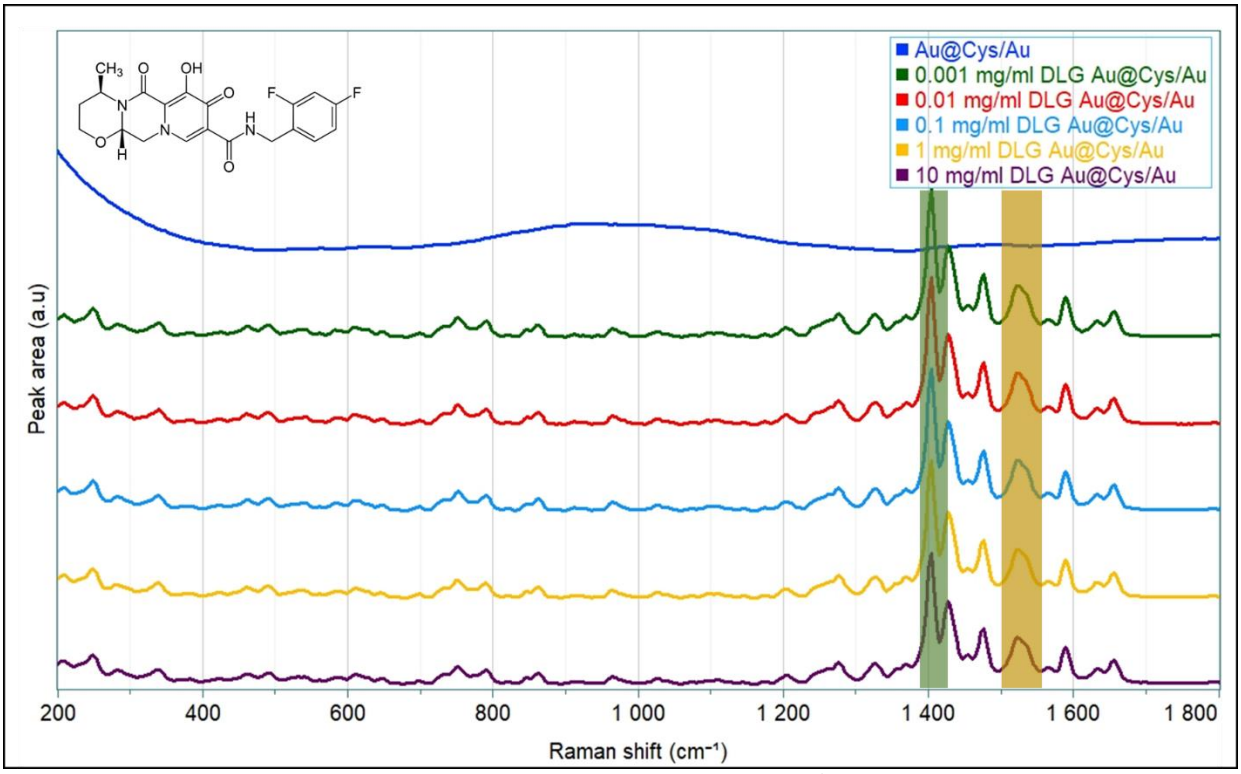

Figure 3.37: Raman spectral overlay of Dolutegravir on gold, 0.001-10 mg/ml. Acquired from 200-1800 cm-1. 532 nm, 12 mW laser power, 100 scans, 10 seconds per scan. Insert: DLG molecular structure.

The spectral data above shows the Raman bands obtained for DLG across a series of concentrations shown in the legend. In short, the amine group bending vibration was detected first at 248 cm^{-1} in range with the powder while the imine and amine bonds were seen in the 1200 and 1320 cm^{-1} with a blue shift seen towards the latter. Alkyl groups were found deformed at 1364 cm^{-1} with methyl groups adjacent at 1403 cm^{-1} both red-shifted compared to the powder sample. In the 1400 cm^{-1} region, a combination of the imine breathing vibration and the bending mode of the methyl groups was detected with a slight blue shift followed by a primary amine bond at 1522 cm^{-1}. Lastly, deformation of the amine bond was detected again at 1522 cm^{-1} followed by imine stretching at 1635 cm^{-1}-, both blue-shifted compared to the powder, this was also the case for the 1652 cm^{-1} deformation and stretching modes of the amine and carbon double bonds of benzene group. In the next section, the silver sensor was used to text DLG and compare Raman peaks for qualitative purposes.

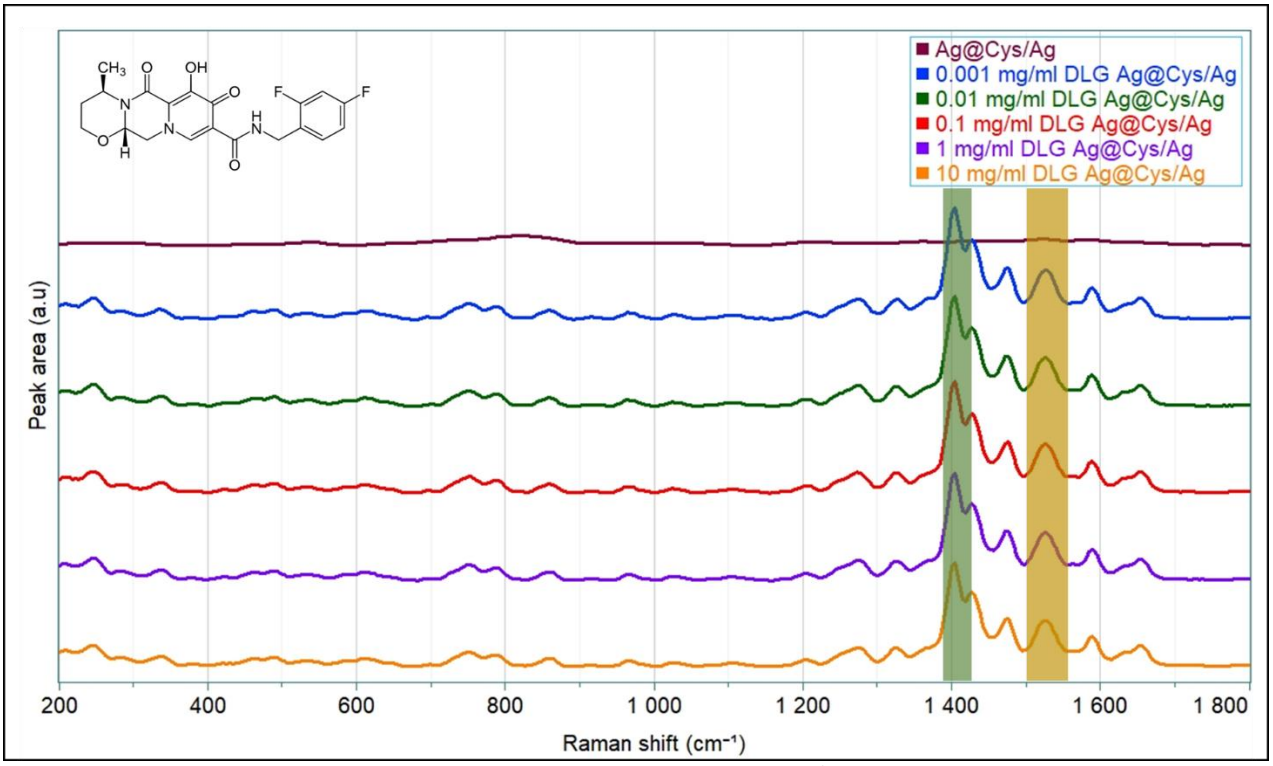

Figure 3.38:Raman spectral overlay of Dolutegravir on silver, 0.001-10 mg/ml. Acquired from 200-1800 cm-1. 532 nm, 12 mW laser power, 100 scans, 10 seconds per scan. Insert: DLG molecular structure.

A Raman spectral evaluation of the DLG on silver sensors was depicted as an overlay seen in figure 38 above where the vibration bands of the analyte across a series of concentrations is shown. The amine group seen in previous experiments was again detected at peak 244 cm^{-1} followed by the stretching modes of of the imine and amine groups at peak 1272 cm^{-1}, both appeared red-shifted which is the opposite of the observations made for glass and gold. A similar mode at 1328 cm^{-1} was detected, this time it was blue-shifted by 5 cm^{-1} similar to the gold sensor. Alkyl and methyl groups were seen in the 1400 cm^{-1} region in deformation mode both red-shifted to different degrees. In the middle of the spectral range, imine and methyl contributions were seen in deformation and bending vibration respectively at 1425 cm^{-1} followed by a blue-shifted amine group in deformation mode at 1477 cm^{-1}. In addition, the primary amine was again detected in a deformed mode at 1525 cm^{-1} while the amine bond reappeared 1582 cm^{-1}, closer to the powder value than the gold data. At the end of the spectra, The imine bond was observed stretching at 1629 cm^{-1} while a combination of deformed amine groups and aromatic carbon bonds in stretching mode arose at 1655 cm^{-1}. Table 15 below is a summary of the Raman bands obtained in this study for DLG.

Table 3.15:Raman bands of Dolutegravir on glass, gold and silver sensors.

Glass	Au@Cys/Au	Ag@Cys/Ag	Reference (cm^{-1})	Assignment
247	242	244	247	ω(H-N-H)
1276	1273	1272	1275	ν (C=N), ν(C-N)
1314	1327	1328	1322	ν (C=N), ν(C-N)
1353	1364	1360	1370	δ(C-H)
1403	1402	1400	1408	$\delta(CH_3)$
1425	1428	1425	1425	δ(N=CH), $\omega(CH_3)$
1456	1476	1477	1471	$\delta(-NH_2)$
1516	1522	1525	1520	δ(C-N-H)
1580	1588	1582	1581	$\delta(-NH_2)$
1655	1635	1629	1631	ν(C=N)
1647	1652	1655	1655	$\delta(-NH_2)$,ν (C=C)

ν=stretching, δ=rocking, ρ=bending (in plane),ω= bending (out of plane), τ= twisting, [33].

In the next section, statistical evaluations of the 1400 cm^{-1} and 1520 cm^{-1} bands are conducted similarly to the DLG experiments on the citrate based chemical sensors.

3.4.6 Statistical analysis of Dolutegravir on glass, gold and silver chemical sensors.

Linear curves were constructed from peak area values vs concentration of DLG samples for glass, gold and silver substrates and compared. The purpose was to derive the R^2 and calibration sensitivity values for further calculations. Figure 3.39 below is a comparison of the linear curves for the DLG peak 1400 cm^{-1} which is assigned to the methyl group.

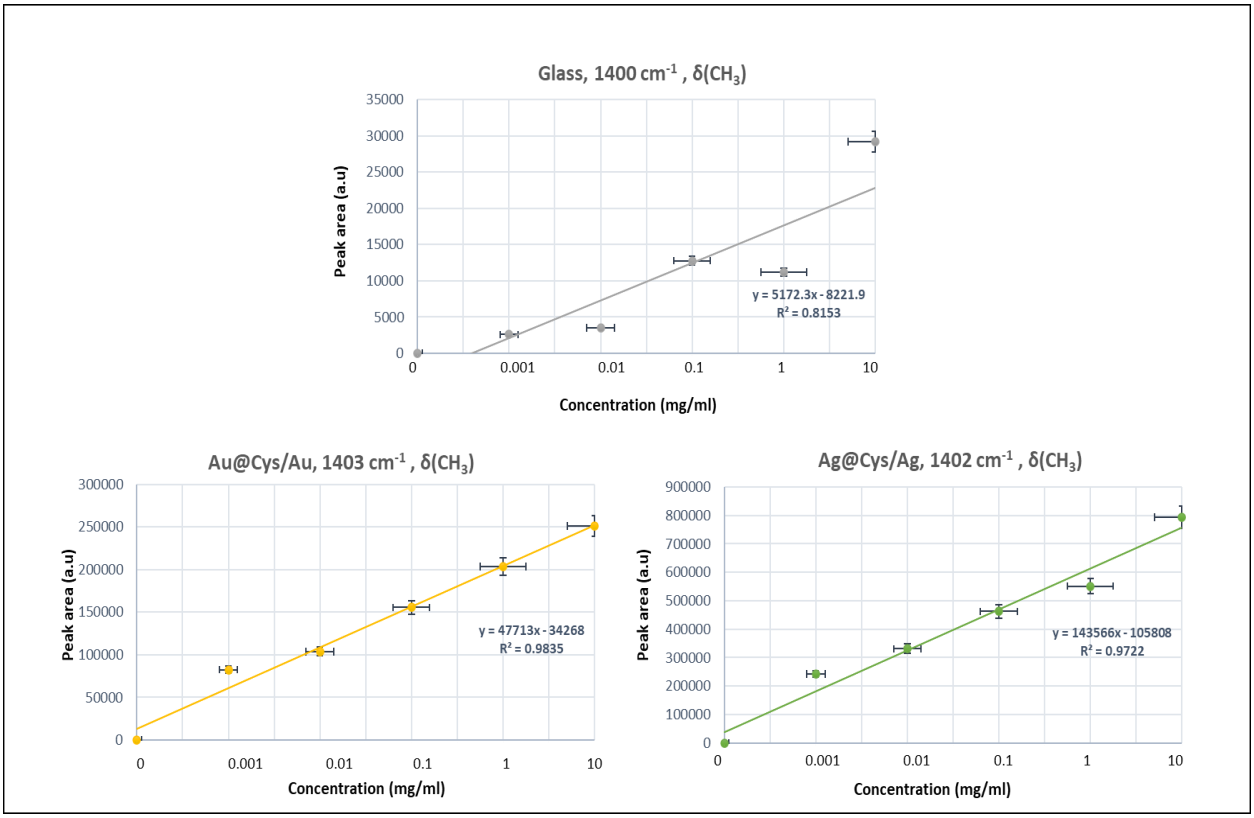

Figure 3.39:Linear regression analysis of Dolutegravir using the methyl group functionality (1408 cm-1). Peak area vs concentration on Glass (Top), Au@Cys/Au (left) and Ag@Cys/Ag (right).

Figure 3.39 above shows the linear plots of the methyl group across the three substrates where the R^2 value of glass seen on the top, produced the lowest value of 0.81 ($p<0.10$) and a slope or calibration sensitivity value of 5172. The gold sample group produced a better R^2 value of 0.98 ($p< 0.01$) and a slope of 47713. The data for silver was 0.97 ($p<0.05$) and 143566 for the R^2 and calibration sensitivities. This trend of data is like citrate experiments where the glass produced the lowest outputs while gold and silver competed for the R^2, with the latter dominating the calibration sensitivity. This outcome could be a consequence of the adsorption and chemical interactions, specifically hydrogen bonding between the sensors and the analyte because the sensors seem to outperform the plain glass surface [62]. The values explained above were used to determine the analytical sensitivity and limit of detection at the end of this section. In the next figure, a comparison of the 1520 cm^{-1} vibration mode is displayed with the corresponding parameter values.

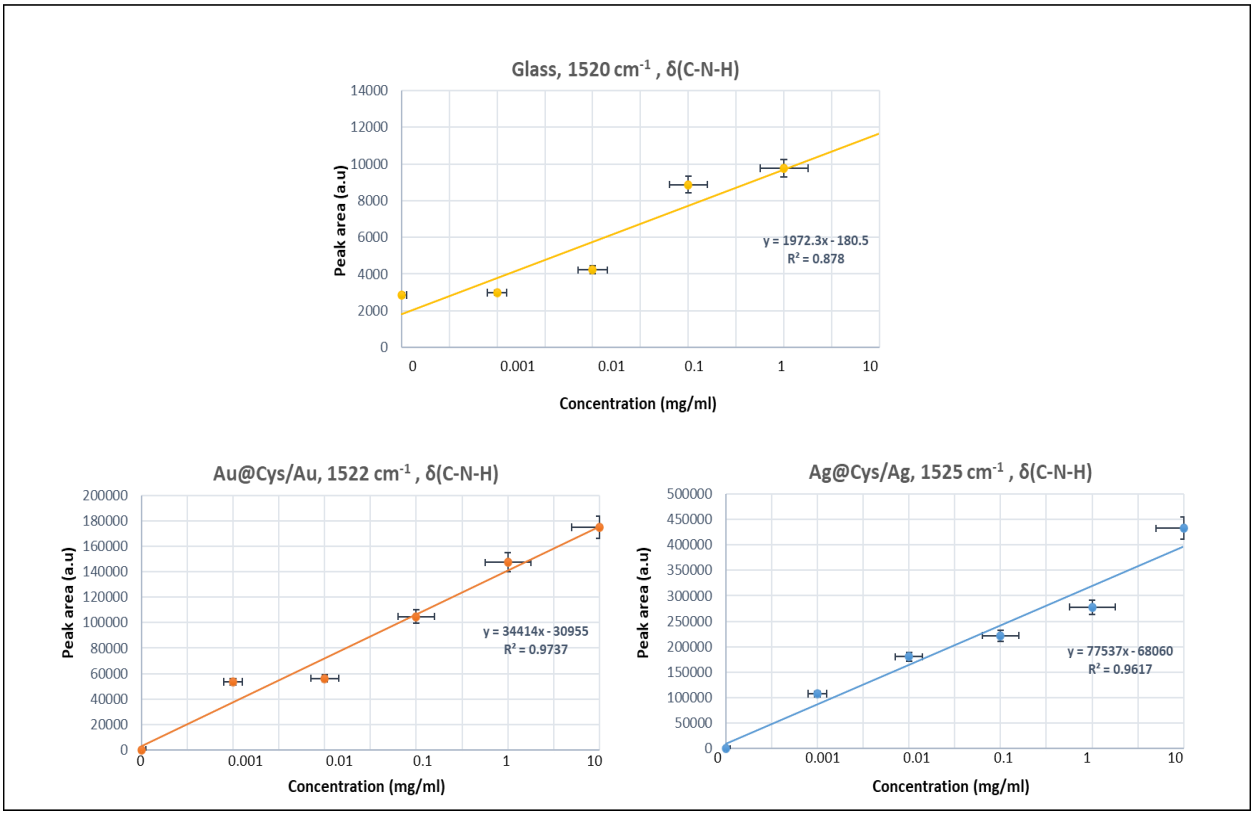

Figure 3.40: Linear regression analysis of Dolutegravir using the primary amine functionality (1520 cm-1). Peak area vs concentration on Glass (Top), Au@Cit/Au (left) and Ag@Cit/Ag (right).

The data inf figure 3.40 above shows the differences in R^2 and calibration sensitivities for the three sample groups for the primary amine functional group. The linear plot for glass shows a R^2 value of 0.87 ($p < 0.10$) and a calibration sensitivity of 1972. The Au@Cys/Au sensor produced a R^2 value 0.97 ($p< 0.01$) and a 34414-slope value while the silver counterpart resulted in 0.96 ($p< 0.01$) and 77537 for both parameters respectively. By observation, the trend seen with the methyl functional group above is also the case for the primary amine where the gold has a better linear response than silver while the latter gives higher calibration sensitivity. These values were processed further to determine the analytical sensitivity and limit of detection to further explore the characteristics for the sensor towards the analyte DLG. The data of this group is summarized in Table 16 below.

Table 3.16: Statistical values of DLG on glass, Au@Cys/Au and Ag@Cys/Ag.

Parameter	Glass	Au@Cit/Au	Ag@Cit/Ag
1400 cm^{-1} , $\delta(CH_3)$			
R^2	0.84	0.98	0.97
Calibration sensitivity (m)	5172	47713	143566
Analytical sensitivity (Y)	77.52	63.11	128
L.O.D (mg/ml)	0.005	0.001	0.0003
RSD (%)	0.67	0.56	0.28
1520 cm^{-1} , δ(C-N-H)			
R^2	0.87	0.97	0.96
Calibration sensitivity (m)	1972	34414	77537
Analytical sensitivity (Y)	29.56	45.5	69.3
L.O.D (mg/ml)	0.01	0.001	0.0005
RSD (%)	1.39	0.84	0.54

From the table above, data from calculations using the peak area of the methyl group at 1400 cm^{-1} and the primary amine was found at 1520 cm^{-1}. In the former case, the trend in analytical sensitivity was lowest from gold at 63.11 to glass at 77.52 and silver with the highest value of 128. This is different from the citrate experiment where the gold was higher than the glass, however, considering the linearity of glass, this value is not reliable because the slope of the curve greatly influences the sensitivity result when the standard deviation is comparable. Furthermore, the hydrophobicity issue of DLG in water can play a role in this trend if undissolved particles were detected by the Raman system. The limit of detection for methyl groups in deformation mode resulted in glass producing the highest value of 0.005 mg/ml while gold and silver sensor were 0.001 and 0.0003 mg/ml respectively. Although this trend is like the citrate study, the low LOD for glass is unreliable in comparison possibly due to the high slope value which was not the case in the former experiments. The metal sensors show a significantly higher analytical sensitivity as a result of the slope value coupled with good linearity. Furthermore, their LOD values are consistent with the range found in the citrate group. This implies molecular interactions between the sensor and analyte played a role in the improved response. For the primary amine, analytical sensitivity was highest on silver at 69.3 followed by gold 45.5 and glass at 29.56 respectively. The limit of detection for this functional group shows a familiar trend where the glass has a high value of 0.01 while gold and silver produce significantly lower values of 0.001 and 0.0005 mg/ml, respectively. These values can be trusted because they are consistent with the citrate trend, and the linearity is in an acceptable range. In the next section, a selectivity and signal enhancement assessment of the peaks of interest was conducted to correlate the sensitivity and detection data seen above, with the signal response and molecular properties of the sensor and analyte.

References

1. Haiss W, Thanh NTK, Aveyard J, Fernig DG. Determination of size and concentration of gold nanoparticles from UV-Vis spectra. Anal Chem. 2007 Jun 1;79(11):4215–21.

2. Jouyban A, Rahimpour E. Sensors/nanosensors based on upconversion materials for the determination of pharmaceuticals and biomolecules: An overview. Talanta [Internet]. 2020;220(July):121383. Available from: https://doi.org/10.1016/j.talanta.2020.121383

3. Dipak Kumar Bhui, Harekrishna Bar, Priyanka Sarkar, Gobinda Prasad Sahoo, Sankar Prasad De, Ajay Misra,Synthesis and UV–vis spectroscopic study of silver nanoparticles in aqueous SDS solution,Journal of Molecular Liquids,Volume 145, Issue 1,2009,Pages 33-37,ISSN 0167-7322,https://doi.org/10.1016/j.molliq.2008.11.014.

4. Das R, Nath SS, Chakdar D, Gope G, Bhattacharjee R. Synthesis of silver nanoparticles and their optical properties. J Exp Nanosci. 2010;5(4):357–62.

5. H Witjes, M van den Brink, W.J Melssen, L.M.C Buydens,Automatic correction of peak shifts in Raman spectra before PLS regression,Chemometrics and Intelligent Laboratory Systems,Volume 52, Issue 1,2000,Pages 105-116,ISSN01697439,https://doi.org/10.1016/S0169-7439(00)00085-X.

6. Singh P. Surface plasmon resonance (SPR) based binding studies of refolded single chain antibody fragments. Biochem Biophys Reports [Internet]. 2018;14(April):83–8. Available from: https://doi.org/10.1016/j.bbrep.2018.04.005

7. Amendola, V.; Pilot, R.; Frasconi, M.; Maragò, O.M.; Iatì, M.A. Surface plasmon resonance in gold nanoparticles: A review. J. Phys. Condens. Matter 2017, 29, 203002.

8. Sun, Z.; Zhao, B.; Lombardi, J.R. ZnO nanoparticle size-dependent excitation of surface Raman signal from adsorbed molecules: Observation of a charge-transfer resonance. Appl. Phys. Lett. 2007, 91, 221106

9. Zhang, L.; Gong, X.; Bao, Y.; Zhao, Y.; Xi, M.; Jiang, C.; Fong, H. Electrospun nanofibrous membranes surface-decorated with silver nanoparticles as flexible and active/sensitive substrates for surface-enhanced Raman scattering. Langmuir 2012, 28, 14433–14440

10. Nirala, N. R., & Shtenberg, G. (2019). Gold Nanoparticle Size-Dependent Enhanced Chemiluminescence for Ultra-Sensitive Haptoglobin Biomarker Detection. Biomolecules, 9(8), 372. https://doi.org/10.3390/biom9080372

11. He RX, Liang R, Peng P, Norman Zhou Y. Effect of the size of silver nanoparticles on SERS signal enhancement. J Nanoparticle Res. 2017;19(8):0–10.

12. Mäntele W, Deniz E. UV–VIS absorption spectroscopy: Lambert-Beer reloaded. Spectrochim Acta Part A Mol Biomol Spectrosc. 2017 Feb 15;173:965–8.

13. Oshina I, Spigulis J. Beer-Lambert law for optical tissue diagnostics: current state of the art and the main limitations. J Biomed Opt. 2021;26(10):100901. doi:10.1117/1.JBO.26.10.100901

14. Shao Y, Yin GZ, Ren X, Zhang X, Wang J, Guo K, et al. Engineering π-π Interactions for enhanced photoluminescent properties: Unique discrete dimeric packing of perylene diimides. RSC Adv [Internet]. 2017;7(11):6530–7. Available from: http://dx.doi.org/10.1039/C6RA28147H

15. M. Kerker, O. Siiman, L. A. Bumm, and D.-S. Wang, "Surface enhanced Raman scattering (SERS) of citrate ion adsorbed on colloidal silver," (1980).Appl. Opt. 19, 3253-3255

16. P. Tarakeshwar, S. Manogaran,Ground state vibrations of citric acid and the citrate trianion—an ab initio study,Spectrochimica Acta Part A: Molecular Spectroscopy,Volume 50, Issue 14,1994,Pages 2327-2343,ISSN 0584-8539,https://doi.org/10.1016/0584-8539(94)E0017-5.

17. Huang Z, Chen X, Li Y, Chen J, Lin J, Wang J, et al. Quantitative determination of citric acid in seminal plasma by using raman spectroscopy. Appl Spectrosc. 2013;67(7):757–60.

18. Kobayashi, H., Ema, K. Raman Spectra of SiO2 Fibers at High Tensile Strain. In: Devine, R.A.B. (eds) The Physics and Technology of Amorphous SiO2 . (1988). Springer, Boston, MA. https://doi.org/10.1007/978-1-4613-1031-0_7

19. Hoang NN, Pham DHY, Nguyen TN. Strain-dependent structure and Raman behaviours in the heavy-ion irradiated manganite at extreme low dose. Sci Rep [Internet]. 2019;9(1):1–10. Available from: http://dx.doi.org/10.1038/s41598-019-55638-1

20.. Pandoli OG, Neto RJG, Oliveira NR, Fingolo AC, Corrêa CC, Ghavami K, et al. Ultra-highly conductive hollow channels guided by a bamboo bio-template for electric and electrochemical devices. J Mater Chem A. 2020;8(7):4030–9.

21. Zhang Y, Wang F, Yin H, Hong M. Nonuniform Distribution of Capping Ligands Promoting Aggregation of Silver Nanoparticles for Use as a Substrate for SERS. Adv Nanoparticles. 2013;02(02):104–11.

22. Aldosari FMM. Characterization of Labeled Gold Nanoparticles for Surface-Enhanced Raman Scattering. Molecules. 2022;27(3):892. Published 2022 Jan 28. doi:10.3390/molecules27030892

23. Langer J, Jimenez de Aberasturi D, Aizpurua J, et al. Present and Future of Surface-Enhanced Raman Scattering. ACS Nano. 2020;14(1):28-117. doi:10.1021/acsnano.9b04224

24. Kudelski A, Hill W. Raman Study on the Structure of Cysteamine Monolayers on Silver. 1999; Available from: https://pubs.acs.org/sharingguidelines

25. Ramkumaar GR, Srinivasan S, Bhoopathy TJ, Gunasekaran S, Prameena B. Vibrational spectroscopic studies on 2'-3'-didehydro-2'- 3'-dideoxythymidine using density functional theory method. J Mol Struct. 2014;1059(1):185–92.

26. Chuchuen O, Henderson MH, Sykes C, Kim MS, Kashuba ADM. Quantitative Analysis of Microbicide Concentrations in Fluids, Gels and Tissues Using Confocal Raman Spectroscopy. PLoS One [Internet]. 2013;8(12):85124. Available from: www.plosone.org

27. Ichimura T, Watanabe H, Morita Y, Verma P, Kawata S, Inouye Y. Temporal fluctuation of tip-enhanced raman spectra of adenine molecules. J Phys Chem C. 2007;111(26):9460–4.

28. Dolgov L, Pidhirnyi D, Dovbeshko G, Lebedieva T, Kiisk V, Heinsalu S, et al. Graphene-Enhanced Raman Scattering from the Adenine Molecules. Nanoscale Res Lett [Internet]. 2016;11(1):1–6. Available from: http://dx.doi.org/10.1186/s11671-016-1418-5

29. Guzmán C, Del Angel G, Gómez R, Galindo F, Zanella R, Torres G, et al. Gold particle size determination on Au/TiO2-CeO2 catalysts by means of carbon monoxide, hydrogen chemisorption and transmission electron microscopy. J Nano Res. 2009;5(1):13–23.

30. Y. Umebayashi, K. Matsumoto, M. Watanabe, S. Ishiguro,Raman spectroscopic study on the solvation steric effect of the manganese(II) ion in solvent mixtures of N,N-dimethylformamide and 1,1,3,3-tetramethylurea,Journal of Molecular Liquids,Volumes 103–104,2003,Pages 331-337,ISSN 0167-7322,https://doi.org/10.1016/S0167-7322(02)00151-4.

31. Du Y, Zhang H, Xue J, Tang W, Fang H, Zhang Q, Li Y, Hong Z. Vibrational spectroscopic study of polymorphism and polymorphic transformation of the anti-viral drug lamivudine. Spectrochim Acta A Mol Biomol Spectrosc 2015;137:1158-63. 10.1016/j.saa.2014.08.128

32. Izo J, Jesus S De, Löbenberg R, Bou-chacra NA. Raman Spectroscopy for Quantitative Analysis in the Pharmaceutical Industry. 2020;24–46.

33. Jerry Hong, Shivang Bhaskar, Joseph T. Golab, James A. Kaduk,Structures of disodium hydrogen citrate mono-hydrate, Na2HC6H5O7(H2O), and di-ammonium sodium citrate, (NH4)2NaC6H5O7, from powder diffraction data,Acta Crystallographica Section E Crystallographic Communications,Volume 76, Part 10,2020,Pages 1572-1578,ISSN 2056-9890, https://doi.org/10.1107/S2056989020011895.

34. Byres M, Cox PJ, Kay G, Nixon E. Supramolecular structures of six adenine-carboxylic acid complexes. CrystEngComm. 2009;11(1):135–42.

35. Mateusz Z. Brela, Oskar Klimas, Marek Boczar, Takahito Nakajima, Marek J. Wójcik,A comparison of the hydrogen bond interaction dynamics in the adenine and thymine crystals: BOMD and spectroscopic study,Spectrochimica Acta Part A: Molecular and Biomolecular Spectroscopy,Volume 237,2020,118398,ISSN 1386-1425, https://doi.org/10.1016/j.saa.2020.118398.

36. Cheng L. Role of Hydrogen Bonding in the Formation of Adenine Chains on Cu(110) Surfaces. Materials (Basel). 2016;9(12):1016. Published 2016 Dec 16. doi:10.3390/ma9121016

37.Otsuka Y, Makino K, Takahashi H. Experimental study on the raman spectra of imine emulsification with chemometrics. J Oleo Sci. 2021;70(8):1109–14.

38. P.Waage Jensen, L.Bonne Jørgensen,Resonance raman spectra of some iron(II) imine complexes,Journal of Molecular Structure,Volume 79,1982,Pages 87-92,ISSN 0022-2860,https://doi.org/10.1016/0022-2860(82)85035-7.

39. Ngo, D., Liu, H., Chen, Z. et al. Hydrogen bonding interactions of H2O and SiOH on a boroaluminosilicate glass corroded in aqueous solution. npj Mater Degrad 4, 1 (2020). https://doi.org/10.1038/s41529-019-0105-2

40. Srikanth A, Abrams CF. Effect of molecular packing and hydrogen bonding on the properties of epoxy-amido amine systems. Comput Mater Sci. 2019;169:1–16.

41. Wang R, Pellerin C, Lebel O. Role of hydrogen bonding in the formation of glasses by small molecules: A triazine case study. J Mater Chem. 2009;19(18):2747–53.

42. Richard D. Bowen, Howell G.M. Edwards, Tereza Varnali,Influence of a methyl substituent on the Raman spectrum of but-3-enyl methyl ether, Spectrochimica Acta Part A: Molecular and Biomolecular Spectroscopy,Volume 93,2012,Pages 26-32,ISSN 1386-1425,https://doi.org/10.1016/j.saa.2012.02.059.

43. Zhang X, Zhou Q, Huang Y, Li Z, Zhang Z. Contrastive analysis of the Raman spectra of polychlorinated benzene: Hexachlorobenzene and benzene. Sensors. 2011;11(12):11510–5.

44. M. Ito, T. Shigeoka, Raman spectra of benzene and benzene-d6 crystals, Spectrochimica Acta,Volume 22, Issue 6,1966,Pages 1029-1044,ISSN 0371-1951,https://doi.org/10.1016/0371-1951(66)80192-3.

45. Sjöberg B, Foley S, Cardey B, Enescu M. An experimental and theoretical study of the amino acid side chain Raman bands in proteins. Spectrochim Acta - Part A Mol Biomol Spectrosc. 2014;128:300–11.

46. Weidner T, Breen NF, Drobny GP, Castner DG. Amide or amine: determining the origin of the 3300 cm(-1) NH mode in protein SFG spectra using 15N isotope labels. J Phys Chem B. 2009;113(47):15423-15426. doi:10.1021/jp908773.

47. Rolfe, S.M., Patel, M.R., Gilmour, I. et al. Defining Multiple Characteristic Raman Bands of α-Amino Acids as Biomarkers for Planetary Missions Using a Statistical Method. Orig Life Evol Biosph 46, 323–346 (2016). https://doi.org/10.1007/s11084-015-9477-7

48. Lian, S., Gao, X., Song, C., Li, H., & Lin, J. (2021). The characteristics of Raman spectroscopy of fenbendazole-gold nanoparticles based on the chemical adsorption effect. Spectrochimica acta. Part A, Molecular and biomolecular spectroscopy, 257, 119799. https://doi.org/10.1016/j.saa.2021.119799

49. R. Wang, X.R. Shen, M. Zhang, R. Devasenathipathy, R. Pang, D.Y. Wu, J.D.Zhang, J. Ulstrup, Z.Q. Tian, Adsorption, chemical enhancement, and low-lyingexcited states of p-methylbenzenethiol on silver and gold nanoparticlesurfaces: a surface-enhanced Raman spectroscopy and density functionaltheory study, J. Phys. Chem. C 123 (2019) 23026–23036.

50. Geoffrey I.N. Waterhouse, Graham A. Bowmaker, James B. MetsonOxygen chemisorption on an electrolytic silver catalyst: a combined TPD and Raman spectroscopic study,Applied Surface Science,Volume 214, Issues 1–4,2003,Pages 36-51,ISSN 0169-4332,https://doi.org/10.1016/S0169-4332(03)00350-7

51. Møller, K. H., Kjaersgaard, A., Hansen, A. S., Du, L., & Kjaergaard, H. G.. Hybridization of Nitrogen Determines Hydrogen-Bond Acceptor Strength: Gas-Phase Comparison of Redshifts and Equilibrium Constants. The journal of physical chemistry. (2018) 122(15), 3899–3908. https://doi.org/10.1021/acs.jpca.8b00541

52. Nobeli, I., Price, S.L., Lommerse, J.P.M. and Taylor, R. Hydrogen bonding properties of oxygen and nitrogen acceptors in aromatic heterocycles. J. Comput. Chem.(1997), 18: 2060-2074. https://doi.org/10.1002/(SICI)1096-987X(199712)18:16<2060::AID-JCC10>3.0.CO;2-S

53. Asiala SM, Schultz ZD. Characterization of hotspots in a highly enhancing SERS substrate. Analyst. 2011;136(21):4472-4479. doi:10.1039/c1an15432j

54. Pilot, R., Signorini, R., Durante, C., Orian, L., Bhamidipati, M., & Fabris, L. (2019). A Review on Surface-Enhanced Raman Scattering. Biosensors, 9(2), 57. https://doi.org/10.3390/bios9020057

55. Gobinda Pradhan, Ashwini Kumar Sharma,Anomalous Raman and photoluminescence blue shift in mono- and a few layered pulsed laser deposited MoS2 thin films,Materials Research Bulletin,Volume 102,2018,Pages 406-411,ISSN 0025-5408,https://doi.org/10.1016/j.materresbull.2018.03.001

56. Zheng X, Chen W, Wang G, Yu Y, Qin S, Fang J, et al. The Raman redshift of graphene impacted by gold nanoparticles. AIP Adv. 2015;5(5):1–8.

57. Le Parc R, Ranieri V, Haines J, Cambon M, Cambon O, Levelut C, et al. In situ high pressure and high temperature Raman studies of (1-x)SiO 2xGeO2 glasses. J Phys Condens Matter. 2009;21(37).

58. Nyamekye, CKA, Weibel, SC, Smith, EA. Directional Raman scattering spectra of metal–sulfur bonds at smooth gold and silver substrates. J Raman Spectrosc. 2021; 52: 1246– 1255. https://doi.org/10.1002/jrs.6124

59. Madzharova F, Heiner Z, Kneipp J. Surface-Enhanced Hyper Raman Spectra of Aromatic Thiols on Gold and Silver Nanoparticles. J Phys Chem C Nanomater Interfaces. 2020;124(11):6233-6241. doi:10.1021/acs.jpcc.0c00294

60. R. Voggu, B. Das, C. S. Rout, and C. N. R. Rao, “Effects of charge transfer interaction of graphene with electron donor and acceptor molecules examined using Raman spectroscopy and cognate techniques,” J. Phys.: Condens. Matter. 20, 472204 (2008).

61. Kim J, Jang Y, Kim NJ, Kim H, Yi GC, Shin Y, et al. Study of Chemical Enhancement Mechanism in Non-plasmonic Surface-enhanced Raman spectroscopy (SERS). Front Chem. 2019;7(August):1–7.

62. Liu S, Zhang M, Huang B, Wu N, Ouyang S. Raman Spectroscopy for the Competition of Hydrogen Bonds in Ternary (H2O-THF-DMSO) Aqueous Solutions. Molecules. 2019;24(20):3666. Published 2019 Oct 11. doi:10.3390/molecules24203666

4. Discussion

The previous chapter focused on reporting the results of the experiments undertaken in this study, with a focus on describing the spectral and statistical data post interpretation. In this chapter, a discussion on the morphology and surface properties of the sensors is opened using results from the microscopy and spectroscopy experiments to characterize the platforms. Secondly the physics and chemistry principles that explain the Raman shifts and chemical sensor's parameters are discussed with the aim of determining the behavior of the sensors in response to the analytes. Furthermore, topics such as intermolecular forces, stereochemistry, bonding mechanisms, and peak shifting are related to chemisorption and physisorption to explain the statistical values observed in the results. Lastly, the data obtained is then compared to other methods of detection to give relevance of this study against already existing techniques.

4.1 Surface coating, morphology, and characterization of the chemical sensors.

The sensor fabrication process began with coating clean glass slides of silica functionality with gold and silver nano-thin layers. It was deemed necessary to do so to remove the interference of glass Raman bands which would affect the signal arising from the analytes [1-2]. Physical vapor deposition was the technique chosen for the first coating process because it provided the advantages of pristine coating of nano-thin films that can be controlled for reproducibility [3-5]. The results from the PVD experiments showed successful coating of gold and silver on the glass slides observed by the images provided in the supplementary section. Secondly, energy-dispersive X-ray spectroscopy (EDS) experiments were conducted as an additional confirmation of gold and silver atoms on the coated surfaces as supplementary data (S1 and S2) [6].

In separate experiments, MNPs of gold and silver stabilized with citrate (Au@Cit, Ag@Cit) and others crosslinked with cysteamine (Au@Cys, Ag@Cys) were synthesized using chemical reduction method. The nanoparticles were evaluated using UV-Vis and TEM for the purpose of confirming their presence by absorption and determining their morphology and size distribution respectively. From the results in 3.1, absorbance bands characteristic of gold and silver were detected for both crosslinkers, this was taken as confirmation [7-8]. Furthermore, silver produced more intense bands than gold even though a lower concentration of the silver starting material was used in the synthesis process. Images from the TEM experiments showed the nanoparticles in spherical and oval shapes, while calculations of particle sizes showed that silver nanoparticles yield a larger particle size distribution than gold for both crosslinkers. A conclusion can be drawn from the UV-Vis and TEM findings that silver was produced in relatively higher concentrations than gold nanoparticles as supported by the Beer Lambart law and the size distribution of the nanoparticles, whose values increase with sample concentration [9-10].

After the characterization of the MNPs, the slides coated by PVD were exposed to nanoparticle solutions of gold and silver for each metal respectively, where adsorption of the molecules onto the metallic surface took place by self-assembly overnight. Thereafter, Raman microscopy experiments were undertaken as explained in section 3.2, where the surface morphology before

and after self-assembly was reported. The images showed a clear change in surface color, with a layer of coating clearly visible for the slides that were exposed to the nanoparticle solutions. In the case of gold slides, an increasing reflection from each image was observed as the layer thickness increased for both crosslinkers (fig 3.4 and 3.9) whereas a dimer pattern was seen for silver samples of similar thickness (fig 3.6 and 3.11). This can be attributed to the difference in response to white light by the two metals arising from their unique optical properties [11-12]. Nonetheless, the differences between the plain metal slides and those coated with the nanoparticles were efficient to confirming adsorption by optical visualization.

Raman spectroscopy analysis of the nanoparticle coated slides was performed to evaluate the molecular properties of the chemical sensors. The results for citrate functionalized sensors in figures 3.5 and 3.7 for gold and silver respectively are reported first. The spectral data showed narrow peaks from gold compared to silver, with the latter containing a broad profile across the three samples of different layer thicknesses. In Raman terms, a broader peak profile implies the responding functional group is undergoing strain due to bond expansion [13]. For example, the stretching vibration mode of the carboxylate ion (1429 cm^{-1}) appears broader and red-shifted on the silver (1425 cm^{-1}) while on gold, the same mode is narrow with a blue-shift value of 1444 cm^{-1}. This means the functional group was compressed on gold, and on silver, it was detected expanding its bond. This observation was seen again in the 800-900 cm^{-1} region using the alpha carbon bond of the carboxylate group where the gold sample group blue-shifted as the bond compressed while the broader peaks of silver correspond to the bond expansion confirmed by the red shift below the powder sample. These trends indicate that the metal sensors exert intermolecular forces on each other in the hotspots for nanoparticles in proximity, causing detectable changes in their Raman shifts [14]. A peak area assessment of the vibrations in the 800-900 cm^{-1} and 1400-1500 cm^{-1} regions was done in section 3.1.1 and the trends showed the most intense response from the silver sample group compared to the gold. This observation can be explained by considering the data from UV-Vis and TEM which show a higher concentration of nanoparticles for silver as well as the particle size consideration. At this point, it was concluded that the principle of plasmon effect dependence on size, coupled with the Beer Lambart law, holds true for the data obtained for the citrate stabilized nanoparticles [15-16].

The experiments conducted on cysteamine functionalized chemical sensors showed different Raman profiles from the citrate study. Because of its molecular structure, cysteamine can only bind using the thiol and amine groups which are bare lone pairs capable of hydrogen bonding [17]. Such interactions can be seen by the broad peaks on both gold and silver spectra on section 3.2.2. Like citrate, the broadening arises from the adsorption of the cysteamine on the sensors in a geometry that causes red shifting in both metal sample groups. For example, the C-S bond found in the 620-696 cm^{-1} region showed a red shift in both the gold and silver sensors, with the latter baring a larger peak area as well as a further red shift trend. Similarly, the amide bond in the 920-980 cm^{-1} region also showed the same profile with silver producing the highest peak area value between the two metals. The results from this set of experiments show band expansion on both metals due to interactions between the crosslinker and the metals. By observation, the thiol

and amine lone pairs can engage in chemical bonding with the metal however, the data shows that the preferred stereochemistry is of a trans orientation with a sulphur bonded on the metal surface as supported by the absence of the thiol group in the 2500 cm^{-1} (table 3 and 4). The large presence of the amine groups at the end of the spectra confirms these findings [18]. In the next section, a discussion on the Raman spectroscopy of APIs was conducted.

4.2 SERS on Tenofovir using gold and silver chemical sensors.

Tenofovir (TDF) is an anti-HIV medication that bares the same structural motif as nucleic acids that make up cellular genetic material and its function is to block DNA replication [19]. For this study, the functional groups that facilitate this important process were investigated using gold and silver chemical sensors. In section 3.3.1, the Raman spectra of TDF on glass, Au@Cit/Au and Ag@Cit/Ag were reported with emphasis on the vibrational modes detected. The major observations from the experiments were firstly, all three substrates produced the same profile characteristic of TDF. However, the spectral quality of the glass sample group had was poor compared to the metal substrates. Molecular assessment via the adenine ring breathing (727 cm^{-1}) and the individual bonds within it,C=N and C-N (1318 cm^{-1}), show unique trends in peak shifting behavior as well as statistical outputs. The glass sample group produced the largest Raman shift value for the adenine with the lowest value found on silver. This implies the ring molecule was more compressed in breathing mode on glass compared to the metallic sensors. Conversely, the imine and amine groups of the ring follow an opposite trend which confirms the possibility of tensile strain between the sensors and the analytes at the point of contact [20].

The cysteamine data in section 3.4.1 shows the spectral quality of silver is better than the gold sample group, which is the same observation made with the citrate. Secondly, the peak shifting behavior of the adenine ring and its individual bonds show a similar red shifting trend found on the citrate data for the adenine ring however, the individual bonds of C=N and C-N had a substantially larger red shift in the 1318 cm^{-1} region for cysteamine. The possible cause can be the interaction between the nitrogen lone pairs of the analyte and the hydrogen atoms of the cysteamine engaged in hydrogen bonding, which is likely to be the first point of energy transfer from the sensor to the analyte in the hotspot (figure 2.3) [21]. Furthermore, the molecular size of cysteamine is smaller than that of citrate, which can allow the former to display more red shifting for the analyte caused by bond expansion within the same molecular environment. This observation is further supported by the amine stretch seen at the end of the spectra (1600 cm^{-1}) where the cysteamine shows a red shifting that indicates bond stretching likely caused by the nitrogen lone pairs and the hydrogens of the amine group, for citrate the red shift is less pronounced (table 5 and 11). This contribution from the carbonyl is lesser, probably due to repulsion forces between the lone pairs of the respective atoms. Thus, when comparing the molecular behavior of both metal sensors towards the analyte, cysteamine shows a better response to its molecular groups because the bulkiness and oxygen content of citrate is likely to cause a mixture of repulsion and attraction forces relative to the smaller amine functionalized cysteamine[22].

The statistical data from the TDF experiments were derived from the peak area values and they showed a better linear fit on the scaffolds compared to the glass, and this supports the difference in spectral quality when compared to figure 3.14. Further confirmation came from the R^2 values for both 727 cm^{-1} and 1318 cm^{-1} vibration modes seen in the linear fits for TDF (3.3.2 and 3.4.2). The improved linearity can be explained by considering the adjacent amine group position on the molecule, which is free from steric hinderance and has more access to the chemical sensor via hydrogen bonding [23-24]. Table 6 summarizes the statistical outputs received from the citrate-based experiments on TDF where the calibration sensitivity for the adenine ring breathing increases from glass to gold, with silver producing the best results. The analytical sensitivity also showed the same trend which implies a good response from the system towards minute changes in sample preparation. The limit of detection was also significantly improved because, apart from the nanoparticle effect, the sensing platform was void of interference from the glass, leading to better detection of both functional groups of the drug. The data from gold and silver also shows the LOD limit gets lower as the slope of their linear fits increases, which is supported by the molecular vibration data. In the case of cysteamine, table 11 shows the two metals outperform the plain glass substrate on all the parameters. Secondly, the parameters follow the trend of glass, gold and silver in terms of values for both functional groups. However, the calibration and analytical sensitivity values are substantially lower than the citrate sensor suspected to be caused by the numerous points of contact available on the sensor via the carboxylates, which are less on the cysteamine. This structural difference and bulkiness of the citrate molecule can create more surface area for adsorption which produces better sensitivity values from linear fitting. In addition, the data from LOD calculations (SA) indicate silver has the lowest value of approx. 3-5 µg/ml whereas gold could use only 10 µg/ml for both crosslinkers. Interestingly, the LOD value for the 727 cm^{-1} vibration is the same for gold on both substrates however, the cysteamine sensor has a lower value for silver substrates. This observation also holds true for the individual bonds of the adenine ring where the LOD value is lower on TDF/Ag@Cys/Ag compared to TDF/Ag@Cit/Ag, this implies cysteamine interaction with silver is better than citrate, as seen from the red shift character. From these observations, it was clear that silver chemical sensors stabilized by cysteamine performed better than gold in the detection of TDF using the adenine ring motif.

4.3 SERS on Lamivudine using gold and silver chemical sensors

Anti-HIV medication Lamivudine is a drug that inhibits HIV growth in host cells via biochemical mechanisms carried out by its molecular functional groups [25]. In this study, the molecular vibrations of the drug were studied using gold and silver chemical sensors. The Raman experiments using citrate and cysteamine crosslinked MNPs were compared with glass in sections 3.3.3 and 3.4.3 and commonalities were established. Firstly, the spectral quality of LAM was more enhanced on the metal substrates compared to glass. Secondly, the Raman bands from the metal substrates showed an overall red shift character, with functional groups expanding their bond lengths in response to the laser photons and chemical sensor. Specifically, the amine group in the 200 cm^{-1} displayed the same red shift response also seen with TDF where its atoms

are less sterically hindered and thus can contact the substrates with more ease. This red shift is more pronounced on silver, which implies more bond contact on this metal compared to gold because of the respectively larger nanoparticle size distribution. The same remarks can be made for the hydroxyl group in R1 which was found in bending mode around the 400 cm^{-1} regions (3.3.3). Conversely, a blue shifting caused by bond compression is seen mostly on the bulky rings themselves relatively, probably from being confined between the nanoparticle hotspots and thus gaining energy from the sensor to move to higher frequencies. The peaks of interest studied during LAM experiments, 1245 cm^{-1} of Ring 2 and 1290 cm^{-1} of ring 1 showed a red shift pattern for the former, while blue shifting was detected for R 1. Intermolecular force considerations imply that the bond expansion in R2 is possible by hydrogen bonding interaction between the amine and the carboxylates, while compression is likely for molecules already experiencing confinement due to the adsorb energy coming from the hot spot [26-27].

The outcomes from LAM experiments using cysteamine stabilized chemical sensors showed the same response from the amine as explained for citrate above, with silver showing the smallest Raman shift. This behavior implies there has been more interaction between the amines of the drug and silver sensor via hydrogen bonding which is possible considering the higher particle sizes of the silver. A red shift trend was also observed for this sample group for amine and the hydroxyl groups, which shows that these sterically free atoms were in contact with the metal sensors and undergoing tensile strain [28-29]. For the chosen peaks, the 1245 cm^{-1} belonging to chemical bonds of R2 and 1290 cm^{-1} of R1, a blue shift character was detected from both metals, which means that the molecular bonds of the functional groups compressed in response to the radiation. This can result from considering that cysteamine provides a less bulky and sterically hindered environment compared to the citrate, this may allow the rings to attempt chemisorption through the rings themselves. If the ring is confined in the hotspot, bond compression is likely to be the chosen response to the input of energy [30]. It is important to note that the blue shift is less on the cysteamine compared to the citrate because the latter is bulkier and thus would foster more bond compression than the smaller cysteamine crosslinker.

Statistical results from the experiments were studied to make connections with the molecular vibrational data of the peaks of interest discussed above. Firstly, the linearity calculations of R^2 values produced the highest value for gold on both functional groups of citrate substrates, while silver and glass reported a lesser quality fit. The reason for the change could arise from the size distribution of the silver MNPs which may affect the quality linear fit since the slope is affected by the amplification effects from the sensor and not the concentration. In the case of a more evenly distributed Au@Cit particle size distribution, a better linear fit is likely. Conversely, the calibration sensitivity values indicate a better slope value for silver on both functional groups and since this parameter is independent of concentration, it gets affected by the variation in nanoparticle size on silver and thus may cause signal improvement by offering more surface plasmons [31]. Interestingly, the concentration dependent analytical sensitivity trend gave the highest value from gold only on R1, and this is possible because the silver sample may cause a higher variation due to its concentration which affects this parameter. While for the less bulky

R2, the concentration dependence works in its favor because analytical sensitivity is not affected by amplification likely caused by a larger size distribution, this is supported by the blue shift character seen in the Raman bands of Au@Cit/Au and Ag@Cit/Ag[32]. Numerical data from the cysteamine sample group showed a better linear fit from the amine group of R2 on gold, similar to the trend seen for the citrates again due to particle size variation. However, R1 had the opposite response from the sensor with the most suitable fit coming from silver unlike the citrate group, the reason being the drug can access the sensor more on a less bulky cysteamine crosslinker, compared to the bigger citrate molecule. Furthermore, R1 is larger than the R2 when considering the oxygen and sulphur atoms and thus in a lesser confined cysteamine environment, the amplification-dependent linear fit is expected to be better on the silver platform because of the size distribution and surface plasmon content [33]. Secondly, the sensitivities show that gold again performed better on the analytical sensitivity, which is affected by the concentration of samples, implying the concentration of silver had a limiting effect on the data. Conversely, the concentration independent calibration sensitivity produced a higher value for silver, which can be attributed to the nanoparticle size effects.

The limits of detection for Au@Cit/Au and Ag@Cit/Ag indicate the best performance comes from the latter for both functional groups, and this is likely caused by the high slope value of Ag@Cit. Likewise, the LOD values of cysteamine linked sensors Au@Cys/Au and Ag@Cys/Ag indicated lower detection values from silver for both molecular groups similar to citrate, which shows the consistency of silver in the detection of Lamivudine under these experimental conditions.

4.4 SERS on Dolutegravir using gold and silver chemical sensors.

Dolutegravir is classified as an integrase inhibitor that works by blocking the viral enzyme HIV integrase from transferring its DNA into the host cell. This chelation mechanism is mediated by binding on the magnesium atoms of the enzyme, using the fluorine atoms on the drug molecule [34-35]. In this section, molecular and statistical results from 3.3.5 and 3.4.5 are discussed with emphasis on the sensor and analyte responses via their vibrational modes. Firstly, this API group showed the least number of Raman bands compared to the other drugs; however, the functional groups in the results were sufficient to determine its structure. The peak shifting profile of the citrate group in 3.3.5 showed a blue shift for the amine group found in 200 cm^{-1} regions towards silver while showing the most red shift on gold and glass producing the same value. This can be explained by the molecular size of the analyte, which is too large to allow bond expansion like the other APIs and in addition. Secondly, the secondary and tertiary amines of DLG are sterically hindered by the cyclic motif of the drug, which hinders their ability to adsorb with the same efficiency as TDF and LAM. The effect of stereochemistry on Raman signals is seen on these amines in the 1270 cm^{-1} area where the steric hinderance is avoided by the hydrogen of the tertiary amine which makes it likely for the atom to engage in hydrogen bonding with the chemical sensors, allowing bond expansion between the C-N atoms. The same behavior was seen with the methyl group within the 1400 cm^{-1} area, this functional group, like the hydrogen, is not on the same plane as the rest of the molecule, this fact gives it room to interact with the sensors

and expand its bond to create a red-shift. Another similar trend was seen again for the methyl group in bending mode at the 1420 cm^{-1} region. The Ag@Cit/Ag sensor was able to cause the largest red shift because of the surface plasmon contribution likely being more than the Au@Cit/Au as seen in previous experiments. The amine group deformation mode showed a red shift character where steric hinderance is expected, and the reason could come from the less hindered secondary amine which may be accessible to the sensor when the right stereochemistry is adopted. This notion is supported by the trend showing the largest red shift from silver.

The cysteamine Raman spectra showed a red shift from amine occurring again at the 200 cm^{-1} and 1270 cm^{-1} this time with larger shifts than the citrate group, which is likely due to the less bulky cysteamine which can allow bond expansion of the analyte molecule. Interestingly, the previously red-shifted amines from the citrate group appeared in bond compression mode and this can be explained by the likelihood the drug molecule was able to chemisorb using the primary amine in the hotspot because the less bulky cysteamine contains less steric hinderance when compared to the citrate. The methyl group produced a red shift response likely caused by the stereochemistry of the molecule, preferring a less hindered orientation for adsorption and signal production. The deformed and sterically hindered amine produced a blue shift, unlike the citrate group because adsorption of the analyte could have been more on the less bulky crosslinker, leading to bond compression by the drug molecules stacked against each other.

Calculations on the parameters of a sensor explored in this section of the study showed the best linear fit came from Au@Cit/Au for the methyl group (1400 cm^{-1}) and the amine group 1500 cm^{-1} area. This was possible by considering that the slope of a linear fit is affected by instrument effects and not concentration, and thus as seen with LAM data, a more evenly distributed particle size from gold produced a better fit against the concentrated Ag@Cit/Ag. When considering the calibration sensitivity alone, the silver sensor supersedes the gold platform because the surface plasmon on the former offers more amplification than the gold. Ag@Cit/Ag also managed to outperform gold on analytical sensitivity, probably because of the former's dependence on the slope value and standard, which is high for silver. The LOD values were lower for silver compared to the gold and this value is inversely proportional to the slope of the linear fit, which is considerably higher on Ag@Cit/Ag. Cysteamine data showed the same trends as the citrate which implies both chemical sensors were affected in a similar way to the bulky DLG molecule. The gold sensor produced the best linear fit again between the metals due to the size distribution issue observed on silver for bulky functional groups. A large difference was seen for the calibration sensitivity on silver as well as the analytical sensitivity. A concern about the solubility of DLG in the water had an effect on the concentration dependent analytical sensitivity as seen for the glass values having higher than expected values compared to the other analytes. Nonetheless, Ag based sensor again outperformed the gold under these experimental conditions.

4.5 Comparisons of detection parameters against other techniques.

In the literature review (chapter 1), different techniques involving analysis of pharmaceutical drugs were discussed in terms of their experimental approach and statistical performances. In this study, the major focus was on the linearity, sensitivity and the limit of detection obtained from the SERS substrates of gold and silver compared to glass for each antiretroviral medication. In research, techniques such as chromatography, spectrometry, voltammetry, and optical methods are widely used in detection and analysis of pharmaceutical agents, ARV formulations included.

For chromatographic techniques, literature reports linearity values of 10-50 μg/ml and LOD values between 0.10-0.45 μg for both ARVs in tablet form [36]. When coupled to mass spectrometry, the linearity has been shown to improve to a range of 0.005-2.5 μg/ml [37]. Studies on bulk drugs of tenofovir, lamivudine and dolutegravir in pharmaceutical form have been published with linear ranges of 27-162 mg/ml using chromatographic methods [38]. Comparatively, as seen in tables 3.6,3.8 and 3.10 , the SERS sensors proposed in this thesis are within the microgram to milligram ranges that the chromatographic techniques are currently offering in literature. An advantage that SERS possess over this technique is the ease of use of the sensing platform and the simplified laser detection method. However, the chromatography technique is still more precise and robust compared to the Raman spectroscopy approach and more research into the latter is a necessity. The SERS method can be used in conjugation with the chromatography and spectrometry methods for a better understanding of the molecular behavior of the analytes.

Voltametric methods have also taken root in the analysis of ARV formulations with high sensitivity and a wide linear range. Studies have reported testing of tenofovir drug formulations using carbon nanotubes as electrical sensors within 0.003- 0.01 μM linear range[39] while other research publications report linear values of 2.39-119 μM for dolutegravir using the same sensing platform[40]. Gold based electrodes were also explored for the detection of ARV emtricitabine, were a linear range of 1- 10^6 μM was realized. These studies show that the electrochemical approach on pharmaceutical analysis is a highly competitive method however, these sensors posses challenges such as lack of durability, reusability and a limitation in determining individual components of complex pharmaceutical mixtures [41]. Furthermore, the sensing platforms used in most of these studies, require the use of expensive molecular coatings often fabricated using complex synthesis techniques. The optical approach of the Raman method allows simultaneous determination of multiple constituents of complex mixtures based by focusing on the molecular properties and detecting the corresponding fingerprint.

In short, the chromatographic and spectrometric techniques are high in sensitivity compared to the Raman technique but they require complex methods and the use of expensive reagents to carry out experiments. On the other hand, electrochemical methods are far less complicated, yet they suffer from lack of repeated use of chemical sensors and multicomponent analysis. These issues can be overcome using the SERS method as seen from the results of this study.

References

1. Alessandro Bertoluzza, Concezio Fagnano, Maria Antonietta Morelli, Vittorio Gottardi, Massimo Guglielmi,Raman and infrared spectra on silica gel evolving toward glass,Journal of Non-Crystalline Solids,Volume 48, Issue 1,1982,Pages 117-128,ISSN 0022-3093,https://doi.org/10.1016/0022-3093(82)90250-2.

2. Branislav Hruška, Tadeáš Gavenda, Filip Vašíček, Roman Svoboda,Raman spectroscopy study of glass corrosion, Vibrational Spectroscopy, Volume 109,2020,103096, ISSN 09242031,https://doi.org/10.1016/j.vibspec.2020.103096

3. Fuyuan Liang, JiaRan Yang, Yuanyuan Zhao, Yexin Zhou, Zilin Yan, JianChao He, Qunhui Yuan, Junwei Wu, Peng Liu, Zheng Zhong, Minfang Han, A review of thin film electrolytes fabricated by physical vapor deposition for solid oxide fuel cells, International Journal of Hydrogen Energy, Volume 47, Issue 87,2022,Pages 36926-36952,ISSN 0360-3199,https://doi.org/10.1016/j.ijhydene.2022.08.237.

4. S.S. Mundra, S.S. Pardeshi, S.S. Bhavikatti, Atul Nagras,Development of an integrated physical vapour deposition and chemical vapour deposition system,Materials Today: Proceedings,Volume 46, Part 2,2021,Pages 1229-1234,ISSN 2214-7853,https://doi.org/10.1016/j.matpr.2021.02.06

5. Nina Schalk, Michael Tkadletz, Christian Mitterer,Hard coatings for cutting applications: Physical vs. chemical vapor deposition and future challenges for the coatings community, Surface and Coatings Technology,Volume 429,2022,127949,ISSN 0257-8972,https://doi.org/10.1016/j.surfcoat.2021.127949.

6. Zina-Sabrina Duma, Tuomas Sihvonen, Jouni Havukainen, Ville Reinikainen, Satu-Pia Reinikainen,Optimizing energy dispersive X-Ray Spectroscopy (EDS) image fusion to Scanning Electron Microscopy (SEM) images, Micron, Volume 163,2022,103361,ISSN 0968-4328,https://doi.org/10.1016/j.micron.2022.103361.

7. Palaniselvam Kuppusamy, Sujung Kim, Sung-Jo Kim, Ki-Duk Song,Antimicrobial and cytotoxicity properties of biosynthesized gold and silver nanoparticles using D. brittonii aqueous extract,Arabian Journal of Chemistry, Volume 15, Issue 11,2022,104217, ISSN 1878-5352,https://doi.org/10.1016/j.arabjc.2022.104217.

8. Balaprasad Ankamwar, Vaishali Kamble, Ujjal Kumar Sur, Chittaranjan Santra,Spectrophotometric evaluation of surface morphology dependent catalytic activity of biosynthesized silver and gold nanoparticles using UV–vis spectra: A comparative kinetic study,Applied Surface Science,Volume 366,2016,Pages 275-283,ISSN 0169-4332,https://doi.org/10.1016/j.apsusc.2016.01.093.

9. Njuguna J, Vanli OA, Liang R. A Review of Spectral Methods for Dispersion Characterization of Carbon Nanotubes in Aqueous Suspensions. J Spectrosc. 2015;2015.

10. M.H.U. Bhuiyan, R. Saidur, M.A. Amalina, R.M. Mostafizur, AKMS Islam,Effect of Nanoparticles Concentration and Their Sizes on Surface Tension of Nanofluids,Procedia Engineering,Volume 105,2015,Pages 431-437,ISSN 1877-7058, https://doi.org/10.1016/j.proeng.2015.05.030.

11. Lu Lu, Gwendolyn Burkey, Ionel Halaciuga, Dan V. Goia,Core–shell gold/silver nanoparticles: Synthesis and optical properties, Journal of Colloid and Interface Science,Volume 392,2013,Pages 90-95,ISSN 0021-9797,https://doi.org/10.1016/j.jcis.2012.09.057.

12. H. Kaçuş, A. Baltakesmez, Z. Çaldıran, Ş. Aydoğan, M. Yılmaz, M. Sevim,Optical and electrical characterization of organic solar cells obtained using gold and silver metal nanoparticles, Materials Today: Proceedings,Volume 46, Part 16,2021,Pages 6986-6990,ISSN 2214-7853,https://doi.org/10.1016/j.matpr.2021.03.276.

13. Xuejing He, Hiroyuki Kagi, Kazuki Komatsu, Satoshi Nakano,Compressibility and blue-shifting O–H stretching bands of magnesium hydroxyfluoride Mg(OH)F up to 20 GPa,

Journal of Solid State Chemistry,Volume 303,2021,122449,ISSN 0022-4596,https://doi.org/10.1016/j.jssc.2021.122449.

14. Dhotel A, Chen Z, Delbreilh L, Youssef B, Saiter JM, Tan L. Molecular motions in functional self-assembled nanostructures. Int J Mol Sci. 2013;14(2):2303-2333. Published 2013 Jan 24. doi:10.3390/ijms14022303

15. Yeshchenko, O.A., Dmitruk, I.M., Alexeenko, A.A. et al. Size and Temperature Effects on the Surface Plasmon Resonance in Silver Nanoparticles. Plasmonics 7, 685–694 (2012). https://doi.org/10.1007/s11468-012-9359-z

16. He, R.X., Liang, R., Peng, P. et al. Effect of the size of silver nanoparticles on SERS signal enhancement. J Nanopart Res 19, 267 (2017). https://doi.org/10.1007/s11051-017-3953-0

17. Atallah C, Charcosset C, Greige-Gerges H. Challenges for cysteamine stabilization, quantification, and biological effects improvement. J Pharm Anal. 2020;10(6):499–516.

18. A. Farcas, L. Janosi, S. Astilean,Size and surface coverage density are major factors in determining thiol modified gold nanoparticles characteristics,Computational and Theoretical Chemistry,Volume 1209,2022,113581,ISSN 2210-271X,https://doi.org/10.1016/j.comptc.2021.113581.

19. Adrian S. Ray, Marshall W. Fordyce, Michael J.M. Hitchcock,Tenofovir alafenamide: A novel prodrug of tenofovir for the treatment of Human Immunodeficiency Virus,Antiviral Research,Volume 125,2016,Pages 63-70,ISSN 0166-3542,https://doi.org/10.1016/j.antiviral.2015.11.009.

20. Daohan Ge, Yuan Zhang, Hui Chen, Guangfu Zhen, Minchang Wang, Jiwei Jiao, Liqiang Zhang, Shining Zhu,Effect of patterned silicon nitride substrate on Raman scattering and stress of graphene,Materials & Design,Volume 198,2021,109338,ISSN 0264-1275,

21. Ouwehand, J., Lauwaert, J., Esquivel, D., Hendrickx, K., Van Speybroeck, V., Thybaut, J.W. and Van Der Voort, P. (2016), Facile Synthesis of Cooperative Acid–Base Catalysts by Clicking Cysteine and Cysteamine on an Ethylene-Bridged Periodic Mesoporous Organosilica. Eur. J. Inorg. Chem., 2016: 2144-2151. https://doi.org/10.1002/ejic.201501179

22. Bian F, Tian YC, Wang R, Yang HX, Xu H, Meng S, et al. Ultrasmall silver nanopores fabricated by femtosecond laser pulses. Nano Lett. 2011;11(8):3251–7.

23. Hong-Qiang Gao, Paul L Boyer, Stefan G Sarafianos, Edward Arnold, Stephen H Hughes,The role of steric hindrance in 3TC resistance of human immunodeficiency virus type-1 reverse transcriptase11Edited by A. R. Fersht,Journal of Molecular Biology,Volume 300, Issue 2,2000,Pages 403-418,ISSN 0022-2836,https://doi.org/10.1006/jmbi.2000.3823.

24. Ilomuanya, M.O., Hameedat, A.T., Akang, E.N. et al. Development and evaluation of mucoadhesive bigel containing tenofovir and maraviroc for HIV prophylaxis. Futur J Pharm Sci 6, 81 (2020). https://doi.org/10.1186/s43094-020-00093-3

25. Laura Waters, Viraj Mehta, Jaideep Gogtay, Marta Boffito,The evidence for using tenofovir disoproxil fumarate plus lamivudine as a nucleoside analogue backbone for the treatment of HIV,Journal of Virus Eradication,Volume 7, Issue 1,2021,100028,ISSN 2055-6640,https://doi.org/10.1016/j.jve.2021.100028

26. Daniel Prezgot, Jack Cruikshank, Merrick Makila-Boivin, Saro Birgani, Anatoli Ianoul,Toward SERS based localized thermometry of Polymer-Supported silver and gold nanostructures,Spectrochimica Acta Part A: Molecular and Biomolecular Spectroscopy,Volume 280,2022,121514,SSN 1386-1425,https://doi.org/10.1016/j.saa.2022.121514.

27. Yasemin ÇELİK, Ayşe KURT,Three dimensional porous Expanded Graphite/Silver Nanoparticles nanocomposite platform as a SERS substrate,Applied Surface Science,Volume 568,2021,150946,ISSN 0169-4332

28. Hui Yan, Meng Zhang, Shuang Wang, Heng Li, Sándor Kunsági-Máté, Shougen Yin,Raman spectroscopy of strained monolayer graphene modulated by monodispersed Au nanoparticles,Applied Surface Science,Volume 610,2023,155531,ISSN 0169-4332,https://doi.org/10.1016/j.apsusc.2022.155531.

29. Thierry Lefèvre, François Paquet-Mercier, Stéphanie Lesage, Marie-Eve Rousseau, Sarah Bédard, Michel Pézolet,Study by Raman spectromicroscopy of the effect of tensile deformation on the molecular structure of Bombyx mori silk,Vibrational Spectroscopy,Volume 51, Issue 1,2009,Pages 136-141,ISSN 0924-2031,https://doi.org/10.1016/j.vibspec.2008.11.012.

30. Wan F, Shi H, Chen W, Gu Z, Du L, Wang P, Wang J, Huang Y. Charge Transfer Effect on Raman and Surface-enhanced Raman spectroscopy of Furfural Molecules. Nanomaterials. 2017; 7(8):210. https://doi.org/10.3390/nano7080210

31. Xiangxian Wang, Jiankai Zhu, Yuan Wu, Yueqi Xu, Yingwen Su, Liping Zhang, Yunping Qi, Xiaolei Wen, Hua Yang,Hybrid surface plasmon effect and SERS characterization in a heterogeneous composite structure of Au nano-array and Ag film,Results in Physics,Volume 17,2020,103175,ISSN 2211-3797,https://doi.org/10.1016/j.rinp.2020.103175.

32. Skoog, A.; Holler, J.; Crouch, S. Principles of Instrumental Analysis; ISE: Balmont, CA, USA, 2007.

33. Luping Du, Xuejin Zhang, Ting Mei, and Xiaocong Yuan, "Localized surface plasmons, surface plasmon polaritons, and their coupling in 2D metallic array for SERS," (2010)Opt. Express 18, 1959-1965

34. Nilavar NM, Paranjape AM, Raghavan SC. Biochemical activity of RAGs is impeded by Dolutegravir, an HIV integrase inhibitor. Cell Death Discov [Internet]. 2020;6(1):4–11. Available from: http://dx.doi.org/10.1038/s41420-020-0281-4

35. Underwood MR, Johns BA, Sato A, Martin JN, Deeks SG, Fujiwara T. The activity of the integrase inhibitor dolutegravir against HIV-1 variants isolated from raltegravir-treated adults. J Acquir Immune Defic Syndr. 2012;61(3):297–301.

36. Adhao VS, Chaudhari SR, Ambhore JP, Sangolkar S, Thenge RR, Cheke RS, et al. Reverse phase-liquid chromatography assisted protocol for simultaneous determination of lamivudine and tenofovir disoproxil

fumarate in combined medication used to control HIV infection: an investigative approach. Futur J Pharm Sci. 2021;7(1).

37. Ramírez-Ramírez A, Sánchez-Serrano E, Loaiza-Flores G, Plazola-Camacho N, Rodríguez-Delgado RG, Figueroa-Damián R, et al. Simultaneous quantification of four antiretroviral drugs in breast milk samples from HIV-positive women by an ultra-high performance liquid chromatography tandem mass spectrometry (UPLC-MS/MS) method. PLoS One. 2018;13(1):1–15.

38. Rao NM, Sankar DG. Development and validation of stability indicating HPLC method for simeltaneous determination of Lamivudine, tenofovir, and Dolutegravir in bulk and their tablet dosage form. Future Journal of Pharmaceutical Sciences. 2015 Dec 1; 1(2): 73-7.

39.Okumu FO, Silwana B, Matoetoe MC. Application of MWCNT/Ag-Pt Nanocomposite Modified GCE for the Detection of Nevirapine in Pharmaceutical Formulation and Biological Samples. Electroanalysis. 2020;32(12):3000–8.

40. M. Manohar, M.A. Marzinke, Application of Chromatography Combined With Mass Spectrometry in Therapeutic Drug Monitoring, Clinical Challenges in Therapeutic Drug Monitoring, ed: Elsevier (2016) 45–70, https://doi.org/ 10.1016/B978-0-12-802025-8.00003-9.

41. N. Thapliyal, N.S.E. Osman, H. Patel, R. Karpoormath, R.N. Goyal, T. Moyo, R. Patel, NiO–ZrO2 nanocomposite modified electrode for the sensitive and selective determination of efavirenz, an anti-HIV drug,“, RSC Adv. 5 (50) (2015) 40057–40064

5. Conclusion

This research project aimed to investigate the applicability of chemical sensors for the detection and characterization of anti-HIV drugs. The necessity for such technology comes from the growing problem of substandard medication being imported onto the African continent, which has an extremely negative impact on the quality of life for people who need the treatment. As a start, a literature survey was conducted where research into the current state of chemical sensor technology for small molecule applications was explored. The research methodology employed in this study involved the synthesis of chemical sensors using already published methods followed by application on Antiretroviral medications.

Chemical sensor fabrication experiments entailed coating nano thin layers of gold and silver metals on the surface of plain glass slides followed by the incorporation of nanoparticles onto the coated surfaces for signal enhancement purposes. Spectroscopic and microscopic analysis showed successful synthesis and coating of the sensors on glass. Secondly, molecular characterization of the sensors showed bond vibrations associated with functional groups of the crosslinkers contained on the sensing platforms. Furthermore, the results showed a satisfactory reduction of the glass signal during Raman experiments which rendered the chemical sensors ready for application. Anti-HIV medication Tenofovir (TDF), Lamivudine (LAM) and Dolutegravir (DLG) were investigated using the chemical sensors where changes in Raman peaks and peak areas were used to determine the sensitivity and limit of detection of the sensors. Research findings from this study show that molecular interactions such as hydrogen bonding facilitate chemisorption of the analytes, which is detectable by red or blue shifting detectable by Raman spectroscopy. Overall, the gold sensors displayed better efficiency in sensitivity and limit of detection than silver when less sterically hindered molecular groups were investigated. On the other hand, silver sensors were better with functional groups in constrained environments where blue shifting because of bond compression and energy transfer was dominant. Nanoparticle size distribution and concentration played a major role in improving the response of the analyte to the sensor platform, with red shifting more pronounced on the smaller cysteamine coupled with gold, which bears a smaller size distribution than silver while blue shifting is evident for the bulkier citrate on silver. Calibration sensitivity also showed a considerable impact on the limit of detection of the sensor, where higher values created lower LOD values comparable with other techniques from similar research. The statistical data discussed in the thesis shows that the methods employed are comparable with existing literature however, more work needs to be done to improve the values of the characterization parameters. It is important to note that the use of SERS specifically on ARV medication is still new and under reported and as such, this thesis presents a novel approach in terms of optical methods for ARV research using Raman spectroscopy and nanomaterial research.

The limitations of the study arise from the inability to determine the enhancement factor at this point due to a lack of consistent control of the particle size distribution using the self-assembly method. Without a consistent size distribution, preferably a Gaussian distribution, the

enhancement factor will not be reproducible. Future work will involve other synthesis techniques such as lithography, that allow a stable size distribution and determination of SERS enhancement factor.

Secondly, other activities will include employing more advanced techniques to produce the sensor platforms ie; Lithography in order to have more reproducibility and higher sensitivity to allow improvement of the sensor characteristics. Lastly, computational modelling must be included to better explain the Raman shift behavior, as well as assist with designing and predicting reaction conditions that bring out the most optimum performance from the sensors. Such work is important in developing cost-effective, simplified methods for monitoring ARV medication as a means of assisting the health care sector with, providing quality health products that ensure an optimum standard of living for citizens of the African continent.

6. Supplementary information

S1: Gold coated slide and EDS data

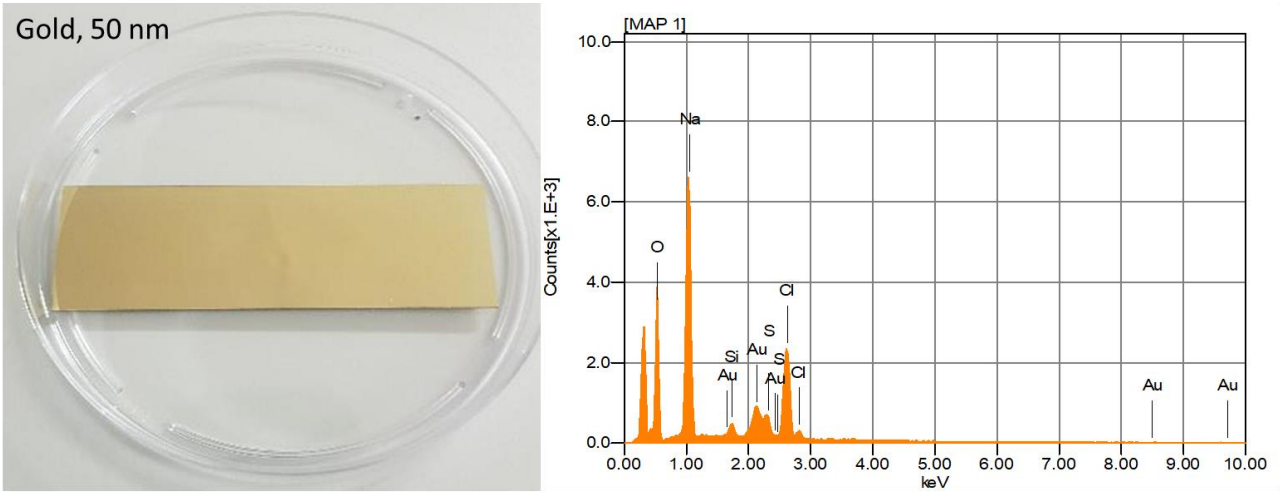

S2: Silver coated slide and EDS data

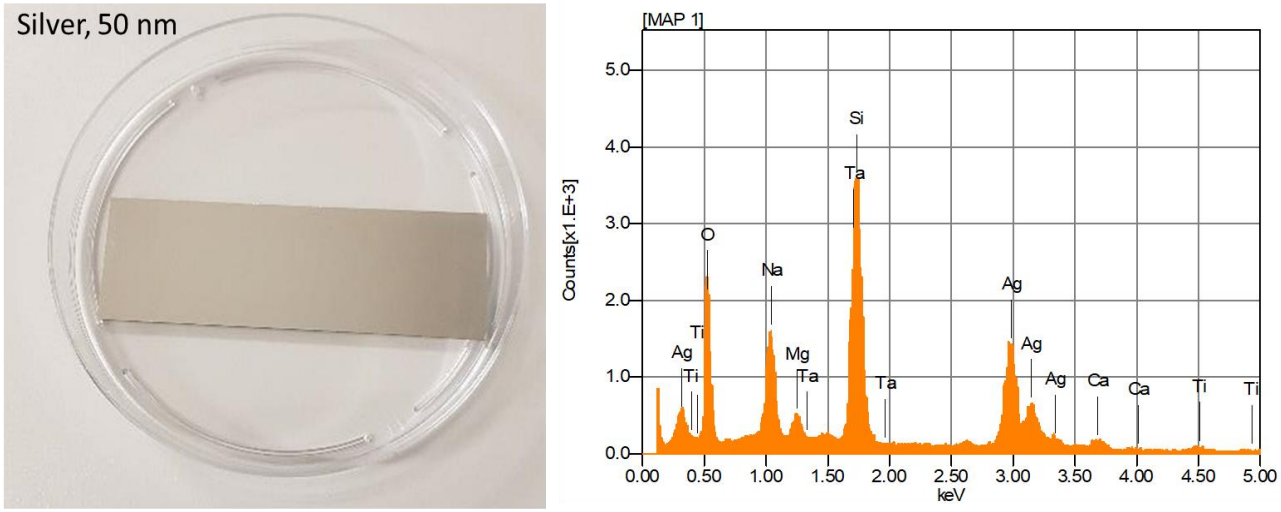

S3: Image of mapping array used for spectral acquisition.

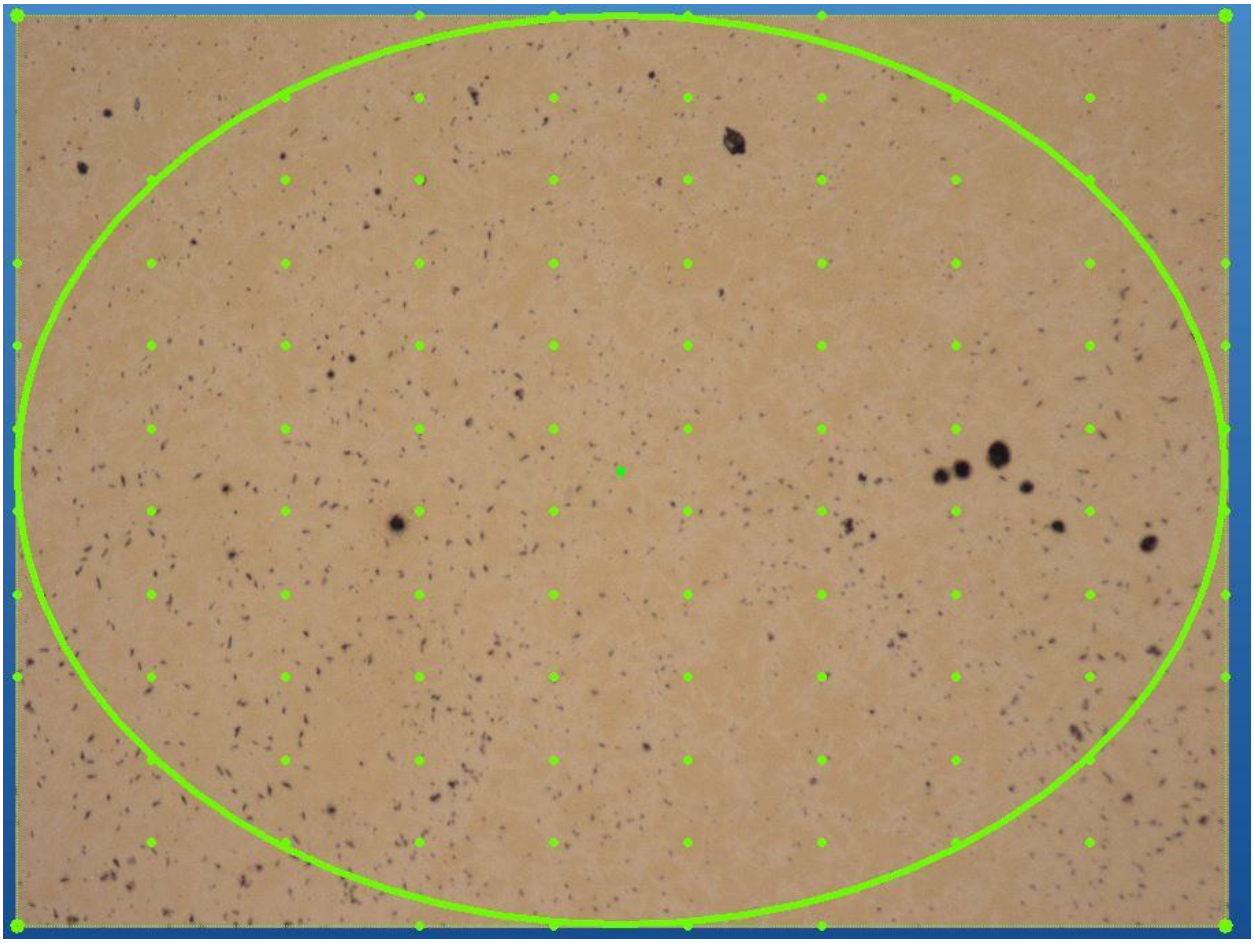

532 nm, 12 mW power, 10x magnification, 200 µm slid width, 100 spots 10 seconds per scan, averaged at 3 scans

S4: Raman spectrum of citrate powder.

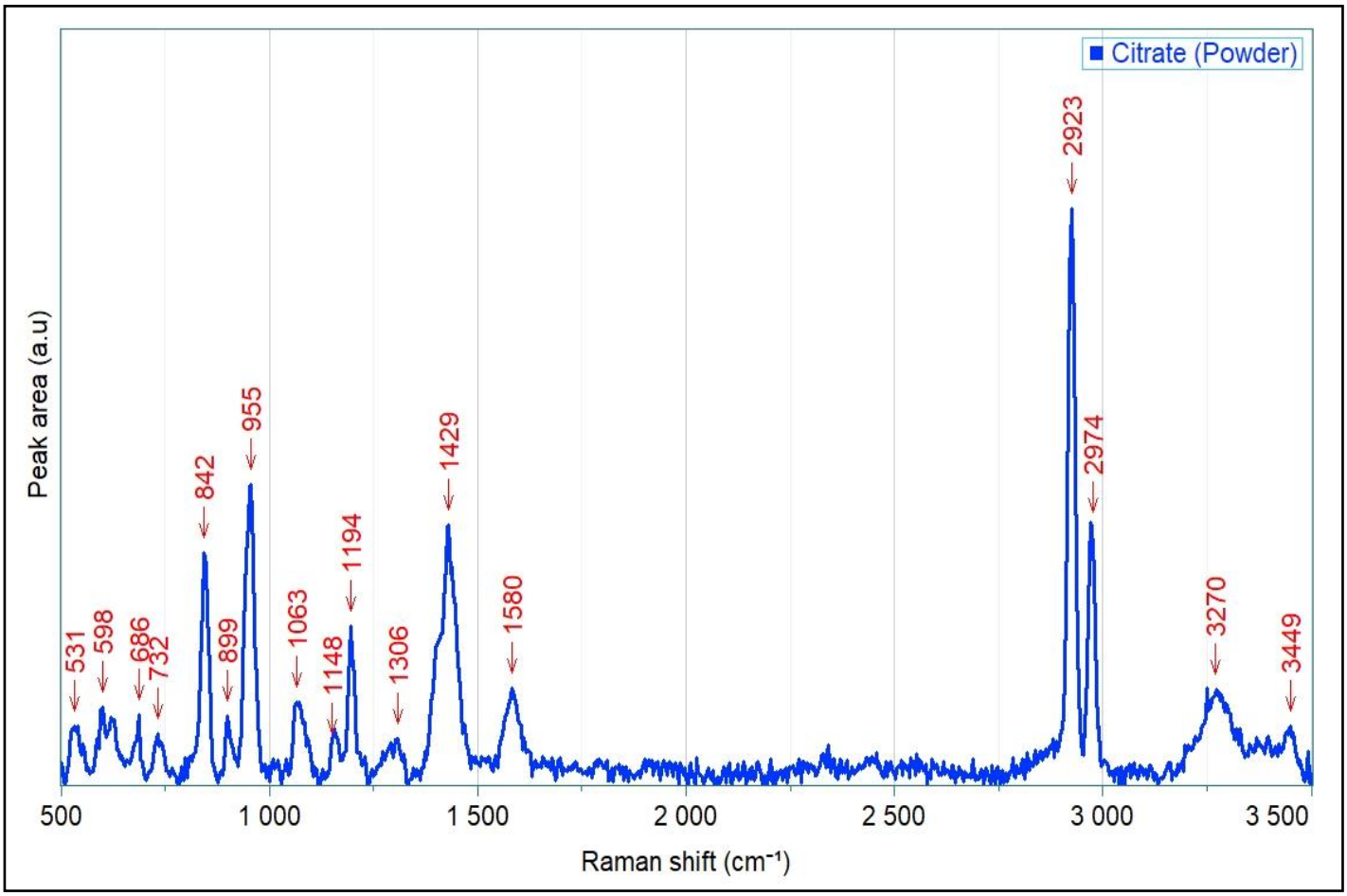

532 nm, 12 mW power, 10x magnification, 200 µm slid width, 100 spots 10 seconds per scan, averaged at 3 scans

S5: Raman spectrum of cysteamine powder.

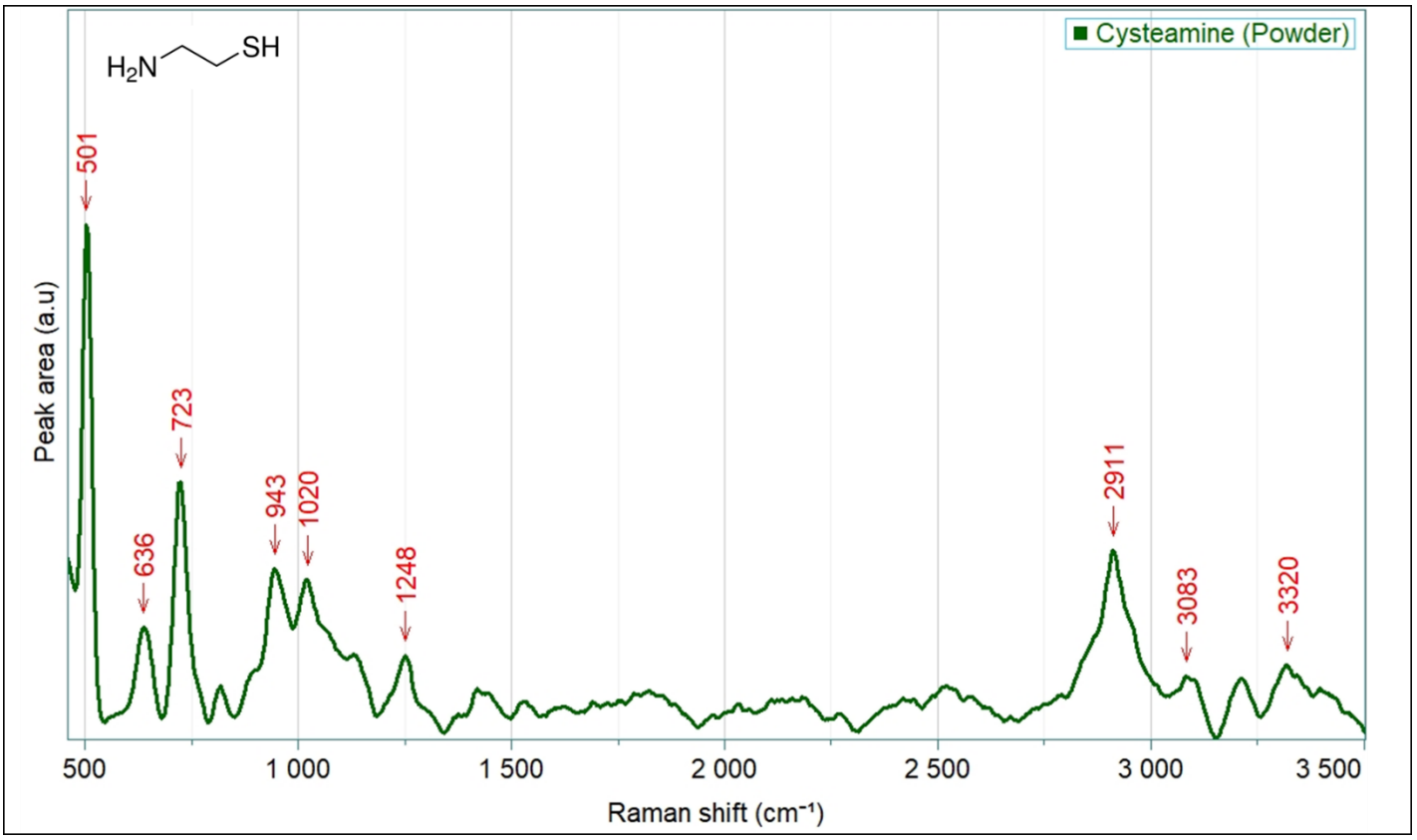

532 nm, 12 mW power, 10x magnification, 200 µm slid width, 100 spots 10 seconds per scan, averaged at 3 scans

S6: Raman spectrum of Tenofovir (TDF) powder

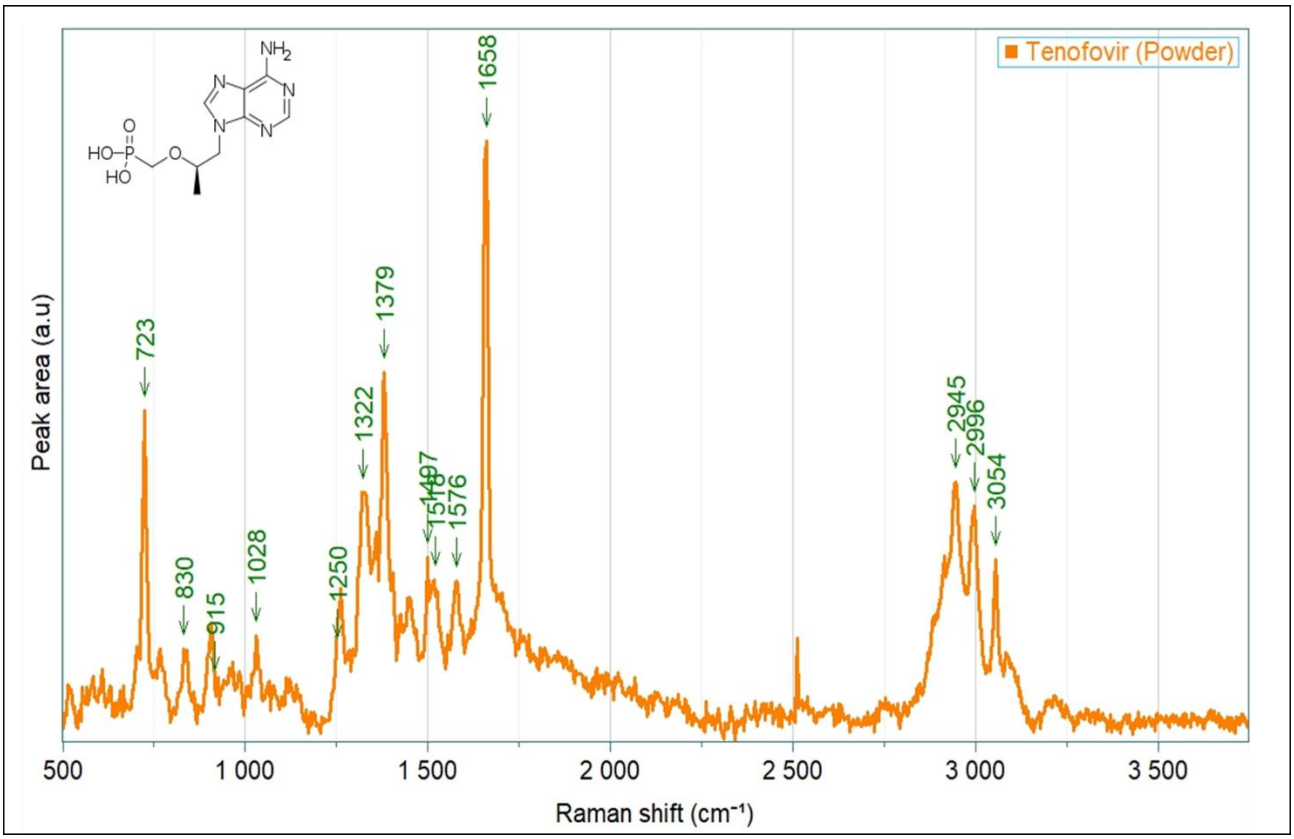

532 nm, 12 mW power, 10x magnification, 200 µm slid width, 100 spots 10 seconds per scan, averaged at 3 scans

S7: Raman spectrum of Lamivudine (LAM) powder

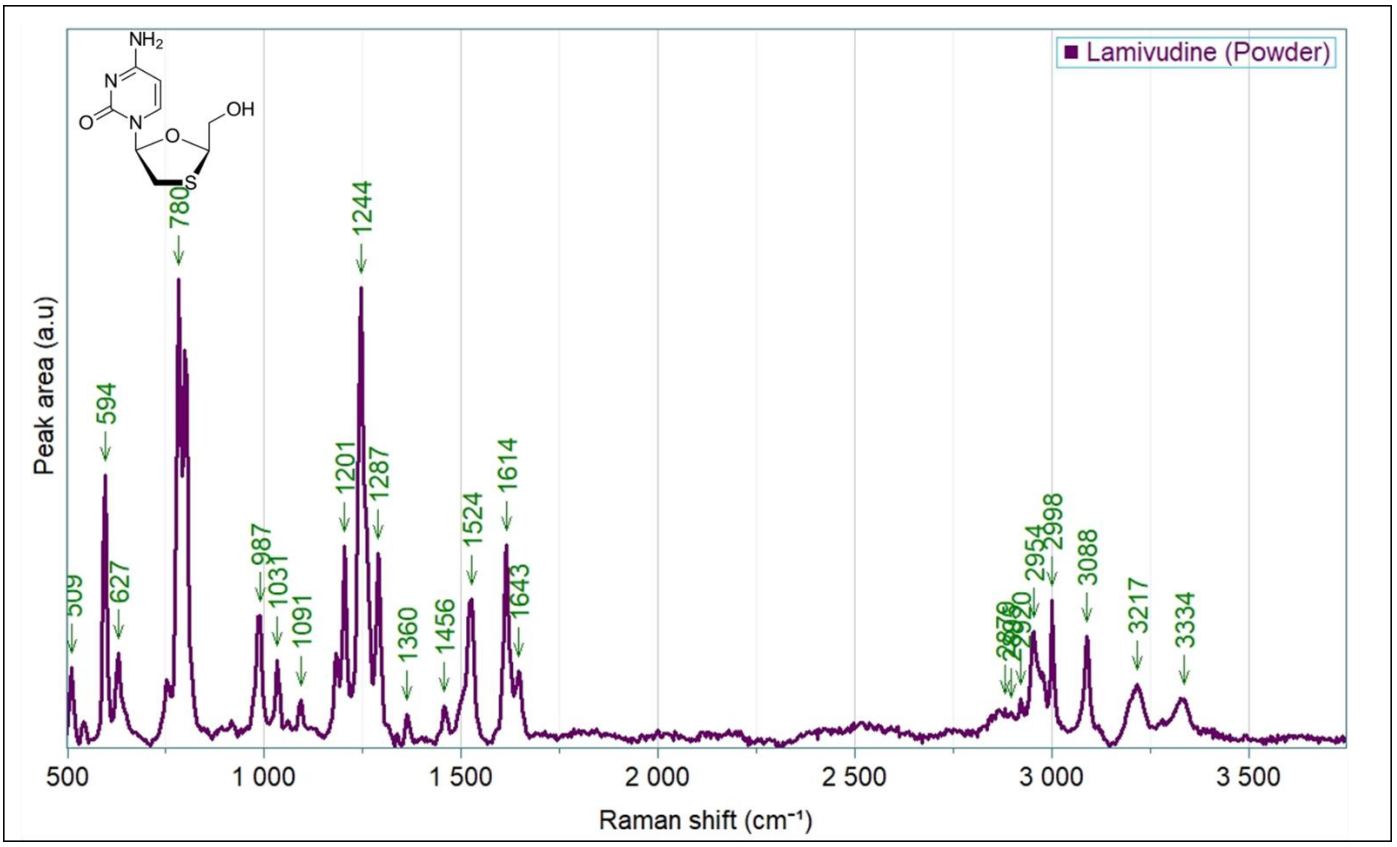

532 nm, 12 mW power, 10x magnification, 200 µm slid width, 100 spots 10 seconds per scan, averaged at 3 scans

S8: Raman spectrum of Dolutegravir (DLG) powder

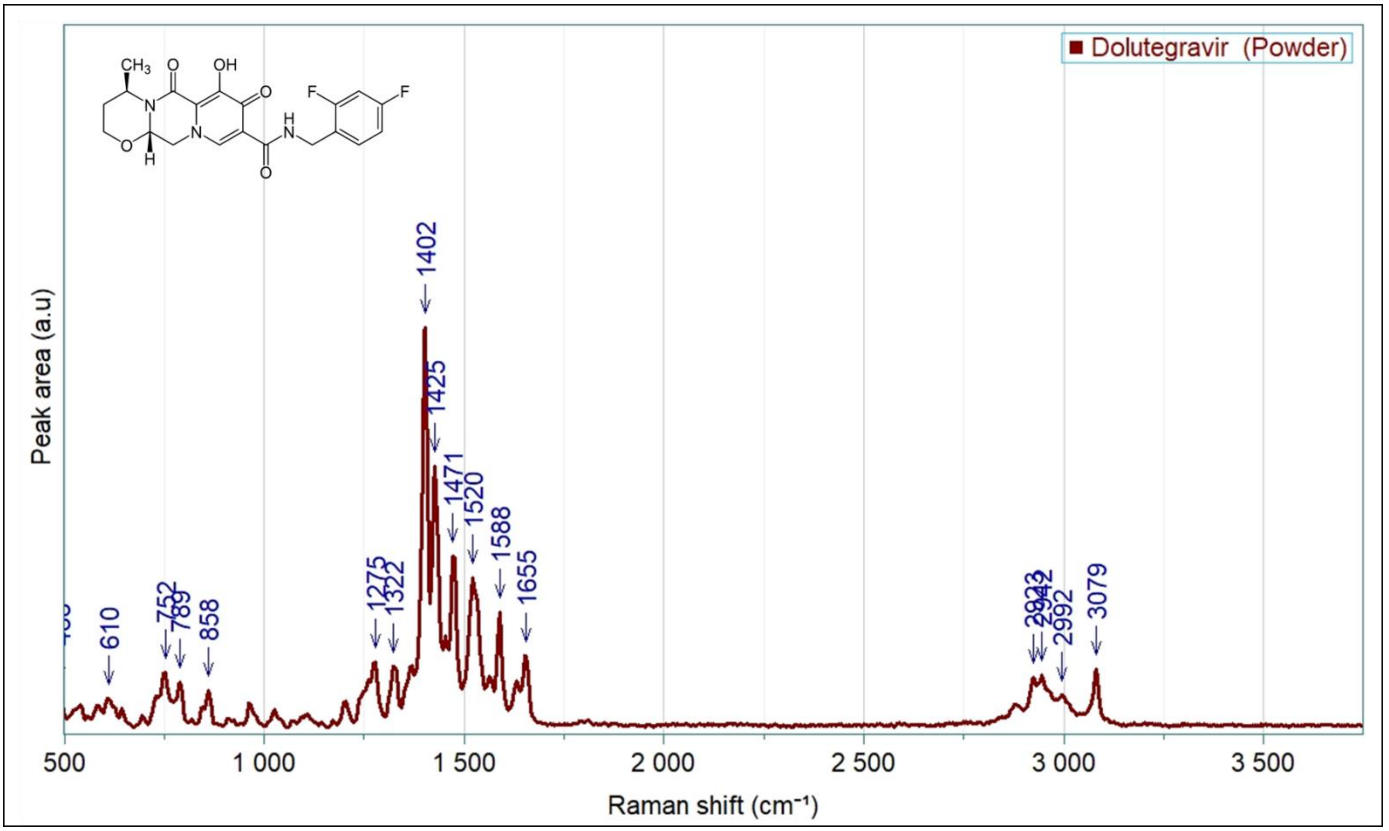

532 nm, 12 mW power, 10x magnification, 200 µm slid width, 100 spots 10 seconds per scan, averaged at 3 scans

S9*:* TDF*/Glass* spectra

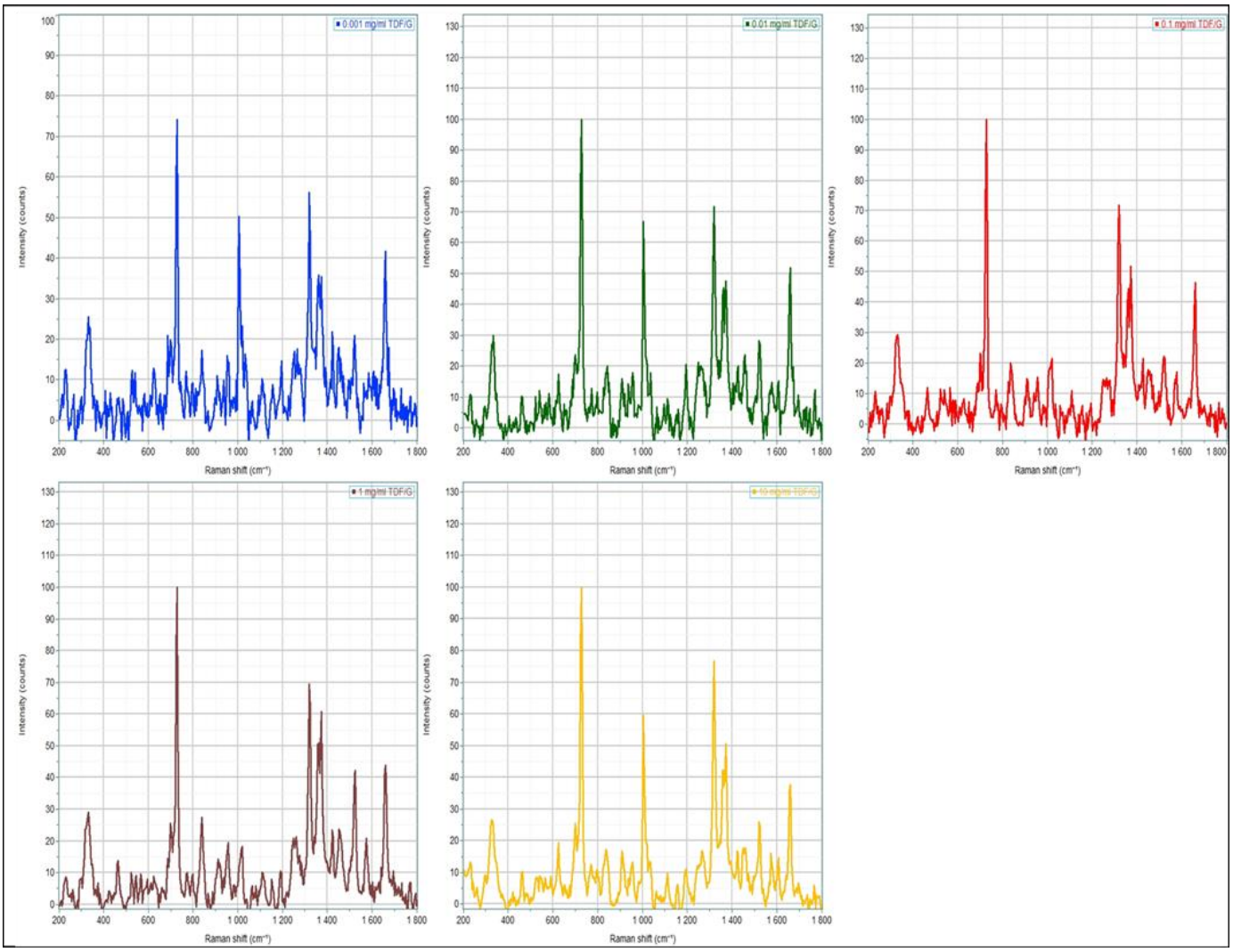

S10: TDF Au@Cit/Au spectra

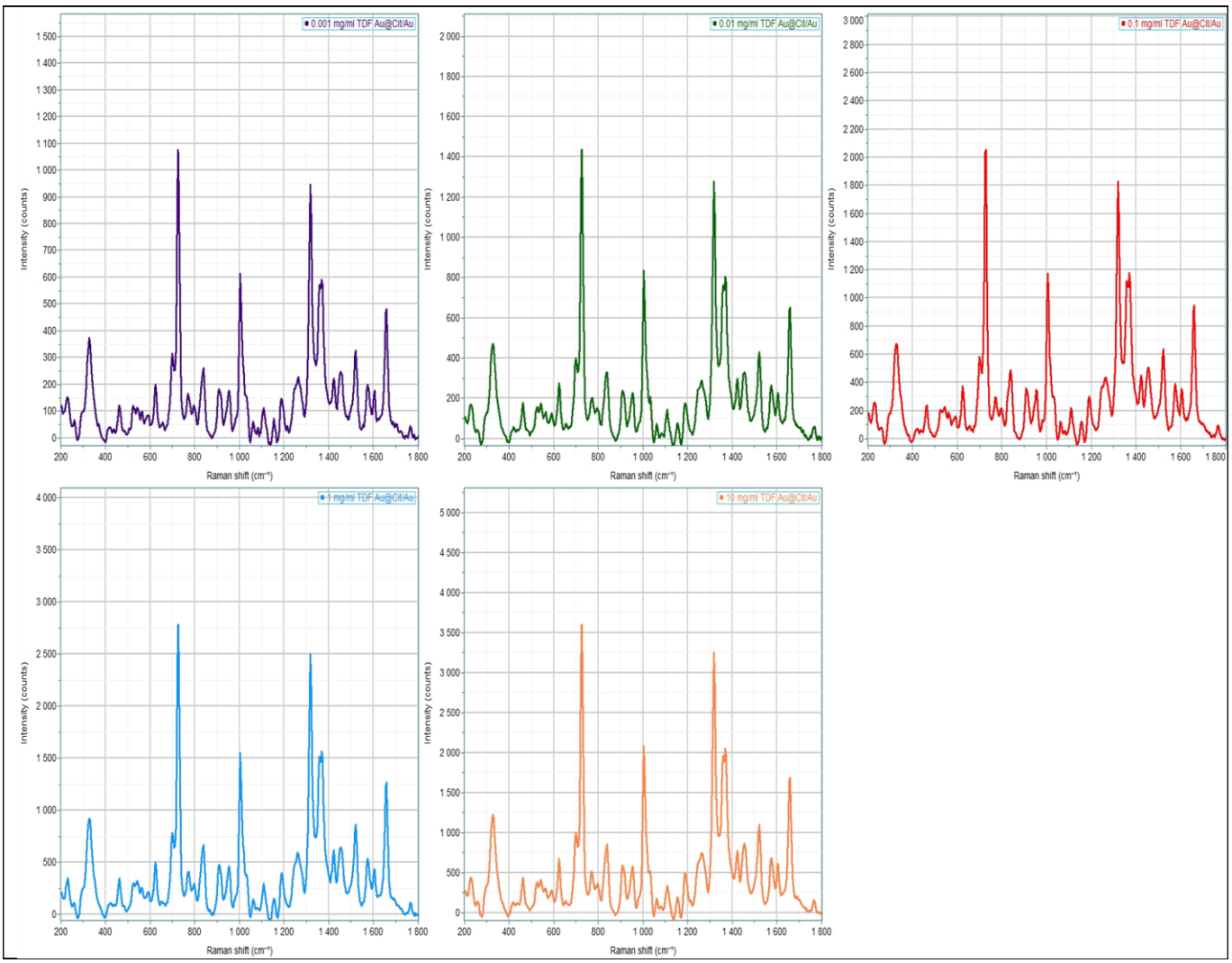

S11: TDF Ag@Cit/Ag spectra

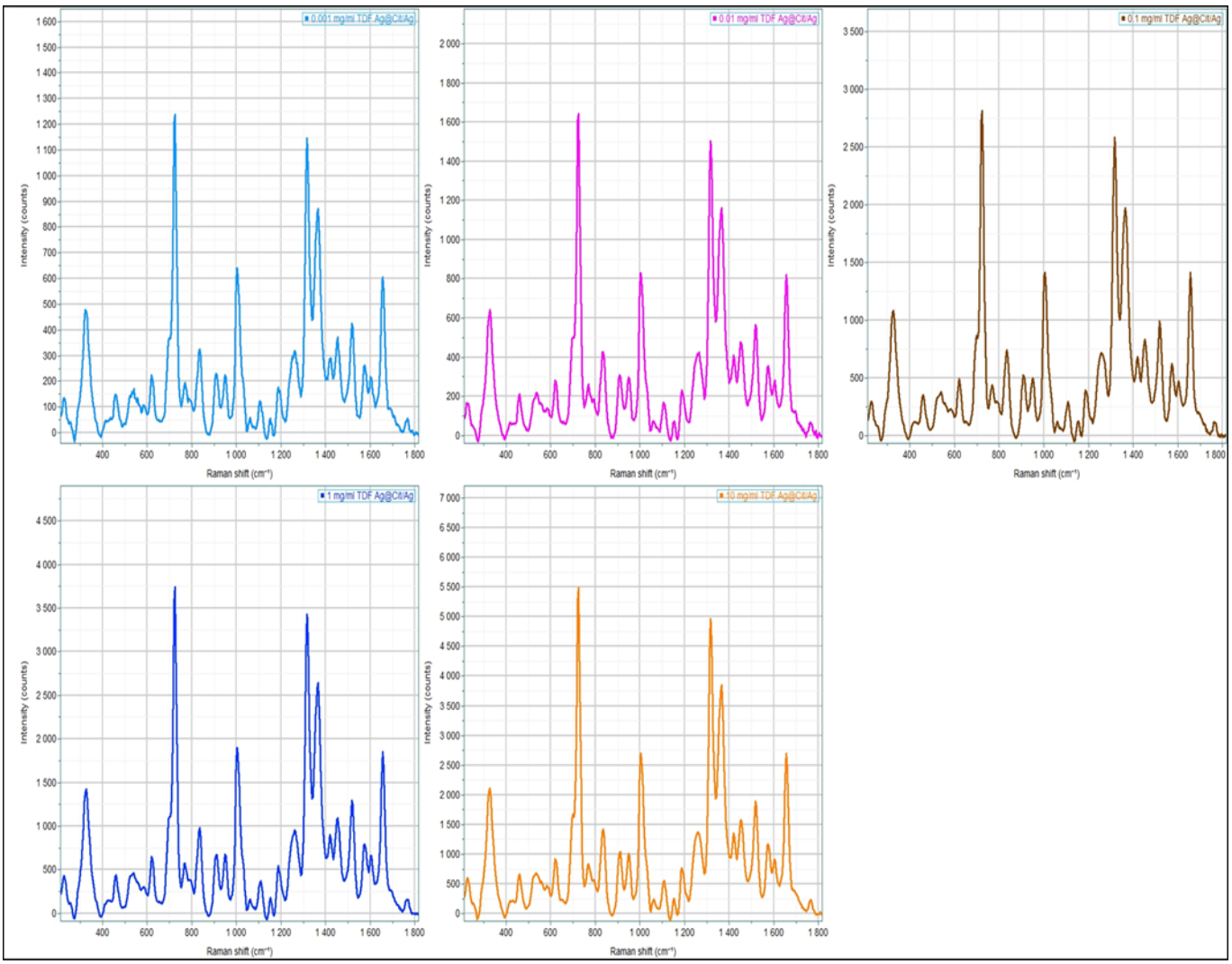

S12 :TDF Au@Cys/Au spectra

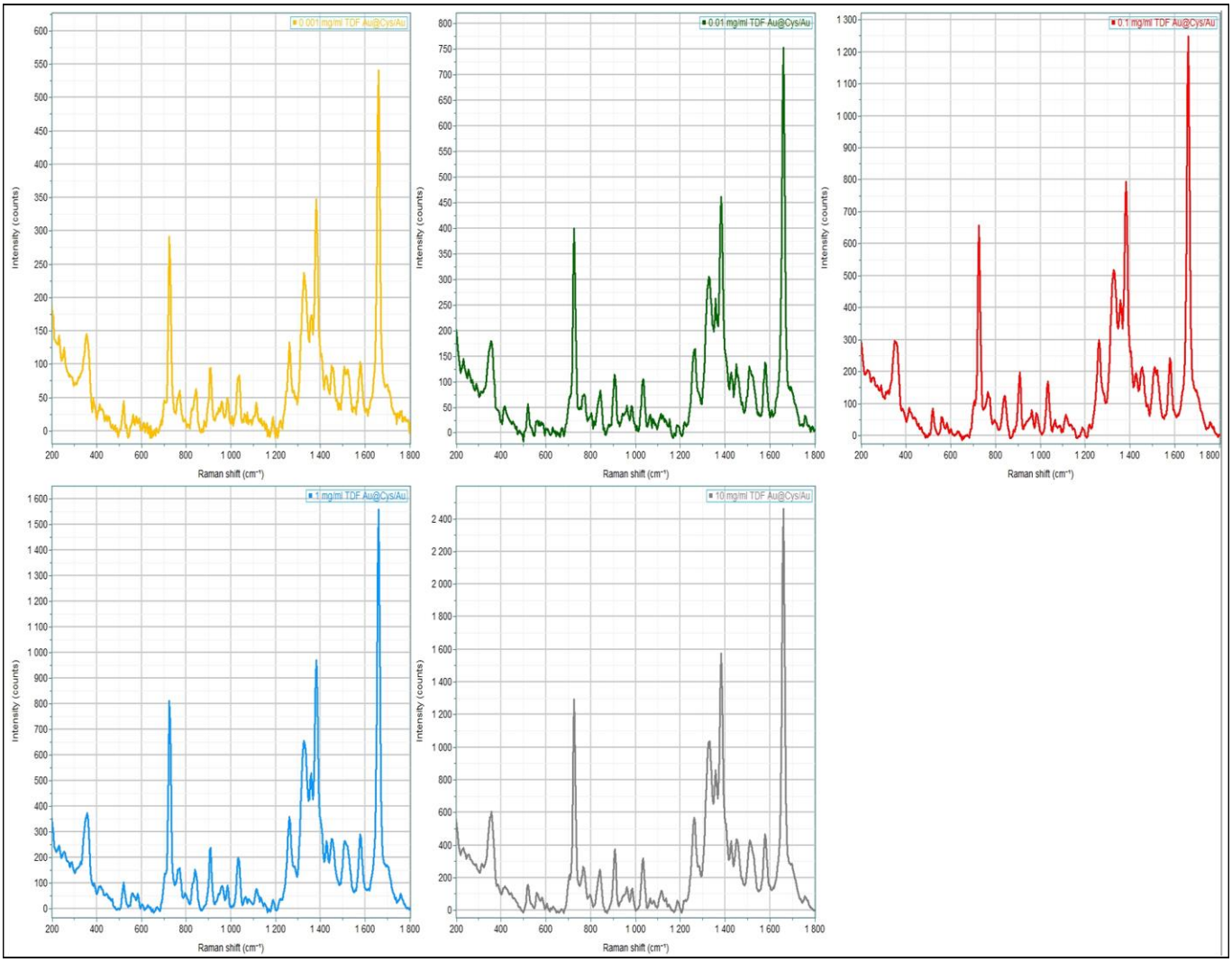

S13: TDF Ag@Cys/Ag spectra

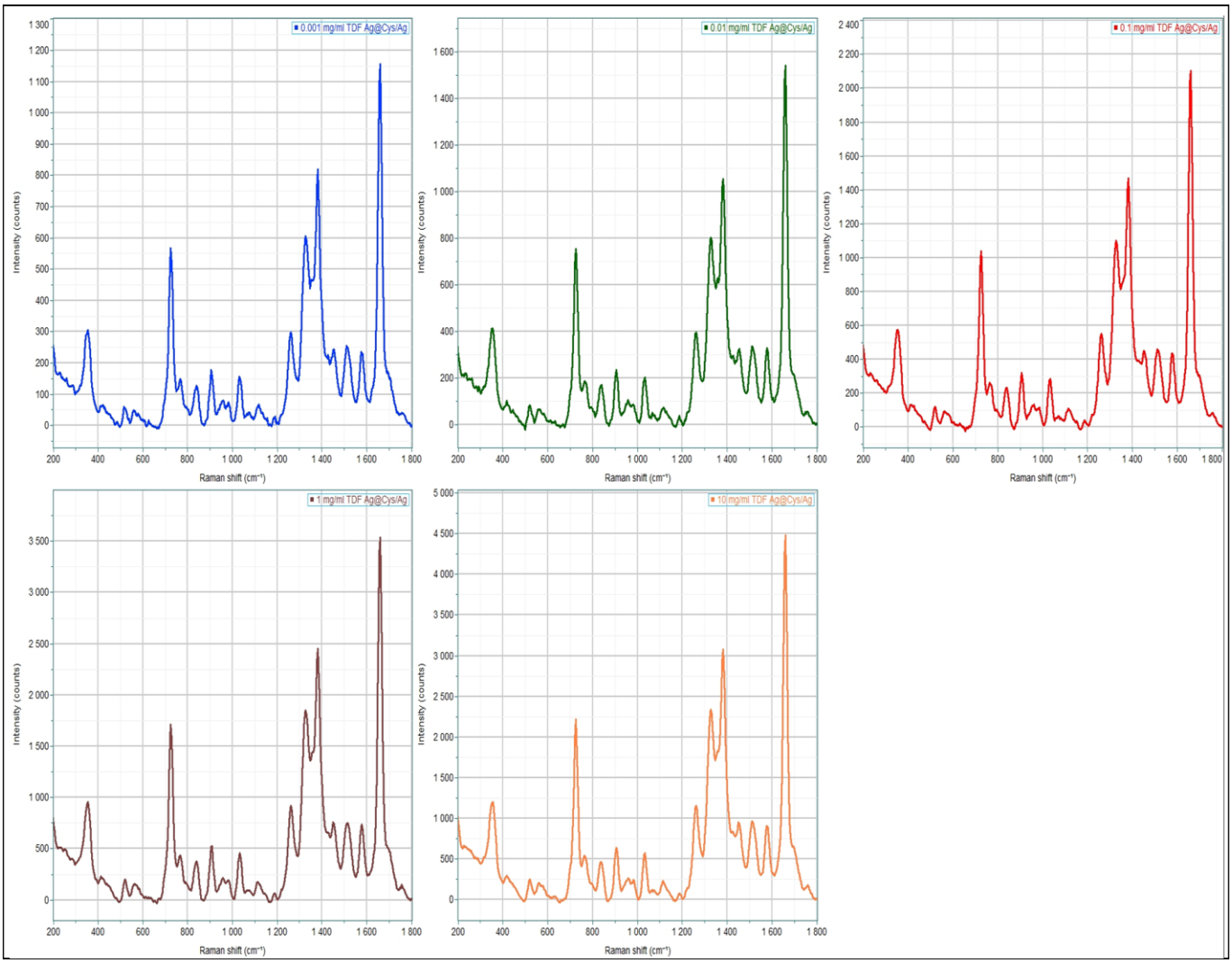

S14: LAM/Glass spectra

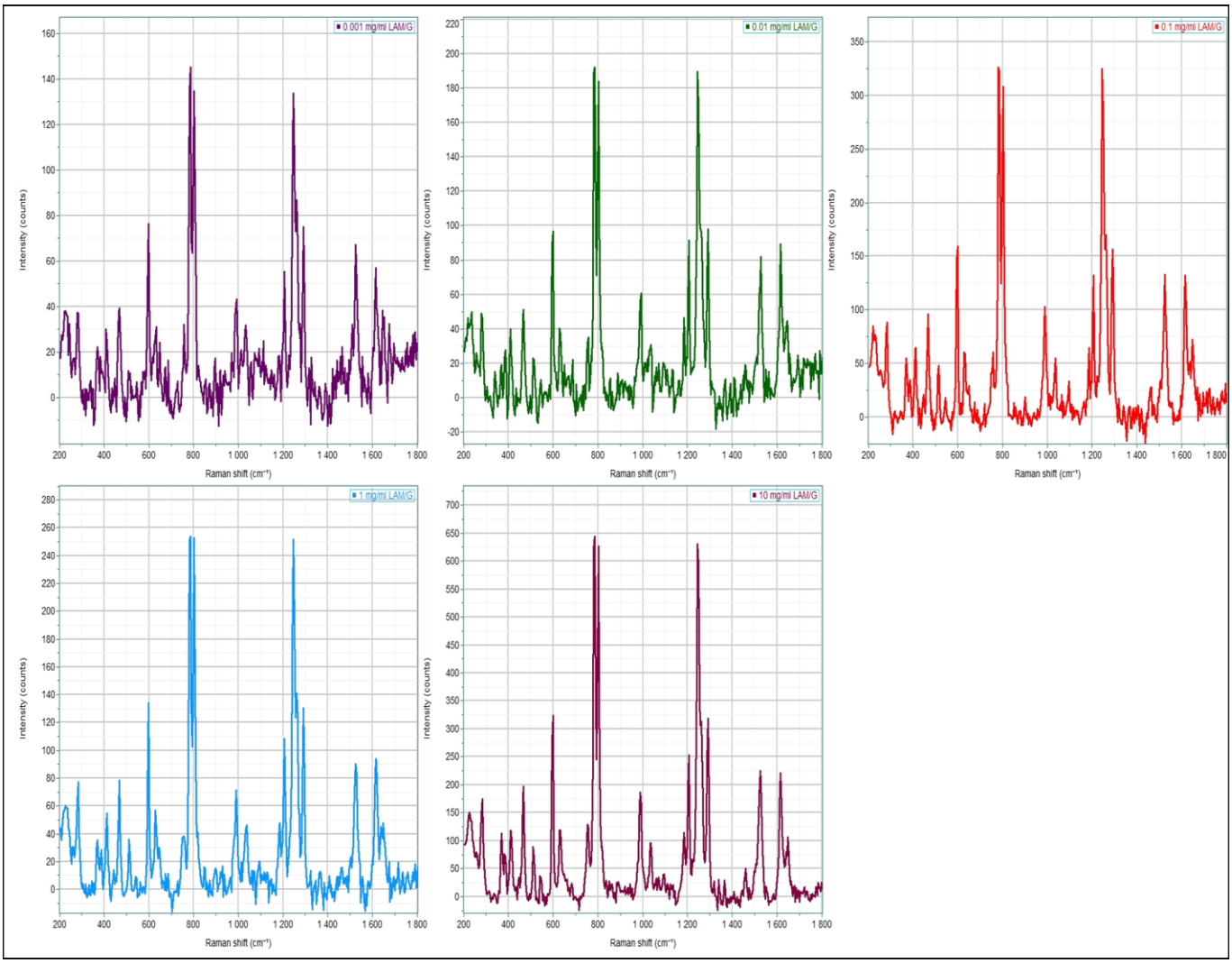

S15: LAM Au@Cit/Au spectra

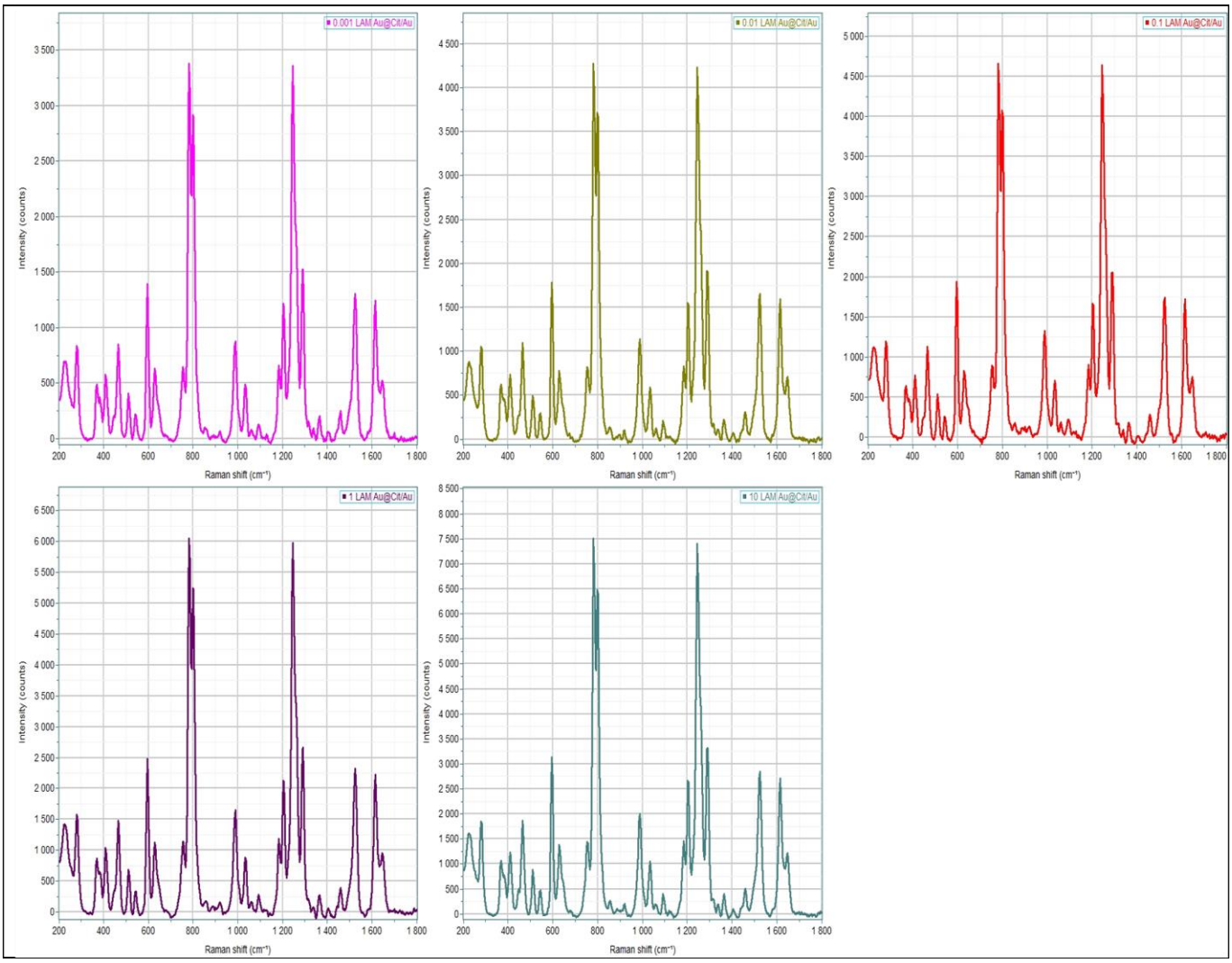

S16: LAM Ag@Cit/Ag spectra

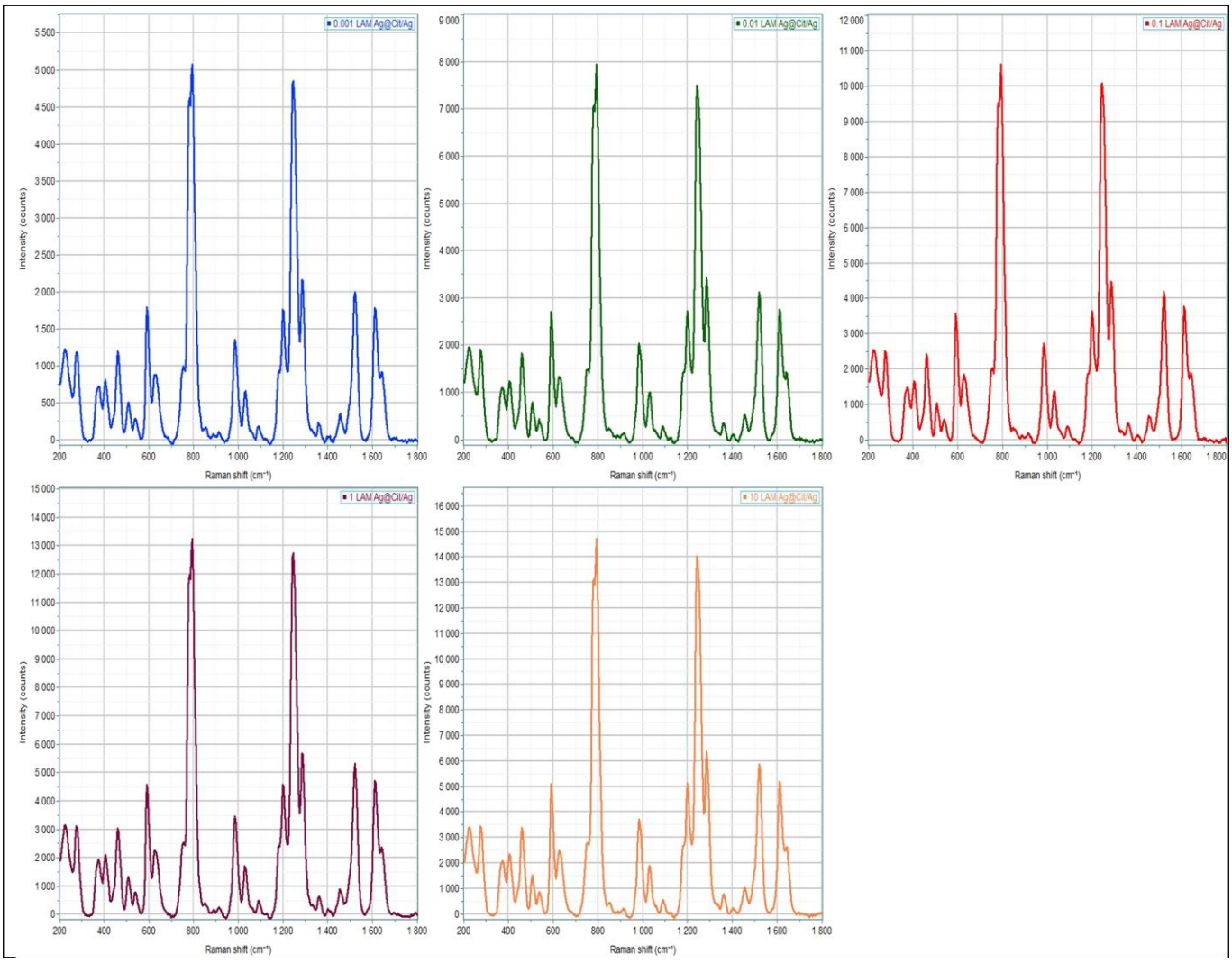

S17: LAM Au@Cys/Au spectra

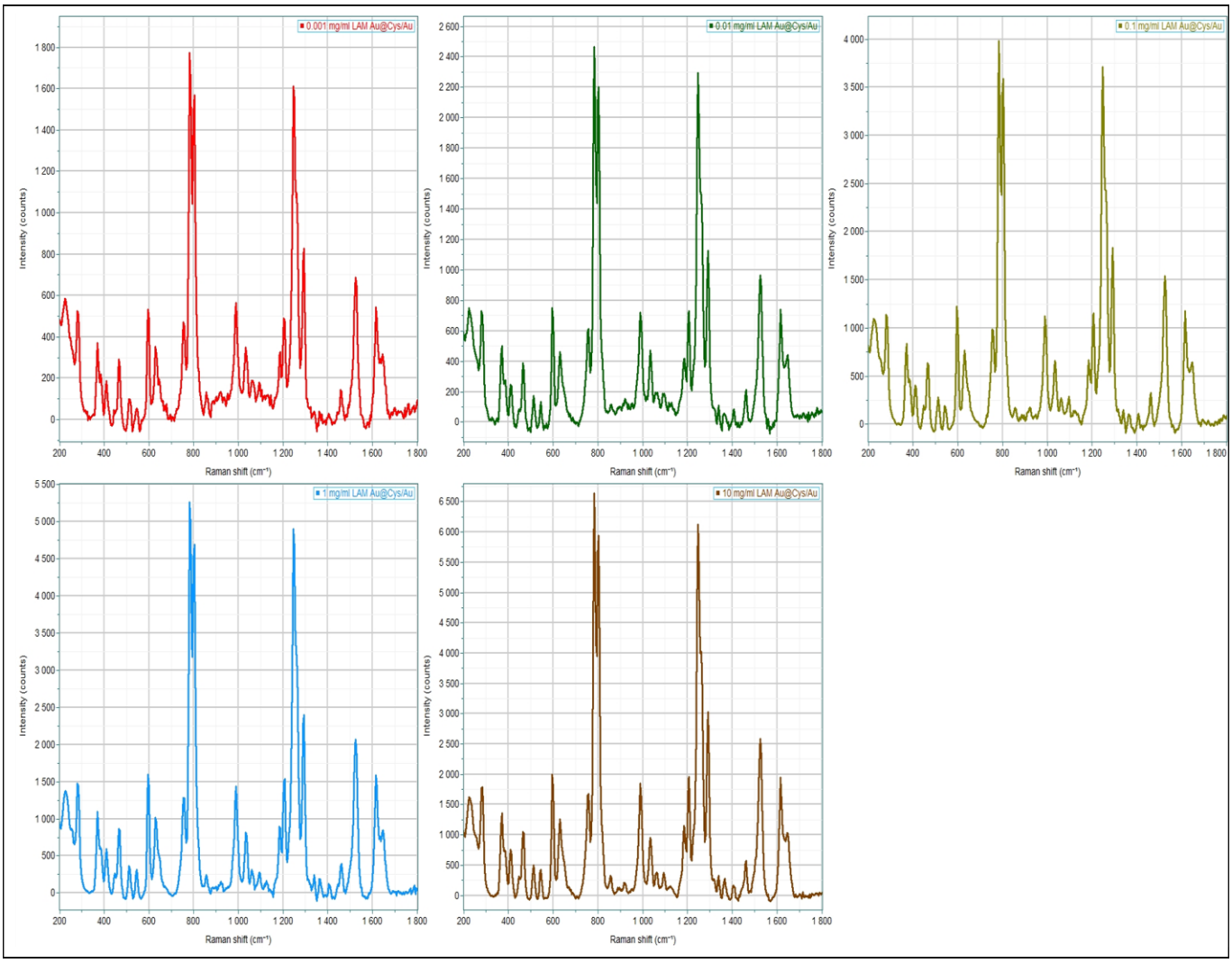

S18: LAM Ag@Cys/Ag spectra

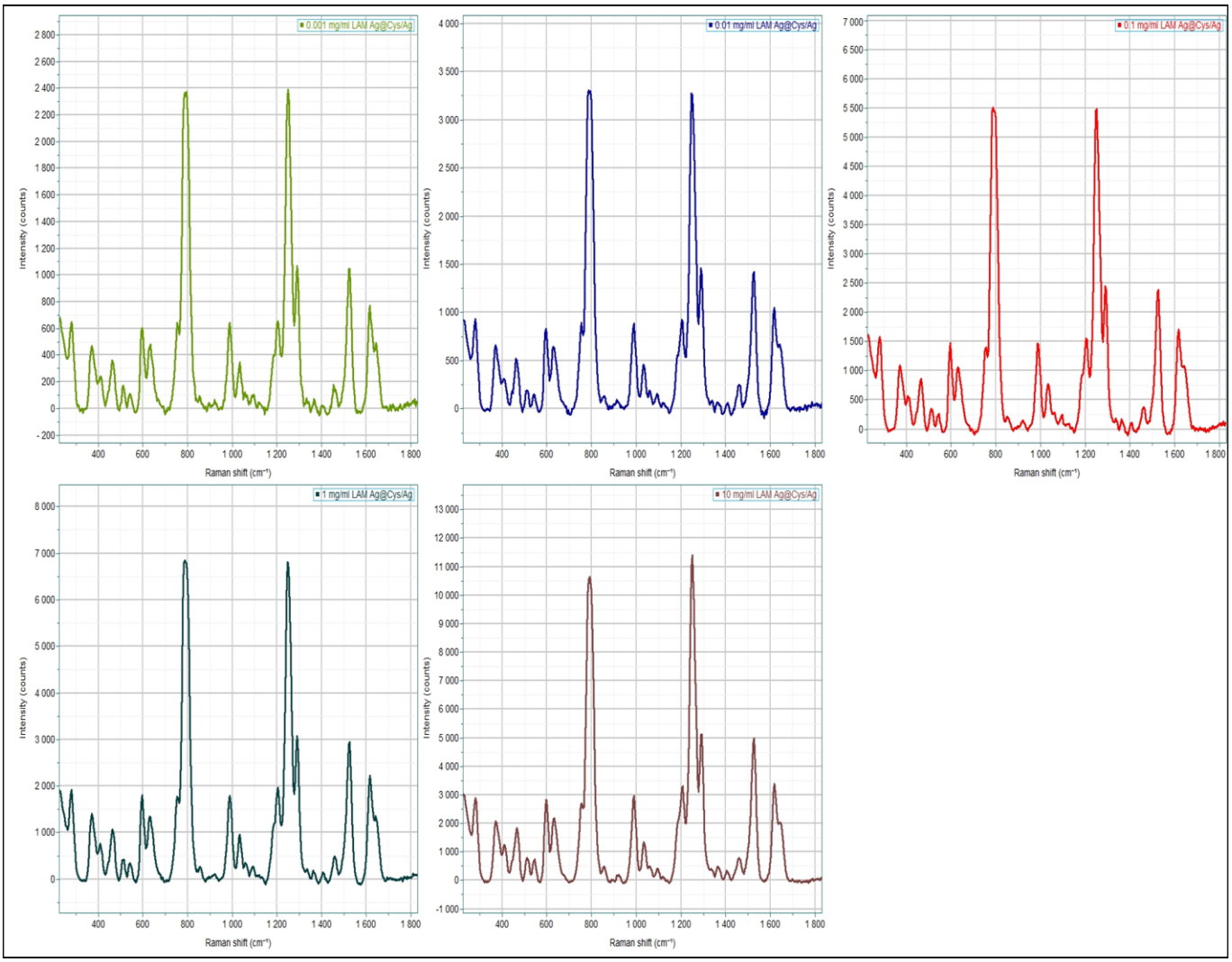

S19: DLG/Glass spectra

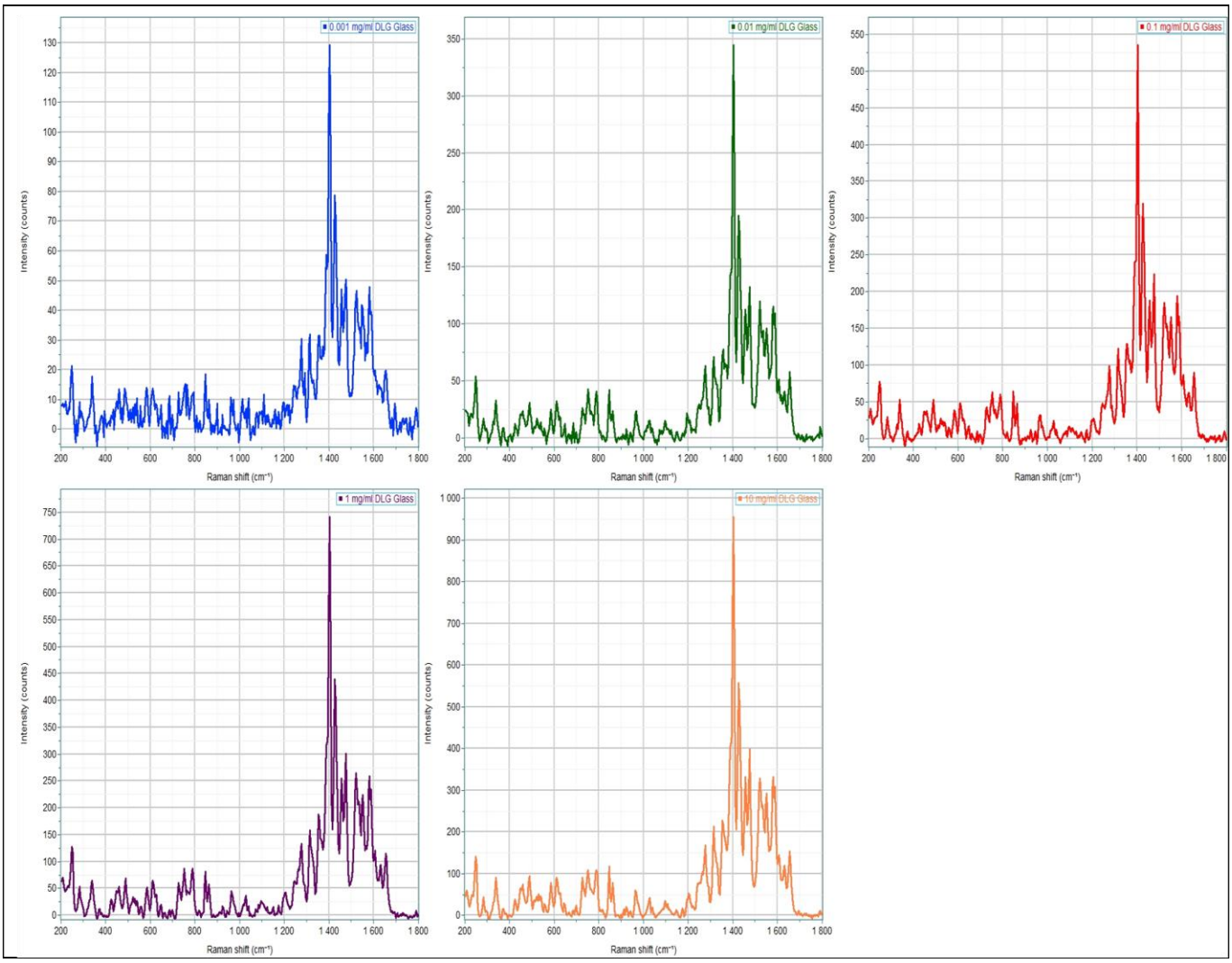

S20: DLG Au@Cit/Au spectra

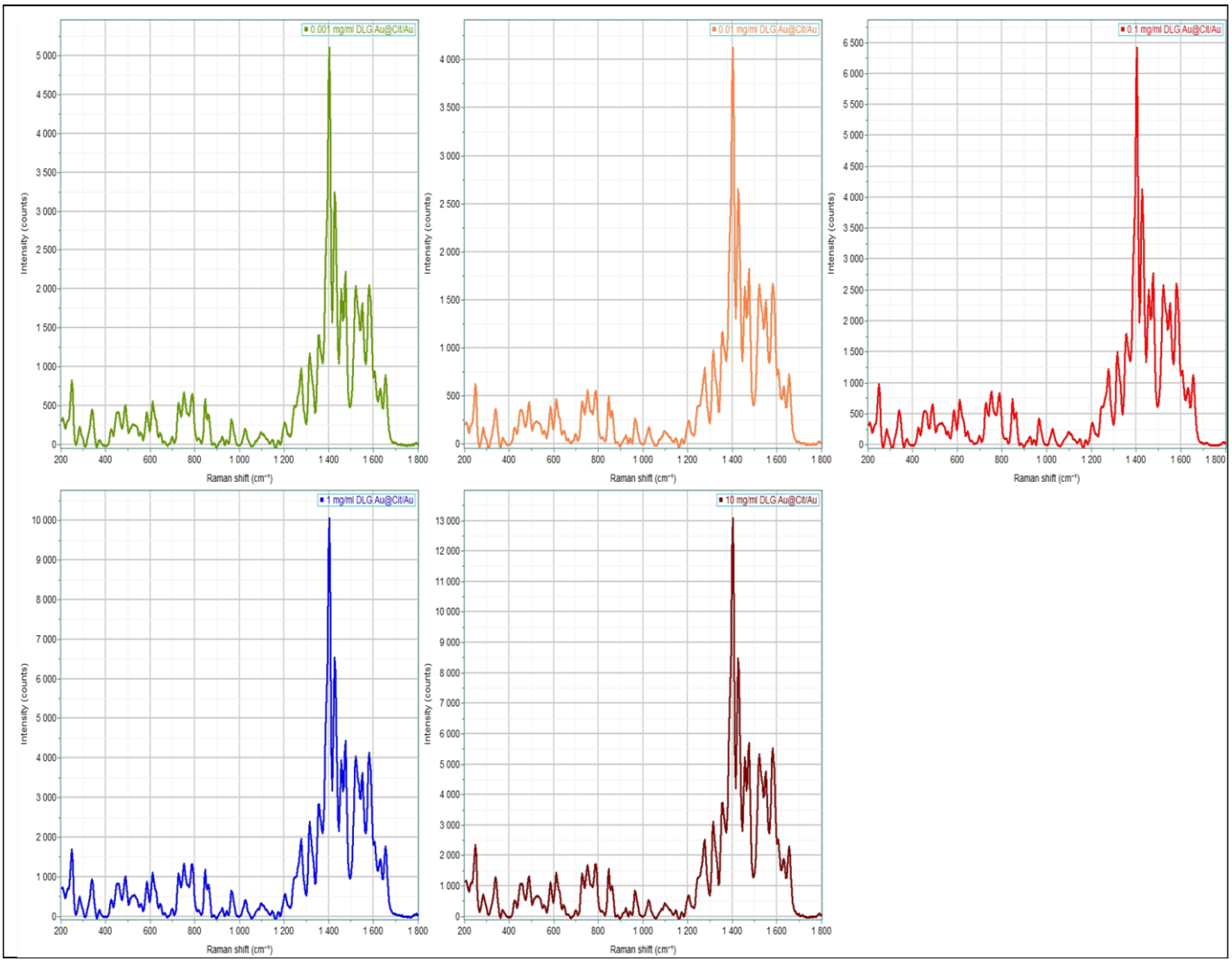

S21: DLG Ag@Cit/Ag spectra

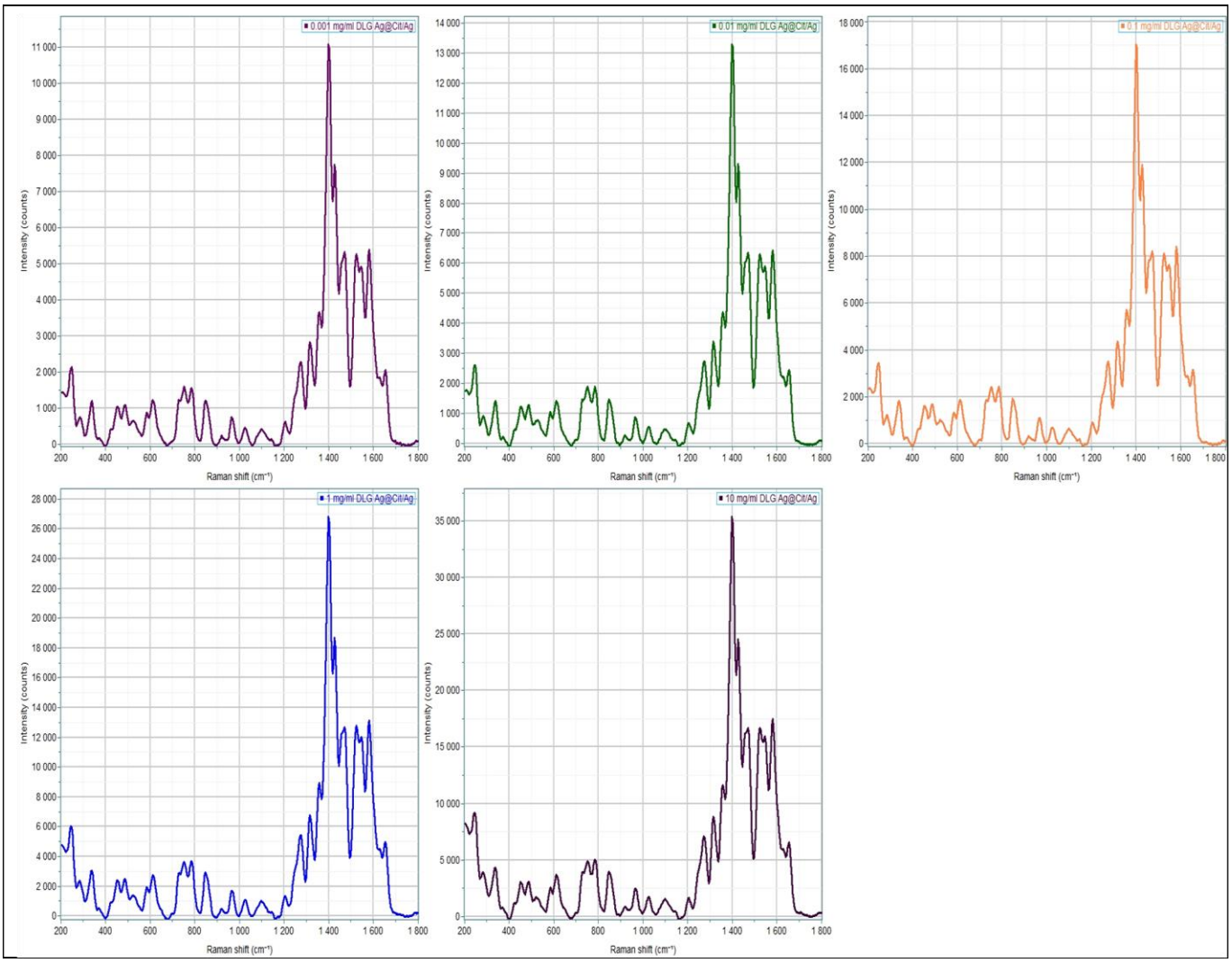

S22: DLG Au@Cys/Au spectra

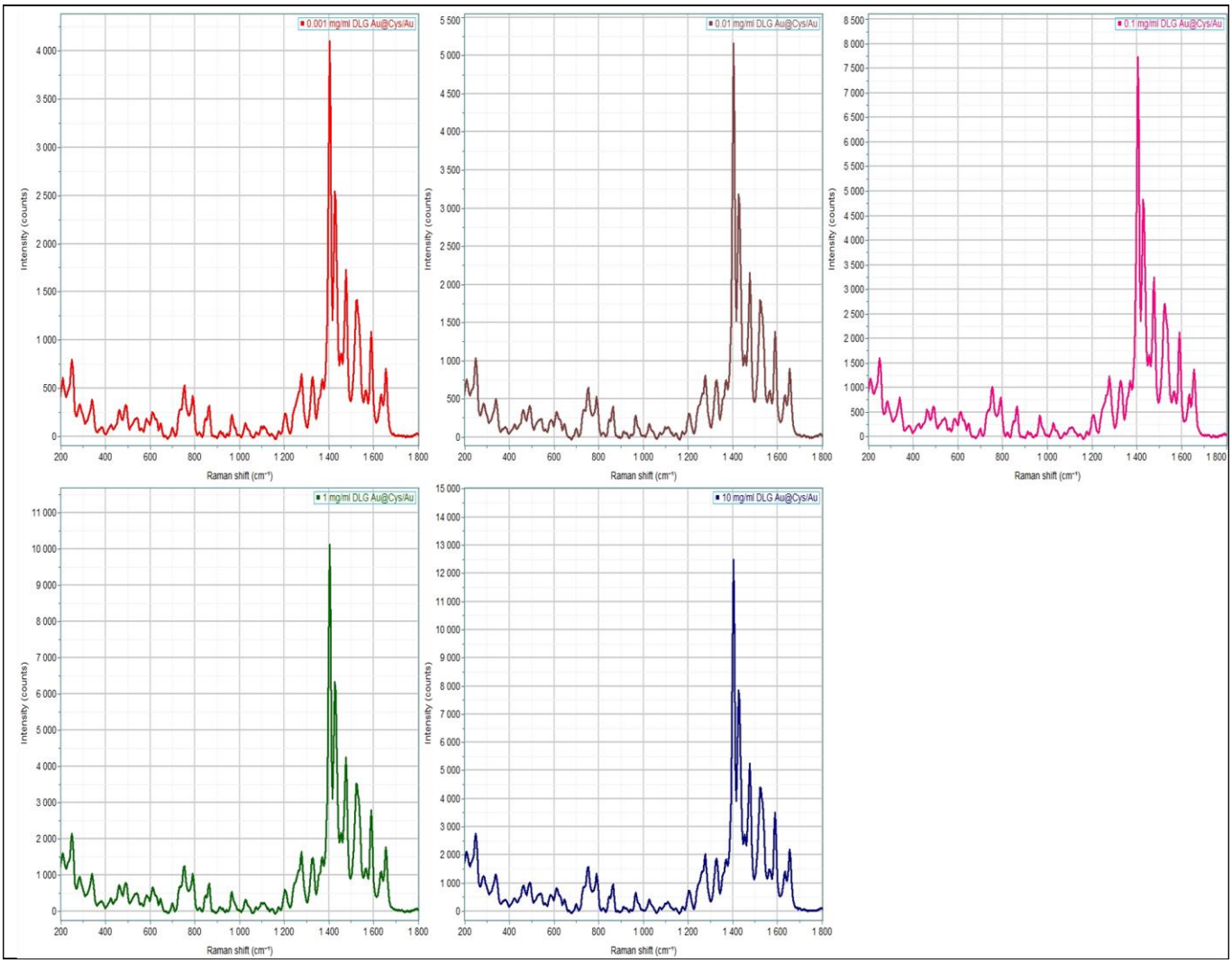

S23: DLG Ag@Cys/Ag spectra

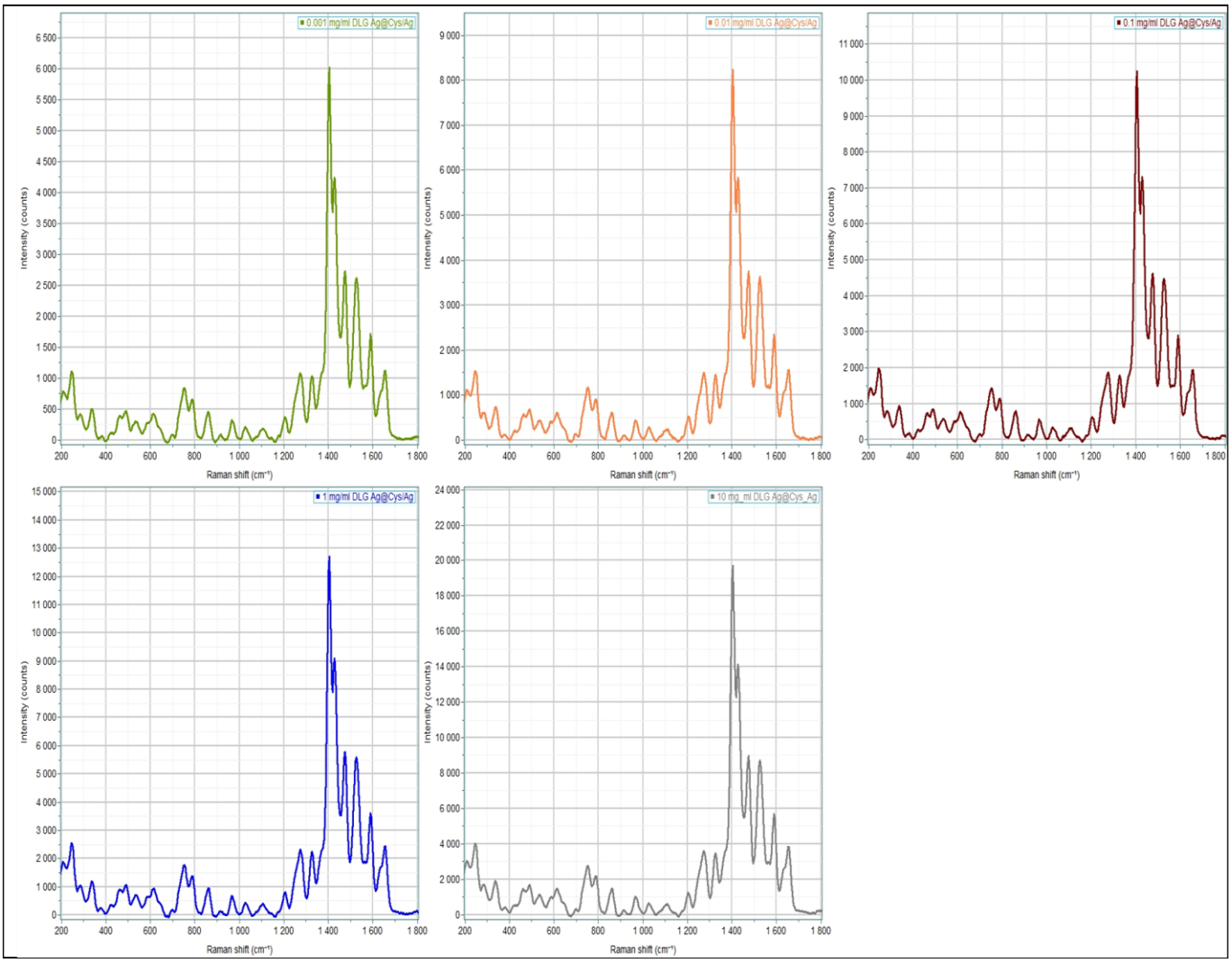

C1: Nanoparticle concentration calculations

In the following calculations, it was assumed that all the initial reagents used were converted into nanoparticles. The solution concentration, metal molar mass and Avogadro's constants were used to calculate the number of nanoparticles per milliliter.

A. Citrate nanoparticles

A1. Au@Citrate

$$\left(\frac{0.43 * 10^{-3} g}{1\ mL}\right)\left(\frac{1\ mol}{197\ g}\right)\left(\frac{6.02 * 10^{23}\ Au\ nanoparticles}{1\ mol}\right) = 1.3 * 10^{18}\ \ Au\ nanoparticles/\ mL$$

A2. Ag@Citrate

$$\left(\frac{0.16 * 10^{-3} g}{1\ mL}\right)\left(\frac{1\ mol}{108\ g}\right)\left(\frac{6.02 * 10^{23} Ag\ nanoparticles}{1\ mol}\right) = 9.1 * 10^{17}\ \ Ag\ nanoparticles/\ mL$$

B. Cysteamine nanoparticles

B1. Au@Cysteamine

$$\left(\frac{1.4 * 10^{-6} g}{1\ mL}\right)\left(\frac{1\ mol}{197\ g}\right)\left(\frac{6.02 * 10^{23}\ Au\ nanoparticles}{1\ mol}\right) = 4.3 * 10^{15}\ \ Au\ nanoparticles/\ mL$$

B2. Ag@Cysteamine

$$\left(\frac{0.1 * 10^{-6} g}{1\ mL}\right)\left(\frac{1\ mol}{108\ g}\right)\left(\frac{6.02 * 10^{23}\ Ag\ nanoparticles}{1\ mol}\right) = 5.5 * 10^{14}\ \ Ag\ nanoparticles/\ mL$$

C2: Statistical calculations for TDF on glass

1. Glass

Linear regression

Concentration (mg/ml)	727 cm^{-1}	1318 cm^{-1}
0	3	0
0.001	1741	1142
0.01	2015	2184
0.1	3280	2102
1	2914	3825
10	3740	3560

Average standard error s_m= 7.65

1.1 727 cm^{-1}, adenine ring

Linear equation from figure 3.16. $y = 670.54x - 64.73,\ R^2 = 0.86;\ n = 5; p < 0.10$

Standard deviation: $s = s_m \times \sqrt{5} = 7.65 \times 2.23 = 17.1$

Mean peak area= 2282

$$RSD = \frac{s}{x(mean)} \times 100 = \frac{17.1}{2282} \times 100 = 0.74\ \%$$

Calibration sensitivity (m)= 670.54

Analytical sensitivity: $\gamma = \frac{m}{s} = \frac{670.54}{17.1} = 39.2$

Limit of detection:

$S_m = \overline{S_{bl}} + ks_{bl}$ $\overline{S_{bl}}$ = 3; k=3, s_m (blank)= 5.37784

s_{bl} = 5.377x2.23= 11.99

$Sm = 3 + 3(5.377x2.23) = 38.9$

$$C_m = \frac{S_m - S_{bl}}{m} = \frac{38.9 - 11.99}{670.54} = 0.05\ mg/ml$$

1.2 1318 cm^{-1}, ring bonds

Linear equation from figure 3.18 for: $y = 736.2x - 441.2, R^2 = 0.91;\ n = 5; p < 0.05$

Standard deviation: $s = s_m \times \sqrt{5} = 7.65 \times 2.23 = 17.1$

Mean peak area= 2315

$$RSD = \frac{s}{x(mean)} \times 100 = \frac{17.1}{2135} \times 100 = 0.75\ \%$$

Calibration sensitivity (m)= 736.2

Analytical sensitivity: $\gamma = \frac{m}{s} = \frac{736.2}{17.1} = 39.2$

Limit of detection (c_m):

$S_m = \overline{S_{bl}} + ks_{bl}$ $\overline{S_{bl}}$ = 3; k=3, s_m (blank)= 5.37784

s_{bl} = 5.377x2.23= 11.99

$Sm = 3 + 3(5.377x2.23) = 38.9$

$$C_m = \frac{S_m - S_{bl}}{m} = \frac{38.9 - 11.99}{736.2} = 0.04\ mg/ml$$

C3: Statistical calculations for TDF on Au@Cit/Au

Concentration (mg/ml)	727 cm^{-1}	1318 cm^{-1}
0	0	0
0.001	23401	28812
0.01	31163	38943
0.1	44582	55615
1	60526	76166
10	78367	99097

Average standard error s_m= 115.43

2.1 727 cm^{-1}, Adenine ring

Linear equation from figure 3.17. $y = 14761x - 11990,\ R^2 = 0.98;\ n = 5; p < 0.01$

Standard deviation: $s = s_m \times \sqrt{5} = 115.43 \times 2.23 = 258$

Mean peak area= 39673

$$RSD = \frac{s}{x(mean)} \times 100 = \frac{258}{39673} \times 100 = 0.64\ \%$$

Calibration sensitivity (m)= 14761

Analytical sensitivity: $\gamma = \frac{m}{s} = \frac{14761}{258} = 57.2$

Limit of detection:

$S_m = \overline{S_{bl}} + ks_{bl}$ $\overline{S_{bl}}$ = 3; k=3, s_m (blank)= 26.2

$s_{bl} = 26.2 \times 2.23$

$Sm = 3 + 3(26.2x2.23) =$178.3

$$C_m = \frac{S_m - \overline{S_{bl}}}{m} = \frac{178.3 - 0}{14761} = 0.01\ mg/ml$$

2.2 1318 cm^{-1}, Ring bonds

Average standard error s_m= 115.43

Linear equation from figure 3.18. $y = 18692x - 15650,\ R^2 = 0.98;\ n = 5; p < 0.01$

Standard deviation : $s = s_m \times \sqrt{5} = 115.43 \times 2.23 = 258$

Mean peak area= 49772

$$RSD = \frac{s}{x(mean)} \times 100 = \frac{258}{49772} \times 100 = 0.51\ \%$$

Calibration sensitivity (m)= 18692

Analytical sensitivity: $\gamma = \frac{m}{s} = \frac{18692}{258} = 72.4$

Limit of detection:

$S_m = \overline{S_{bl}} + ks_{bl}$ $\overline{S_{bl}}$ = 3; k=3, s_m (blank)= 26.2

$s_{bl} = 26.2 \times 2.23$

$Sm = 3 + 3(26.2x2.23) =$178.3

$$C_m = \frac{S_m - S_{bl}}{m} = \frac{178.3 - 0}{18692} = 0.009\ mg/ml$$

C4: Statistical calculations for TDF on Ag@Cit/Ag

Concentration (mg/ml)	727 cm^{-1}	1318 cm^{-1}
0	0	0
0.001	40289	34948
0.01	53445	45788
0.1	91599	78873
1	121710	104700
10	178482	151392

Average standard error s_m= 238.56

3.1 727 cm^{-1}, Adenine ring

Linear equation from figure 3.17. $y = 33566x - 36562,\ R^2 = 0.97;\ n = 5; p < 0.01$

Standard deviation : $s = s_m \times \sqrt{5} = 238.56 \times 2.23 = 531$

Mean peak area= 80920.8

$$RSD = \frac{s}{x(mean)} \times 100 = \frac{531}{80920.8} \times 100 = 0.65\ \%$$

Calibration sensitivity (m)= 33566

Analytical sensitivity: $\gamma = \frac{m}{s} = \frac{33566}{238.56} = 53$

Limit of detection:

$S_m = \overline{S_{bl}} + ks_{bl}$ $\overline{S_{bl}}$ = 3; k=3, s_m (blank)= 26.2

$s_{bl} = 26.2 \times 2.23$

$Sm = 3 + 3(26.2x2.23)$ =178.3

$$C_m = \frac{S_m - \overline{S_{bl}}}{m} = \frac{178.3 - 0}{33566} = 0.005 mg/ml$$

3.2 1318 cm^{-1}, Ring bonds

Linear equation from figure 3.18. $y = 28551x - 30647,\ R^2 = 0.97;\ n = 5; p < 0.01$

Standard deviation : $s = s_m \times \sqrt{5} = 238.56 \times 2.23 = 531$

Mean peak area= 69283.5

$$RSD = \frac{s}{x(mean)} \times 100 = \frac{531}{69283.5} \times 100 = 0.76\ \%$$

Calibration sensitivity (m)= 33566

Analytical sensitivity: $\gamma = \frac{m}{s} = \frac{28551}{238.56} = 119.7$

Limit of detection:

$S_m = \overline{S_{bl}} + ks_{bl}$ $\overline{S_{bl}}$ = 3; k=3, s_m (blank)= 26.2

$s_{bl} = 26.2 \times 2.23$

$Sm = 3 + 3(26.2x2.23) =$178.3

$$C_m = \frac{S_m - \overline{S_{bl}}}{m} = \frac{178.3 - 0}{28551} = 0.006mg/ml$$

ST1: TDF/Au@Cys/Au

Concentration (mg/ml)	Average standard error (s_m)	Peak area (721 cm^{-1})	Peak area (1318 cm^{-1})
0	12.0906	0	0
0.001	86.8782	6351.75	12015.06
0.01	108.19	8721.96	15493.67
0.1	172.776	14287.43	26302.05
1	158.844	17637.86	30348.23
10	325.634	28179.4	33287.88
Mean (Peak area)		12529.73	19574.48
Average error		144.0688	144.0688
RSD (%)		2.564088	1.641287
Standard deviation		321.2734	321.2734
Analytical sensitivity		16.03618	20.65219
Sm		80.88611	80.88611
Limit of detection (mg/ml)		0.0157	0.012191

ST2: TDF/Ag@Cys/Ag

Concentration (mg/ml)	Average standard error (s_m)	Peak area (721 cm^{-1})	Peak area (1318 cm^{-1})
0	6.46208	0	0
0.001	102.09	18501.64	36819.79
0.01	140.253	24598.16	49019.22
0.1	276.088	33927.86	66995.73
1	312.235	55925.61	112658.4
10	571.321	72300.69	142338.8
Mean (Peak area)		34208.99	19574.48
Average error		234.7415	234.7415
RSD (%)		1.53	1.641287
Standard deviation		523.47	523.47
Analytical sensitivity		26.3	52.24
Sm		43.2	43.2
Limit of detection (mg/ml)		0.003	0.0015

ST3: LAM/Glass

Concentration (mg/ml)	Average standard error (s_m)	Peak area (1244 cm^{-1})	Peak area (1318 cm^{-1})
0	275	400	20.82
0.001	15.9	2739.74	1532.08
0.01	17.8	3887.24	1004.52
0.1	19.65	5163.96	2657.32
1	22.8	6661.96	3191.8
10	42.7	13991.36	6369.08
Mean (Peak area)		5474.043333	19574.48
Average error		65.64	65.64
RSD (%)		2.67	1.641287
Standard deviation		146.38	146.38
Analytical sensitivity		15.8	7.49
Sm		2239.75	1860
Limit of detection (mg/ml)		0.79	1.67

ST4: LAM/Au@Cit/Au

Concentration (mg/ml)	Average standard error (s_m)	Peak area (1244 cm^{-1})	Peak area (1318 cm^{-1})
0	26.8843	18858	15035
0.001	178.547	38110	31081.3
0.01	194.253	79540	39097.66
0.1	241.918	95289.91	41804.26
1	311.705	122683.93	54387.82
10	363.711	151869.16	67738.13
Mean (Peak area)		84391	19574.48
Average error		219.5	219.5
RSD (%)		0.58	1.17
Standard deviation		489.4	489.4
Analytical sensitivity		54.54	19.62
Sm		84391	0.0187
Limit of detection (mg/ml)		0.0067	1.67

ST5: LAM/Ag@Cit/Ag

Concentration (mg/ml)	Average standard error (s_m)	Peak area (1244 cm^{-1})	Peak area (1318 cm^{-1})
0	26.89	1178	1050.57
0.001	451.47	198724	87813
0.01	969.93	230867	139625
0.1	1283	412846	182393
1	1615.33	521097	231270
10	1831.6	631542	259765
Mean (Peak area)		332709	150319
Average error		1029.7	1029.7
RSD (%)		0.69	1.52
Standard deviation		2296	2296.23
Analytical sensitivity		53.5	11.6
Sm		1357	1230
Limit of detection (mg/ml)		0.001	0.006

ST7: LAM/Au@Cys/Au

Concentration (mg/ml)	Average standard error (s_m)	Peak area (1244 cm^{-1})	Peak area (1318 cm^{-1})
0	9.5846	0	0
0.001	183.72	33068.15	16904.21
0.01	312.072	47059.88	22946.63
0.1	480.685	76067.8	37371.56
1	615.239	100509.4	48964.97
10	868.981	125641.1	61878.4
Mean (Peak area)		63724	150319
Average error		411	411
RSD (%)		1.44	2.92
Standard deviation		918.1	918.1
Analytical sensitivity		26.7	13
Sm		64.1	64.1
Limit of detection (mg/ml)		0.002	0.005

ST8: LAM/Ag@Cys/Ag

Concentration (mg/ml)	Average standard error (s_m)	Peak area (1400 cm^{-1})	Peak area (1517 cm^{-1})
0	6.46208	0	0
0.001	187.206	33068.15	22718.1
0.01	338.117	47059.88	38523
0.1	550.094	76067.8	99737.17
1	666.796	100509.4	125248.5
10	1096.34	125641.1	167089.4
			0
Mean (Peak area)		788997.	75552
Average error		474.16	474.16
RSD (%)		1.65	0.28
Standard deviation		1057	1057
Analytical sensitivity		91.24	32.5
Sm		43.23	194.8
Limit of detection (mg/ml)		0.0004	0.001

ST9: DLG/Glass

Concentration (mg/ml)	Average standard error (s_m)	Peak area (1400 cm^{-1})	Peak area (1517 cm^{-1})
0	8.56292	0	0
0.001	9.72111	8599	2851
0.01	26.2972	10526	2977
0.1	33.8714	11765	4218
1	69.7075	13800	8870
10	87.9324	24198	9766
			0
Mean (Peak area)		11481	4780
Average error		39.34	29.9
RSD (%)		0.76	1.39
Standard deviation		87.7	66.7
Analytical sensitivity		58.9	29.5
Sm		57.2	26.5
Limit of detection (mg/ml)		0.01	0.01

ST 10: DLG/Au@Cit/Au

Concentration (mg/ml)	Average standard error (s_m)	Peak area (1400 cm^{-1})	Peak area (1517 cm^{-1})
0	29.12	0	0
0.001	478.25	52573	57868
0.01	482.435	82978	85156
0.1	721.876	129097	108828
1	1109.33	202244	160845
10	57.9324	263031	211381
			0
Mean (Peak area)		121653	4780
Average error		479.8	479.8
RSD (%)		0.87	1.02
Standard deviation		1070	1070
Analytical sensitivity		48.9	37.1
Sm		194.8	194.8
Limit of detection (mg/ml)		0.003	0.004

ST 11: DLG/Ag@Cit/Ag

Concentration (mg/ml)	Average standard error (s_m)	Peak area (1400 cm^{-1})	Peak area (1517 cm^{-1})
0	29.12	0	0
0.001	1998	397639	213071
0.01	1697.77	556002	295762
0.1	3407.97	855867	403005
1	4059.78	1346780	632476
10	5723.24	1577697	726190
			0
Mean (Peak area)		788997.	378417
Average error		2819.	479.8
RSD (%)		0.79	0.28
Standard deviation		6287	1070
Analytical sensitivity		50.15	133
Sm		194.8	194.8
Limit of detection (mg/ml)		0.0006	0.001

ST 12: DLG/Au@Cys/Au

Concentration (mg/ml)	Average standard error (s_m)	Peak area (1400 cm^{-1})	Peak area (1517 cm^{-1})
0	6.46208	0	0
0.001	187.206	33068.15	22718.1
0.01	338.117	47059.88	38523
0.1	550.094	76067.8	99737.17
1	666.796	100509.4	125248.5
10	1096.34	125641.1	167089.4
			0
Mean (Peak area)		788997.	75552
Average error		474.16	474.16
RSD (%)		1.65	0.28
Standard deviation		1057	1057
Analytical sensitivity		91.24	32.5
Sm		43.23	194.8
Limit of detection (mg/ml)		0.0004	0.001

ST 13: DLG/Ag@Cys/Ag

Concentration (mg/ml)	Average standard error (s_m)	Peak area (1400 cm^{-1})	Peak area (1517 cm^{-1})
0	6.46208	0	0
0.001	187.206	33068.15	22718.1
0.01	338.117	47059.88	38523
0.1	550.094	76067.8	99737.17
1	666.796	100509.4	125248.5
10	1096.34	125641.1	167089.4
			0
Mean (Peak area)		788997.	75552
Average error		474.16	474.16
RSD (%)		1.65	0.28
Standard deviation		1057	1057
Analytical sensitivity		91.24	32.5
Sm		43.23	194.8
Limit of detection (mg/ml)		0.0004	0.001